Springer Theses

Recognizing Outstanding Ph.D. Research

Xabier Marcano

Lepton Flavor Violation from Low Scale Seesaw Neutrinos with Masses Reachable at the LHC

Springer

Springer Theses

Recognizing Outstanding Ph.D. Research

Aims and Scope

The series “Springer Theses” brings together a selection of the very best Ph.D. theses from around the world and across the physical sciences. Nominated and endorsed by two recognized specialists, each published volume has been selected for its scientific excellence and the high impact of its contents for the pertinent field of research. For greater accessibility to non-specialists, the published versions include an extended introduction, as well as a foreword by the student’s supervisor explaining the special relevance of the work for the field. As a whole, the series will provide a valuable resource both for newcomers to the research fields described, and for other scientists seeking detailed background information on special questions. Finally, it provides an accredited documentation of the valuable contributions made by today’s younger generation of scientists.

Theses are accepted into the series by invited nomination only and must fulfill all of the following criteria

- They must be written in good English.
- The topic should fall within the confines of Chemistry, Physics, Earth Sciences, Engineering and related interdisciplinary fields such as Materials, Nanoscience, Chemical Engineering, Complex Systems and Biophysics.
- The work reported in the thesis must represent a significant scientific advance.
- If the thesis includes previously published material, permission to reproduce this must be gained from the respective copyright holder.
- They must have been examined and passed during the 12 months prior to nomination.
- Each thesis should include a foreword by the supervisor outlining the significance of its content.
- The theses should have a clearly defined structure including an introduction accessible to scientists not expert in that particular field.

More information about this series at http://www.springer.com/series/8790

Xabier Marcano

Lepton Flavor Violation from Low Scale Seesaw Neutrinos with Masses Reachable at the LHC

Doctoral Thesis accepted by
the Autonomous University of Madrid, Madrid, Spain

Springer

Author
Dr. Xabier Marcano
Laboratory for Theoretical Physics of Orsay, CNRS
University of Paris-Sud
Orsay, France

Supervisor
Prof. María José Herrero
Departamento de Física Teórica, Instituto de Física Teórica
Universidad Autónoma de Madrid
Madrid, Spain

ISSN 2190-5053 ISSN 2190-5061 (electronic)
Springer Theses
ISBN 978-3-319-94603-0 ISBN 978-3-319-94604-7 (eBook)
https://doi.org/10.1007/978-3-319-94604-7

Library of Congress Control Number: 2018945459

Printed on acid-free paper

This Springer imprint is published by the registered company Springer International Publishing AG part of Springer Nature
The registered company address is: Gewerbestrasse 11, 6330 Cham, Switzerland

Nire aitxitxari,
honaino bere erruz heldu naizelako.

Supervisor's Foreword

The Standard Model (SM) of elementary particles and their fundamental interactions was finally completed in 2012, when the ATLAS and CMS experiments at the Large Hadron Collider (LHC) discovered the missing piece in the model, the Higgs boson. It was the last step of a long journey where both theory and experiment worked together to build one of the most successful theories in physics. Looking back, we realized that flavor physics was at the origin of many breakthroughs in particle physics. Looking forward, we could expect the same for beyond the SM (BSM) field.

Nowadays, there are some theoretical and experimental open problems showing that the SM needs to be extended, being one of the clearest related to neutrino physics. In the last two decades, several experiments have observed neutrino oscillations, a forbidden phenomenon in the SM and directly related to the existence of nonzero neutrino masses. The origin of these masses is still a mystery. It could be different from the rest of the fermions, and it is directly related to their Majorana or Dirac nature. In order to distinguish among the many theoretical models trying to explain neutrino masses, we could again invoke flavor physics to help us in this task. This is the main philosophy followed in this thesis by Xabier Marcano.

Along this thesis, Xabier Marcano explores the phenomenological implications on lepton flavor violating (LFV) physics in the so-called low-scale seesaw models, well-motivated theories for explaining the smallness of neutrino masses. This thesis contains new and relevant contributions to LFV processes, in particular in the Z boson decays and in the Higgs sector, a research area that the LHC is exploiting since the discovery of the new boson. The results in this thesis are interesting not only for the Z and H boson decays, but also for other LFV processes mediated by these particles, such as three-body lepton decays $\ell_m \to \ell_k \ell_k \ell_k$, μ-e conversion in heavy nuclei, or many other processes that are and will be looked for at present and future experiments. Moreover, as the new heavy neutrinos in these models could potentially be produced at the LHC, Xabier Marcano also investigates new experimental signals in which LFV plays a crucial role.

As a final remark, I would like to emphasize that this thesis, beyond presenting new results and many useful formulas, contains a broad introduction about the importance of LFV for BSM and its connection with neutrino physics. For the non-experts in the field, this thesis is a good starting point to understand how lepton flavor violating physics could help solving the quest of the origin of neutrino masses.

Madrid, Spain
April 2018

Prof. María José Herrero

Abstract

Flavor physics has been crucial in the development of particle physics, and it will keep being so in the future. Nowadays, this kind of process, in particular lepton flavor changing observed in neutrino oscillations, gives us the clearest evidence of the fact that the Standard Model of fundamental interactions needs to be modified. Some of the most popular theories that try to assess this issue postulate the existence of new heavy right-handed neutrinos, with masses in the energy range that the LHC experiment is currently exploring. In this thesis, we study the connection between the possible existence of these neutrinos and charged lepton flavor changing physics. We consider the inverse seesaw model as a particular realization of a low-scale seesaw model and analyze its lepton flavor violating phenomenology, in particular the Higgs and Z boson decays to two charged leptons of different flavor. Moreover, we also explore the possibility of having new exotic lepton flavor violating signals at the LHC, coming from the production and decay of these new heavy neutrinos.

Acknowledgements

A long journey comes here to its end. One feels like Frodo and Sam at Mount Doom, exhausted after a long way, but satisfied to have completed it. Along these years, I have fought against books, computations and codes, I have discussed with people over and over again, and I have dedicated enough hours as to come and back again from Mordor a couple of times. And yet, looking behind, I realize all that I have learnt, and, above all, how much I have enjoyed. Because, in the end, all this should be about that, about enjoying. And I have been able to do so thanks to the people for whom, at this point, I have nothing but words of gratefulness.

The first responsible for all this has been *la jefa*, María José. We might have had some bad moments, but we have also had good ones. Starting at the master, we have gone through five years of discussions to reach the throne of stubbornness. I still do not know who won this war. In any case, all that made me learnt about physics and about much more. You have taught me to fight for my beliefs, for my own thoughts, to follow what my intuition says, although sometimes it might look as a nonsense, because that is how in the end one finds the solution to any problem in physics and in life. With you I have taken my first steps as a researcher and that is something I will always keep with me.

Looking back, I see myself in the bachelor confronting my first physics problems with my classmates, and with this I obviously mean throwing chalk pieces to target with he-who-must-not-be-named on it. We were really good at that. I enjoyed a lot studying with Alize, Ander and María. We built a great group, the best one I have been part of, as we were capable of solving even the unsolvable problems. We spent a lot of hours together, specially you and I, Reto. Together we proved that one can obtain a *Bikain* degree with specialization in ping-pong with extreme weather conditions.

Later on I landed at the IFT, an environment which was hard to improve in order to do those weird things we do and that we like so much. Specially because of the people that live in it. Here I have met forever friends and colleagues, because spending so much time together is really bonding. And if I have spent a lot of time with someone, that has been Josu. Master, schools, workshops… we felt dumber than everyone a lot of times, but being together helped us to move forward and to solve any problem with just one kick.

Javi, you were the last one to arrive at the office, but you soon deserved your place in it. You contributed to the card games, Simpsons and football, even as a *comunio* consultant, I could not have asked for much more. I was glad to leave the office and the King in the Poch crown in good hands. Take care of them and, most importantly, do not lose them in a crazy bet.

Víctor, you have been the example to follow. I have always seen in you the way of surviving in this phenoworld, sometimes so hard and unfair for students, who work more than anyone and whose results never come out as expected. But you were capable of dealing with it with a smile, always seeing the bright side and showing us that if you persevere things end up working. I have really enjoyed having you around, talking with you about physics and preparing our FAE lessons, and I really wish that we will finally work together.

Irene, Miguel… you were weirdos, always playing with strings, but we loved you anyway, and we made fun of, I mean with, you. By the way, I am still waiting for the video… Together with Ana, Leyre, Aitor and Santi I have had lots of fun, both inside and outside of the IFT, playing Pocha or at la Pocha. Also with the members of the IFuTsal, and I hope that now that I am not a burden, you could bring the cup to the fifth floor.

Beyond the students, the IFT has brought me the opportunity of discussing with experts of this world and ambush them with questions. Thanks to Enrique for his patience, for having answered all my questions, for making me think about new ones and for answering those new ones too. To Carlos, because you know everything, and because you have given me the opportunity to have a glimpse of the outreach world. To Sven, for his super excitement about phenomenology and for the beer, something I hope he will show in a *Pheno-Beer* some day. To Jesús, for sharing with me his infinite bibliography. To Luca, Choco et al., for showing me that you can be a great physicist and at the same time a great human being, although I have not yet forgiven you for the *Pheno-Coffee* mess… And above all, to Juanjo. You are a tornado of wisdom, of passion for physics. From you I have learnt a lot about physics, but also a lot about enjoying it. I have to admit that the fourth floor at the IFT has not been the same without you.

Thanks to the members of the committee, for accepting my invitation and for dedicating their time to evaluate this thesis.

I would also like to thank my older brothers. Miguel, you welcomed us in your office and you taught us the basic rules to survive in this world, like the one of getting a couch and a beamer for the office. Ana, you gave us the first impulse at the early days. And Ernesto, what can I say to you, you have always been there, helping me with everything, inside and outside work. I have had a lot of fun working with you and I hope we keep doing so, because if we don't, you won't get tickets for Ipurua.

During these years I have had the opportunity to work with amazing people. Besides the ones already mentioned, I have to thank Cédric, for having the patience of sharing his knowledge about what, in the end, has been the pillar of this thesis.

To my godmother Valentina, for her advice. To Ale and Roberto, for having computed even the loops of the shoelaces. To Richard, although we have not worked together yet, for showing me that *collider physics* can be fun. To the Chiral Troupe and to their meetings that were an excellent material for a *13 Rue del Percebe* story. Thanks to all of you for helping me work this thesis out.

Beyond physics, I have felt the support of a lot of people. In Madrid, I had my half Danish friends, specially the Sergios, Miguel and Blabla, and this latter one has to be included for your amount of talking. Also thanks to Carmen and Luis, for making me feel like home since the first moment.

In Eibar I left my family, the one that never forgot me despite the years I spent away. I want to thank my *Ama*, for always and so much fighting for all of us; to my *Aita*, for teaching me so many things, like football, cooking, puzzles and, above all, the Athletic; to my sister, for making us laugh with her extravagant stories; to my aunts and uncles, for always showing me their support wherever I did; to my *Amama*, for cooking the best *fritos* in the world; and specially to my *Aitxitxa*, for putting the numbers in my head during all those evenings teaching me multiplications in his living room, for making me realize how fun it is to wonder about why things happen. Eskerrik asko.

There is also the other family, the one chooses. La mosca, Ibargain, Argatxa… the name is not important, people do not change. Thanks for being always there, for offering me a place where I can forget about everything, where I can be lazy without thinking about anything else, something we are really good at. Thanks for not letting me lose the *Ilusión* of returning to the Holy Land and for painting my face *color esperanza*. MGHP.

At this point, there is only one name missing, albeit it is the one that should have appeared first and with golden letters. More than anyone, you helped me within physics and beyond, as when you bring me to the Zoo to see the raccoons… Claudia, it is you, because you made this work possible with all your patience and effort for solving my problems, for turning my bad days into good ones. Having you with me makes things just better and makes me feel something difficult to explain with words. Or, if there was a word for it, that would be Fringe. Indeed.

Contents

Chapter 1
Introduction

The 4th of July of 2012, the ATLAS and CMS collaborations at the CERN Large Hadron Collider (LHC) announced the discovery [1, 2] of the last missing piece of the Standard Model (SM) [3–6] of fundamental interactions, the Higgs boson. This discovery completed one of the most successful theories in the annals of Physics, a predictive model able to describe with an extraordinary precision most of the known phenomena in Particle Physics. Nevertheless, there are at present some experimental evidences, as neutrino masses, dark matter or the baryon asymmetry of the universe, and theoretical issues, like the hierarchy problem, the strong-CP problem or the flavor puzzle, which the SM fails to explain, inviting us to a journey towards new physics beyond the SM (BSM).

The SM is a quantum field theory based on the $SU(3)_C \times SU(2)_L \times U(1)_Y$ gauge symmetry that describes three of the four known fundamental interactions among elemental particles, i.e., the strong, weak and electromagnetic interactions. To its particle spectrum belong the fermions, constituents of matter, the spin one bosons, force carriers, and the Higgs scalar boson, the remnant of the mass generation procedure via the Brout-Englert-Higgs (BEH) mechanism [7–10]. This mechanism explains how the spontaneous electroweak symmetry breaking (EWSB) generates the observed masses for the gauge W and Z bosons, as well as for all the fermions but the neutrinos, which remain massless in the SM.

Historically, experimental searches for flavor violating processes have been essential for the theoretical developments in Particle Physics, as the Glashow-Iliopoulos-Maiani (GIM) mechanism [11] for explaining the lack of signal from flavor changing neutral currents or the Cabibbo-Kobayashi-Maskawa (CKM) quark mixing matrix [12, 13] for the flavor changing charged currents. Likewise, the most clear experimental evidence for new physics at present comes from lepton flavor violation (LFV) in the neutrino sector. As we just said, neutrinos are massless by construction in the SM. However, experimental evidences of LFV in neutrino oscillations, first observed by the Super-Kamiokande [14] and SNO [15, 16] collaborations, have showed that neutrinos do have masses, implying that the SM needs

X. Marcano, *Lepton Flavor Violation from Low Scale Seesaw Neutrinos with Masses Reachable at the LHC*, Springer Theses, https://doi.org/10.1007/978-3-319-94604-7_1

to be modified. Moreover, if ongoing or future experiments could detect a positive signal from the yet not observed LFV processes in the charged sector, a new window to physics beyond the SM and beyond neutrino masses would be opened.

Looking at the SM particle spectrum, we see that the absence of right-handed (RH) neutrino fields in the theory forbids the neutrinos from interacting with the Higgs field and, thus, from acquiring a mass after the EWSB. Therefore, the simplest way of incorporating neutrino masses to the SM would be adding the missing RH neutrino fields, ν_R. This way, neutrinos could interact with the Higgs field via a Yukawa coupling Y_ν and obtain, after the EWSB, a Dirac mass $m_D = vY_\nu$ proportional to the Higgs vacuum expectation value (vev), which we normalize as $v = 174$ GeV. Nonetheless, this minimal extension of the SM sets out further questions: why are neutrinos so different than the rest of the fermions? Why are their masses much smaller with respect to other fermion masses? Moreover, since neutrinos have no color nor electric charge, they could be Majorana fermions, i.e., they could be their own antiparticles. If true, this would be certainly a novelty in Particle Physics.

Having a closer look to the new added ν_R fields, we realize that they are singlets under the full SM gauge group and, therefore, there is nothing that forbids them from having a Majorana mass m_M. These two different masses, m_D and m_M, are the basic ingredients of the well known type-I seesaw model [17–21], which usually assumes that the Majorana mass scale m_M is much heavier than m_D and than the electroweak scale v. In such case, the physical neutrino spectrum consists on one heavy and one light Majorana neutrino per generation, with masses of the order of m_M and m_D^2/m_M, respectively. Therefore, the type-I seesaw elegantly explains the smallness of the observed light neutrino masses as the ratio of two very distinct mass scales m_D and m_M. Inspecting the light neutrino mass scale $m_\nu \sim m_D^2/m_M$, we also see that in order to have the experimentally suggested $m_\nu \sim \mathcal{O}(\text{eV})$ with large Yukawa couplings $Y_\nu \sim \mathcal{O}(1)$, we need very heavy type-I seesaw masses of $m_M \sim \mathcal{O}(10^{14}\text{ GeV})$. On the other hand, lighter right-handed neutrino masses at the TeV range would demand small couplings $Y_\nu \sim \mathcal{O}(10^{-5})$. One way or the other, most of the phenomenology is suppressed in this type-I seesaw model. For instance, small corrections to the mass of the Higgs in this kind of models have been found in a complementary work that has not been included in this Thesis [22]. Therefore, the simplicity of this argument is what makes this model appealing and, at the same time, what makes it difficult to be tested in other low energy observables beyond the light neutrino masses themselves.

Interesting variations of this simple type-I seesaw model that have a much richer phenomenology are the low scale seesaw models. In this kind of models, some new symmetry is invoked with the aim of protecting the light neutrinos of having large masses and, therefore, allowing the new heavy neutrinos to have lower masses and large Yukawa couplings at the same time. A particular realization of these low scale seesaw models, on which we will focus this Thesis, is the inverse seesaw (ISS) model [23–25], which assumes an approximately conserved total lepton number (LN) symmetry. In the limit of exact LN conservation, the light neutrinos will be massless. However, if this symmetry is broken by some mass parameter, the light neutrinos have a small Majorana mass proportional to this LN breaking parameter.

On the other hand, we can expect this parameter to be naturally small, in the sense of 't Hooft [26], since setting it to zero increases the symmetry of the model. Therefore, in the ISS model the lightness of the neutrino masses is related to the smallness of a LN symmetry breaking mass parameter.

In the ISS model, the above demanded small LN breaking is obtained by introducing new fermionic singlets in pairs (ν_R, X) of opposite LN, and assuming that the LN conservation is only violated by a small Majorana mass μ_X for the X fields. Then, the physical spectrum consists of light Majorana neutrinos with masses suppressed by the smallness of μ_X, and two heavy nearly degenerate Majorana neutrinos per generation, which form pseudo-Dirac pairs and indeed behave almost as Dirac fermions, contrary to the heavy neutrinos of the standard type-I seesaw. Interestingly, since the μ_X scale ensures the smallness of light neutrino masses, the heavy neutrino states can have, at the same time, both large Yukawa couplings to the SM neutrinos and masses of the order of a few TeV or below, being therefore reachable at the LHC. This makes the ISS model an appealing model, with a rich phenomenology that can be tested at present or near-future experiments. These include, among others, studies of lepton flavor universality violation in meson leptonic and semileptonic decays [27, 28], lepton electric dipole moments [29, 30], lepton magnetic moments [31], heavy neutrino production at colliders [32–39], dark matter [40], leptogenesis [41, 42] and charged LFV processes [43–54].

On the theoretical side, the SM also suffers from some undesired properties, as the so-called hierarchy problem. This problem refers to the instability of the Higgs sector under radiative corrections if some new physics at a large scale is introduced. In order to illustrate this idea we can consider the Higgs boson mass, m_H, and compute its radiative corrections under the assumption that there is no new physics until the Planck mass $M_{\mathrm{P}} \sim 10^{19}$ GeV, where the gravitational effects start playing a role. By doing this, we find that the quantum corrections Δm_H^2 grow as the square of the new physics scale, which gives a value very far from the experimentally measured value $m_H = 125.09 \pm 0.21(\text{stat.}) \pm 0.11(\text{syst.})$ GeV [55]. Thus, in order to obtain a prediction that is compatible with this experimental value, a very fine tuned cancellation among the bare mass and the quantum corrections is needed, which is not very natural without any further explanation nor extra symmetry.

One of the most popular and elegant solutions to this problem is provided by supersymmetry (SUSY) [56–58], a new symmetry that relates fermions and bosons. In its simplest and minimal extension of the SM, known as the Minimal Supersymmetric Standard Model (MSSM) [59–61], each fermion of the SM has a spin-zero partner, called sfermion, with the same mass and quantum numbers as the original fermion; equivalently, all the SM bosons have spin one-half partners. The fact that there are fermions and bosons with the same couplings and masses gives the needed cancellation of the dangerous quantum corrections to the Higgs boson mass, providing an elegant solution to the hierarchy problem. Of course, doubling the SM spectrum is a strong prediction that experiments have tested and, unfortunately, the SUSY part of the MSSM spectrum has not been found yet. This means that, if SUSY exists in Nature, it cannot be an exact symmetry and it must be broken, such that the SUSY particles must be heavier than the SM ones. This breaking, however, cannot spoil completely the nice solution to the hierarchy problem, so SUSY needs to be softly broken [62], i.e., the dominant quadratic dependence on the new physics scale of Δm_H^2 still cancels out, although a logarithmic dependence remains.

Once these soft SUSY breaking terms are included, the MSSM is still a viable model with a very appealing phenomenology. Nevertheless, since it is constructed from the SM, it also demands a mechanism for neutrino mass generation. Following the previous discussion, we can consider again the ISS model and embed it in a supersymmetric context, adding to the MSSM spectrum new neutrinos and sneutrinos which can have both masses at a few TeV scale or below and with large couplings. This way, this SUSY-ISS model combines the appealing features of both frameworks, the SUSY and the ISS ones.

The best way of experimentally proving that any model beyond the SM is correct would be directly detecting the new particles that it predicts. Nevertheless, this task can in many cases be very difficult if these new particles are too heavy as to be directly produced in present experiments, so a first indication of their existence could come from their indirect implications to some other low energy observables. In the particular case of neutrino mass models, one of the optimal places for this purpose is again looking for LFV processes, concretely in the charged lepton sector, which can be quantumly induced via heavy neutrino loop effects.

Processes involving charged lepton flavor violation (cLFV) are forbidden in the SM if neutrinos are massless, and extremely suppressed if the small neutrino masses from oscillation data are ad-hoc added to the SM. Consequently, a positive signal in any of the experimental searches for cLFV processes would automatically imply the existence of new physics, and it must be indeed beyond the SM with minimally added neutrino masses. Although no such processes have been observed yet, this is a very active field that is being explored by many experiments which have set upper bounds to this kind of cLFV processes. At present, the strongest bounds have been found in the μ-e transitions, as the radiative $\mu \to e\gamma$ decay or μ-e conversion in heavy nuclei, whose branching ratios have been bounded to be below 4.2×10^{-13} and 7.0×10^{-13} by the MEG [63] and SINDRUM II [64] collaborations, respectively. Moreover, next generation of experiments are expected to improve in several orders of magnitude the sensitivities for LFV μ-e transitions, reaching the impressive range of 10^{-18} for μ-e conversion in nuclei by the PRISM experiment in J-PARC [65]. On the other hand, present bounds on transitions in the τ-μ and τ-e sectors are less constraining, with, for example, upper bounds of about 10^{-8} for LFV tau decays from BABAR [66] and BELLE [67, 68]. Therefore, there is some more room in these sectors than in the μ-e one for having large LFV signals that new experiments as BELLE-II [69] would be able to test in the near future.

Additionally, the currently running LHC has also many things to say about cLFV. First of all, the fact that a new particle, the Higgs boson, has been discovered opens a new window for possible deviations from the SM that definitely needs to be explored. In particular, three new cLFV channels are introduced in the cLFV market, the LFV Higgs boson decays into two leptons of different flavor, $H \to \ell_k \bar{\ell}_m$, $k \neq m$, which have already been searched by the CMS [70–72] and ATLAS [73] experiments. Even though CMS saw a small but intriguing excess in the $H \to \tau\mu$ channel after run-I [70], it has not been confirmed yet with run-II data and, at present, they have been able to set an upper bound of 2.5×10^{-3} [72]. These searches of LFV Higgs decays, as well as other explorations of the Higgs sector, will continue and surely be improved with more data after new LHC runs.

Other interesting observables that the LHC is also looking for are the LFV Z boson decays into two leptons of different flavor $Z \to \ell_k \bar{\ell}_m$ [73, 74]. Interestingly, after the run-I, ATLAS has already reached the previous sensitivities from the LEP experiment [75, 76], even improving the bound for the $Z \to \mu e$ channel. As for the Higgs searches, LFV Z decays will certainly continue during the new runs, so hopefully new interesting data will come from ATLAS and CMS. Nevertheless, the best sensitivities for LFV Z decays are expected from next generation of lepton colliders, as long as they can work as Z factories with a very clean environment. In particular, at future linear colliders, with an expected sensitivity of 10^{-9} [77, 78], or at a Future Circular e^+e^- Collider (such as FCC-ee (TLEP) [79]), where it is estimated that up to 10^{13} Z bosons would be produced and the sensitivities to LFV Z decay rates could be improved up to 10^{-13}.

The main motivation of this Thesis, therefore, is to explore the connection between the existence of new right-handed neutrino particles with masses of a few TeV or below, reachable at the LHC, and the existence of LFV in the charged lepton sector. We are particularly interested in the two models above described, the ISS and the SUSY-ISS model, which are very appealing models since they can provide right-handed neutrino states with masses at the TeV range and, at the same time, with large couplings. Charged LFV phenomenology within massive neutrino models has been studied before [80–105], also in the ISS [43–54]. In this Thesis, we concentrate mainly in studying the predictions for the LFV Higgs and Z boson decays, which as we said are extremely timely to explore in the light of the recent discovery of the Higgs boson and the new LHC data on the LFV Z decays. In addition, we also make new predictions for other cLFV processes like $\ell_m \to \ell_k \gamma$ and $\ell_m \to \ell_k \ell_k \ell_k$, as well as for other lepton flavor preserving observables that will be also relevant in the context of the models we consider here.

We fully study for the first time the LFV H decays in presence of right-handed neutrinos in the ISS model, as well as in presence of sneutrinos in the SUSY-ISS model. We perform this study following two different approaches. First we present, based on the results for the type-I seesaw model in Ref. [91], the results for the full one-loop computation done in the physical neutrino mass basis. Second, we use the mass insertion approximation technique, which works in the electroweak basis and allows us to obtain useful and simple formulas for the LFV H decay rates. For the numerical evaluation, we show that large LFV rates can be obtained focusing on particular directions of the parameter space where μ-e transitions, the experimentally most constrained ones, are highly suppressed. Along this same line of research, we provide a new proposal for the building of these phenomenologically interesting scenarios with suppressed μ-e transitions. These scenarios are based on the μ_X parametrization, which is a new parametrization proposed in this Thesis. On the other hand, LFV Z decay rates in the ISS model have been first explored in Ref. [50]. Therefore, in the case of these observables, we directly present a more specific study in those particular directions of the parameters space with suppressed μ-e transitions, that give large allowed LFVZD rates. In this sense, we perform a complementary study of that previously done.

As we said, we are interested in models with right-handed neutrinos at the TeV range, since they belong to the scale of energies that the LHC is now probing. In the ISS model, due to the pseudo-Dirac character of the heavy neutrinos, standard collider searches looking for lepton number violating final states with two same-sign leptons, the 'smoking gun' signature of Majorana fermions [106–109], are not efficient. Therefore, here we propose to use instead lepton flavor violating final states in order to discriminate events from the production and decay of the low scale seesaw heavy neutrinos. In particular, we focus on exotic $\tau^{\pm}\mu^{\mp}jj$ or $\tau^{\pm}e^{\mp}jj$ final states with no missing transverse energy, which could be produced in scenarios with ν_R masses at and below the TeV range and where LFV is favored in the τ-μ or τ-e sector, respectively.

This Thesis is organized as follows. In Chap. 2 we review neutrino oscillation physics and its connection with the need of introducing neutrino masses. We discuss some popular neutrino mass models, paying special attention to models with right-handed neutrinos with TeV range masses, as the inverse seesaw model and its SUSY version. These are the two models that we will consider for exploring in detail the LFV phenomenology in the following Chapters. Moreover, when studying the neutrino sector of these models, we present a new parametrization, which we refer to as the μ_X parametrization, that will turn out to be very useful for exploring the parameter space while being always in agreement with neutrino oscillation data.

In Chap. 3 we address the importance of charged LFV processes in the search of new physics and summarize the experimental status. Then, we revisit the LFV lepton decays in the ISS model, meaning the radiative $\ell_m \to \ell_k\gamma$ and three-body $\ell_m \to \ell_k\ell_k\ell_k$ decays with $k \neq m$. This new study of these processes will allow us to learn about the behavior of the LFV as a function of the ISS parameters, as well as to emphasize the advantages of using our μ_X parametrization. As a result of this study, we will find some interesting phenomenological scenarios, well motivated by present experimental bounds, where LFV τ-μ or τ-e transitions are favored while keeping the μ-e transitions highly suppressed. These will be useful for exploring LFV H and Z decays. Furthermore, we also discuss in this Chapter the implications of right-handed neutrinos with TeV masses to other relevant low energy observables, which we will consider as constraints when looking for maximum allowed rates in the next Chapters.

Chapter 4 is devoted to the study of the LFV Higgs decay (LFVHD) rates in the ISS and SUSY-ISS models. We present the results of the full one-loop calculation of the LFVHD rates in the ISS model and systematically study their dependence with the different parameters of this model. In order to better understand the results, we perform a complete and independent calculation of these rates using the mass insertion approximation, which will allow us to derive a simple expression for an effective LFV $H\ell_k\ell_m$ vertex, very useful for any author that wishes to make a fast estimation of the LFVHD rates in this kind of models. This complete analysis will serve us to conclude on the maximum LFVHD rates allowed by present experimental constraints. Moreover, we explore these rates in the SUSY-ISS model, showing that the new SUSY loops including sleptons and sneutrinos may considerably enhance the maximum allowed rates, reaching values close to the present experimental sensitivities.

In Chap. 5 we study the LFV Z boson decays (LFVZD) in the ISS model. We focus our analysis on the previously introduced phenomenological scenarios, where large allowed LFV rates in the τ-μ and τ-e sector can be achieved. We compare our finding to previous works in the literature and show that, in these interesting directions of the ISS parameter space, large allowed rates can be obtained, well within the reach of next generation of experiments searching for LFVZD.

In Chap. 6 we focus on low scale seesaw neutrino production at the LHC. We study the possibility of detecting the production and decay of the ISS heavy neutrinos searching for exotic LFV $\ell_k^\pm \ell_m^\mp jj$ events, with $k \neq m$, and with no missing transverse energy. Alternatively to standard Majorana neutrino searches at colliders that are not relevant for the ISS model, our proposal explores the fact that the new heavy neutrino states can have non-trivial flavor structure, leading to this kind of interesting LFV signals. Concretely, we will apply this idea to the production of exotic $\tau\mu jj$ events within the previously introduced scenarios, finding promising results for the future LHC runs.

Finally, we summarize the main conclusions at the end of this document.

The contents presented in this Thesis, summarized along in this chapter and Chaps. 2–5, the Conclusions and the Appendices, are original works that have been published in Refs. [110–114] and in the conference proceedings [115–119].

References

1. G. Aad et al. (ATLAS), Phys. Lett. **B716**, 1 (2012). https://doi.org/10.1016/j.physletb.2012.08.020, arXiv:1207.7214 [hep-ex]
2. S. Chatrchyan et al. (CMS), Phys. Lett. **B716** 30 (2012). https://doi.org/10.1016/j.physletb.2012.08.021, arXiv:1207.7235 [hep-ex]
3. S.L. Glashow, Nucl. Phys. **22**, 579 (1961). https://doi.org/10.1016/0029-5582(61)90469-2
4. M. Gell-Mann, Phys. Lett. **8**, 214 (1964). https://doi.org/10.1016/S0031-9163(64)92001-3
5. S. Weinberg, Phys. Rev. Lett. **19**, 1264 (1967). https://doi.org/10.1103/PhysRevLett.19.1264
6. A. Salam, in *8th Nobel Symposium Lerum*, Sweden, May 19–25, 1968. Conf. Proc. **C680519**, 367 (1968)
7. P.W. Higgs, Phys. Lett. **12**, 132 (1964). https://doi.org/10.1016/0031-9163(64)91136-9
8. F. Englert, R. Brout, Phys. Rev. Lett. **13**, 321 (1964). https://doi.org/10.1103/PhysRevLett.13.321
9. G.S. Guralnik, C.R. Hagen, T.W.B. Kibble, Phys. Rev. Lett. **13**, 585 (1964). https://doi.org/10.1103/PhysRevLett.13.585
10. P.W. Higgs, Phys. Rev. **145**, 1156 (1966). https://doi.org/10.1103/PhysRev.145.1156
11. S.L. Glashow, J. Iliopoulos, L. Maiani, Meeting of the Italian school of physics and weak interactions Bologna, Italy, April 26–28, 1984. Phys. Rev. **D2**, 1285 (1970). https://doi.org/10.1103/PhysRevD.2.1285
12. N. Cabibbo, Meeting of the Italian school of physics and weak interactions Bologna, Italy, April 26–28, 1984. Phys. Rev. Lett. **10**, 531 (1963). (648(1963)). https://doi.org/10.1103/PhysRevLett.10.531

13. M. Kobayashi, T. Maskawa, Prog. Theor. Phys. **49**, 652 (1973). https://doi.org/10.1143/PTP.49.652
14. Y. Fukuda et al. (Super-Kamiokande), Phys. Rev. Lett. **81**, 1562 (1998). https://doi.org/10.1103/PhysRevLett.81.1562, arXiv:hep-ex/9807003 [hep-ex]
15. Q.R. Ahmad et al. (SNO), Phys. Rev. Lett. **87**, 071301 (2001). https://doi.org/10.1103/PhysRevLett.87.071301, arXiv:nucl-ex/0106015 [nucl-ex]
16. Q.R. Ahmad et al. (SNO), Phys. Rev. Lett. **89**, 011301 (2002). https://doi.org/10.1103/PhysRevLett.89.011301, arXiv:nucl-ex/0204008 [nucl-ex]
17. P. Minkowski, Phys. Lett. **B67**, 421 (1977). https://doi.org/10.1016/0370-2693(77)90435-X
18. M. Gell-Mann, P. Ramond, R. Slansky, in *Supergravity Workshop Stony Brook, New York, September 27–28, 1979*. Conf. Proc. **C790927**, 315 (1979). arXiv:1306.4669 [hep-th]
19. T. Yanagida, in *Proceedings: Workshop on the Unified Theories and the Baryon Number in the Universe: Tsukuba, Japan, February 13–14, 1979*. Conf. Proc. **C7902131**, 95 (1979)
20. R.N. Mohapatra, G. Senjanovic, Phys. Rev. Lett. **44**, 912 (1980). https://doi.org/10.1103/PhysRevLett.44.912
21. J. Schechter, J.W.F. Valle, Phys. Rev. **D22**, 2227 (1980). https://doi.org/10.1103/PhysRevD.22.2227
22. S. Heinemeyer, J. Hernandez-Garcia, M.J. Herrero, X. Marcano, A.M. Rodriguez-Sanchez, Adv. High Energy Phys. **2015**, 152394 (2015). https://doi.org/10.1155/2015/152394, arXiv:1407.1083 [hep-ph]
23. R.N. Mohapatra, Phys. Rev. Lett. **56**, 561 (1986). https://doi.org/10.1103/PhysRevLett.56.561
24. R.N. Mohapatra, J.W.F. Valle, in *Proceedings, 23RD International Conference on High Energy Physics, JULY 16–23, 1986, Berkeley, CA*. Phys. Rev. **D34**, 1642 (1986). https://doi.org/10.1103/PhysRevD.34.1642
25. J. Bernabeu, A. Santamaria, J. Vidal, A. Mendez, J.W.F. Valle, Phys. Lett. **B187**, 303 (1987). https://doi.org/10.1016/0370-2693(87)91100-2
26. G. 't Hooft, Recent Developments in Gauge Theories, in *Proceedings, Nato Advanced Study Institute, Cargese, France, August 26–September 8, 1979*, NATO Sci. Ser. B **59**, 135 (1980). https://doi.org/10.1007/978-1-4684-7571-5_9
27. A. Abada, D. Das, A.M. Teixeira, A. Vicente, C. Weiland, JHEP **02**, 048 (2013). https://doi.org/10.1007/JHEP02(2013)048, arXiv:1211.3052 [hep-ph]
28. A. Abada, A.M. Teixeira, A. Vicente, C. Weiland, JHEP **02**, 091 (2014). https://doi.org/10.1007/JHEP02(2014)091, arXiv:1311.2830 [hep-ph]
29. A. Abada, T. Toma, JHEP **02**, 174 (2016). https://doi.org/10.1007/JHEP02(2016)174, arXiv:1511.03265 [hep-ph]
30. A. Abada, T. Toma, JHEP **08**, 079 (2016). https://doi.org/10.1007/JHEP08(2016)079, arXiv:1605.07643 [hep-ph]
31. A. Abada, V. De Romeri, A.M. Teixeira, JHEP **09**, 074 (2014). https://doi.org/10.1007/JHEP09(2014)074, arXiv:1406.6978 [hep-ph]
32. C.-Y. Chen, P.S.B. Dev, Phys. Rev. **D85**, 093018 (2012). https://doi.org/10.1103/PhysRevD.85.093018, arXiv:1112.6419 [hep-ph]
33. P.S. Bhupal Dev, R. Franceschini, R.N. Mohapatra, Phys. Rev. **D86**, 093010 (2012). https://doi.org/10.1103/PhysRevD.86.093010, arXiv:1207.2756 [hep-ph]
34. A. Das, N. Okada, Phys. Rev. **D88**, 113001 (2013). https://doi.org/10.1103/PhysRevD.88.113001, arXiv:1207.3734 [hep-ph]
35. A. Das, P.S. Bhupal Dev, N. Okada, Phys. Lett. **B735**, 364 (2014). https://doi.org/10.1016/j.physletb.2014.06.058, arXiv:1405.0177 [hep-ph]
36. G. Bambhaniya, S. Goswami, S. Khan, P. Konar, T. Mondal, Phys. Rev. **D91**, 075007 (2015). https://doi.org/10.1103/PhysRevD.91.075007, arXiv:1410.5687 [hep-ph]
37. G. Bambhaniya, S. Khan, P. Konar, T. Mondal, Phys. Rev. **D91**, 095007 (2015). https://doi.org/10.1103/PhysRevD.91.095007, arXiv:1411.6866 [hep-ph]
38. A. Das, N. Okada, Phys. Rev. **D93**, 033003 (2016). https://doi.org/10.1103/PhysRevD.93.033003, arXiv:1510.04790 [hep-ph]

39. A. Das, P. Konar, S. Majhi, JHEP **06**, 019 (2016). https://doi.org/10.1007/JHEP06(2016)019, arXiv:1604.00608 [hep-ph]
40. A. Abada, G. Arcadi, M. Lucente, JCAP **1410**, 001 (2014). https://doi.org/10.1088/1475-7516/2014/10/001, arXiv:1406.6556 [hep-ph]
41. J. Garayoa, M.C. Gonzalez-Garcia, N. Rius, JHEP **02**, 021 (2007). https://doi.org/10.1088/1126-6708/2007/02/021, arXiv:hep-ph/0611311 [hep-ph]
42. A. Abada, G. Arcadi, V. Domcke, M. Lucente, JCAP **1511**, 041 (2015). https://doi.org/10.1088/1475-7516/2015/11/041, arXiv:1507.06215 [hep-ph]
43. F. Deppisch, J.W.F. Valle, Phys. Rev. **D72**, 036001 (2005). https://doi.org/10.1103/PhysRevD.72.036001, arXiv:hep-ph/0406040 [hep-ph]
44. F. Deppisch, T.S. Kosmas, J.W.F. Valle, Nucl. Phys. **B752**, 80 (2006). https://doi.org/10.1016/j.nuclphysb.2006.06.032, arXiv:hep-ph/0512360 [hep-ph]
45. P.S.B. Dev, R.N. Mohapatra, Phys. Rev. **D81**, 013001 (2010). https://doi.org/10.1103/PhysRevD.81.013001, arXiv:0910.3924 [hep-ph]
46. M. Hirsch, T. Kernreiter, J.C. Romao, A. Villanova del Moral, JHEP **01**, 103 (2010). https://doi.org/10.1007/JHEP01(2010)103, arXiv:0910.2435 [hep-ph]
47. A. Abada, D. Das, C. Weiland, JHEP **03**, 100 (2012). https://doi.org/10.1007/JHEP03(2012)100, arXiv:1111.5836 [hep-ph]
48. A. Abada, D. Das, A. Vicente, C. Weiland, JHEP **09**, 015 (2012). https://doi.org/10.1007/JHEP09(2012)015, arXiv:1206.6497 [hep-ph]
49. M. Hirsch, F. Staub, A. Vicente, Phys. Rev. **D85**, 113013 (2012). [Erratum: Phys. Rev.D91,no.5,059902(2015)]. https://doi.org/10.1103/PhysRevD.91.059902, https://doi.org/10.1103/PhysRevD.85.113013, arXiv:1202.1825 [hep-ph]
50. A. Abada, V. De Romeri, S. Monteil, J. Orloff, A.M. Teixeira, JHEP **04**, 051 (2015). https://doi.org/10.1007/JHEP04(2015)051, arXiv:1412.6322 [hep-ph]
51. A. Abada, M.E. Krauss, W. Porod, F. Staub, A. Vicente, C. Weiland, JHEP **11**, 048 (2014). https://doi.org/10.1007/JHEP11(2014)048, arXiv:1408.0138 [hep-ph]
52. A. Abada, V. De Romeri, A.M. Teixeira, JHEP **02**, 083 (2016). https://doi.org/10.1007/JHEP02(2016)083, arXiv:1510.06657 [hep-ph]
53. A. Abada, D. Bečirević, M. Lucente, O. Sumensari, Phys. Rev. **D91**, 113013 (2015). https://doi.org/10.1103/PhysRevD.91.113013, arXiv:1503.04159 [hep-ph]
54. A. Abada, V. De Romeri, J. Orloff, A.M. Teixeira, Eur. Phys. J. **C77**, 304 (2017). https://doi.org/10.1140/epjc/s10052-017-4864-z, arXiv:1612.05548 [hep-ph]
55. G. Aad et al. (ATLAS, CMS), in *Proceedings, Meeting of the APS Division of Particles and Fields (DPF 2015): Ann Arbor, Michigan, USA, 4–8 Aug 2015*, Phys. Rev. Lett. **114**, 191803 (2015). https://doi.org/10.1103/PhysRevLett.114.191803, arXiv:1503.07589 [hep-ex]
56. Yu.A. Golfand, E.P. Likhtman, JETP Lett. **13**, 323 (1971), [Pisma Zh. Eksp. Teor. Fiz.13,452(1971)]
57. D.V. Volkov, V.P. Akulov, Phys. Lett. **46B**, 109 (1973). https://doi.org/10.1016/0370-2693(73)90490-5
58. J. Wess, B. Zumino, Nucl. Phys. **B70**, 39 (1974). https://doi.org/10.1016/0550-3213(74)90355-1
59. H.E. Haber, G.L. Kane, Phys. Rept. **117**, 75 (1985). https://doi.org/10.1016/0370-1573(85)90051-1
60. J.F. Gunion, H.E. Haber, Nucl. Phys. **B272**, 1 (1986), [Erratum: Nucl. Phys.B402,567(1993)]. https://doi.org/10.1016/0550-3213(86)90340-8, https://doi.org/10.1016/0550-3213(93)90653-7
61. J.F. Gunion, H.E. Haber, in *Proceedings, 23RD International Conference on High Energy Physics, JULY 16–23, 1986, Berkeley, CA*, Nucl. Phys. **B278**, 449 (1986), [Erratum: Nucl. Phys.B402,569(1993)]. https://doi.org/10.1016/0550-3213(93)90654-8, https://doi.org/10.1016/0550-3213(86)90050-7
62. L. Girardello, M.T. Grisaru, Nucl. Phys. **B194**, 65 (1982). https://doi.org/10.1016/0550-3213(82)90512-0

63. A.M. Baldini et al. (MEG), Eur. Phys. J. **C76**, 434 (2016). https://doi.org/10.1140/epjc/s10052-016-4271-x, arXiv:1605.05081 [hep-ex]
64. W.H. Bertl et al. (SINDRUM II), Eur. Phys. J. **C47**, 337 (2006). https://doi.org/10.1140/epjc/s2006-02582-x
65. A. Alekou et al., in *Proceedings, 2013 Community Summer Study on the Future of U.S. Particle Physics: Snowmass on the Mississippi (CSS2013): Minneapolis, MN, USA, July 29–August 6, 2013* (2013). http://inspirehep.net/record/1256506/files/arXiv:1310.0804.pdf, arXiv:1310.0804 [physics.acc-ph]
66. B. Aubert et al., BaBar. Phys. Rev. Lett. **104**, 021802 (2010). https://doi.org/10.1103/PhysRevLett.104.021802, arXiv:0908.2381 [hep-ex]
67. K. Hayasaka et al., Phys. Lett. **B687**, 139 (2010). https://doi.org/10.1016/j.physletb.2010.03.037, arXiv:1001.3221 [hep-ex]
68. K. Hayasaka, in 22nd Rencontres de Blois on Particle Physics and Cosmology Blois, Loire Valley, France, July 15–20, 2010 (2010). http://inspirehep.net/record/873396/files/arXiv:1010.3746.pdf, arXiv:1010.3746 [hep-ex]
69. T. Aushev et al. (2010). arXiv:1002.5012 [hep-ex]
70. V. Khachatryan et al., CMS. Phys. Lett. B **749**, 337 (2015). https://doi.org/10.1016/j.physletb.2015.07.053, arXiv:1502.07400 [hep-ex]
71. V. Khachatryan et al. (CMS), Phys. Lett. **B763**, 472 (2016). https://doi.org/10.1016/j.physletb.2016.09.062, arXiv:1607.03561 [hep-ex]
72. CMS Collaboration, Search for lepton flavour violating decays of the Higgs boson to $\mu\tau$ and $e\tau$ in proton-proton collisions at $\sqrt{s} = 13$ TeV, (2017), CMS-PAS-HIG-17-001
73. G. Aad et al. (ATLAS), Eur. Phys. J. **C77**, 70 (2017). https://doi.org/10.1140/epjc/s10052-017-4624-0, arXiv:1604.07730 [hep-ex]
74. G. Aad et al. (ATLAS), Phys. Rev. **D90**, 072010 (2014). https://doi.org/10.1103/PhysRevD.90.072010, arXiv:1408.5774 [hep-ex]
75. R. Akers et al. (OPAL), Z. Phys. **C67**, 555 (1995). https://doi.org/10.1007/BF01553981
76. P. Abreu et al. (DELPHI), Z. Phys. **C73**, 243 (1997). https://doi.org/10.1007/s002880050313
77. G. Wilson, Neutrino oscillations: are lepton-flavor violating Z decays observable with the CDR detector? (Nov 1998), dESY-ECFA LC Workshops held at Frascati
78. G. Wilson, Update on experimental aspects of lepton-flavour violation, (March 1999), dESY-ECFA LC Workshops held at Oxford
79. A. Blondel, E. Graverini, N. Serra, M. Shaposhnikov (collaboration FCC-ee study Team), in *Proceedings, 37th International Conference on High Energy Physics (ICHEP 2014): Valencia, Spain, July 2–9, 2014*, vol. 273–275 (2016), pp. 1883–1890. https://doi.org/10.1016/j.nuclphysbps.2015.09.304, arXiv:1411.5230 [hep-ex]
80. G. Mann, T. Riemann, Ann. Phys. **40**, 334 (1984)
81. M. Dittmar, A. Santamaria, M.C. Gonzalez-Garcia, J.W.F. Valle, Nucl. Phys. **B332**, 1 (1990). https://doi.org/10.1016/0550-3213(90)90028-C
82. A. Pilaftsis, Phys. Lett. **B285**, 68 (1992). https://doi.org/10.1016/0370-2693(92)91301-O
83. J.G. Korner, A. Pilaftsis, K. Schilcher, Phys. Rev. **D47**, 1080 (1993). https://doi.org/10.1103/PhysRevD.47.1080, arXiv:hep-ph/9301289 [hep-ph]
84. J.G. Korner, A. Pilaftsis, K. Schilcher, Phys. Lett. **B300**, 381 (1993). https://doi.org/10.1016/0370-2693(93)91350-V, arXiv:hep-ph/9301290 [hep-ph]
85. A. Ilakovac, A. Pilaftsis, Nucl. Phys. **B437**, 491 (1995). https://doi.org/10.1016/0550-3213(94)00567-X, arXiv:hep-ph/9403398 [hep-ph]
86. A. Ilakovac, Phys. Rev. **D62**, 036010 (2000). https://doi.org/10.1103/PhysRevD.62.036010, arXiv:hep-ph/9910213 [hep-ph]
87. J.I. Illana, M. Jack, T. Riemann (1999). http://www-library.desy.de/cgi-bin/showprep.pl?LC-TH-2000-007, arXiv:hep-ph/0001273 [hep-ph]
88. J.I. Illana, T. Riemann, Phys. Rev. **D63**, 053004 (2001). https://doi.org/10.1103/PhysRevD.63.053004, arXiv:hep-ph/0010193 [hep-ph]
89. J.A. Casas, A. Ibarra, Nucl. Phys. **B618**, 171 (2001). https://doi.org/10.1016/S0550-3213(01)00475-8, arXiv:hep-ph/0103065 [hep-ph]

90. J.I. Illana, M. Masip, Eur. Phys. J. **C35**, 365 (2004). https://doi.org/10.1140/epjc/s2004-01816-3, arXiv:hep-ph/0307393 [hep-ph]
91. E. Arganda, A.M. Curiel, M.J. Herrero, D. Temes, Phys. Rev. **D71**, 035011 (2005). https://doi.org/10.1103/PhysRevD.71.035011, arXiv:hep-ph/0407302 [hep-ph]
92. E. Arganda, M.J. Herrero, Phys. Rev. **D73**, 055003 (2006). https://doi.org/10.1103/PhysRevD.73.055003, arXiv:hep-ph/0510405 [hep-ph]
93. S. Antusch, E. Arganda, M.J. Herrero, A.M. Teixeira, JHEP **11**, 090 (2006). https://doi.org/10.1088/1126-6708/2006/11/090, arXiv:hep-ph/0607263 [hep-ph]
94. A. Abada, C. Biggio, F. Bonnet, M.B. Gavela, T. Hambye, JHEP **12**, 061 (2007). https://doi.org/10.1088/1126-6708/2007/12/061, arXiv:0707.4058 [hep-ph]
95. E. Arganda, M.J. Herrero, A.M. Teixeira, JHEP **10**, 104 (2007). https://doi.org/10.1088/1126-6708/2007/10/104, arXiv:0707.2955 [hep-ph]
96. E. Arganda, M.J. Herrero, J. Portoles, JHEP **06**, 079 (2008). https://doi.org/10.1088/1126-6708/2008/06/079, arXiv:0803.2039 [hep-ph]
97. A. Abada, C. Biggio, F. Bonnet, M.B. Gavela, T. Hambye, Phys. Rev. **D78**, 033007 (2008). https://doi.org/10.1103/PhysRevD.78.033007, arXiv:0803.0481 [hep-ph]
98. M.B. Gavela, T. Hambye, D. Hernandez, P. Hernandez, JHEP **09**, 038 (2009). https://doi.org/10.1088/1126-6708/2009/09/038, arXiv:0906.1461 [hep-ph]
99. A. Ilakovac, A. Pilaftsis, Phys. Rev. **D80**, 091902 (2009). https://doi.org/10.1103/PhysRevD.80.091902, arXiv:0904.2381 [hep-ph]
100. M.J. Herrero, J. Portoles, A.M. Rodriguez-Sanchez, Phys. Rev. **D80**, 015023 (2009). https://doi.org/10.1103/PhysRevD.80.015023, arXiv:0903.5151 [hep-ph]
101. J.A. Casas, J.M. Moreno, N. Rius, R. Ruiz de Austri, B. Zaldivar, JHEP **03**, 034 (2011). https://doi.org/10.1007/JHEP03(2011)034, arXiv:1010.5751 [hep-ph]
102. D.N. Dinh, A. Ibarra, E. Molinaro, S.T. Petcov, JHEP **08**, 125 (2012), [Erratum: JHEP09,023(2013)]. https://doi.org/10.1007/JHEP09(2013)023, https://doi.org/10.1007/JHEP08(2012)125, arXiv:1205.4671 [hep-ph]
103. R. Alonso, M. Dhen, M.B. Gavela, T. Hambye, JHEP **01**, 118 (2013). https://doi.org/10.1007/JHEP01(2013)118, arXiv:1209.2679 [hep-ph]
104. A. Ilakovac, A. Pilaftsis, L. Popov, Phys. Rev. **D87** 053014 (2013). https://doi.org/10.1103/PhysRevD.87.053014, arXiv:1212.5939 [hep-ph]
105. J. Herrero-Garcia, N. Rius, A. Santamaria, JHEP **11**, 084 (2016). https://doi.org/10.1007/JHEP11(2016)084, arXiv:1605.06091 [hep-ph]
106. A. Pilaftsis, Z. Phys. **C55**, 275 (1992). https://doi.org/10.1007/BF01482590, arXiv:hep-ph/9901206 [hep-ph]
107. A. Datta, M. Guchait, A. Pilaftsis, Phys. Rev. **D50**, 3195 (1994). https://doi.org/10.1103/PhysRevD.50.3195, arXiv:hep-ph/9311257 [hep-ph]
108. F. del Aguila, J.A. Aguilar-Saavedra, R. Pittau, JHEP **10**, 047 (2007). https://doi.org/10.1088/1126-6708/2007/10/047, arXiv:hep-ph/0703261 [hep-ph]
109. A. Atre, T. Han, S. Pascoli, B. Zhang, JHEP **05**, 030 (2009). https://doi.org/10.1088/1126-6708/2009/05/030, arXiv:0901.3589 [hep-ph]
110. E. Arganda, M.J. Herrero, X. Marcano, C. Weiland, Phys. Rev. **D91**, 015001 (2015). https://doi.org/10.1103/PhysRevD.91.015001, arXiv:1405.4300 [hep-ph]
111. E. Arganda, M.J. Herrero, X. Marcano, C. Weiland, Phys. Rev. **D93**, 055010 (2016). https://doi.org/10.1103/PhysRevD.93.055010, arXiv:1508.04623 [hep-ph]
112. E. Arganda, M.J. Herrero, X. Marcano, C. Weiland, Phys. Lett. **B752**, 46 (2016). https://doi.org/10.1016/j.physletb.2015.11.013, arXiv:1508.05074 [hep-ph]
113. V. De Romeri, M.J. Herrero, X. Marcano, F. Scarcella, Phys. Rev. **D95**, 075028 (2017). https://doi.org/10.1103/PhysRevD.95.075028, arXiv:1607.05257 [hep-ph]
114. E. Arganda, M. Herrero, X. Marcano, R. Morales, A. Szynkman, Phys. Rev. **D95**, 095029 (2017). https://doi.org/10.1103/PhysRevD.95.095029, arXiv:1612.09290 [hep-ph]
115. E. Arganda, M.J. Herrero, X. Marcano, C. Weiland, in *Proceedings, 49th Rencontres de Moriond on Electroweak Interactions and Unified Theories: La Thuile, Italy, March 15–22, 2014* (2014), pp. 401–406. http://inspirehep.net/record/1298825/files/arXiv:1406.0384.pdf, arXiv:1406.0384 [hep-ph]

116. E. Arganda, M.J. Herrero, X. Marcano, C. Weiland, in *Proceedings, 37th International Conference on High Energy Physics (ICHEP 2014): Valencia, Spain, July 2–9, 2014*, Nucl. Part. Phys. Proc. **273–275**, 1685 (2016). https://doi.org/10.1016/j.nuclphysbps.2015.09.272, arXiv:1410.5779 [hep-ph]
117. E. Arganda, M.J. Herrero, X. Marcano, C. Weiland, in *Prospects in Neutrino Physics (NuPhys2015) London, UK, December 16-18, 2015* (2016). http://inspirehep.net/record/1460836/files/arXiv:1605.05660.pdf, arXiv:1605.05660 [hep-ph]
118. V. De Romeri, M.J. Herrero, X. Marcano, F. Scarcella, in *16th Hellenic School and Workshops on Elementary Particle Physics and Gravity (CORFU2016) Corfu, Corfu Island, Greece, August 31–September 19, 2016* (2017). http://inspirehep.net/record/1597438/files/arXiv:1705.00485.pdf, arXiv:1705.00485 [hep-ph]
119. M.J. Herrero, E. Arganda, X. Marcano, R. Morales, A. Szynkman, in *Proceedings, 2017 European Physical Society Conference on High Energy Physics (EPS-HEP 2017): Venice, Italy, July 5–12, 2017*, PoS **EPS-HEP2017**, 114 (2017), arXiv:1710.02510 [hep-ph]

Chapter 2
Seesaw Models with Heavy Neutrinos at the TeV Energy Range

In this Chapter we motivate the need of going beyond the Standard Model for explaining lepton flavor changing neutrino oscillation data and review some of the most popular models for this task, the seesaw models. We will concentrate specially in the so-called low scale seesaw models, one of which will be of special relevance for this Thesis: the inverse seesaw model. Finally, we will introduce a Supersymmetric version of the latter, the SUSY-ISS, an interesting model that combines the appealing features of the Minimal Supersymmetric Standard Model and the inverse seesaw model. Along this Chapter, we derive the μ_X parametrization in Sect. 2.3, useful for accommodating neutrino oscillation data, which is a genuine contribution of this Thesis and was first published in Ref. [1]. The implementation of the ISS model in the SUSY framework, as given in Eqs. (2.64)–(2.74), and the derivation of the interaction Lagrangian in the physical SUSY-ISS basis in Eq. (2.77) and in Appendix D are original works of this Thesis that have been published in Ref. [2].

2.1 Neutrino Oscillations

In the Standard Model (SM) the neutrinos, and antineutrinos, come in three different flavors. When they are produced by the standard charged current, they are always produced together with a charged lepton, which is the one that labels them: if the neutrino is produced with an e^+ or e^-, we name it as electron-neutrino (ν_e) or electron-antineutrino ($\bar{\nu}_e$), respectively; if it is produced with a μ^+ or μ^-, we have a ν_μ or $\bar{\nu}_\mu$; and if it is produced with τ^+ or τ^-, it is a ν_τ or $\bar{\nu}_\tau$. This one-to-one identification with the charged lepton sector is, at the same time, what allows us to detect and identify these elusive particles. These three neutrino flavor states $\nu_\ell \equiv \left(\nu_e, \nu_\mu, \nu_\tau\right)$ form a basis that we will refer to as the interaction basis.

Neutrinos only suffer from weak interactions and, consequently, they can travel long distances without interacting with anything. Their evolution is given by the Schrödinger equation, whose solutions are plane waves with energies defined by the eigenvalues of the 3×3 neutrino mass matrix. These stationary solutions define a

X. Marcano, *Lepton Flavor Violation from Low Scale Seesaw Neutrinos with Masses Reachable at the LHC*, Springer Theses, https://doi.org/10.1007/978-3-319-94604-7_2

new basis, the so-called mass or physical basis[1] $\nu_\alpha \equiv (\nu_1, \nu_2, \nu_3)$, which in general does not coincide with the above introduced interaction basis. This misalignment is the origin of the neutrino oscillation phenomena.

The relation between the two bases can be written as:

$$\nu_\ell = \sum_{\alpha=1}^{3} \left(U_{\rm PMNS}\right)_{\ell\alpha} \nu_\alpha , \tag{2.1}$$

where the $U_{\rm PMNS}$ is a unitary 3×3 rotation matrix, analogous to the CKM matrix in the quarks sector, whose name comes from Pontecorvo, who proposed neutrino oscillations [3], and from Maki-Nakagawa-Sakata, who introduced the mixing matrix [4].

When a neutrino is produced, it is in a specific flavor state, which can be expressed as a superposition of the mass eigenstates. If neutrinos were massless or degenerate in mass, all the mass eigenstates would have the same time evolution and, consequently, the initial flavor state would remain unchanged. In such a situation, we could say that the individual lepton flavor numbers, i.e., L_e, L_μ and L_τ, were preserved. On the contrary, if physical neutrinos had non-degenerate masses, each of the mass eigenstates would evolve differently in time, modifying the initial superposition and therefore the flavor of the initial neutrino state. This process, which is a direct consequence of non-degenerate neutrino masses, is known as neutrino oscillation and implies that individual lepton flavor numbers are not conserved. In the ultrarelativistic limit, the oscillation probability in vacuum from a flavor ν_ℓ to a flavor $\nu_{\ell'}$ is given by [5]:

$$\mathcal{P}_{\nu_\ell \to \nu_{\ell'}}\left(L, E\right) = \sum_{\alpha,\beta=1}^{3} U^*_{\ell\alpha} U_{\ell'\alpha} U_{\ell\beta} U^*_{\ell'\beta} \exp\left(-i \frac{\Delta m^2_{\alpha\beta} L}{2E}\right), \tag{2.2}$$

where $U \equiv U_{\rm PMNS}$ to shorten the notation, $E \sim |\boldsymbol{p}|$ is the neutrino energy, L is the distance between the source and the detector, and $\Delta m^2_{\alpha\beta} \equiv m^2_\alpha - m^2_\beta$ are the squared mass differences.

Several experiments involving solar, atmospheric, reactor and accelerator neutrinos have established the evidences for neutrino oscillations and, therefore, for neutrino masses (see Ref. [6] for a review). Nevertheless, and in spite of this experimental effort, there are still open issues related to neutrino oscillations and masses.

First of all, we do not know the absolute neutrino mass scale, although we know that it is at the eV scale or below from the upper limits on the effective electron neutrino mass in β decays, given by the Mainz [7] and Troitsk [8] experiments:

$$m_\beta < 2.05 \text{ eV} \quad \text{at } 95\% \text{ C.L.} \tag{2.3}$$

Additional information on the absolute neutrino mass scale, can be obtained from cosmological observations, which are sensitive to the sum of the light neutrino masses.

[1] Assuming the simplest scenario where only three physical neutrinos exist.

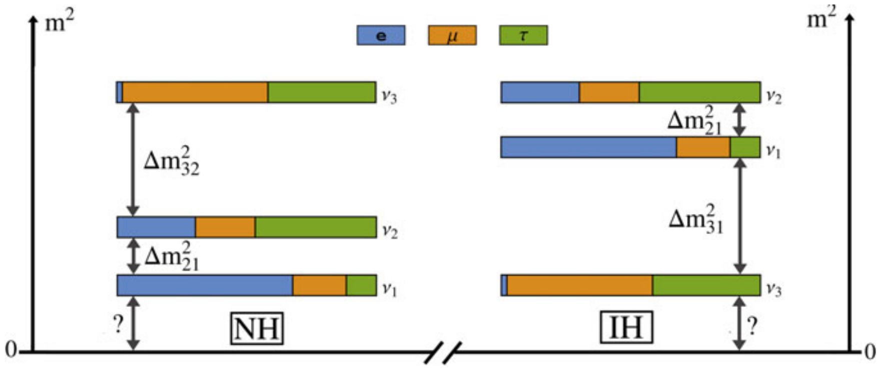

Fig. 2.1 The two possible neutrino mass orderings, known as normal (left) and inverted (right) hierarchies. The colors represent the flavor composition of each of the physical neutrinos: blue for ν_e, orange for ν_μ and green for ν_τ

At present, there are only upper bounds on this quantity, being the most constraining ones provided by the Planck collaboration [9]:

$$\sum m_\nu < 0.23 \text{ eV}. \tag{2.4}$$

Measuring neutrino oscillations in vacuum allows us to know the mass differences $|\Delta m^2_{21}|$ and $|\Delta m^2_{31}|$, but it does not tell us anything about neither the absolute neutrino mass scale nor the neutrino mass hierarchy. Additional measurements of matter effects or the Mikheev-Smirnov-Wolfenstein (MSW) effects [10–14] in neutrino oscillations can help solving the sign degeneracies. Nowadays, matter effects in the sun have made possible to know that $\Delta m^2_{21} > 0$, but the sign of Δm^2_{31} is a mystery yet. Therefore, two orderings are still possible, as shown if Fig. 2.1: a Normal Hierarchy (NH) where $m_{\nu_1} < m_{\nu_2} < m_{\nu_3}$ and an Inverted Hierarchy (IH) where $m_{\nu_3} < m_{\nu_1} < m_{\nu_2}$. Solving this degeneracy is one of the most important open issues in neutrino physics.

Second, being neutrinos the only electrically neutral fermions in the SM, they could be Majorana particles, i.e., they could be their own antiparticles. This would be in contrast to the rest of the SM model Dirac fermions, for which their antiparticle is a different state. This hypothetical Majorana character of the neutrinos, although very common in theoretical models as we will see later, does not have any impact on neutrino oscillations and, therefore, new observables to discern between Majorana and Dirac fermions need to be considered. The fact that a lepton can be its own antiparticle is directly related to the conservation of the total Lepton Number (LN) violation, since a Majorana mass terms breaks LN in two units. Consequently, LN violating processes are usually considered as the smoking gun signatures for Majorana neutrinos, like like neutrinoless double beta decay (for a review on $0\nu\beta\beta$, see for instance Refs. [15, 16]). Unfortunately, no experimental evidence has been found yet for any LN violating processes, so knowing if neutrinos are Majorana or Dirac fermions is still an open issue.

Third, massive neutrinos add new CP-violating phases to the SM parameters. For the case of three massive neutrinos, the PMNS matrix in Eq. (2.1) introduces one CP-violating phase if neutrinos are Dirac fermions, known as the Dirac CP phase, and two extra Majorana CP-violating phases if neutrinos are Majorana fermions. However, neutrino oscillations are only sensitive to the Dirac phase and this dependence appears via a particular combination of several oscillation parameters, known as the Jarlskog invariant [17] $J_{CP} = \mathrm{Im}\big(U_{\mu 3} U^*_{e3} U_{e2} U^*_{\mu 2}\big)$. This fact makes difficult to measure the Dirac phase in oscillation experiments, but experiments as T2K, NOνA, or future Hyper-K or Dune, may be able to do it in the next years. On the other hand, the extra Majorana phases do not play any role in neutrino oscillations. Nevertheless, they can be important for trying to explain the matter-antimatter asymmetry of the universe though the mechanism known as Baryogenesis via Leptogenesis (for a review see, for instance, Ref. [18]).

Finally, we may wonder how many neutrinos do exist in Nature. Despite the fact that there are some anomalies [19–27] pointing towards the existence of eV-KeV scale sterile neutrinos, we will assume in this Thesis that there are only three light neutrinos, which is the minimal requirement to fit neutrino oscillation observations. In this situation, the unitary PMNS matrix in Eq. (2.1) can be parametrized in its standard form as:

$$U_{\mathrm{PMNS}} = \begin{pmatrix} c_{12}c_{13} & s_{12}c_{13} & s_{13}e^{-i\delta} \\ -s_{12}c_{23} - c_{12}s_{23}s_{13}e^{i\delta} & c_{12}c_{23} - s_{12}s_{23}s_{13}e^{i\delta} & s_{23}c_{13} \\ s_{12}s_{23} - c_{12}c_{23}s_{13}e^{i\delta} & -c_{12}s_{23} - s_{12}c_{23}s_{13}e^{i\delta} & c_{23}c_{13} \end{pmatrix} \cdot P, \quad (2.5)$$

where $c_{ij} = \cos\theta_{ij}$ and $s_{ij} = \sin\theta_{ij}$ with θ_{ij} the neutrino mixing angles, δ is the CP-violating Dirac phase and the diagonal matrix $P = \mathrm{diag}(1, e^{i\phi_1}, e^{i\phi_2})$ accounts for the two extra CP-phases that do not play any role in neutrino oscillations, as we said before. In order to consider all the experimental neutrino oscillation data in a consistent way, we will take the results from the global fit analysis done by the NuFIT group [28]. Assuming a Normal Hierarchy, they obtain at the 1σ level:

$$\begin{aligned} \sin^2\theta_{12} &= 0.306^{+0.012}_{-0.012}, & \Delta m^2_{21} &= 7.50^{+0.19}_{-0.17} \times 10^{-5}\mathrm{eV}^2, \\ \sin^2\theta_{23} &= 0.441^{+0.027}_{-0.021}, & \Delta m^2_{31} &= 2.524^{+0.039}_{-0.040} \times 10^{-3}\mathrm{eV}^2, \\ \sin^2\theta_{13} &= 0.02166^{+0.00075}_{-0.00075}, & \delta &= 261^{+51}_{-59}, \end{aligned} \quad (2.6)$$

while for the Inverted Hierarchy they give

$$\begin{aligned} \sin^2\theta_{12} &= 0.306^{+0.012}_{-0.012}, & \Delta m^2_{21} &= 7.50^{+0.19}_{-0.17} \times 10^{-5}\mathrm{eV}^2, \\ \sin^2\theta_{23} &= 0.587^{+0.020}_{-0.024}, & \Delta m^2_{32} &= -2.514^{+0.038}_{-0.041} \times 10^{-3}\mathrm{eV}^2, \\ \sin^2\theta_{13} &= 0.02179^{+0.00076}_{-0.00076}, & \delta &= 277^{+40}_{-46}. \end{aligned} \quad (2.7)$$

2.2 Seesaw Models for Neutrino Masses

At the time that the SM was built, there were no evidences for neutrino masses. Moreover, experiments showed that neutrinos produced in charged weak interactions were left-handed (LH) fields, while antineutrinos were right-handed (RH). These facts were minimally satisfied in the SM by a chiral LH flavor field $\nu_{\ell_L} \equiv (\nu_\ell)_L$, which together with the LH charged lepton field forms a $SU(2)_L$ doublet, as required by the SM gauge symmetry. As a result, right-handed neutrino fields were left out and neutrinos were treated as massless fields by the SM.

Nowadays the status has changed. The strong experimental evidences of neutrino oscillations, as mentioned in the previous section, have established that neutrinos do have masses, claiming for new physics beyond the SM to accommodate this new situation. In a very simple and minimalistic choice, one could reconsider the addition of RH neutrino fields to the SM, in such a way that neutrinos could obtain their masses via their Yukawa interaction with the Higgs field, mimicking the mass generation for the rest of the SM fermions,

$$\mathcal{L}_{\text{Yuk}} = -Y_\nu^{ij}\overline{L_i}\widetilde{\Phi}\nu_{R_j} + h.c. \tag{2.8}$$

where Y_ν is the neutrino Yukawa coupling matrix, $L = (\nu_L \;\ell_L)^T$ is the $SU(2)_L$ lepton doublet and $\widetilde{\Phi} = i\sigma_2\Phi^*$ with Φ the Higgs $SU(2)_L$ doublet:

$$\Phi = \begin{pmatrix} G^+ \\ v + \frac{1}{\sqrt{2}}(H + iG^0) \end{pmatrix}, \quad \widetilde{\Phi} = i\sigma_2\Phi^* = \begin{pmatrix} v + \frac{1}{\sqrt{2}}(H - iG^0) \\ -G^- \end{pmatrix}. \tag{2.9}$$

After the Electroweak Symmetry Breaking (EWSB), this Lagrangian term leads to a Dirac mass term for neutrinos $m_\nu = m_D = vY_\nu$, with $v = 174$ GeV. In order for this mass to be at the eV scale, as suggested by neutrino oscillations, the Yukawa coupling needs to be very small, of the order of 10^{-11}. This value would extremely suppress any kind of phenomenology beyond neutrino oscillations. Moreover, such a tiny neutrino Yukawa coupling is five orders of magnitude smaller than the electron Yukawa coupling and eleven orders with respect to the top Yukawa coupling, so it would make even worse the flavor puzzle problem of understanding the hierarchy of the fermion masses.

On the other hand, having a closer look to the new added ν_R fields, we realize that they are singlets under the full SM gauge group and, therefore, there is nothing that protects them from having a Majorana mass term. In that situation, physical neutrinos will be Majorana particles.

In order to work with Majorana fermions, it is very useful to introduce the particle-antiparticle conjugation operator $\hat{C}$, which is defined as [5, 29]:

$$\hat{C} : \psi \to \psi^C = \mathcal{C}\bar{\psi}^T. \tag{2.10}$$

This matrix $\mathcal{C}$ fulfills:

$$\mathcal{C}^{-1}\gamma_\mu\mathcal{C} = -\gamma_\mu^T, \quad \mathcal{C}^{-1}\gamma_5\mathcal{C} = \gamma_5^T, \quad \mathcal{C}^\dagger = \mathcal{C}^{-1} = -\mathcal{C}^*, \tag{2.11}$$

which, in the Weyl representation, can be satisfied by chosing $\mathcal{C} = i\gamma_2\gamma_0$. Consequently, this operator $\hat{C}$ flips the chirality of chiral fields:

$$\hat{C}: \psi_L \to (\psi_L)^C = (\psi^C)_R, \quad \psi_R \to (\psi_R)^C = (\psi^C)_L, \tag{2.12}$$

meaning that the antiparticle of a LH field is a RH field. Moreover, the fact that Majorana fermions coincide with their antiparticle can be expressed in terms of this operator as:

$$\psi^C = \psi. \tag{2.13}$$

These relations will be very useful when considering models with Majorana neutrinos, as the standard seesaw models.

On a more model independent ground, we could make use of the effective Lagrangians formalism in order to try a bottom up approach to the neutrino mass problem. In this approach, we assume that the SM is an effective theory of a more complete but unknown theory, which in general will contain new symmetries and fields at a heavy scale Λ. If we knew the complete theory at high energies, we could integrate out all the heavy fields with masses above the electroweak scale and obtain a low energy Lagrangian in terms only of the SM fields. The modifications with respect to the SM Lagrangian would then be a series of new non-renormalizable operators suppressed by the heavy scale Λ, which encode all the new physics effects at low energy. Unfortunately, we do not know the complete theory to follow this top down way. Therefore, with the aim of covering any possible high energy theory for neutrino physics, we can alternatively write the most general non-renormalizable $SU(2)_L \times U(1)_Y$ invariant Lagrangian that involves neutrino and other SM fields, the low energy fields. This will lead us to an effective Lagrangian that can be generically written as the SM Lagrangian extended with a series of higher order non-renormalizable operators,

$$\mathcal{L}_{\text{eff}} = \mathcal{L}_{\text{SM}} + \delta\mathcal{L}_{d=5} + \delta\mathcal{L}_{d=6} + \cdots \tag{2.14}$$

where d stands for the dimension of the operators in $\delta\mathcal{L}_d$, which will be suppressed by $d-4$ inverse powers of the heavy scale Λ.

It is illustrative to look at the $d=5$ Lagrangian. Since neutrinos are members of a $SU(2)_L$ doublet, there is only one possible operator, first written by Weinberg [30] and named after him, contributing to $\delta\mathcal{L}_5$, given by:

$$\delta\mathcal{L}_{d=5} = \frac{1}{2}\frac{c_{ij}}{\Lambda}\left(\overline{L_i^C}\widetilde{\Phi}^*\right)\left(\widetilde{\Phi}^\dagger L_j\right), \tag{2.15}$$

where c_{ij} are dimensionless complex coefficients and $i, j = 1, 2, 3$. After the EWSB, this operator gives a Majorana mass term for the neutrinos:

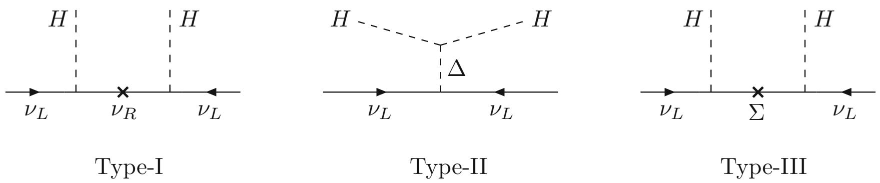

Fig. 2.2 Diagrams for the tree level light Majorana mass generation in the type-I (left), type-II (middle) and type-III (right) seesaw models

$$\delta\mathcal{L}_{d=5} \to \frac{v^2 c_{ij}}{2\Lambda}\left(\overline{\nu_i^C}\nu_j + h.c.\right). \tag{2.16}$$

Interestingly, this Majorana mass term is naturally small, suppressed by the new physics scale. The higher the scale Λ, the lower the neutrino mass, as if they were playing with a seesaw. This is the idea behind the so-called seesaw models, the simplest renormalizable models leading to this relation after integrating out the new heavy particles responsible of generating neutrino masses at the tree level.

Looking at the Weinberg operator, we can already learn some properties about the new particles of the seesaw models. In order to be gauge invariant, these new particles can be either singlets or triplets of $SU(2)_L$, since they need to couple to two $SU(2)$ doublets in a gauge invariant way. On the other hand, they can be either fermions or scalars, so we can define three[2] possible seesaw models according to what new type of fields they add to the SM: fermionic singlets (type-I), scalar triplets (type-II) or fermionic triplets (type-III), as shown in Fig. 2.2.

Before going to the details of these seesaw models, we want to emphasize that any high energy theory that introduces a Majorana mass term for the neutrinos leads to the Weinberg operator in Eq. (2.15) when integrating out the heavy fields, as it is the only one that can be written at lowest order. This implies that, in order to distinguish between the different neutrino theories, we need to consider their implications beyond the neutrino mass generations. In terms of the effective Lagrangian in Eq. (2.14), this means looking for the effect of the $d = 6$ operators [31] or higher. As we will see later, lepton flavor violating phenomenology is one of the optimal places for studying this task.

Type-I Seesaw Model

The type-I seesaw model [32–36] extends the SM with right-handed neutrinos ν_R, which are fermionic singlets under the full SM gauge group. As mentioned above, these new fields allow the neutrinos to have a Yukawa interaction with the Higgs field, as well as a Majorana mass term for themselves. The Lagrangian of the type-I seesaw can be thus written as:

$$\mathcal{L}_{\rm type-I} = -Y_\nu^{ij}\overline{L_i}\widetilde{\Phi}\nu_{Rj} - \frac{1}{2}m_M^{ij}\overline{\nu_{Ri}^C}\nu_{Rj} + h.c. \tag{2.17}$$

[2]The choice of a scalar singlet is not possible due to the structure of the Weinberg operator.

where the first term is the Yukawa Lagrangian as in Eq. (2.8) and in the second term m_M is a symmetric Majorana mass matrix. If we assign to the ν_R fields the same lepton number than to the L fields, we realize that the Yukawa interaction conserves LN, while the Majorana mass term breaks it in two units. Therefore, this model introduces a new scale that explicitly breaks LN. After the EWSB, Eq. (2.17) leads to a neutrino mass Lagrangian that, in the electroweak interaction basis reads as:

$$\mathcal{L}^{\text{mass}}_{\text{type-I}} = -m_D^{ij}\overline{\nu_{Li}^C}\nu_{Rj} - \frac{1}{2}m_M^{ij}\overline{\nu_{Ri}^C}\nu_{Rj} + h.c. = -\frac{1}{2}\overline{N_L}\begin{pmatrix} 0 & m_D \\ m_D^T & m_M \end{pmatrix} N_L^C + h.c. \tag{2.18}$$

where we have defined the LH fields as a column vector $N_L = (\nu_{Li}, \nu_{Ri}^C)^T$. From this mass Lagrangian, we identify the neutrino Majorana mass matrix in the EW basis:

$$M^{\nu}_{\text{type-I}} = \begin{pmatrix} 0 & m_D \\ m_D^T & m_M \end{pmatrix}. \tag{2.19}$$

It is illustrative to consider first the case where there is only one generation of neutrinos. In that context, all the parameters in Eq. (2.19) are just numbers and $M^{\nu}_{\text{type-I}}$ is a 2×2 mass matrix which, in the seesaw limit, defined by choosing the two involved scales very distant, $m_D \ll m_M$, has the following two eigenvalues:

$$m_\nu \simeq -\frac{m_D^2}{m_M} = -\frac{v^2 Y_\nu^2}{m_M}, \quad m_N \simeq m_M. \tag{2.20}$$

One of the physical neutrinos is then a heavy state N with a mass close to the LN breaking scale m_M, while the other is a light state ν with a small mass m_ν suppressed by m_M^{-1}. This desired suppression is a particular realization of Eq. (2.16), and can be understood as the tree level processes in the left plot of Fig. 2.2.

For a more realistic model, we can add three[3] RH fields to the SM spectrum. In that case, $M^{\nu}_{\text{type-I}}$ is a 6×6 matrix which, again in the seesaw limit, can be block-diagonalized by the following 6×6 approximate unitary matrix:

$$U_\xi^\nu = \begin{pmatrix} (\mathbb{1} - \frac{1}{2}\xi^*\xi^T) & \xi^*(\mathbb{1} - \frac{1}{2}\xi^T\xi^*) \\ -\xi^T(\mathbb{1} - \frac{1}{2}\xi^*\xi^T) & (\mathbb{1} - \frac{1}{2}\xi^T\xi^*) \end{pmatrix} + \mathcal{O}(\xi^4)\,, \tag{2.21}$$

where we have introduced the small seesaw matrix parameter $\xi = m_D m_M^{-1}$. This rotation leads to two separated 3×3 mass matrices, given by:

$$U_\xi^{\nu T} M^{\nu}_{\text{type-I}} U_\xi^\nu \simeq \begin{pmatrix} -m_D m_M^{-1} m_D^T & 0 \\ 0 & m_M \end{pmatrix} \equiv \begin{pmatrix} m_\nu & \\ & m_N \end{pmatrix}. \tag{2.22}$$

[3] Although the addition of two neutrinos is enough for explaining neutrino oscillation data, we prefer to add one RH per generation.

We see again that there are two sectors, one light sector whose mass matrix m_ν is suppressed by m_M^{-1} and a heavy sector with masses close to m_M.

Without lost of generality, we can decide to work in the basis where m_M is already diagonal and, therefore, we only need to diagonalize the light mass matrix. In order to be in agreement with neutrino oscillation data, we can impose this light matrix to be diagonalized by the proper $U_{\rm PMNS}$ matrix and to have the right eigenvalues. This can be done by requiring:

$$m_\nu \simeq -m_D m_M^{-1} m_D^T \equiv U^*_{\rm PMNS} m_\nu^{\rm diag} U^\dagger_{\rm PMNS}. \tag{2.23}$$

In this equation, $m_\nu^{\rm diag}$ contains the masses of the physical light neutrino states and the $U_{\rm PMNS}$ matrix the mixing angles, as explained in the previous section. Equation (2.23) can be solved for m_D, leading to the Casas-Ibarra parametrization [37] of the Dirac mass matrix:

$$m_D^T = i\sqrt{m_N^{\rm diag}}\, R \sqrt{m_\nu^{\rm diag}}\, U^\dagger_{\rm PMNS}, \tag{2.24}$$

where we have used the relation $m_N^{\rm diag} \simeq m_M$ so as to express everything in terms of the physical masses. This parametrization allow us to use as input parameters the physical masses, the experimentally measured mixing angles and an unknown 3×3 complex orthogonal matrix R.

As we said, the type-I seesaw model is a simple extension of the SM that explains the smallness of the neutrino masses as a ratio of two very distant scales, the low Dirac mass and the high Majorana mass scales. In order to accommodate light neutrino masses in the eV scale, this ratio needs to be very small. Following Eq. (2.20), we see that large $Y_\nu \sim 1$ couplings imply GUT scale Majorana masses of $m_M \sim 10^{14}$ GeV. On the other hand, TeV scale heavy neutrinos require very small Yukawa couplings, of the order of 10^{-5}. As a consequence, one way or the other, most of the new phenomenology related with these new heavy neutrinos, as well as their direct production at colliders, will be then very suppressed.

Type-II Seesaw Model

The type-II seesaw model [36, 38–41] addes a new scalar $SU(2)_L$ triplet with hypercharge 2 to the SM. In contrast with the fermionic singlets of the type-I seesaw, this new triplet does not interact only with the neutrino fields, but also with the rest of the SM fields, so the full Lagrangian is more involved. Nevertheless, for the purpose of our discussion of neutrino mass generation, it is enough to consider the following relevant terms:

$$\mathcal{L}_{\rm type-II} = -\frac{1}{2} Y_\Delta^{ij} \overline{L_i^C}\, \widetilde{\Delta} L_j - \mu \Phi^T i\sigma_2 \Delta^\dagger \Phi - \frac{1}{2} M_\Delta^2 {\rm Tr}\big(\Delta^\dagger\Delta\big) + h.c. \tag{2.25}$$

Here, Δ stands for the new scalar $SU(2)$ triplet, defined as:

$$\Delta = \begin{pmatrix} \Delta^+/\sqrt{2} & \Delta^{++} \\ \Delta^0 & -\Delta^+/\sqrt{2} \end{pmatrix}. \tag{2.26}$$

The first term in Eq. (2.25) is a Yukawa like interaction between the SM $SU(2)_L$ leptonic doublet L and the scalar triplet, with coupling Y_Δ and $\widetilde{\Delta} = i\sigma_2\Delta^*$. The other two terms are part of the new scalar potential in this model, with M_Δ the mass of the triplet and μ the coupling of the triplet scalar with two Higgs doublets. The full scalar potential, given in Ref. [42] for instance, sets the vacuum expectation values for the neutral components of both the doublet and triplet scalars. In the limit where the triplet is heavy, $M_\Delta \gg v$, its vev is given by,

$$v_\Delta \simeq \mu \frac{v^2}{M_\Delta^2}, \tag{2.27}$$

which then gives a Majorana mass for the neutrinos of

$$m_\nu \simeq v_\Delta Y_\Delta. \tag{2.28}$$

Diagrammatically, this mass term can be understood as the tree level process in the middle of Fig. 2.2.

We can now understand how the type-II seesaw can explain the smallness of the neutrino masses. Looking at these equations, we see that, on one hand, small Yukawa couplings or heavy triplet masses is a possibility, as in the type-I seesaw. On the other hand, in these equations there is an extra scale μ, which in the case of being small, could explain the smallness of m_ν even for large Y_Δ and low M_Δ. Furthermore, assigning to the triplet a leptonic number $L = 2$, we see that the only LN violating term is precisely the one proportional to this μ parameter and, therefore, it is natural [43] to consider μ to be small, as setting it to zero would increase the symmetry of the model. As a result, the smallness of neutrino masses is related somehow to a small breaking of a symmetry.

However, the addition of a new scalar to the SM spectrum will in general modify the Higgs sector or contribute to electroweak precision observables, which are constrained by experiments. For instance, precision measurements of the electroweak ρ parameter set an upper bound on the new scalar triplet vev of $v_\Delta \lesssim 3$ GeV. Fortunately, such a small v_Δ can be again explained by a small LN violating mass scale μ. Additionally, the (double) charged components of the scalar triplet could also induce potentially large tree level flavor changing processes, not observed yet by any experiment.

Type-III Seesaw Model

The type-III seesaw model [44] explains the neutrino masses by adding a new fermionic $SU(2)_L$ triplet to the SM spectrum, which is defined as:

$$\Sigma = \begin{pmatrix} \Sigma^0/\sqrt{2} & \Sigma^+ \\ \Sigma^- & \Sigma^0/\sqrt{2} \end{pmatrix}. \tag{2.29}$$

As the ν_R of the type-I seesaw model, this Σ couples to the LH neutrinos and to the Higgs doublet, with a Lagrangian given by

$$\mathcal{L}_{\text{type-III}} = -Y_\Sigma^{ij}\overline{L_i}\widetilde{\Phi}\Sigma - \frac{1}{2}M_\Sigma^{ij}\mathrm{Tr}\left(\overline{\Sigma_i^C}\Sigma_j\right) + h.c. \tag{2.30}$$

This Lagrangian is very similar to Eq. (2.17), with the Yukawa coupling Y_Σ and the Majorana mass M_Σ. Consequently, in the seesaw limit $M_\Sigma \gg vY_\Sigma$, the obtained light neutrino mass matrix is equivalent to the one in Eq. (2.23):

$$m_\nu \simeq -vY_\Sigma M_\Sigma^{-1} vY_\Sigma^T. \tag{2.31}$$

The tree level diagram generating this neutrino mass is shown in the right panel of Fig. 2.2, which is the same as in the type-I seesaw with Σ instead of ν_R. Actually, in this model the neutral component of Σ behaves like the right-handed neutrino of the type-I seesaw. Nevertheless, being the Σ a $SU(2)_L$ triplet, it also has gauge couplings to the SM. This fact can lead to new phenomenology, such as tree-level flavor changing currents mediated by the charged components $\Sigma^\pm$, which so far have not been observed experimentally.

These three types of seesaw mechanisms are some examples of models for generating light neutrino masses. There are many other proposals in the literature, which try different approaches to explain the lightness of neutrino masses. For instance, in the models known as radiative seesaw models, the tree level neutrino masses are forbidden, so they need to be generated at the loop level and, therefore, they are naturally suppressed with respect to the rest of fermion masses (see Ref. [45] for a recent review). This is the case in the Zee-Babu model [46, 47]. Another option could be to assume that there is a symmetry protecting the neutrinos from having a tree level mass term, which is spontaneously broken with a small vev that generates small neutrino masses, as some R-parity violating supersymmetric models [48–50]. For a review of neutrino mass models, see for instance Refs. [51, 52].

In this Thesis, we are interested in the phenomenology of right-handed neutrinos with masses at the TeV scale, such that they can lead to not very suppressed low energy effects. We are also interested in the possibility of producing them at colliders. As we said, the type-I seesaw model introduces ν_R fields that can indeed be at the TeV, although in this case their Yukawa coupling is so small than it suppresses most of the phenomenological implications. An interesting way out of this situation is to invoke a symmetry that protects the light neutrino masses even in the case of low right-handed masses and large Yukawa couplings. This is the main idea behind low scale seesaw models, as the inverse seesaw model, that we describe in full detail in the following.

2.3 The Inverse Seesaw Model and Its Parametrizations

As we discussed above, the original type-I seesaw model cannot have right-handed neutrinos with masses at the TeV scale and large Yukawa couplings and, at the same time, accommodate light neutrino masses at the eV range. In low scale seesaw models this interesting situation is accomplished by making use of extra symmetries, for instance a common assumption is global lepton number conservation. In order to better understand this idea, we can first consider the simplified situation of one generation, where there is only one left-handed neutrino as in the SM, and add two extra fermionic singlets, ν_R and X. The ν_R field is like in the type-I seesaw model, a right-handed partner of the ν_L, singlet under the full SM group and with lepton number $L = -1$, while the new singlet X has the opposite lepton number $L = 1$. In the limit where LN is conserved, the only terms that we can add to the SM Lagrangian are:

$$\mathcal{L} = -Y_\nu \overline{L}\widetilde{\Phi}\nu_R - M_R \overline{\nu_R^C} X + h.c. \tag{2.32}$$

which, after the EWSB, leads to the following neutrino Majorana mass matrix in the EW (ν_L, ν_R^C, X^C) basis:

$$M^\nu = \begin{pmatrix} 0 & m_D & 0 \\ m_D & 0 & M_R \\ 0 & M_R & 0 \end{pmatrix}. \tag{2.33}$$

Diagonalizing this matrix we obtain two degenerate Majorana neutrinos, which form one single Dirac neutrino, and one massless neutrino. This means that imposing exact LN conservation gives rise to massless neutrinos and, therefore, we need to include a LN breaking in order to generate neutrino masses. If this breaking is small, the neutrino masses will be small. As a result, in these low scale seesaw models the smallness of neutrino masses is related to a small breaking of a symmetry, which is natural in the sense of 't Hooft [43].

Different models can be defined following this idea, depending on where we introduce the small LN violating scale that generates the masses for the light neutrinos. Including Majorana mass terms for the new fermionic singlets, we end up with the inverse seesaw (ISS) model [53–55], whereas a LN violating interaction between the ν_L and X fields defines the linear seesaw (LSS) model vch:2Akhmedov:1995ip,ch:2Akhmedov:1995vm. In this Thesis, we will work in the framework of the inverse seesaw model, although most of our results will also apply to other models as the linear seesaw, since we will see that they can be easily related.

We consider a realization of the inverse seesaw model adapted to three generations where three[4] pairs of fermionic singlets (ν_R, X) are added to the SM. The ISS Lagrangian in this case is given by

$$\mathcal{L}_{\rm ISS} = -Y_\nu^{ij}\overline{L_i}\widetilde{\Phi}\nu_{Rj} - M_R^{ij}\overline{\nu_{Ri}^C}X_j - \frac{1}{2}\mu_R^{ij}\overline{\nu_{Ri}^C}\nu_{Rj} - \frac{1}{2}\mu_X^{ij}\overline{X_i^C}X_j + h.c., \tag{2.34}$$

with the favor indices i, j running from 1 to 3. Here, Y_ν is the 3×3 neutrino Yukawa coupling matrix, as in Eq. (2.17), M_R is a lepton number conserving complex 3×3 mass matrix, and μ_R and μ_X are Majorana complex 3×3 symmetric mass

[4] Although the minimal realization of the ISS model that accounts for oscillation data only needs two fermionic pairs [58], usually referred to as the (2,2)-ISS, we prefer to add one pair for each SM family, usually denoted by (3,3)-ISS.

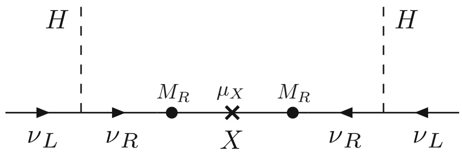

Fig. 2.3 Diagram for the tree level light Majorana mass generation in the ISS model

matrices that violate LN conservation by two units. As we said, these two LN violating scales are naturally small in this model, as setting them to zero would restore the conservation of LN, thus enlarging the symmetry of the model. After the EWSB, we obtain the complete 9×9 neutrino mass matrix, which again in the EW $(\nu_{L_i}, \nu_{R_i}^C, X_i^C)$ basis, reads,

$$M_{\text{ISS}}^{\nu} = \begin{pmatrix} 0 & m_D & 0 \\ m_D^T & \mu_R & M_R \\ 0 & M_R^T & \mu_X \end{pmatrix}. \tag{2.35}$$

Since this complex mass matrix is symmetric, it can be diagonalized using a 9×9 unitary matrix U_ν according to

$$U_\nu^T M_{\text{ISS}}^{\nu} U_\nu = \text{diag}(m_{n_1}, \ldots, m_{n_9}), \tag{2.36}$$

where n_i are the nine physical neutrino Majorana states, with masses m_{n_i}, respectively, and related to the electroweak eigenstates through the rotation U_ν as:

$$\begin{pmatrix} \nu_L^C \\ \nu_R \\ X \end{pmatrix} = U_\nu P_R \begin{pmatrix} n_1 \\ \vdots \\ n_9 \end{pmatrix}, \quad \begin{pmatrix} \nu_L \\ \nu_R^C \\ X^C \end{pmatrix} = U_\nu^* P_L \begin{pmatrix} n_1 \\ \vdots \\ n_9 \end{pmatrix}. \tag{2.37}$$

As we did for the type-I seesaw, it is interesting to consider first the simplified scenario where there is only one generation of (ν_L, ν_R, X). In that case, all the parameters in Eq. (2.35) are just numbers and M_{ISS}^{ν} is a 3×3 mass matrix which, in the $\mu_X \ll m_D, M_R$ limit of approximate LN conservation, has the following three eigenvalues:

$$m_\nu \simeq \frac{m_D^2}{m_D^2 + M_R^2} \mu_X, \tag{2.38}$$

$$m_{N_1, N_2} \simeq \pm\sqrt{M_R^2 + m_D^2} + \frac{M_R^2 \mu_X}{2(m_D^2 + M_R^2)} + \frac{\mu_R}{2}. \tag{2.39}$$

We see that the mass m_ν of one of the states is small, since it is proportional to the small parameter μ_X, and, therefore, it can be associated to the light neutrino states observed in neutrino oscillations. Notice that, contrary to the type-I seesaw model where the lightness of m_ν is related to a suppression of a large LN breaking scale, here it is proportional to a small LN breaking scale, μ_X, motivating the model name

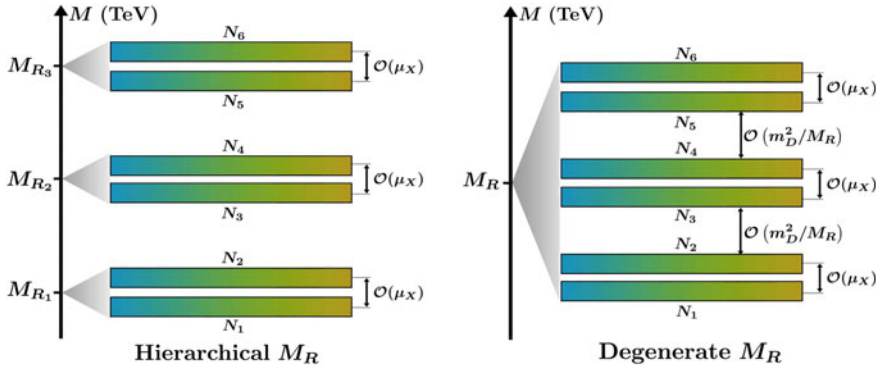

Fig. 2.4 Schematic distribution for the mass spectrum of the six ISS heavy neutrinos, $N_{i=1,...,6}$ with $m_{N_1} < \cdots < m_{N_6}$. For hierarchical M_R, with $M_{R_1} < M_{R_2} < M_{R_3}$ here, there are three quasidegenerate states with masses $m_{N_1} \simeq m_{N_2} \simeq M_{R_1}$, $m_{N_3} \simeq m_{N_4} \simeq M_{R_2}$ and $m_{N_5} \simeq m_{N_6} \simeq M_{R_3}$. For degenerate M_R, meaning $M_{R_{1,2,3}} \equiv M_R$, all the heavy neutrino masses are close to M_R, with small separations between the pairs of $\mathcal{O}(m_D^2/M_R)$. In both cases, there are small $\mathcal{O}(\mu_X)$ splittings between the quasidegenerate neutrinos. We demand that the light neutrino sector is as in Fig. 2.1 by using the parametrizations described in this section. The color code represents the fact that heavy neutrinos can have a non-trivial flavor structure, which we will further study in Chap. 6

of inverse seesaw. In the seesaw limit $m_D \ll M_R$, it can be further simplified to $m_\nu \sim \mu_X m_D^2/M_R^2$, which can be understood as the result of the diagram in Fig. 2.3. The other two mass eigenstates have almost degenerate heavy masses, m_{N_1,N_2}, which combine to form a pseudo-Dirac pair. Notice that the μ_R Majorana mass term for the ν_R fields does not enter in Eq. (2.38), meaning that μ_R does not generate light neutrino masses at the tree level. The effects of this new scale appear only at one-loop level in the light neutrino masses and are, consequently, more suppressed. Therefore, we will set μ_R to zero for the rest of this Thesis and consider a small μ_X as the only lepton number violating parameter leading to the light neutrino masses.

A similar pattern of neutrino masses occurs in our three generations case, with one light and two nearly degenerate heavy neutrinos per generation. In the mass range of our interest with $\mu_X \ll m_D \ll M_R$, the mass matrix $M_{\rm ISS}^\nu$ can be diagonalized by blocks [59], leading to six heavy neutrinos that form quasidegenerate pairs with masses approximately given by the eigenvalues of M_R and with splittings of order $\mathcal{O}(\mu_X)$. We display schematically the heavy neutrino mass spectrum in Fig. 2.4. Regarding the light neutrino sector, it contains three light Majorana neutrinos, whose 3×3 mass matrix is as follows:

$$M_{\rm light} \simeq m_D M_R^{T^{-1}} \mu_X M_R^{-1} m_D^T. \tag{2.40}$$

In the same manner as we did in Eq. (2.23), we can ensure the agreement with neutrino oscillation data by demanding:

$$M_{\rm light} \equiv U_{\rm PMNS}^* m_\nu^{\rm diag} U_{\rm PMNS}^\dagger. \tag{2.41}$$

Then, we can solve this equation for m_D, as we did before to obtain the Casas-Ibarra parametrization. In fact, this can be easily done by analogy with the type-I seesaw. Defining a new 3×3 mass matrix as

$$M = M_R \mu_X^{-1} M_R^T, \tag{2.42}$$

the light neutrino mass matrix can be written similarly to Eq. (2.23):

$$M_{\text{light}} \simeq m_D M^{-1} m_D^T. \tag{2.43}$$

Therefore, we can modify the Casas-Ibarra parametrization in Eq. (2.24) to define a new version for the ISS given by:

$$m_D^T = V^\dagger \sqrt{M^{\text{diag}}} R \sqrt{m_\nu^{\text{diag}}} U_{\text{PMNS}}^\dagger, \tag{2.44}$$

where V is a unitary matrix that diagonalizes M according to $M = V^\dagger M^{\text{diag}} V^*$ and, as before, R is an unknown complex orthogonal matrix that can be written as

$$R = \begin{pmatrix} c_2 c_3 & -c_1 s_3 - s_1 s_2 c_3 & s_1 s_3 - c_1 s_2 c_3 \\ c_2 s_3 & c_1 c_3 - s_1 s_2 s_3 & -s_1 c_3 - c_1 s_2 s_3 \\ s_2 & s_1 c_2 & c_1 c_2 \end{pmatrix}, \tag{2.45}$$

with $c_i \equiv \cos\theta_i$, $s_i \equiv \sin\theta_i$ and θ_1, θ_2, and θ_3 are arbitrary complex angles.

The Casas-Ibarra parametrization has been extensively used in the literature for accommodating light neutrino data in this type of models. We propose here an alternative parametrization that we find very useful to ensure the agreement with oscillation data in the ISS model.[5] The main idea is to use precisely the new scale μ_X to codify light neutrino masses and mixings. This can be done by solving Eq. (2.41) for μ_X instead of m_D, which defines our μ_X parametrization:

$$\mu_X = M_R^T \, m_D^{-1} \, U_{\text{PMNS}}^* m_\nu U_{\text{PMNS}}^\dagger \, m_D^{T\,-1} M_R. \tag{2.46}$$

Notice that we have assumed that the Dirac mass matrix, or equivalently the Yukawa coupling matrix, is not singular so it can be inverted.

Of course, physics does not depend on the parametrization one chooses, however the efficiency in exploring the model parameter space does. When using this new parametrization, we see two important advantages. First, Eq. (2.41) is quadratic in m_D, so solving it leads to a redundancy reflected in the orthogonal matrix R that introduces six new unknown parameters to scan over. In contrast, Eq. (2.41) is linear in μ_X, and therefore the μ_X parametrization does not introduce any new parameter and the parameter space can be easily explored. Second, the μ_X parametrization

[5]Nevertheless, this idea could be generically applied to any model with a new scale responsible of explaining the smallness of neutrino masses.

considers Y_ν and M_R as input parameters, while the Casas-Ibarra parametrization works with μ_X as input instead of Y_ν. As we will see, the relevant parameters for the LFV and related phenomenology in these models are the Yukawa coupling and main source of the LFV, Y_ν, and the heavy mass scale M_R. Therefore, being able to treat them as independent input parameters is important for studying the LFV phenomenology in these models. Furthermore, this latter point will be also important in order to understand the decoupling behavior of the different observables in the limit of very heavy right-handed neutrinos. All these issues will become clear in the following Chapters.

In order to complete the theoretical set up of the model, we specify next all the relevant neutrino interactions in their mass basis. These include the neutrino Yukawa couplings, the gauge couplings of the charged and neutral gauge bosons, $W^\pm$ and Z, and the couplings of the corresponding Goldstone bosons, $G^\pm$ and G^0:

$$\mathcal{L}_W = -\frac{g}{\sqrt{2}} \sum_{i=1}^{3} \sum_{j=1}^{9} W_\mu^- \bar{\ell}_i B_{\ell_i n_j} \gamma^\mu P_L n_j + h.c., \tag{2.47}$$

$$\mathcal{L}_Z = -\frac{g}{4c_W} \sum_{i,j=1}^{9} Z_\mu \bar{n}_i \gamma^\mu \Big[C_{n_i n_j} P_L - C^*_{n_i n_j} P_R \Big] n_j, \tag{2.48}$$

$$\mathcal{L}_H = -\frac{g}{2m_W} \sum_{i,j=1}^{9} H \bar{n}_i C_{n_i n_j} \Big[m_{n_i} P_L + m_{n_j} P_R \Big] n_j, \tag{2.49}$$

$$\mathcal{L}_{G^\pm} = -\frac{g}{\sqrt{2} m_W} \sum_{i=1}^{3} \sum_{j=1}^{9} G^- \bar{\ell}_i B_{\ell_i n_j} \Big[m_{\ell_i} P_L - m_{n_j} P_R \Big] n_j + h.c, \tag{2.50}$$

$$\mathcal{L}_{G^0} = -\frac{ig}{2m_W} \sum_{i,j=1}^{9} G^0 \bar{n}_i C_{n_i n_j} \Big[m_{n_i} P_L - m_{n_j} P_R \Big] n_j, \tag{2.51}$$

where $P_{R,L} = (1 \pm \gamma^5)/2$ are the usual chirality projectors and,

$$B_{\ell_i n_j} = U^{\nu *}_{ij}, \tag{2.52}$$

$$C_{n_i n_j} = \sum_{k=1}^{3} U^\nu_{ki} U^{\nu *}_{kj}. \tag{2.53}$$

These coupling matrices follow the subsequent interesting identities [60]:

$$\sum_{k=1}^{N} B_{\ell_1 n_k} B^*_{\ell_2 n_k} = \delta_{\ell_1 \ell_2}, \quad \sum_{k=1}^{N} B_{\ell n_k} C_{n_k n_i} = B_{\ell n_i}, \quad \sum_{k=1}^{N} C_{n_i n_k} C^*_{n_j n_k} = \sum_{k=1}^{3} B^*_{\ell_k n_i} B_{\ell_k n_j} = C_{n_i n_j},$$
$$\sum_{k=1}^{N} m_{n_k} C_{n_i n_k} C_{n_j n_k} = 0, \quad \sum_{k=1}^{N} m_{n_k} B_{\ell n_k} C^*_{n_k n_i} = 0, \quad \sum_{k=1}^{N} m_{n_k} B_{\ell_1 n_k} B_{\ell_2 n_k} = 0, \tag{2.54}$$

where N stands for the total number of neutrinos, i.e., $N = 9$ for the ISS realization we are considering.

2.3.1 The Linear Seesaw Model

Finally, we want to briefly comment on the other low scale seesaw model above mentioned, the linear seesaw model, and its relation with the ISS model. As we said, in the LSS model the LN violating mass scale is introduced via a Yukawa coupling, $\widetilde{Y}_\nu$, between the ν_L and the X singlets, in contrast to the ISS model where the LN violating scale is introduced via the Majorana mass terms. For simplicity, we focus this discussion on the one generation case, although it can be easily generalized to more generations. In this case, the neutrino mass matrix in the linear seesaw, in the same EW basis (ν_L, ν_R^C, X^C), reads as:

$$M^\nu_{\rm LSS} = \begin{pmatrix} 0 & m_D & \widetilde{m}_D \\ m_D & 0 & M_R \\ \widetilde{m}_D & M_R & 0 \end{pmatrix}, \tag{2.55}$$

where $\widetilde{m}_D = v\widetilde{Y}_\nu$ and the other parameters are as before. Assuming an approximate LN symmetry, this new Yukawa interaction will be small, leading to a light neutrino mass. This is given, for $\widetilde{m}_D \ll m_D \ll M_R$, by,

$$m_\nu \simeq -2\widetilde{m}_D \frac{m_D}{M_R}, \tag{2.56}$$

which is linear in m_D, motivating the name of the model.

In order to show the relation between the linear and inverse seesaw models, first we may notice that they are identical in the limit of massless neutrinos, i.e., in the limit of exact LN conservation. When LN is violated in the linear seesaw model via a non-zero $\widetilde{m}_D$, we can redefine the fermionic singlets in such a way that $\widetilde{m}_D$ is rotated away. This can be done by performing a rotation [61] of $\tan\theta = \widetilde{m}_D/m_D$ between the (ν_R, X) fields. Then

$$\begin{pmatrix} 1 & 0 & 0 \\ 0 & c & s \\ 0 & -s & c \end{pmatrix} \begin{pmatrix} 0 & m_D & \widetilde{m}_D \\ m_D & 0 & M_R \\ \widetilde{m}_D & M_R & 0 \end{pmatrix} \begin{pmatrix} 1 & 0 & 0 \\ 0 & c & -s \\ 0 & s & c \end{pmatrix} = \begin{pmatrix} 0 & m_D/c & 0 \\ m_D/c & M_R s_2 & M_R c_2 \\ 0 & M_R c_2 & -M_R s_2 \end{pmatrix}, \tag{2.57}$$

where $c = \cos\theta$, $s = \sin\theta$, $c_2 = \cos 2\theta$ and $s_2 = \sin 2\theta$. Since $\widetilde{m}_D \ll m_D$, $\tan\theta$ is small and, therefore, the mass matrix in this rotated basis has the same pattern as the ISS mass matrix in Eq. (2.35). Given this relation, we emphasize again that the results and general conclusions of this Thesis, computed and studied for the particular case of the ISS model, could be applicable to other low scale seesaw models, like the linear seesaw model.

It is important to notice that in this kind of low scale seesaw models, in contrast to the standard type-I seesaw, there are three different scales which play different roles. In the particular case of the ISS model, μ_X controls the smallness of the light neutrino masses, M_R the masses of the new heavy neutrinos and $m_D = vY_\nu$ the interaction between the new added neutrino sector and the SM ν_L fields. Since they are independent, we can have at the same time large Yukawa couplings, $Y_\nu^2/4\pi \sim \mathcal{O}(1)$, and right-handed neutrinos in the TeV range, i.e., reachable at present experiments like the LHC. These two properties make the ISS model in particular, and low scale seesaw models in general, interesting models with a rich phenomenology that we wish to explore further in this Thesis.

2.3.2 The SUSY Inverse Seesaw Model

The Higgs mechanism of the SM introduces a fundamental scalar particle, the recently found Higgs boson, whose mass has been experimentally set to $m_H = 125.09 \pm 0.21\,(\text{stat.}) \pm 0.11\,(\text{syst.})$ GeV [62]. Being a fundamental scalar, it will receive huge contributions via quantum corrections if a new heavy scale associated to some new physics is introduced, for instance, if gravitational effects are introduced at the Planck mass scale $M_P \sim 10^{19}$ GeV. This instability of the Higgs sector under radiative corrections is known as the hierarchy problem and it is one of the main theoretical problems of the SM. One of the most popular and elegant solutions to this problem is provided by supersymmetry (SUSY) [63–65]. This is a new symmetry that relates fermions with bosons, such that their contributions to the radiative corrections to the Higgs boson mass exactly cancel. Therefore, it introduces a new symmetry that protects the scalar sector from unnaturally large radiative corrections.

The minimal SUSY extension of the SM is the Minimal Supersymmetric Standard Model (MSSM) [66–68]. We can understand the way this model extends the SM in two steps. First, for consistency reasons, it adds a second scalar $SU(2)_L$ doublet to the SM, in a way that one of the doublets is responsible of giving masses to the up-type fermions and the other one to the down-type fermions. Then, it doubles all the particles in the spectrum introducing a SUSY partner for each field. For a full review of SUSY and the MSSM, we refer the reader to Refs. [69, 70]. However, in this minimal extension of the SM, neutrinos remain massless as in the SM and, therefore, it needs to be further extended in order to explain neutrino oscillation data. Here, we shortly summarize the most relevant aspects of the simplest SUSY version of the inverse seesaw model, introducing the new neutrino and sneutrino sectors needed for our forthcoming phenomenological studies, in particular for the LFV Higgs decay computations in Sect. 4.2.

In the simplest supersymmetric realization of the ISS model, the SUSY-ISS model in short, the MSSM superfield content is supplemented by three pairs of gauge singlet chiral superfields $\widehat{N}_i$ and $\widehat{X}_i$ with opposite lepton numbers ($i = 1, 2, 3$). As in the original ISS model, this allows to write a Yukawa interaction term for the neutrinos, with coupling Y_ν, a heavy mass term $\widetilde{M}_R$ between the extra singlets, and a Majorana mass term $\widetilde{\mu}_X$ for the X fields. The SUSY-ISS model is then defined by the following superpotential:

$$W = W_{\text{MSSM}} + \varepsilon_{ab} \widehat{N} Y_\nu \widehat{H}_2^b \widehat{L}^a + \widehat{N} \widetilde{M}_R \widehat{X} + \frac{1}{2} \widehat{X} \widetilde{\mu}_X \widehat{X}, \tag{2.58}$$

with $\varepsilon_{12} = 1$ and

$$W_{\text{MSSM}} = \varepsilon_{ab} \left[\widehat{E} Y_e \widehat{H}_1^a \widehat{L}^b + \widehat{D} Y_D \widehat{H}_1^a \widehat{Q}^b + \widehat{U} Y_U \widehat{H}_2^b \widehat{Q}^a - \mu \widehat{H}_1^a \widehat{H}_2^b \right]. \tag{2.59}$$

Here, all chiral superfields are taken to be left-handed. This means that $\widehat{Q}$ and $\widehat{L}$ are respectively the chiral superfields involving the left-handed $SU(2)_L$ doublets Q_L and L_L, as well as their SUSY partners. For instance, the the spin 0 and spin $\frac{1}{2}$ components of $\widehat{L}$ are $(\widetilde{\nu}_L, \widetilde{e}_L)$ and (ν_L, e_L). On the other hand, the chiral superfields $\widehat{D}$, $\widehat{U}$, $\widehat{E}$ contain the d_R^c, u_R^c and e_R^c fields and their partners, for example, we have $\widehat{E} = \left[(\widetilde{e_R})^*, (e_R)^c\right]$. The down- and up-type Higgs bosons, $\widehat{H}_1$ and $\widehat{H}_2$ respectively, are defined as

$$\widehat{H}_1 = \begin{pmatrix} \hat{h}_1^0 \\ \hat{h}_1^- \end{pmatrix}, \quad \widehat{H}_2 = \begin{pmatrix} \hat{h}_2^+ \\ \hat{h}_2^0 \end{pmatrix}, \tag{2.60}$$

and μ is the Higgs superfield mass parameter. The couplings $Y_{e,D,U}$ are the Yukawa coupling matrices. The generation indices have been suppressed for simplicity and it should be understood in a tensor notation as $\widehat{N} Y_\nu \widehat{H}_2^b \widehat{L}^a = \widehat{N}_i (Y_\nu)_{ij} \widehat{H}_2^b \widehat{L}_j^a$.

Exact SUSY invariance requires any particles to have the same mass of its SUSY partner, meaning that the SM spectrum should have a SUSY copy with the same corresponding masses. Nevertheless, the lack of any signal from such new particles in the experiments has excluded this situation and, therefore, if SUSY exists in Nature, it must be broken. This breaking, however, cannot spoil the above commented solution to the hierarchy problem, so it needs to be softly broken.

Even if we do not know the SUSY breaking mechanism, we can parametrize it by introducing a set of well established soft SUSY breaking terms [71]. In the SUSY-ISS model, this soft SUSY breaking Lagrangian is given by

$$
\begin{aligned}
-\mathcal{L}_{\text{soft}} = &- \mathcal{L}_{\text{soft}}^{\text{MSSM}} + \widetilde{\nu}_R^T\, m^2_{\tilde{\nu}_R}\, \widetilde{\nu}_R^* + \left[\widetilde{\nu}_R^\dagger (A_\nu Y_\nu) \widetilde{\nu}_L h_2^0 - \widetilde{\nu}_R^\dagger (A_\nu Y_\nu) \widetilde{e}_L h_2^+ + h.c. \right] \\
&+ \widetilde{X}^T m^2_{\tilde{X}} \widetilde{X}^* + \left[\widetilde{X}^\dagger (B_X \widetilde{\mu}_X) \widetilde{X}^* + \widetilde{\nu}_R^\dagger (B_R \widetilde{M}_R) \widetilde{X}^* + h.c. \right],
\end{aligned} \tag{2.61}
$$

with

$$
\begin{aligned}
-\mathcal{L}_{\text{soft}}^{\text{MSSM}} = &\, \widetilde{e}_R^T\, m^2_{\tilde{e}}\, \widetilde{e}_R^* + \widetilde{d}_R^T\, m^2_{\tilde{d}}\, \widetilde{d}_R^* + \widetilde{u}_R^T\, m^2_{\tilde{u}}\, \widetilde{u}_R^* + m^2_{H_1} |H_1|^2 + m^2_{H_2} |H_2|^2 \\
&+ \delta_{ab} (\widetilde{Q}^a)^\dagger m^2_{\tilde{Q}} \widetilde{Q}^b + \delta_{ab} (\widetilde{L}^a)^\dagger m^2_{\tilde{L}} \widetilde{L}^b + \frac{1}{2} \left[M_1 \bar{\lambda}_b \lambda_b + M_2 \bar{\lambda}_W^\alpha \lambda_W^\alpha + M_3 \bar{\lambda}_g^\alpha \lambda_g^\alpha + h.c. \right] \\
&+ \varepsilon_{ab} \left[(\widetilde{u}_R^\dagger (A_u Y_u) \widetilde{Q}^a H_2^b + \widetilde{d}_R^\dagger (A_d Y_d) \widetilde{Q}^b H_1^a + \widetilde{e}_R^\dagger (A_e Y_e) \widetilde{L}^b H_1^a + B\mu H_2^a H_1^b + h.c. \right].
\end{aligned} \tag{2.62}
$$

These SUSY breaking Lagrangians introduce a set of new unknown parameters to the SUSY-ISS model. From the MSSM Lagrangian, we have the squark and slepton soft masses, $m^2_{\tilde{e},\tilde{d},\tilde{u},\tilde{Q},\tilde{L}}$, the Higgs sector soft masses $m^2_{H_{1,2}}$ and $B\mu$, the gaugino soft masses $M_{1,2,3}$ and the trilinear couplings for squarks and sleptons, $A_{u,d,e}$. In the SUSY-ISS model, there are some extra soft parameters related to the new added fields, in particular, the soft masses $m^2_{\tilde{\nu}_R,\tilde{X}}$, $B_X \widetilde{\mu}_X$ and $B_R \widetilde{M}_R$, and the trilinear coupling A_ν.

All these new parameters could, in principle, have a non-trivial flavor structure. Nevertheless, when studying the SUSY-ISS model, and for the sake of simplicity, we will take all soft SUSY breaking masses, as well as the lepton number conserving mass term $\widetilde{M}_R$, to be flavor diagonal. This way, the only sources of flavor violation are the neutrino Yukawa coupling Y_ν, and the lepton number violating mass term $\widetilde{\mu}_X$. The only exception will be $m^2_{\tilde{L}}$, which receives radiative corrections via the renormalization group equations (RGE), from a heavy scale M with universal soft SUSY breaking parameters down to the heavy neutrino scale M_R. These corrections are also governed by Y_ν and, for phenomenological purposes, can be described as [72]:

$$
\left(\Delta m^2_{\tilde{L}}\right)_{ij} = -\frac{1}{8\pi^2} (3M_0^2 + A_0^2) \left(Y_\nu^\dagger \log \frac{M}{M_R} Y_\nu \right)_{ij}. \tag{2.63}
$$

After the EWSB, the neutrino sector is as in the previous ISS model, therefore the analysis of the mass matrix diagonalization and the discussion about using the Casas-Ibarra or the μ_X parametrization for accommodating oscillation data is the same as before. Hence, it is enough to describe the new SUSY sector, and the sneutrino mass matrix $M^2_{\tilde{\nu}}$, which is defined by

$$-\mathcal{L}^{\tilde{\nu}}_{\rm mass} = \frac{1}{2}\left(\tilde{\nu}_L^\dagger, \tilde{\nu}_L^T, \tilde{\nu}_R^T, \tilde{\nu}_R^\dagger, \tilde{X}^T, \tilde{X}^\dagger\right) M^2_{\tilde{\nu}} \begin{pmatrix} \tilde{\nu}_L \\ \tilde{\nu}_L^* \\ \tilde{\nu}_R^* \\ \tilde{\nu}_R \\ \tilde{X}^* \\ \tilde{X} \end{pmatrix}, \tag{2.64}$$

where $\tilde{\nu}_L$, $\tilde{\nu}_R$ and $\tilde{X}$ are vectors made of 3 weak eigenstates each and they are defined in a similar fashion, e.g. $\tilde{\nu}_L = (\tilde{\nu}_L^{(e)}, \tilde{\nu}_L^{(\mu)}, \tilde{\nu}_L^{(\tau)})^T$. The complete 18×18 sneutrino mass matrix is then expressed in terms of 3×3 submatrices, giving:

$$M^2_{\tilde{\nu}} = \begin{pmatrix} M^2_{LL} & 0 & 0 & M^2_{LR} & m_D M_R^* & 0 \\ 0 & (M^2_{LL})^T & (M^2_{LR})^* & 0 & 0 & m_D^* M_R \\ 0 & (M^2_{LR})^T & M^2_{RR} & 0 & M_R \mu_X^* & (B_R M_R^*)^* \\ (M^2_{LR})^\dagger & 0 & 0 & (M^2_{RR})^T & B_R M_R^* & M_R^* \mu_X \\ M_R^T m_D^\dagger & 0 & \mu_X M_R^\dagger & (B_R M_R^*)^\dagger & M^2_{XX} & 2(B_X \mu_X^*)^\dagger \\ 0 & M_R^\dagger m_D^T & (B_R M_R^*)^T & \mu_X^* M_R^T & 2(B_X \mu_X^*) & (M^2_{XX})^T \end{pmatrix}, \tag{2.65}$$

with

$$M^2_{LL} = m_D m_D^\dagger + m^2_{\tilde{L}} + \mathbb{1}\frac{m_Z}{2}\cos 2\beta, \tag{2.66}$$

$$M^2_{LR} = -\frac{\mu}{\tan\beta} m_D + m_D A_\nu^\dagger, \tag{2.67}$$

$$M^2_{RR} = m_D^T m_D^* + M_R M_R^\dagger + m^2_{\tilde{\nu}_R}, \tag{2.68}$$

$$M^2_{XX} = M_R^T M_R^* + \mu_X \mu_X^* + m^2_{\tilde{X}}. \tag{2.69}$$

Then, the sneutrino mass matrix is diagonalized by using:

$$\tilde{U}^\dagger M^2_{\tilde{\nu}} \tilde{U} = M^2_{\tilde{n}} = \mathrm{diag}(m^2_{\tilde{n}_1}, \ldots, m^2_{\tilde{n}_{18}}), \tag{2.70}$$

which corresponds to the following rotation between the interaction and mass basis

$$\begin{pmatrix} \tilde{\nu}_L \\ \tilde{\nu}_L^* \\ \tilde{\nu}_R^* \\ \tilde{\nu}_R \\ \tilde{X}^* \\ \tilde{X} \end{pmatrix} = \tilde{U} \begin{pmatrix} \tilde{n}_1 \\ \vdots \\ \vdots \\ \vdots \\ \tilde{n}_{18} \end{pmatrix}. \tag{2.71}$$

Notice that the basis used in Eq. (2.64) uses the sneutrino electroweak eigenstates, and their complex conjugate states and they fulfill:

$$\tilde{\nu}_i = \tilde{U}_{i,j}\tilde{n}_j, \tag{2.72}$$

$$\tilde{\nu}_i^* = \tilde{U}_{3+i,j}\tilde{n}_j, \tag{2.73}$$

but at the same time:

$$(\tilde{\nu}_i)^* = \tilde{U}^*_{i,j}\tilde{n}_j, \tag{2.74}$$

since the physical sneutrinos are real scalar fields. While both Eqs. (2.73) and (2.74) are equally valid, we choose Eq. (2.73).

The mass matrices of the other SUSY particles, namely the charginos, neutralinos, and charged sleptons, are the same as in the SUSY type-I seesaw studied in Ref. [73], so we will use their definitions of the corresponding rotation matrices, which in turn were based on the conventions of Ref. [67] for the charginos and neutralinos. Specifically, U and V will be the matrices that rotate the chargino states and N the one that rotates the neutralino states. In addition, combinations of rotation matrices for the neutralinos are defined as

$$\begin{aligned} N'_{a1} &= \quad N_{a1}\cos\theta_W + N_{a2}\sin\theta_W, \\ N'_{a2} &= -N_{a1}\sin\theta_W + N_{a2}\cos\theta_W. \end{aligned} \tag{2.75}$$

As for the charged sleptons, they are diagonalized by

$$\tilde{\ell}' = R^{(\ell)}\tilde{\ell}, \tag{2.76}$$

where $\tilde{\ell}' = (\tilde{e}_L, \tilde{e}_R, \tilde{\mu}_L, \tilde{\mu}_R, \tilde{\tau}_L, \tilde{\tau}_R)^T$ are the weak eigenstates and $\tilde{\ell} = (\tilde{\ell}_1, \ldots, \tilde{\ell}_6)^T$ are the mass eigenstates.

Finally, we introduce the relevant interaction terms from the Lagrangian that will be needed later in the study of the LFV Higgs decays. Following again the notation in Ref. [73], these terms are given in the mass basis by

$$\begin{aligned} \mathcal{L}_{\tilde{\chi}_j^-\ell\tilde{\nu}_\alpha} &= -g\,\bar{\ell}\left[A^{(\ell)}_{L\alpha j}P_L + A^{(\ell)}_{R\alpha j}P_R\right]\tilde{\chi}_j^-\tilde{\nu}_\alpha + h.c., \\ \mathcal{L}_{\tilde{\chi}_a^0\ell\tilde{\ell}_\alpha} &= -g\bar{\ell}\left[B^{(\ell)}_{L\alpha a}P_L + B^{(\ell)}_{R\alpha a}P_R\right]\tilde{\chi}_a^0\tilde{\ell}_\alpha + h.c., \\ \mathcal{L}_{H_x\tilde{s}_\alpha\tilde{s}_\beta} &= -iH_x\left[g_{H_x\tilde{\nu}_\alpha\tilde{\nu}_\beta}\tilde{\nu}^*_\alpha\tilde{\nu}_\beta + g_{H_x\tilde{\ell}_\alpha\tilde{\ell}_\beta}\tilde{\ell}^*_\alpha\tilde{\ell}_\beta\right], \\ \mathcal{L}_{H_x\tilde{\chi}_i^-\tilde{\chi}_j^-} &= -gH_x\bar{\tilde{\chi}}_i^-\left[W^{(x)}_{Lij}P_L + W^{(x)}_{Rij}P_R\right]\tilde{\chi}_j^-, \\ \mathcal{L}_{H_x\tilde{\chi}_a^0\tilde{\chi}_b^0} &= -\frac{g}{2}H_x\bar{\tilde{\chi}}_a^0\left[D^{(x)}_{Lab}P_L + D^{(x)}_{Rab}P_R\right]\tilde{\chi}_b^0, \\ \mathcal{L}_{H_x\ell\ell} &= -gH_x\bar{\ell}\left[S^{(x)}_{L,\ell}P_L + S^{(x)}_{R,\ell}P_R\right]\ell. \end{aligned} \tag{2.77}$$

The coupling factors here are given in terms of the SUSY-ISS model parameters in Appendix D.

Summarizing, in this Chapter we have seen that the experimental evidences for neutrino masses have established the need of new physics in order to add neutrino masses to the SM. We have reviewed some popular neutrino mass generation models, paying special attention to two low scale seesaw models, the ISS and the SUSY-ISS models, which add heavy neutrinos with masses at the reach of the LHC. We have discussed in detail the neutrino sector of these models and introduce a new parametrization, the μ_X parametrization, that allows to accommodate neutrino oscillation data while choosing as input parameters the Yukawa coupling matrix and the heavy neutrino mass matrix M_R, i.e., the most relevant parameters for our forthcoming study of the charged LFV observables.

References

1. E. Arganda, M.J. Herrero, X. Marcano, C. Weiland, Phys. Rev. **D91**, 015001 (2015). https://doi.org/10.1103/PhysRevD.91.015001, arxiv:1405.4300 [hep-ph]
2. E. Arganda, M.J. Herrero, X. Marcano, C. Weiland, Phys. Rev. D **91**, 055010 (2016). arXiv:1508.04623 [hep-ph]
3. B. Pontecorvo, Sov. Phys. JETP **6**, 429 (1957), [Zh. Eksp. Teor. Fiz. 33, 549 (1957)]
4. Z. Maki, M. Nakagawa, S. Sakata, Prog. Theor. Phys. **28**, 870 (1962). https://doi.org/10.1143/PTP.28.870
5. C. Giunti, W.C. Kim, *Fundamentals of Neutrino Physics and Astrophysics* (Oxford University Press, 2007)
6. C. Patrignani et al. (Particle Data Group), Chin. Phys. **C40**, 100001 (2016). https://doi.org/10.1088/1674-1137/40/10/100001
7. C. Kraus et al., Eur. Phys. J. C **40**, 447 (2005). arXiv:hep-ex/0412056 [hep-ex]
8. V.N. Aseev et al. (Troitsk), Phys. Rev. **D84**, 112003 (2011). https://doi.org/10.1103/PhysRevD.84.112003, arXiv:1108.5034 [hep-ex]
9. P.A.R. Ade et al. (Planck), Astron. Astrophys. **571**, A16 (2014). https://doi.org/10.1051/0004-6361/201321591, arXiv:1303.5076 [astro-ph.CO]
10. L. Wolfenstein, Phys. Rev. **D17**, 2369 (1978). https://doi.org/10.1103/PhysRevD.17.2369
11. L. Wolfenstein, Phys. Rev. **D20**, 2634 (1979). https://doi.org/10.1103/PhysRevD.20.2634
12. S.P. Mikheev, A.Yu. Smirnov, Sov. J. Nucl. Phys. **42**, 913 (1985), [Yad. Fiz. 42, 1441 (1985)]
13. S.P. Mikheev, A.Yu. Smirnov, Nuovo Cim. **C9**, 17 (1986). https://doi.org/10.1007/BF02508049
14. S.P. Mikheev, A.Yu. Smirnov, Sov. Phys. JETP **64**, 4 (1986), [Zh. Eksp. Teor. Fiz. 91, 7 (1986)], arXiv:0706.0454 [hep-ph]
15. J.D. Vergados, H. Ejiri, F. Simkovic, Rept. Prog. Phys. **75**, 106301 (2012). arXiv:1205.0649 [hep-ph]
16. S. Dell'Oro, S. Marcocci, M. Viel, F. Vissani, Adv. High Energy Phys. **2016**, 2162659 (2016). arXiv:1601.07512 [hep-ph]
17. C. Jarlskog, Z. Phys. **C29**, 491 (1985). https://doi.org/10.1007/BF01565198
18. S. Davidson, E. Nardi, Y. Nir, Phys. Rept. **466**, 105 (2008). arXiv:0802.2962 [hep-ph]
19. M.A. Acero, C. Giunti, M. Laveder, Phys. Rev. D **78**, 073009 (2008). arXiv:0711.4222 [hep-ph]
20. C. Giunti, M. Laveder, Phys. Rev. C **83**, 065504 (2011). arXiv:1006.3244 [hep-ph]
21. T.A. Mueller et al., Phys. Rev. C **83**, 054615 (2011). arXiv:1101.2663 [hep-ex]
22. P. Huber, Phys. Rev. **C84**, 024617 (2011), [Erratum: Phys. Rev.C85, 029901(2012)]. https://doi.org/10.1103/PhysRevC.85.029901, https://doi.org/10.1103/PhysRevC.84.024617, arXiv:1106.0687 [hep-ph]
23. G. Mention, M. Fechner, T. Lasserre, T.A. Mueller, D. Lhuillier, M. Cribier, A. Letourneau, Phys. Rev. D **83**, 073006 (2011). arXiv:1101.2755 [hep-ex]

24. A. Aguilar-Arevalo et al. (LSND), Phys. Rev. **D64**, 112007 (2001). https://doi.org/10.1103/PhysRevD.64.112007, arXiv:hepex/0104049 [hep-ex]
25. A.A. Aguilar-Arevalo et al. (MiniBooNE), Phys. Rev. Lett. **98**, 231801 (2007). https://doi.org/10.1103/PhysRevLett.98.231801, arXiv:0704.1500 [hep-ex]
26. A.A. Aguilar-Arevalo et al. (MiniBooNE), Phys. Rev. Lett. **105**, 181801 (2010). https://doi.org/10.1103/PhysRevLett.105.181801, arXiv:1007.1150 [hep-ex]
27. A.A. Aguilar-Arevalo et al. (MiniBooNE), Phys. Rev. Lett. **110**, 161801 (2013). https://doi.org/10.1103/PhysRevLett.110.161801, arXiv:1303.2588 [hep-ex]
28. I. Esteban, M.C. Gonzalez-Garcia, M. Maltoni, I. Martinez-Soler, T. Schwetz, JHEP **01**, 087 (2017). arXiv:1611.01514 [hep-ph]
29. E. Akhmedov (2014), arXiv:1412.3320 [hep-ph]
30. S. Weinberg, Phys. Rev. Lett. **43**, 1566 (1979). https://doi.org/10.1103/PhysRevLett.43.1566
31. A. Abada, C. Biggio, F. Bonnet, M.B. Gavela, T. Hambye, JHEP **12**, 061 (2007). arXiv:0707.4058 [hep-ph]
32. P. Minkowski, Phys. Lett. **B67**, 421 (1977). https://doi.org/10.1016/0370-2693(77)90435-X
33. M. Gell-Mann, P. Ramond, R. Slansky, *Supergravity Workshop Stony Brook, New York, September 27-28, 1979*, Conf. Proc. **C790927**, 315 (1979), arXiv:1306.4669 [hepth]
34. T. Yanagida, Proceedings: Workshop on the Unified Theories and the Baryon Number in the Universe: Tsukuba, Japan, February 13–14, 1979. Conf. Proc. **C7902131**, 95 (1979)
35. R.N. Mohapatra, G. Senjanovic, Phys. Rev. Lett. **44**, 912 (1980). https://doi.org/10.1103/PhysRevLett.44.912
36. J. Schechter, J.W.F. Valle, Phys. Rev. **D22**, 2227 (1980). https://doi.org/10.1103/PhysRevD.22.2227
37. J.A. Casas, A. Ibarra, Nucl. Phys. B **618**, 171 (2001). arXiv:hep-ph/0103065 [hepph]
38. M. Magg, C. Wetterich, Phys. Lett. **B94**, 61 (1980). https://doi.org/10.1016/0370-2693(80)90825-4
39. C. Wetterich, Nucl. Phys. **B187**, 343 (1981). https://doi.org/10.1016/0550-3213(81)90279-0
40. G. Lazarides, Q. Sha, C. Wetterich, Nucl. Phys. **B181**, 287 (1981). https://doi.org/10.1016/0550-3213(81)90354-0
41. R.N. Mohapatra, G. Senjanovic, Phys. Rev. **D23**, 165 (1981). https://doi.org/10.1103/PhysRevD.23.165
42. A. Arhrib, R. Benbrik, M. Chabab, G. Moultaka, M.C. Peyranere, L. Rahili, J. Ramadan, Phys. Rev. D **84**, 095005 (2011). arXiv:1105.1925 [hep-ph]
43. G. 't Hooft, *Recent Developments in Gauge Theories. Proceedings, Nato Advanced Study Institute, Cargese, France, August 26–September 8, 1979*, NATO Sci. Ser. B **59**, 135 (1980). https://doi.org/10.1007/978-1-4684-7571-5_9
44. R. Foot, H. Lew, X.G. He, G.C. Joshi, Z. Phys. **C44**, 441 (1989). https://doi.org/10.1007/BF01415558
45. Y. Cai, J. Herrero-García, M. A. Schmidt, A. Vicente, R. R. Volkas, (2017), arXiv:1706.08524 [hep-ph]
46. A. Zee, Nucl. Phys. B **264**, 99 (1986)
47. K.S. Babu, Phys. Lett. **B203**, 132 (1988). https://doi.org/10.1016/0370-2693(88)91584-5
48. C.S. Aulakh, R.N. Mohapatra, Phys. Lett. **B119**, 136 (1982). https://doi.org/10.1016/0370-2693(82)90262-3
49. L.J. Hall, M. Suzuki, Nucl. Phys. **B231**, 419 (1984). https://doi.org/10.1016/0550-3213(84)90513-3
50. R. Barbier et al., Phys. Rept. **420**, 1 (2005). arXiv:hep-ph/0406039 [hep-ph]
51. R.N. Mohapatra et al., Rept. Prog. Phys. **70**, 1757 (2007). arXiv:hep-ph/0510213 [hepph]
52. E. Ma, Proceedings, 15th Hellenic School and Workshops on Elementary Particle Physics and Gravity (CORFU2015): Corfu, Greece, September 1–25, 2015, PoS **CORFU2015**, 009 (2016)
53. R.N. Mohapatra, Phys. Rev. Lett. **56**, 561 (1986). https://doi.org/10.1103/PhysRevLett.56.561
54. R.N. Mohapatra, J.W.F. Valle, *Proceedings, 23RD International Conference on High Energy Physics, JULY 16-23, 1986, Berkeley, CA*, Phys. Rev. **D34**, 1642 (1986). https://doi.org/10.1103/PhysRevD.34.1642

55. J. Bernabeu, A. Santamaria, J. Vidal, A. Mendez, J. W. F. Valle, Phys. Lett. **B187**, 303 (1987). https://doi.org/10.1016/0370-2693(87)91100-2
56. E.K. Akhmedov, M. Lindner, E. Schnapka, J.W.F. Valle, Phys. Lett. B **368**, 270 (1996). arXiv:hep-ph/9507275 [hep-ph]
57. E.K. Akhmedov, M. Lindner, E. Schnapka, J.W.F. Valle, Phys. Rev. D **53**, 2752 (1996). arXiv:hep-ph/9509255 [hep-ph]
58. A. Abada, M. Lucente, Nucl. Phys. B **885**, 651 (2014). arXiv:1401.1507 [hep-ph]
59. M.C. Gonzalez-Garcia, J.W.F. Valle, Phys. Lett. **B216**, 360(1989). https://doi.org/10.1016/0370-2693(89)91131-3
60. A. Ilakovac, A. Pilaftsis, Nucl. Phys. B **437**, 491 (1995). arXiv:hep-ph/9403398 [hepph]
61. E. Ma, Mod. Phys. Lett. A **24**, 2161 (2009). arXiv:0904.1580 [hep-ph]
62. G. Aad et al. (ATLAS, CMS), *Proceedings, Meeting of the APS Division of Particles and Fields (DPF 2015): Ann Arbor, Michigan, USA, 4-8 Aug 2015*, Phys. Rev. Lett. **114**, 191803 (2015). https://doi.org/10.1103/PhysRevLett.114.191803, arXiv:1503.07589 [hep-ex]
63. Yu. A. Golfand, E. P. Likhtman, JETP Lett. **13**, 323 (1971), [Pisma Zh. Eksp. Teor. Fiz. 13, 452 (1971)]
64. D.V. Volkov, V.P. Akulov, Phys. Lett. **46B**, 109 (1973). https://doi.org/10.1016/0370-2693(73)90490-5
65. J. Wess, B. Zumino, Nucl. Phys. **B70**, 39 (1974). https://doi.org/10.1016/0550-3213(74)90355-1
66. H.E. Haber, G.L. Kane, Phys. Rept. **117**, 75 (1985). https://doi.org/10.1016/0370-1573(85)90051-1
67. J.F. Gunion, H.E. Haber, Nucl. Phys. **B272**, 1 (1986), [Erratum: Nucl. Phys. B402 ,567(1993)]. https://doi.org/10.1016/0550-3213(86)90340-8, https://doi.org/10.1016/0550-3213(93)90653-7
68. J.F. Gunion, H.E. Haber, *Proceedings, 23RD International Conference on High Energy Physics, JULY 16-23, 1986, Berkeley, CA*, Nucl. Phys. **B278**, 449 (1986), [Erratum: Nucl. Phys. B 402, 569 (1993)]. https://doi.org/10.1016/0550-3213(93)90654-8, https://doi.org/10.1016/0550-3213(86)90050-7
69. H.E. Haber, in *Theoretical Advanced Study Institute (TASI 92): From Black Holes and Strings to Particles Boulder, Colorado, June 3-28, 1992* (1993) pp. 0589–688, arXiv:hepph/93062079306207 [hep-ph]
70. S.P. Martin, Adv. Ser. Direct. High Energy Phys **21**, 1 (2010), [Adv. Ser. Direct. High Energy Phys. 18, 1(1998)]. https://doi.org/10.1142/9789814307505_0001, arXiv:hep-ph/9709356 [hep-ph]
71. L. Girardello, M.T. Grisaru, Nucl. Phys. **B194**, 65 (1982). https://doi.org/10.1016/0550-3213(82)90512-0
72. J. Hisano, T. Moroi, K. Tobe, M. Yamaguchi, Phys. Rev. D **53**, 2442 (1996). arXiv:hep-ph/9510309 [hep-ph]
73. E. Arganda, A.M. Curiel, M.J. Herrero, D. Temes, Phys. Rev. D **71**, 035011 (2005). arXiv:hep-ph/0407302 [hep-ph]

Chapter 3
Phenomenological Implications of Low Scale Seesaw Neutrinos on LFV

In this Chapter we revisit some of the most relevant phenomenological implications of right-handed neutrinos with TeV scale masses, paying special attention to their lepton flavor violating consequences. After reviewing the experimental status of charged LFV searches, we discuss in detail the LFV radiative and three-body lepton decays in presence of right-handed neutrinos at the TeV scale. Furthermore, we also study other observables that are modified by the new neutrino sector, such as electroweak precision observables, or processes with lepton number violation or lepton flavor universality violation. This Chapter will be very useful and illustrative to learn the general ideas about LFV from TeV right-handed neutrinos and to describe the main points of our analysis, as well as to introduce the set of observables that we will consider as potential constraints when studying maximum allowed predictions for LFV Higgs and Z decays in the forthcoming Chapters. The content of this Chapter, except Sect. 3.1, is original work of this Thesis. It includes the proposal of new scenarios with suppressed μ-e transitions, the geometrical interpretation of the associated neutrino Yukawa coupling matrix, as well as the phenomenological consequences of these mentioned scenarios. All these new contributions have been published in Refs. [1, 2].

3.1 Experimental Status of Charged LFV and Constraints

Lepton flavor violating processes are forbidden in the SM due to the assumption of massless neutrinos, therefore any observation of lepton flavor violation would automatically imply the presence of new physics beyond the SM. This was the case when LFV was observed in neutrino oscillations, what led to the need of extending the SM to include neutrino masses, as we discussed in Chap. 2. Interestingly, if neutrino masses and mixings are minimally added to the SM, they radiatively induce LFV in the charged lepton sector (cLFV), although with extremely small ratios, suppressed by the smallness of the neutrino masses. For instance, using neutrino oscillation data in Eq. (2.6), the predictions for the $\mu \to e\gamma$ ratio are of the order of 10^{-50}.

X. Marcano, *Lepton Flavor Violation from Low Scale Seesaw Neutrinos with Masses Reachable at the LHC*, Springer Theses, https://doi.org/10.1007/978-3-319-94604-7_3

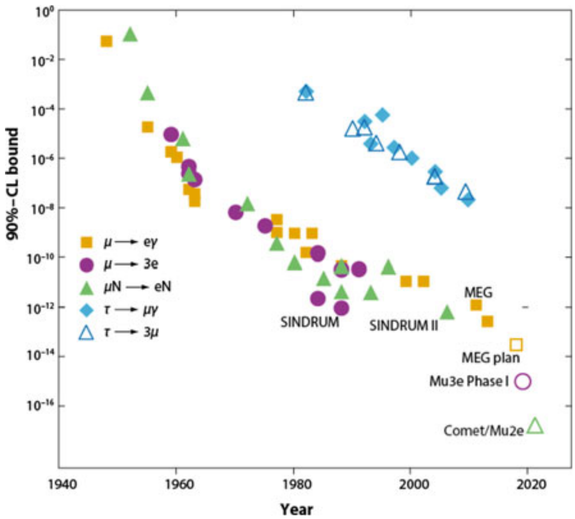

Fig. 3.1 Evolution of cLFV transition upper limits from several experiments, including expected sensitivities for some next generation experiments. Figure borrowed from Ref. [3]

Consequently, a positive experimental signal for cLFV would open a new window for BSM physics and could also help throwing light on the question of what is the mechanism that generates the neutrino masses.

Unfortunately, cLFV has not been observed yet in Nature, although there is an extensive experimental program developing different strategies to look for new physics signals in the charged lepton sector and, indeed, there are already very competitive upper bounds on several cLFV processes. One of the standard searches focuses on the radiative decay of a muon into a electron and a photon, concretely on the $\mu^+ \to e^+\gamma$ channel, which has impressively evolved from the first bound of less than a 10% by Hincks and Pontecorvo [4] in 1947, to the latest upper bound by the MEG collaboration [5] of 4.2×10^{-13} in 2016. We schematically show this evolution in Fig. 3.1, borrowed from Ref. [3]. For a complete historical review see, for instance, Refs. [6, 7]. In the next few years, the upgrade from MEG to MEG-II [8] is expected to improve the sensitivity to this cLFV channel in one order of magnitud.

Another possible LFV decay channel of the muon is $\mu \to 3e$, complementary to the $\mu \to e\gamma$ channel and very interesting for many BSM models. The best current upper bound is provided by SINDRUM [9] which sets $\text{BR}(\mu^+ \to e^+e^+e^-) < 1.0 \times 10^{-12}$, although a huge improvement is expected to be obtained by the Mu3e experiment [10]. This experiment has been proposed at PSI, with the aim of reaching decay rates up to $\mathcal{O}(10^{-15})$ with the current muon beamline and $\mathcal{O}(10^{-16})$ if an upgrade to a High Intensity Muon Beam (HiMB) is achieved at PSI.

Alternatively to muon decays, LFV between muons and electrons has been extensively searched for in $\mu \to e$ conversion experiments. Here, muons are stopped in a thin layer and form muonic atoms, in which a muon can be converted into an electron,

$$\mu^- + N \to e^- + N\,. \tag{3.1}$$

Table 3.1 Present upper bounds and future expected sensitivities for cLFV transitions

LFV Obs.	Present bound ($90\% CL$)		Future sensitivity	
BR($\mu \to e\gamma$)	4.2×10^{-13}	MEG (2016) [5]	6×10^{-14}	MEG-II [8]
BR($\tau \to e\gamma$)	3.3×10^{-8}	BABAR (2010) [11]	10^{-9}	BELLE-II [12]
BR($\tau \to \mu\gamma$)	4.4×10^{-8}	BABAR (2010) [11]	10^{-9}	BELLE-II [12]
BR($\mu \to eee$)	1.0×10^{-12}	SINDRUM (1988) [9]	10^{-16}	Mu3E (PSI) [10]
BR($\tau \to eee$)	2.7×10^{-8}	BELLE (2010) [13]	$10^{-9,-10}$	BELLE-II [12]
BR($\tau \to \mu\mu\mu$)	2.1×10^{-8}	BELLE (2010) [13]	$10^{-9,-10}$	BELLE-II [12]
BR($\tau \to \mu\eta$)	2.3×10^{-8}	BELLE (2010) [14]	$10^{-9,-10}$	BELLE-II [12]
CR($\mu - e$, Ti)	4.3×10^{-12}	SINDRUM II (2004) [15]	10^{-18}	PRISM (J-PARC) [16]
CR($\mu - e$, Au)	7.0×10^{-13}	SINDRUM II (2006) [17]		
CR($\mu - e$, Al)			3.1×10^{-15}	COMET-I (J-PARC) [18]
			2.6×10^{-17}	COMET-II (J-PARC) [18]
			2.5×10^{-17}	Mu2E (Fermilab) [19]

Such a conversion in the field of the nucleus has as a clear signal the emission of a monochromatic electron of $E \simeq 100$ MeV, where the precise value of its energy depends on the nucleus [20]. Current upper bound comes from the SINDRUM II collaboration, which is set to 7.0×10^{-13} using gold atoms [17]. Nevertheless, a strong experimental effort is planned in this direction, implying extraordinary expected sensitivities of $\mathcal{O}(10^{-18})$ for the next generation of μ-e conversion experiments, as PRISM [16] at J-PARC or Mu2E at Fermilab [19]. Interestingly, these μ-e conversion experiments can also be used to look for a muon conversion into a positron

$$\mu^- + N(A, Z) \to e^+ + N(A, Z-2)\,, \tag{3.2}$$

in a process that violates, besides lepton flavor, total lepton number in two units. These searches are complementary to other experiments looking for LN violation, like neutrinoless double beta decay ($0\nu\beta\beta$), and therefore, they are very interesting for testing the Majorana character of the neutrinos. Although the experimental signal is not as clear as in the μ^--e^- conversions, the SINDRUM II collaboration was able to set a very compelling upper bound on the $\mu^- + \mathrm{Ti} \to e^+ + \mathrm{Ca(g.s.)}$ transition of 4.3×10^{-12} at the 90% CL [15]. Furthermore, additional cLFV evidences are being

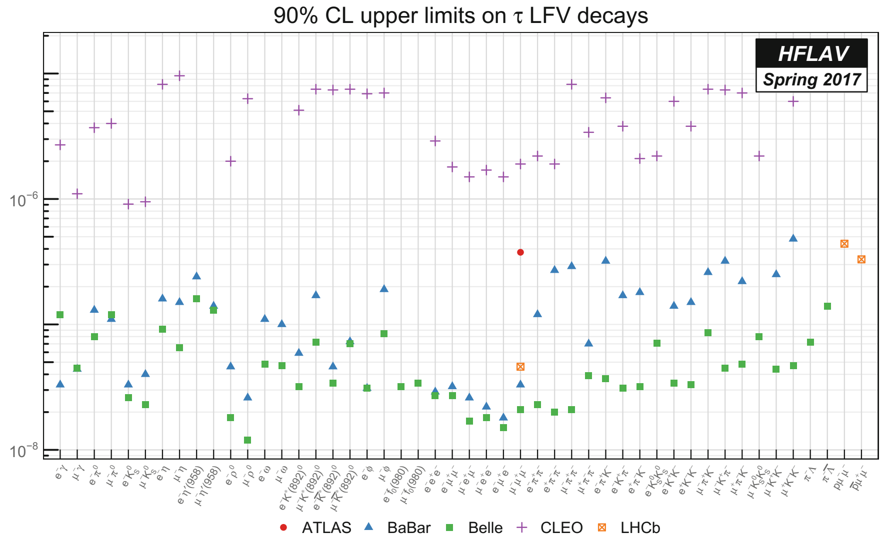

Fig. 3.2 Summary on present LFV τ decay upper limits by the HFLAV group [21]

looked for, like $\mu^+e^- \to \mu^-e^+$ transitions of muonium atoms. We refer to Ref. [6] for a complete review of cLFV in muon transitions.

In order to study LFV processes in the tau sector, we need to look at B factories. The BABAR collaboration put the most constraining upper bounds of LFV radiative tau decays, setting $\text{BR}(\tau^\pm \to \mu^\pm\gamma) < 4.4 \times 10^{-8}$ and $\text{BR}(\tau^\pm \to e^\pm\gamma) < 3.3 \times 10^{-8}$ [11]. On the other hand, BELLE was able to constraint LFV three body decays [13], setting $\text{BR}(\tau^- \to \mu^-\mu^+\mu^-) < 2.1 \times 10^{-8}$, $\text{BR}(\tau^- \to e^-e^+e^-) < 2.7 \times 10^{-8}$, and similar bounds for mixed combinations of muons and electrons in the final state. The LHCb collaboration has also performed searches for $\tau^- \to \mu^-\mu^+\mu^-$ decays, finding an upper bound of 4.6×10^{-8} [22]. This analysis, done with 1 fb^{-1} of proton-proton collision at $\sqrt{s} = 7$ TeV and 2 fb^{-1} at 8 TeV, already has a sensitivity close to the best current bounds, so we could expect that LHCb can tell us something new about this decay channel in a near future. Moreover, in 2018, the BELLE-II experiment [12] will start its operation with the aim of improving the sensitivities to both types of LFV τ decays in up to two orders of magnitude. We summarize the current upper bounds, as well as future expected sensitivities, on cLFV transitions in Table 3.1.

An interesting feature about τ leptons is that their mass is large enough to decay into hadrons. This fact opens a new experimental window looking for semileptonic LFV tau decays. We summarize current upper bounds on the LFV τ decays in Fig. 3.2, taken from the Heavy Flavor Average (HFLAV) group [21], which are around 10^{-8}–10^{-7}. Nevertheless, we can expect that BELLE-II will improve these sensitivities in about two orders of magnitude.

Table 3.2 Present upper bounds for some LFV/LNV meson decays

LFV/LNV Obs.	Present bound (90% CL)	
$\mathrm{BR}(\pi^0 \to \mu e)$	3.59×10^{-10}	KTeV (2008) [23]
$\mathrm{BR}(K_L \to \mu e)$	4.7×10^{-12}	BNL E871 (1998) [24]
$\mathrm{BR}(K_L \to \pi^0 \mu e)$	7.56×10^{-11}	KTeV (2008) [23]
$\mathrm{BR}(K_L \to \pi^0 \pi^0 \mu e)$	1.64×10^{-10}	KTeV (2008) [23]
$\mathrm{BR}(K^+ \to \pi^+ \mu^+ e^-)$	1.3×10^{-11}	BNL E777/865 (2005) [25]
$\mathrm{BR}(K^+ \to \pi^+ \mu^- e^+)$	5.2×10^{-10}	BNL E865 (2000) [26]
$\mathrm{BR}(K^+ \to \pi^- \mu^+ e^+)$	5.0×10^{-10}	BNL E865 (2000) [26]
$\mathrm{BR}(K^+ \to \pi^- e^+ e^+)$	6.4×10^{-10}	BNL E865 (2000) [26]
$\mathrm{BR}(K^+ \to \pi^- \mu^+ \mu^+)$	1.1×10^{-9}	NA48/2 (2010) [27]
$\mathrm{BR}(B^+ \to K^- \mu^+ \mu^+)$	5.4×10^{-8}	LHCb (2012) [28]
$\mathrm{BR}(B^+ \to \pi^- \mu^+ \mu^+)$	5.8×10^{-8}	LHCb (2012) [28]

Experimental searches of meson decays are also extremely interesting for looking for both LFV and LNV processes. LFV neutral kaon decay, $K_L \to \mu e$, has been extensively searched at experiments (see Ref. [7] for a review) and currently the most stringent bound by the BNL collaboration sets $\mathrm{BR}(K_L \to \mu^\pm e^\mp) < 4.7 \times 10^{-12}$ [24]. Other LFV or LNV K_L or π^0 decays, as well as charged kaon $K^+ \to \pi^\pm \ell_1^\pm \ell_2^\mp$ decays, have been searched at several experiments, although no positive signal has been found yet. We summarize in Table 3.2 some of these upper bounds.

We conclude this overview about cLFV experimental searches by commenting on possible Z and Higgs boson LFV decays. LEP, as a Z factory, searched for LFV $Z \to \ell\ell'$ decays with no luck [29, 76]. Thus, it established upper limits to these processes, as we summarize in Table 3.3, which are still the most constraining ones when a tau lepton is involved. At present, these processes are being searched at the LHC and ATLAS is already at the level of LEP results for the LFV Z decay rates, and even better for $Z \to \mu e$ channel [31]. Thus, we can expect that new LHC runs would help testing these channels. Moreover, the sensitivities to LFV Z decay rates are expected to highly improve at the next generation of colliders. In particular, following the discussion in Ref. [32], the future linear colliders are expected to reach sensitivities of 10^{-9} [33, 34], and at a Future Circular e^+e^- Collider (such as FCC-ee (TLEP) [35]), where it is estimated that up to 10^{13} Z bosons would be produced, the sensitivities to LFVZD rates could be improved up to 10^{-13}. More recently, the discovery of the Higgs boson has opened new channels for looking for LFV in the charged sector with the LFV H decays $H \to \ell\ell'$. The first search of this kind was done by CMS for $H \to \tau\mu$ at $\sqrt{s} = 7$ TeV [39] and, interestingly, a 2.4σ excess was found with a best fit value of

$$\mathrm{BR}(H \to \tau\mu) = 8.4^{+3.9}_{-3.7} \times 10^{-3}\,, \tag{3.3}$$

Table 3.3 Present upper bounds at 95% CL on LFV decays of Z and H bosons

LFV Obs.	Present bounds (95% CL)			
BR($Z \to \mu e$)	1.7×10^{-6}	LEP (1995) [29]	7.50×10^{-7}	ATLAS (2014) [31]
BR($Z \to \tau e$)	9.8×10^{-6}	LEP (1995) [29]		
BR($Z \to \tau \mu$)	1.2×10^{-5}	LEP (1995) [30]	1.69×10^{-5}	ATLAS (2014) [36]
BR($H \to \mu e$)	3.5×10^{-4}	CMS (2016) [37]		
BR($H \to \tau e$)	6.1×10^{-3}	CMS (2017) [38]	1.04×10^{-2}	ATLAS (2016) [36]
BR($H \to \tau \mu$)	2.5×10^{-3}	CMS (2017) [38]	1.43×10^{-2}	ATLAS (2016) [36]

which coincided with a smaller excess of around 1σ at ATLAS. Unfortunately, this excess has not been confirmed with more data at $\sqrt{s} = 8$ TeV neither with the LHC run II. Therefore, both ATLAS and CMS have constraint these ratios at the $\mathcal{O}(10^{-3,-4})$, as summarized in Table 3.3. All these bounds have been obtained using the run-I data at $\sqrt{s} = 7$ and 8 TeV, with the exception of the very recent result by CMS [38], where the upper bounds BR$(H \to \tau e) < 0.61\%$ and BR$(H \to \tau\mu) < 0.25\%$ have been set after analyzing 35.9 fb^{-1} of data at $\sqrt{s} = 13$ TeV. These upper bounds improve previous constraints from indirect measurements at LHC [40] by roughly one order of magnitude (see also [41]), and it is close to the previous estimates in [42] that predicted sensitivities of 4.5×10^{-3} (see also, [43]). The future perspectives for LFVHD searches are encouraging due to the expected high statistics of Higgs events at future hadronic and leptonic colliders. Although, to our knowledge, there is no realistic study, including background estimates, of the expected future experimental sensitivities for these kinds of rare LFVHD events, a naive extrapolation from the present situation can be done. For instance, the future LHC runs with $\sqrt{s} = 14$ TeV and total integrated luminosity of first 300 fb^{-1} and later 3000 fb^{-1} expect the production of about 25 and 250 millions of Higgs events, respectively, to be compared with 1 million Higgs events that the LHC produced after the first runs [44–46]. These large numbers suggest an improvement in the long-term sensitivities to BR$(H \to \ell_k \bar{\ell}_m)$ of at least two orders of magnitude with respect to the present sensitivity. Similarly, at the planned lepton colliders, like the international linear collider (ILC) with[1] $\sqrt{s} = 1$ TeV and 2.5 ab^{-1} [47], and the future electron-positron circular collider (FCC-ee) as the TLEP with $\sqrt{s} = 350$ GeV and 10 ab^{-1} [48], the expectations are of about 1 and 2 million Higgs events, respectively, with much lower backgrounds due to the cleaner environment, which will also allow for a large improvement in LFV Higgs decay searches with respect to the current sensitivities.

Overall, we see that an incredible experimental effort is being made in searching for charged lepton flavor violating processes. As we said, any positive signal will

[1] We thank J. Fuster for private communication with the updated ILC perspectives.

automatically imply the existence of new physics even beyond the SM model with a minimal ad-hoc addition of neutrino masses. Nowadays, the lack of such a signal has allowed to several experiments to establish upper bounds on this kind of processes, specially in μ-e transitions, where the bounds are in general several orders of magnitude stronger than the equivalent ones for τ-e or τ-μ sectors. Nevertheless, we hope that the expected improved sensitivities for next generation of experiments will find evidences for new physics in the form of charged lepton flavor violation.

3.2 Study of $\ell_m \to \ell_k\gamma$ and $\ell_m \to \ell_k\ell_k\ell_k$ in the ISS

In order to better understand the implications on cLFV phenomenology of the TeV scale right-handed neutrinos, we first explore in this section the LFV lepton decays that, as we can see in Table 3.1, are one of the most constrained cLFV observables. Concretely, we will consider the ISS model as a specific realization of low scale seesaw models and study in this section the LFV radiative decays $\ell_m \to \ell_k\gamma$ and the LFV three body decays $\ell_m \to \ell_k\ell_k\ell_k$ with $k \neq m$. The numerical estimations will be done using the full one-loop formulas given in Refs. [49, 50], which we collect in Appendix A for completeness.

In all the forthcoming study, we will always impose agreement with light neutrino data[2] in Eq. (2.6). For that purpose, we will make use of one of the two parametrizations described in Sect. 2.3 at a time, i.e., the Casas-Ibarra parametrization given in Eq. (2.44) or the μ_X parametrization in Eq. (2.46). By comparing the results when using these two parametrizations we will learn about the advantages and disadvantages of using one parametrization or the other for exploring the parameter space of the model.

We focus first on the LFV radiative decays, since their analytical expressions are simpler and therefore very useful to gain intuition about cLFV processes in this kind of models. We stress that all the numerical estimates and plots are made using the full formulas in Appendix A. Nevertheless, for the purpose of the discussion, we have derived the following simple but useful approximated expression:

$$\mathrm{BR}(\ell_m \to \ell_k\gamma) \approx \frac{\alpha_W^3 s_W^2}{1024\pi^2 m_W^4}\frac{m_{\ell_m}^5}{\Gamma_{\ell_m}}\frac{v^4}{M_R^4}\left|\left(Y_\nu Y_\nu^\dagger\right)_{km}\right|^2, \tag{3.4}$$

which works quite well for a single heavy mass scale, $M_R = M_R\mathbb{1}$, and in the seesaw limit $vY_\nu \ll M_R$, as we will see.

We display in Fig. 3.3 the numerical results for the LFV $\ell_m \to \ell_k\gamma$ decay rates when using the Casas-Ibarra parametrization to accommodate neutrino oscillation data. As explained before, this parametrization builds the Yukawa coupling matrix taking M_R, μ_X, m_ν^{diag} and the orthogonal matrix R as input parameters in Eq. (2.44).

---

[2] We will show our results for the case of a Normal Hierarchy, although similar results have been obtained for an Inverted Hierarchy.

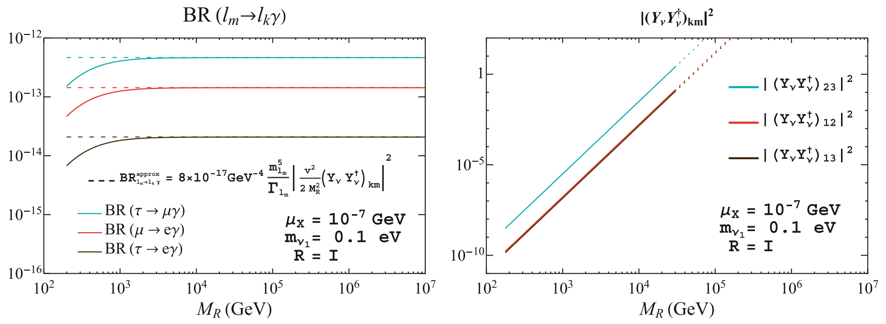

Fig. 3.3 Comparison of the full one-loop (solid lines) and approximate (dashed lines) rates for the radiative decays $\ell_m \to \ell_k\gamma$ as functions of M_R and their relation with the $(Y_\nu Y_\nu^\dagger)_{km}$ non-diagonal matrix elements in the Casas-Ibarra parametrization. Dotted lines in the right panel indicate non-perturbative Yukawa coupling according to $|Y_\nu^{ij}|^2/4\pi > 1.5$. The other input parameters are set to $\mu_X = 10^{-7}$ GeV, $m_{\nu_1} = 0.1$ eV, and $R = \mathbb{1}$

In this first plot, we consider a simplified scenario where both M_R and μ_X matrices are diagonal and degenerate, i.e., $M_R \equiv M_R\mathbb{1}$ and $\mu_X \equiv \mu_X\mathbb{1}$. Concretely, we set $\mu_X = 10^{-7}$ GeV, $m_{\nu_1} = 0.1$ eV and $R = \mathbb{1}$, while we vary M_R from 200 to 10^7 GeV. The left panel of Fig. 3.3 illustrates the numerical predictions of BR($\ell_m \to \ell_k\gamma$) rates in this scenario, using both the full analytical expression in Eq. (A.5) (solid lines) and the approximated expression in Eq. (3.4) (dashed lines). This plot already shows that the approximated expression works very well for large enough values of M_R, as we anticipated. Therefore, we can make use of Eq. (3.4) in order to understand the analytical dependence of these ratios with de heavy neutrino mass M_R.

In this left panel of Fig. 3.3 we clearly see that these rates saturate to a constant value for increasing M_R, leading to an apparent non-decoupling behavior with the mass of the heavy neutrinos. Nevertheless, this non-decoupling effect is an artifact of the Casas-Ibarra parametrization, since it induces a M_R dependence in the Yukawa coupling matrix, although they are both in principle independent parameters. More precisely, looking at Eq. (2.44) we can see that the elements of the relevant combination in Eq. (3.4), $(Y_\nu Y_\nu^\dagger)$, grow with M_R approximately as M_R^2, as can be seen in the right panel of Fig. 3.3. Therefore, the final prediction for BR($\ell_m \to \ell_k\gamma$) is constant with M_R.

We will deal with this kind of apparent non-decoupling effects every time we use the Casas-Ibarra parametrization. The growing of the Y_ν coupling with M_R will compensate the suppression coming from the heavy mass scale running in the loops, leading to a fake violation of the decoupling theorem [51]. Nevertheless, we have checked that for constant value of the Yukawa coupling the predictions for the different one-loop processes considered in this Thesis decrease with M_R, as can be seen for the LFV radiative decay rates in Eq. (3.4). This expected decoupling behavior will become manifest when using the μ_X parametrization, since it works with Y_ν and M_R as independent input parameters.

Finally, we can compare the results for the LFV radiative decay rates in Fig. 3.3 with the present experimental upper bounds in Table 3.1. We see that, for this choice of parameters, $\mu \to e\gamma$ is the closest one to its upper bound of 4.2×10^{-13} [5]. Being this bound much stronger that the ones on LFV radiative τ decays, we found that $\mu \to e\gamma$ is the most constraining radiative decay for most of the parameter space of the model. Moreover, looking at Table 3.1, we see that in general strongest cLFV bounds will come from processes involving a μ-e transition, not only from the mentioned $\mu \to e\gamma$, but also from $\mu \to eee$ or μ-e transitions in nuclei. Consequently, we can try to find areas in the parameter space where these strong bounds are avoided by a suppressed prediction of μ-e transitions. We can then expect that the largest allowed τ-μ and τ-e transitions will lie precisely in these areas.

3.2.1 Proposal of Scenarios with Suppressed μ-e Transitions

Motivated by the fact that experimental searches in Table 3.1 show much more constrained cLFV processes in the μ-e sector than in the other τ-μ and τ-e sectors, we look for phenomenological scenarios where μ-e transitions are suppressed. In order to do this, we find more useful to consider the μ_X parametrization instead of the Casas-Ibarra one, since it allow us to consider the Yukawa coupling directly as an input parameter. Looking again at Eq. (3.4), we learn that, for diagonal and degenerate M_R matrix, the relevant Yukawa combination for cLFV processes is $Y_\nu Y_\nu^\dagger$, which is simplified to $Y_\nu Y_\nu^T$ in the case of real matrices.[3] Then, it will be very useful and instructive to consider a geometrical interpretation of the Yukawa matrix where its entries are interpreted as the components of three generic $(\boldsymbol{n}_e, \boldsymbol{n}_\mu, \boldsymbol{n}_\tau)$ neutrino vectors in flavor space,

$$Y_\nu = \begin{pmatrix} Y_\nu^{11} & Y_\nu^{12} & Y_\nu^{13} \\ Y_\nu^{21} & Y_\nu^{22} & Y_\nu^{23} \\ Y_\nu^{31} & Y_\nu^{32} & Y_\nu^{33} \end{pmatrix} \equiv f \begin{pmatrix} \boldsymbol{n}_e \\ \boldsymbol{n}_\mu \\ \boldsymbol{n}_\tau \end{pmatrix}, \tag{3.5}$$

which for the relevant combination in cLFV processes give:

$$Y_\nu Y_\nu^T = f^2 \begin{pmatrix} |\boldsymbol{n}_e|^2 & \boldsymbol{n}_e \cdot \boldsymbol{n}_\mu & \boldsymbol{n}_e \cdot \boldsymbol{n}_\tau \\ \boldsymbol{n}_e \cdot \boldsymbol{n}_\mu & |\boldsymbol{n}_\mu|^2 & \boldsymbol{n}_\mu \cdot \boldsymbol{n}_\tau \\ \boldsymbol{n}_e \cdot \boldsymbol{n}_\tau & \boldsymbol{n}_\mu \cdot \boldsymbol{n}_\tau & |\boldsymbol{n}_\tau|^2 \end{pmatrix}. \tag{3.6}$$

This means that the 9 input parameters determining the Y_ν matrix can be seen as the 3 modulus of these three vectors ($|\boldsymbol{n}_e|$, $|\boldsymbol{n}_\mu|$, $|\boldsymbol{n}_\tau|$), the 3 relative *flavor* angles between them $(\theta_{\mu e}, \theta_{\tau e}, \theta_{\tau\mu})$, with $\theta_{ij} \equiv \widehat{\boldsymbol{n}_i \boldsymbol{n}_j}$, and 3 extra angles $(\theta_1, \theta_2, \theta_3)$ that parametrize a global rotation $\mathcal{O}$ of these 3 vectors that does not change their relative

[3] In the following derivation of the μ-e suppressed scenarios, we will assume the situation of having real matrices in order to avoid potential constraints from lepton electric dipole moments.

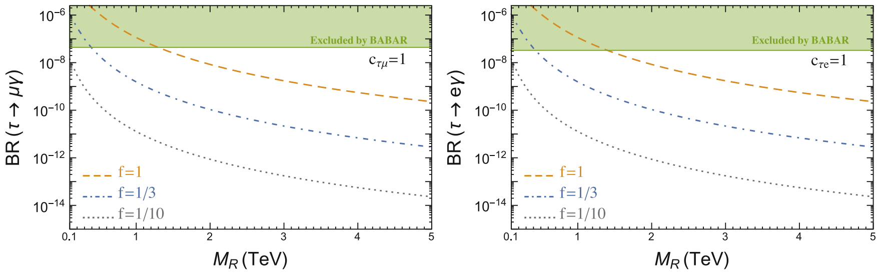

Fig. 3.4 Predictions for the BR($\tau \to \mu\gamma$) and BR($\tau \to e\gamma$) as functions of M_R in the μ_X parametrization. The input Y_ν matrix is written as explained in the text, with different values of the strength parameter f. In the left (right) panel τ-μ (τ-e) transitions are maximized by setting $c_{\tau\mu}(c_{\tau e}) = 1$. The other cosines are set to zero, the modulus $|\boldsymbol{n}_{e,\mu,\tau}| = 1$ and $\mathcal{O} = \mathbb{1}$

angles. In addition, we have introduced an extra parameter f that characterizes the global Yukawa coupling strength and that will be useful in forthcoming analysis. Since the combination $Y_\nu Y_\nu^T/f^2$ is symmetric, it only depends on 6 parameters that we take to be the 3 modulus ($|\boldsymbol{n}_e|$, $|\boldsymbol{n}_\mu|$, $|\boldsymbol{n}_\tau|$) and the cosine of the three flavor angles ($c_{\mu e}$, $c_{\tau e}$, $c_{\tau\mu}$), with $c_{ij} \equiv \cos\theta_{ij}$. The names of the angles are motivated by the fact that the cosine of the angle θ_{ij} controls the LFV transitions in the ℓ_i-ℓ_j sector, which we write in short as $\text{LFV}_{\ell_i\ell_j}$. It is interesting to notice that the global rotation $\mathcal{O}$ does not enter in the $Y_\nu Y_\nu^T$ combination and, therefore, it will not affect any of the cLFV processes studied in this work.

Before going to the scenarios with suppressed μ-e transitions, we study in Fig. 3.4 the predictions for the LFV radiative decay rates in terms of the most relevant parameters in this parametrization. In the left panel, we show BR($\tau \to \mu\gamma$) in a scenario where τ-μ transitions are maximized by setting[4] $c_{\tau\mu} = 1$, while they are suppressed in the τ-e and μ-e sectors, $c_{\tau e} = c_{\mu e} = 0$. Equivalently, the right panel displays BR($\tau \to e\gamma$) in a scenario where τ-e transitions are favored. Both plots show the dependence of these observables on the heavy neutrino mass scale M_R for several values of the Yukawa coupling strength factor f.

First of all, we see that both observables show the expected decoupling behavior with M_R. This is in contrast with the apparent non-decoupling effects we saw in Fig. 3.3 when using the Casas-Ibarra parametrization. As we explained before, the difference is that now the Yukawa coupling is treated as an independent parameter and, therefore, the dominant dependence on the M_R comes from the mass in the propagators of the right-handed neutrinos running in the loops and whose effects decrease as M_R becomes heavier. On the other hand, the rates are bigger the larger the Yukawa coupling strength f is, as expected. Moreover, although not shown here, we have checked that the rates for $\tau \to \mu\gamma$ ($\tau \to e\gamma$) grow with $c_{\tau\mu}$ ($c_{\tau e}$), $|\boldsymbol{n}_\tau|$ and $|\boldsymbol{n}_\mu|$ ($|\boldsymbol{n}_e|$), while being independent of the other parameters, in particular the

[4]We actually set $c_{\tau\mu} = 0.99$ for this plot, since the μ_X parametrization in Eq. (2.46) requests a non-singular Y_ν. Nevertheless, the results for cLFV processes are basically the same as setting $c_{\tau\mu} = 1$.

rotation matrix $\mathcal{O}$. In summary, the full radiative decays rates follow the behavior of the approximated formula in Eq. (3.4).

Second, we learn that the predictions for $\tau \to \mu\gamma$ in the left panel are the same than those for $\tau \to e\gamma$ in the right panel. The reason for this similarity is that they are related by the interchange $\boldsymbol{n}_\mu \leftrightarrow \boldsymbol{n}_e$ in Eq. (3.5) and, therefore, we expect to have basically the same results in both scenarios. Based on this relation, we will show most of our results only for the τ-μ sector, knowing that the conclusions for the τ-e sector can be obtained by just exchanging $\boldsymbol{n}_\mu$ with $\boldsymbol{n}_e$.

Third, we observe that the predictions can reach the present experimental upper bounds from BABAR (see Table 3.1) and, therefore, they will constrain our parameter space when exploring other observables. In particular, for these scenarios with favored τ-μ or τ-e transitions, maximum values of $f \sim \mathcal{O}(0.5-1)$ for $M_R = 1$ TeV, or minimum values for M_R of $\sim \mathcal{O}(1$–$2)$ TeV for $f = 1$, are allowed. In the future, searches at BELLE-II are expected to improve the sensitivity up to 10^{-9} for these channels, so they will be able to probe values of $f \gtrsim 0.3$ for 1 TeV neutrinos.

As we have seen, using this geometrical interpretation of the Yukawa matrix the μ-e suppression can be easily realized by just assuming that $\boldsymbol{n}_e$ and $\boldsymbol{n}_\mu$ are orthogonal vectors, i.e., $c_{\mu e} = 0$. Such condition defines a family of ISS scenarios that can be parametrized using the following Yukawa matrix:

$$Y_\nu = A \cdot \mathcal{O} \quad \text{with} \quad A \equiv f \begin{pmatrix} |\boldsymbol{n}_e| & 0 & 0 \\ 0 & |\boldsymbol{n}_\mu| & 0 \\ |\boldsymbol{n}_\tau| c_{\tau e} & |\boldsymbol{n}_\tau| c_{\tau\mu} & |\boldsymbol{n}_\tau| \sqrt{1 - c_{\tau e}^2 - c_{\tau\mu}^2} \end{pmatrix}, \tag{3.7}$$

where $\mathcal{O}$ is the above commented orthogonal rotation matrix, which does not enter in the product $Y_\nu Y_\nu^T$, and f is again the parameter controlling the global strength of the Yukawa coupling matrix. The fact that we are assuming real and non-singular Y_ν imposes the condition $c_{\tau e}^2 + c_{\tau\mu}^2 < 1$. Notice that the Y_ν matrix in Eq. (3.7) is the most general one that satisfies the condition $\left(Y_\nu Y_\nu^T\right)_{\mu e} = 0$.

We can now explore the predictions for BR($\ell_m \to \ell_k \gamma$) when this kind of scenarios are considered. Looking at Eq. (3.4), we can easily see that the LFV radiative decays of the τ lepton depend on the most relevant parameters, f, M_R and $c_{\tau\ell}$ as follows:

$$\text{BR}(\tau \to \ell\gamma) \sim \frac{v^4 f^4}{M_R^4}\, c_{\tau\ell}^2 \quad \text{with } \ell = e, \mu. \tag{3.8}$$

The case of $\mu \to e\gamma$ is different, since the assumption $c_{\mu e} = 0$ cancels the leading order contribution given by the approximate formula in Eq. (3.4), and therefore the first relevant contribution in this observable is of higher order in the expansion series in powers of the Yukawa coupling over M_R. Specifically, it is of the type $v^4 (Y_\nu Y_\nu^T Y_\nu Y_\nu^T)/M_R^4$. Consequently, it is suppressed with respect to Eq. (3.8) and the predicted rates for this observable turn out to depend on the product of both $c_{\tau e}$ and $c_{\tau\mu}$:

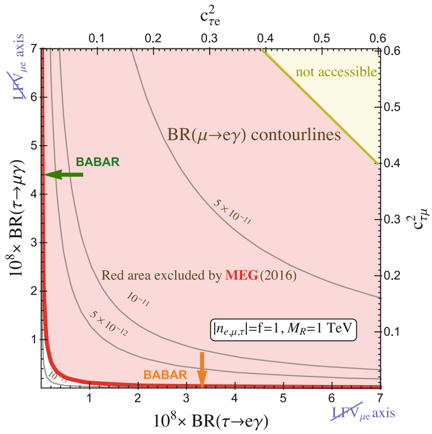

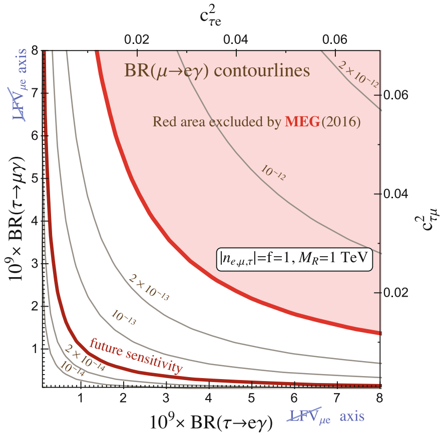

Fig. 3.5 Left panel: Contour lines for BR($\mu \to e\gamma$) as a function of BR($\tau \to e\gamma$) and BR($\tau \to \mu\gamma$) rates, for fixed $M_R = 1$ TeV, $|\boldsymbol{n}_{e,\mu,\tau}| = f = 1$ values and varying $c^2_{\tau e}$ and $c^2_{\tau\mu}$ from 0 to 0.6, as shown in the right and top axes. The yellow area represents the region that cannot be accessed with real Yukawa matrices. The red area is excluded by the upper bound on $\mu \to e\gamma$ from MEG, while the orange (green) arrow marks the present upper bound on $\tau \to e\gamma$ ($\tau \to \mu\gamma$) from BABAR, see Table 3.1. Right panel: Zoom on the lower left corner of the plot in the left panel which allows for a better reading of the region allowed by present experimental data. The extra darker red line represents the future expected sensitivity of 4×10^{-14} by MEG-II [8]

$$\mathrm{BR}(\mu \to e\gamma) \sim \frac{v^8 f^8}{M_R^8}\, c^2_{\tau e} c^2_{\tau\mu}\,. \tag{3.9}$$

Therefore, in order to define a scenario where all μ-e transitions are completely suppressed, i.e., $\left(Y_\nu Y_\nu^T\right)_{\mu e} = \left(Y_\nu Y_\nu^T Y_\nu Y_\nu^T\right)_{\mu e} = \cdots = 0$, we see that the condition $c_{\mu e} = 0$ is not enough and that we also need $c_{\tau e} = 0$ or $c_{\tau\mu} = 0$.

These behaviors of the BR($\ell_m \to \ell_k\gamma$) rates are numerically illustrated in Fig. 3.5, where the full one-loop formulas in Appendix A have been used. These plots show contourlines for BR($\mu \to e\gamma$) in terms of the other radiative decay rates. It also displays the above commented correlations between the BR($\tau \to \mu\gamma$) and BR($\tau \to e\gamma$) rates and the parameters $c_{\tau\mu}$ and $c_{\tau e}$, respectively. The contour lines for BR($\mu \to e\gamma$) are obtained by varying $c^2_{\tau\mu}$ and $c^2_{\tau e}$ within the interval (0, 0.6), which in turn provide predictions for BR($\tau \to \mu\gamma$) and BR($\tau \to e\gamma$) that are represented in the vertical and horizontal axes respectively. This is for the simple case with $|\boldsymbol{n}_{e,\mu,\tau}| = f = 1$, $M_R = 1$ TeV and $\mathcal{O} = \mathbb{1}$ (although we checked again that the rates do not depend on $\mathcal{O}$), but similar qualitative conclusions can be obtained for other choices of these parameters. Notice that the above mentioned condition of $c^2_{\tau e} + c^2_{\tau\mu} < 1$ from the Yukawa matrix in Eq. (3.7) makes the yellow area, where $c^2_{\tau e} + c^2_{\tau\mu} \geq 1$, not accesible to our analysis. We also find that the rates for $\tau \to \mu\gamma$ ($\tau \to e\gamma$) can in general be large and, for the values of the parameters selected in this plot, they are of the order of the present upper bounds from BABAR [11], marked here with a green

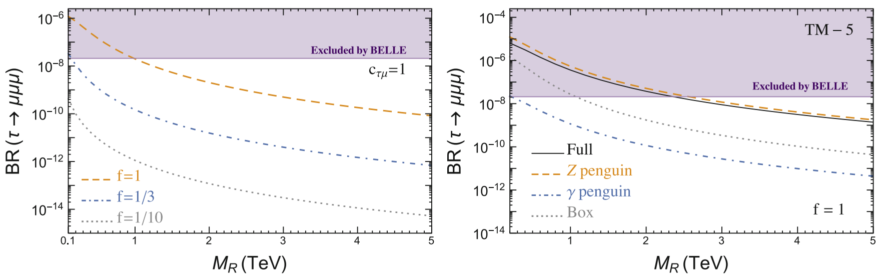

Fig. 3.6 BR($\tau \to \mu\mu\mu$) as a function of M_R in two TM-like scenarios with $c_{\tau\mu} = 1$ and $c_{\tau e} = 0$. Left panel: Full predictions for $|\boldsymbol{n}_{e,\mu,\tau}| = 1$ and three values of f. Right panel: Full prediction (solid line) in the TM-5 scenario with $f = 1$, decomposed in its contributions from γ penguin (blue dot-dashed), boxes (gray dotted) and Z penguin (yellow dashed), the dominant one. Purple shadowed area is excluded by BELLE

(orange) arrow. Moreover, we see that they depend just on $c^2_{\tau\mu}$ ($c^2_{\tau e}$), in agreement with the approximate expression in Eq. (3.8).

We also learn that the predictions for BR($\mu \to e\gamma$) are between 3 and 4 orders of magnitude smaller than the τ radiative decay rates, as expected from Eq. (3.9). Nevertheless, they are still above the upper bound from the MEG experiment for most of the parameter space. In fact, the MEG bound excludes everything but the area close to the axes, since the BR($\mu \to e\gamma$) goes asymptotically to zero when approaching the axes, as can be seen in the zoom over the lower left corner, shown in the right panel of Fig. 3.5. When lying just on top of these axes, the predictions for BR($\mu \to e\gamma$) completely vanish, as seen in Eq. (3.9), implying that BR($\tau \to e\gamma$) must be small in order to allow for large BR($\tau \to \mu\gamma$), and viceversa.

Therefore, we can identify our phenomenological scenarios with suppressed μ-e transitions, which we will refer to as ISS-$\cancel{\text{LFV}}_{\mu e}$, with the two axes in Fig. 3.5. We then consider two classes of scenarios: the TM scenarios along the LFV$_{\tau\mu}$ axis ($c_{\tau e} = 0$) that may give sizable rates for τ-μ transitions, but always give negligible contributions to LFV$_{\mu e}$ and LFV$_{\tau e}$; and the TE scenarios along the LFV$_{\tau e}$ axis ($c_{\tau\mu} = 0$) that may lead to large rates only for the τ-e transitions. In Table 3.4 we list some specific examples that we will use along this Thesis for the numerical estimates of our selected TM scenarios. Equivalent examples for the TE scenarios are obtained by exchanging μ and e everywhere in these TM scenarios. Notice that we introduced the notation $Y^{(1)}_{\tau\mu}$, $Y^{(2)}_{\tau\mu}$ and $Y^{(3)}_{\tau\mu}$ for the Yukawa matrices in the scenarios TM-5, TM-6 and TM-7, respectively, which corresponds to the original notation in Ref. [1]. We will indistinguishably use both notations along this Thesis.

We can next study the predictions for the LFV three body decays $\ell_m \to \ell_k\ell_k\ell_k$ in this kind of scenarios. Figure 3.6 shows the BR($\tau \to \mu\mu\mu$) rates in a TM-like scenario of maximized τ-μ transitions, i.e., $c_{\tau\mu} = 1$ and $c_{\tau e} = c_{\mu e} = 0$, although the general conclusions are the same for BR($\tau \to eee$) in a TE scenario. In the left panel, the dependence of the full decay rate is displayed as a function of M_R for different values of f. We clearly see that the rates are again large, within present and future

Table 3.4 TM scenarios for numerical estimates of large τ-μ transitions. Notation '$\simeq$' means $c_{\tau\mu} = 0.99$ instead of 1 in order to have non-singular Y_ν matrices, see Eq. (2.46). The notation $Y_{\tau\mu}^{(1-3)}$ corresponds to the original one introduced in Ref. [1]. Equivalent TE scenarios are easily obtained by exchanging μ and e in these TM ones

Scenario name	$c_{\tau\mu}$	$\lvert\boldsymbol{n}_e\rvert$	$\lvert\boldsymbol{n}_\mu\rvert$	$\lvert\boldsymbol{n}_\tau\rvert$	Example
TM-1	$1/\sqrt{2}$	1	1	1	$Y_\nu = f\begin{pmatrix} 1 & 0 & 0 \\ 0 & 1 & 0 \\ 0 & 1/\sqrt{2} & 1/\sqrt{2} \end{pmatrix}$
TM-2	1	1	1	1	$Y_\nu \simeq f\begin{pmatrix} 1 & 0 & 0 \\ 0 & 1 & 0 \\ 0 & 1 & 0 \end{pmatrix}$
TM-3	$1/\sqrt{2}$	0.1	1	1	$Y_\nu = f\begin{pmatrix} 0.1 & 0 & 0 \\ 0 & 1 & 0 \\ 0 & 1/\sqrt{2} & 1/\sqrt{2} \end{pmatrix}$
TM-4	1	0.1	1	1	$Y_\nu \simeq f\begin{pmatrix} 0.1 & 0 & 0 \\ 0 & 1 & 0 \\ 0 & 1 & 0 \end{pmatrix}$
TM-5	1	$\sqrt{2}$	1.7	$\sqrt{3}$	$Y_\nu \equiv Y_{\tau\mu}^{(1)} = f\begin{pmatrix} 0 & 1 & -1 \\ 0.9 & 1 & 1 \\ 1 & 1 & 1 \end{pmatrix}$
TM-6	1/3	$\sqrt{2}$	$\sqrt{3}$	$\sqrt{3}$	$Y_\nu \equiv Y_{\tau\mu}^{(2)} = f\begin{pmatrix} 0 & 1 & 1 \\ 1 & 1 & -1 \\ -1 & 1 & -1 \end{pmatrix}$
TM-7	0.1	$\sqrt{2}$	$\sqrt{3}$	1.1	$Y_\nu \equiv Y_{\tau\mu}^{(3)} = f\begin{pmatrix} 0 & -1 & 1 \\ -1 & 1 & 1 \\ 0.8 & 0.5 & 0.5 \end{pmatrix}$
TM-8	1	1/2	1/3	1/4	$Y_\nu \simeq f\begin{pmatrix} 1 & 0 & 0 \\ 0 & 0.5 & 0 \\ 0 & 0.08 & 0.32 \end{pmatrix}$
TM-9	0.77	0.1	0.46	$\sqrt{2}$	$Y_\nu = f\begin{pmatrix} 0.1 & 0 & 0 \\ 0 & 0.46 & 0.04 \\ 0 & 1 & 1 \end{pmatrix}$
TM-10	0.64	0.1	0.94	$\sqrt{2}$	$Y_\nu = f\begin{pmatrix} 0 & 0.1 & 0 \\ 0.94 & 0 & 0.08 \\ 1 & 0 & -1 \end{pmatrix}$

experimental sensitivities, specially for large f values and low M_R. For example, in this particular case of $c_{\tau\mu} = 1$, the present bound from BELLE of $\mathrm{BR}(\tau \to \mu\mu\mu) < 2.1 \times 10^{-8}$ excludes large couplings of $f \gtrsim 1$ for heavy neutrinos below 1 TeV. Future expected sensitivities at BELLE-II may be able to probe values of M_R up to 2–3 TeV for $f = 1$.

As in the case of the radiative decay $\tau \to \mu\gamma$, we see again that the rates decrease with increasing M_R, manifesting the decoupling behavior expected when using the μ_X parametrization. Although we do not show all the plots here, we have explored how the rates for $\tau \to \mu\mu\mu$ depend on the most relevant parameters finding that they grow with f, $c_{\tau\mu}$, $|\boldsymbol{n}_\tau|$ and $|\boldsymbol{n}_\mu|$, whereas they are independent of $c_{\tau e}$, $c_{\mu e}$, $|\boldsymbol{n}_e|$ and the rotation $\mathcal{O}$.

Nevertheless, the dependence of $\tau \to \mu\mu\mu$ on these parameters is not exactly equal to that of $\tau \to \mu\gamma$, since the former receives contributions from different types of diagrams, namely, the γ-penguin, Z-penguin and box diagrams. In order to better understand this, we display separately the contributions from each type of diagram to the total decay rate in the right panel of Fig. 3.6. We choose the TM-5 scenario from Table 3.4, although similar qualitative results are found for other TM scenarios. The dependences on f, M_R and $c_{\tau\mu}$ are slightly different for each of the contributions, leading to a more complicated dependence for the total decay rate. Moreover, we see that, for this value of f, the dominant contribution is mostly coming from the Z-penguin. This fact will be important when studying the LFV Z decay rates $Z \to \ell_k\bar{\ell}_m$ in Chap. 5.

In the rest of this Thesis we will consider the two parametrizations described in Chap. 2. We will consider more generic searches using the Casas-Ibarra parametrization for scanning the ISS parameter space, although in that case it will be difficult to access to these particular directions and, therefore, to conclude on maximum allowed rates. Therefore, we will focus on the scenarios in Table 3.4 for studying maximum allowed LFV rates involving τ leptons making sure that we are not generating potentially constrained μ-e transitions.

3.3 Other Implications from Low Scale Seesaw Neutrinos

Generically, the addition of heavy Majorana neutrinos to the particle content of the SM has a phenomenological impact on several low energy observables via their mixing with the active neutrinos. These observables can be related to lepton flavor violation, as the ones above studied, lepton number violation, lepton universality or others. Therefore, we want to ensure that our forthcoming analysis in Chaps. 4, 5 and 6 comply with the relevant theoretical and experimental constraints in all the regimes of the considered right handed neutrino masses and couplings. We briefly discuss in the following the constraints that we have found to be the most relevant ones for the present Thesis and which we consequently include in our analysis. For this study we have used our own *Mathematica* code which includes all the relevant formulas for the constraining observables that are taken from the literature and that we include in Appendix B for completeness.

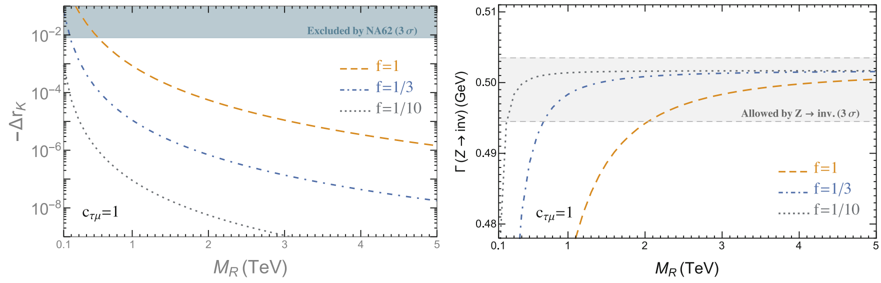

Fig. 3.7 Predictions for Δr_k and $\Gamma(Z \to \text{inv.})$ as functions of M_R. In both plots we set $|\boldsymbol{n}_{e,\mu,\tau}| = 1$, $c_{\tau\mu} = 1, c_{\mu e} = c_{\tau e} = 0, \mathcal{O} = \mathbb{1}$ and consider three values of f. The shadowed band in the left (right) plot is the present excluded (allowed) region at 3σ

3.3.1 Lepton Flavor Universality

Leptonic and semileptonic decays of pseudoscalar mesons (π, K, D, D_s, B) could put important constraints on the mixing between the active and the sterile neutrinos in the ISS model, as it has been shown in Refs. [52, 53]. In particular, the most severe bounds arise from the violation of lepton universality in leptonic kaon decays.[5] Following these references, we consider the contributions of the sterile neutrinos to the Δr_k parameter, defined as:

$$\Delta r_k = \frac{R_K}{R_K^{\text{SM}}} - 1 \quad \text{with} \quad R_K = \frac{\Gamma(K^+ \to e^+\nu)}{\Gamma(K^+ \to \mu^+\nu)}. \tag{3.10}$$

The comparison of the theoretical calculation in the SM [54, 55] with the recent measurements from the NA62 collaboration [56, 57] shows that the experimental measurements agree with the SM prediction within 1σ:

$$\Delta r_k = (4 \pm 4) \times 10^{-3}. \tag{3.11}$$

We compute the new physics contributions to Δr_k using the formulas listed in Appendix B that we take from Ref. [52] and compare the results with the bound in Eq. (3.11) at the 3σ level.

We display in Fig. 3.7 our numerical findings using the μ_X parametrization. In particular, we choose for this plot a maximized τ-μ scenario with $c_{\tau\mu} = 1$, $c_{\tau e} = c_{\mu e} = 0$, $|\boldsymbol{n}_{e,\mu,\tau}| = 1$, $\mathcal{O} = \mathbb{1}$ and three different values of f. We see that Δr_k is always negative, meaning that $R_K < R_K^{SM}$. Nevertheless, R_K tends to R_K^{SM}, and hence $\Delta r_k \to 0$, for large values of M_R, as the new physics effects decouple with the heavy scale. We also see that the deviations from the SM values are larger for larger values of f, implying that the bound from NA62 can exclude the parameter space

[5]We do not consider other lepton universality tests in view of the fact that they give similar bounds, as in the case of Δr_π, or they are less constraining, like the ones involving τ leptons [53].

region of low M_R and large f. Furthermore, we have found that this observable is also independent of the rotation matrix $\mathcal{O}$ and very sensitive to the modulus $|\boldsymbol{n}_e|$ and $|\boldsymbol{n}_\mu|$, as expected. Actually, the bound from this observable becomes an important constraint at low values of M_R when the ratio between $|\boldsymbol{n}_e|$ and $|\boldsymbol{n}_\mu|$ is different from one.

3.3.2 The Invisible Decay Width of the Z Boson

The invisible decay width of the Z boson puts very strong constraints on how many neutrinos with masses below m_Z are present. The Z invisible decay width was measured in LEP to be [58]:

$$\Gamma(Z \to \text{inv.})_{\text{Exp}} = 499 \pm 1.5 \text{ MeV}, \tag{3.12}$$

which is about 2σ below the SM prediction:

$$\Gamma(Z \to \text{inv.})_{\text{SM}} = \sum_\nu \Gamma(Z \to \nu\bar{\nu})_{\text{SM}} = 501.69 \pm 0.06 \text{ MeV}. \tag{3.13}$$

Although we are not considering the possibility of having $m_N < m_Z$ here, the presence of sterile neutrinos affects the tree level predictions of the Z invisible width even if they are above the kinematical threshold, since they modify the couplings of the active neutrinos to the Z boson. We compute the tree level predictions using the formulas provided in Ref. [53], which we collect in Appendix B for completeness, and we further include the ρ parameter that accounts for the part of the radiative corrections coming from SM loops, i.e.,

$$\Gamma(Z \to \text{inv.})_{\text{ISS}} = \sum_{\substack{i,j=1 \\ i\leq j}}^{3} \Gamma(Z \to n_i n_j)_{\text{ISS}} = \rho\Gamma(Z \to \text{inv.})^{\text{tree}}_{\text{ISS}}\,, \tag{3.14}$$

where n_i runs over all kinematically allowed neutrinos and ρ is evaluated as:

$$\rho = \frac{\Gamma(Z \to \text{inv.})_{\text{SM}}}{\Gamma(Z \to \text{inv.})^{\text{tree}}_{\text{SM}}}. \tag{3.15}$$

We have also estimated the size of the extra loop corrections induced by the new heavy neutrino states using the formulas of Ref. [59] and found out that they are numerically very small compared with the SM loop corrections, in agreement with Ref. [59], and therefore we will neglect them in the following.

We show our numerical results as a function of M_R in Fig. 3.7, for $c_{\tau\mu} = 1$ and three values of f. We see again that the deviations from the SM value decrease with M_R while they grow with f. Moreover, we found that the Z invisible width only

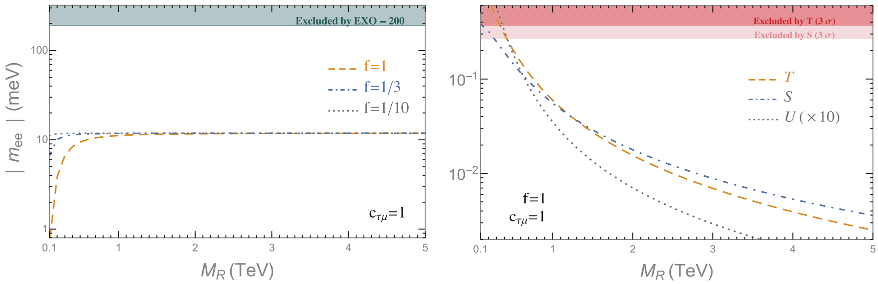

Fig. 3.8 Predictions for $|m_{ee}|$ and the Electroweak Precision Parameters S, T, U (the latter enhanced by a factor of 10 to see it more clearly) as functions of M_R. In both plots we set $|\boldsymbol{n}_{e,\mu,\tau}| = 1$, $c_{\tau\mu} = 1$, $c_{\mu e} = c_{\tau e} = 0$, $\mathcal{O} = \mathbb{1}$ and for three different values of f. The shadowed bands are the present excluded regions at 3σ

depends on M_R, f and the modulus $|\boldsymbol{n}_{e,\mu,\tau}|$, while it is not dependent on $\mathcal{O}$ and on the flavor angles $(c_{\tau\mu}, c_{\tau e})$, as it was expected, since when adding all the possible neutrino final states in Eq. (3.14) the dependence on $\mathcal{O}$ and on the flavor angles appearing in each channel disappears in the sum. When comparing with data we require our predictions to be within the 3σ experimental band, see Eq. (3.12). As we can see in Fig. 3.7, the Z invisible width provides in general quite strong constraints, indeed comparable or even tighter in some cases than the previous constraints from the LFV lepton decays. For instance, for this scenario with $c_{\tau\mu} = 1$ and $f = 1$, this observable also excludes M_R values lower than around 1–2 TeV, similar to the constraints from $\tau \to \mu\gamma$ and $\tau \to \mu\mu\mu$.

3.3.3 Neutrinoless Double Beta Decay

Models that introduce neutrinos with Majorana mass terms allow for lepton number violating processes, such as neutrinoless double beta decay [60]. Within the ISS framework with 6 sterile fermions added to the SM particle content, the effective neutrino mass m_{ee} is given by [61–63]

$$m_{ee} \simeq \sum_{i=1}^{9} (B_{en_i})^2\, p^2 \frac{m_{n_i}}{p^2 - m_{n_i}^2} \simeq \left(\sum_{i=1}^{3} (B_{en_i})^2\, m_{n_i} \right) + p^2 \left(\sum_{i=4}^{9} (B_{en_i})^2 \frac{m_{n_i}}{p^2 - m_{n_i}^2} \right), \tag{3.16}$$

where $p^2 \simeq -(125\ \text{MeV})^2$ is an average estimate over different values from different decaying nucleus of the virtual momentum of the neutrino exchanged in the process.

Although current experiments are searching for neutrinoless double beta decay, it has not been observed yet. This lack of signal has allowed to the experiments with highest sensitivity such as GERDA [64], EXO-200 [65, 66] and KamLAND-ZEN [67] to set strong bounds on the neutrino effective mass. These bounds on the effective neutrino Majorana mass in Eq. (3.16) lie in the range

$$|m_{ee}| \lesssim 140\ \text{meV} - 700\ \text{meV}\,. \tag{3.17}$$

In our analysis, we will apply the most recent constraint of $|m_{ee}| \lesssim 190$ meV from Ref. [66].

Figure 3.8 displays the behavior of m_{ee} with M_R for different values of the Yukawa strength f. As can be seen in this plot, a maximum value of $|m_{ee}| \sim 10$ meV is reached at large $M_R \gtrsim 1$ TeV and for all studied values of f. We have checked that this asymptotic value depends linearly on the mass of the light active neutrinos, i.e.,

$$m_{\nu_1} \sim 0.01(0.1)\,\text{eV} \rightarrow |\mathrm{m_{ee}}| \sim 0.01(0.1)\,\text{eV}\,. \tag{3.18}$$

As a conclusion, we learn that the prediction for this observable will be below the current experimental bound and, therefore, it will not impose an important constraint to our parameter space.

3.3.4 Electroweak Precision Observables

The addition of new physics in the neutrino sector will, in general, modify the prediction of Electroweak Precision Observables (EWPO), which are well determined by experiments. We take into account the constraints to the ISS model from EWPO by computing the S, T and U parameters [68] and comparing our predictions to the experimental results [58]:

$$S = -0.03 \pm 0.10\,, \qquad T = 0.01 \pm 0.12\,, \qquad U = 0.05 \pm 0.10\,. \tag{3.19}$$

We use the formulas from Ref. [69] (which we report in Appendix B) and compare them with the 3σ experimental bands.

We show in Fig. 3.8 the prediction for S, T and U versus M_R, choosing again a scenario with maximized τ-μ transitions. As can be seen, the predictions rapidly decrease with M_R and, in consequence, the constraints from these observables are in general weaker than from the LFV lepton decays and from the Z invisible width. In this an most of the studied scenarios, we have found that the most constraining EWPO is the T parameter and next, although quite close, the S parameter. For instance, for $f = 1$ and $c_{\tau\mu} = 1$ we find that M_R below around 300 GeV are excluded by T.

3.3.5 Heavy Neutrino Decay Widths

In this Thesis, we are considering sizable neutrino Yukawa couplings, so we should check that they are still within the perturbative regime. In order to impose perturba-

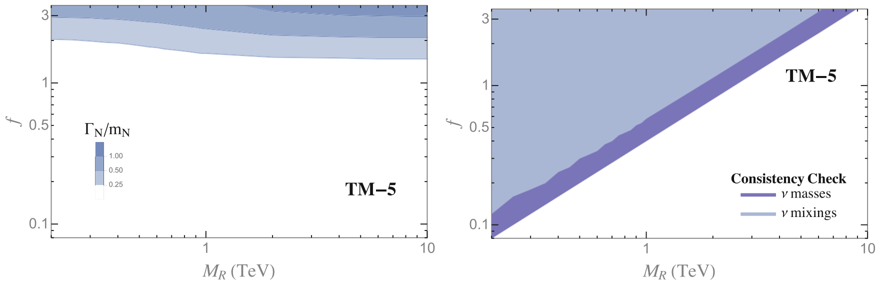

Fig. 3.9 Theoretical constraints from the requirement of perturbativity (left panel) and from the consistency of the μ_X parametrization (right panel), for the scenario TM-5. The regions excluded by the constraints are the shadowed areas

tivity we will either choose a direct constraint on the maximum allowed size of the Yukawa matrix entries, for instance $|Y_\nu^{ij}|^2/(4\pi) < 1$ or, alternatively, we will apply a constraint on an observable that grows with this Yukawa coupling, like it is the case of the total width of the heavy neutrinos. When choosing the second method, we will require that the total decay width of each heavy neutrino is always somehow smaller than the corresponding heavy neutrino mass.

The computation of the total decay width, in the limit $M_R \gg m_D$ that we work with, is reduced to a few possible decay channels. In this limit, the masses of all the heavy neutrinos are almost degenerate, close to M_R with small differences of $\mathcal{O}(m_D^2 M_R^{-1})$ between the different pseudo-Dirac pairs, see Fig. 2.4, and therefore, their potential decays into other heavy neutrinos are suppressed. In consequence, the dominant decay channels are simply $N_j \to Z\nu_i$, $H\nu_i$ and $W^\pm \ell_i^\mp$, and the total neutrino width can be then easily computed by adding the corresponding partial widths of these four decays. The partial decay width of the decay channel $N_j \to W\ell_i$ is given by:

$$\Gamma_{N_j \to W\ell_i} = \frac{\sqrt{\left(m_{N_j}^2 - m_{\ell_i}^2 - m_W^2\right)^2 - 4m_{\ell_i}^2 m_W^2}}{16\pi m_{N_j}^3} \, |\overline{F_W}|^2 \,. \tag{3.20}$$

The other channels have similar expressions and the corresponding form factors are defined as,

$$|\overline{F_H}|^2 = \frac{g^2 m_{N_j}^4}{4m_W^2} \left\{ (1-\sqrt{x_i})^2 \left[(1-\sqrt{x_i})^2 - x_H \right] |C_{n_i n_j}|^2 + 4\sqrt{x_i}\left(2 + 2x_i - x_H\right)\left(\mathrm{Re}C_{n_i n_j}\right)^2 \right\},$$
$$|\overline{F_Z}|^2 = \frac{g^2 m_{N_j}^4}{4m_W^2} \left\{ \left[\left(1 - x_i\right)^2 + x_Z\left(1 + x_i - 6\sqrt{x_i}\right) - 2x_Z^2 \right] |C_{n_i n_j}|^2 + 12 x_Z \sqrt{x_i}\left(\mathrm{Re}C_{n_i n_j}\right)^2 \right\},$$
$$|\overline{F_W}|^2 = \frac{g^2 m_{N_j}^4}{4m_W^2} |B_{\ell_i N_j}|^2 \left\{ (1-x_i)^2 + x_W(1+x_i) - 2x_W^2 \right\}, \tag{3.21}$$

where $x_H \equiv m_H^2/m_{N_j}^2$, $x_Z \equiv m_Z^2/m_{N_j}^2$, $x_W \equiv m_W^2/m_{N_j}^2$ and $x_i \equiv m_i^2/m_{N_j}^2$ with m_i the mass of the corresponding lepton. The total width is then computed as

$$\Gamma_{N_j} = \sum_{i=1}^{3} \left(\Gamma_{N_j \to h\nu_i} + \Gamma_{N_j \to Z\nu_i} + 2\, \Gamma_{N_j \to W^+\ell_i^-} \right). \tag{3.22}$$

When summing over all flavors $i = 1, 2, 3$ in the final state, the four ratios turn out to be approximately equal [70]:

$$\text{BR}(N_j \to H\nu) = \text{BR}(N_j \to Z\nu) = \text{BR}(N_j \to W^+\ell^-) = \text{BR}(N_j \to W^-\ell^+) = 25\%\,. \tag{3.23}$$

We have explored three different assumptions to comply with the perturbative unitary condition. In particular we have taken:

$$\frac{\Gamma_{N_i}}{m_{N_i}} < 1, \frac{1}{2}, \frac{1}{4} \quad \text{for } i = 1, \ldots, 6\,. \tag{3.24}$$

The results for the TM-5 scenario from Table 3.4 are displayed in the left panel of Fig. 3.9, although similar qualitative results are found for other scenarios. Here, we show the areas in the (M_R, f) plane that are excluded by the different assumptions in Eq. (3.24). We find that this perturbativity requirement is not much sensitive to M_R, giving an excluded area in the (M_R, f) plane that is a nearly horizontal band located at the top, which constrains basically just the size of the global Yukawa coupling f, in the most restricted scenarios, to be below order 2–3.

For the rest of this Thesis, we will take the second choice, 1/2, in Eq. (3.24) when we decide to use heavy neutrino widths as perturbativity criteria.

3.3.6 Validity Range of the μ_X Parametrization

As explained before, one of the novelties of this Thesis is the introduction and use of the μ_X parametrization as a tool for exploring the model parameter space being always in agreement with oscillation data. In order to check the validity range of this parametrization, we require that both the predicted light neutrino mass squared differences and the neutrino mixing angles that we obtain from the diagonalization of the full neutrino mass matrix in Eq. (2.35), lie within the 3σ experimental bands [71–75].

More specifically, we demand that the corresponding entries of the U_ν matrix that refer to the light neutrino sub-block agree with the 3σ range given in Ref. [71]:

$$|U_{\text{PMNS}}^{3\sigma}| = \begin{pmatrix} 0.801 \to 0.845 & 0.514 \to 0.580 & 0.137 \to 0.158 \\ 0.225 \to 0.517 & 0.441 \to 0.699 & 0.614 \to 0.793 \\ 0.246 \to 0.529 & 0.464 \to 0.713 & 0.590 \to 0.776 \end{pmatrix}. \tag{3.25}$$

We show in the right panel of Fig. 3.9 the predictions for the constraints found in the (M_R, f) plane for the TM-5 scenario. As can be seen in this figure, the bounds obtained from the constraints on the active neutrinos squared mass differences are in this scenario stronger than the ones from the light neutrino mixing matrix entries. For other scenarios, like TM-8, we have checked that this can be reversed, i.e., the constraints from the neutrino mixings can be stronger than from the neutrino masses. Additionally, we have also compared the range of validity of this parametrization for two values of the input lightest neutrino mass, 0.1 and 0.01 eV (the chosen value for Fig. 3.9), and we have concluded that the μ_X parametrization works better for the case with a smaller value of the light neutrino mass.

In general, we found that the area in the (M_R, f) parameter space that is allowed by all the experimental bounds above studied is also allowed by the consistency checks of the μ_X parametrization, meaning that the parametrization works well for the parameter space allowed by data. Nevertheless, the validity of this parametrization can be improved by considering next order contributions to M_{light} in Eq. (2.40), as it was done in Ref. [76].

Summarizing, in this Chapter we have learnt that the presence of right-handed neutrinos at the TeV scale can have a large impact in many low energy observables if their couplings are sizable. Since the aim of this Thesis is to study LFV consequences of these ν_R fields, we focused mostly on the LFV radiative and three-body decays of the leptons, i.e., $\ell_m \to \ell_k \gamma$ and $\ell_m \to \ell_k \ell_k \ell_k$ with $k \neq m$. This study allowed us to acquire some general ideas about LFV processes in this kind of models, to discuss the advantages and disadvantages of using the two parametrizations described in Chap. 2, as well as to introduce the phenomenological TM and TE scenarios in Table 3.4, where the experimentally most constrained μ-e transitions are ad-hoc suppressed. Additionally, we also reviewed the effects of the TeV neutrinos in other observables, including processes with lepton number violation, lepton flavor universality violation, precision physics or theoretical implications, as perturbativity of the new Yukawa coupling. All these observables will be important in the following Chapters, as they will constraint the allowed parameter space for our study of maximum LFV H and Z decays in presence of TeV right-handed neutrinos.

References

1. E. Arganda, M.J. Herrero, X. Marcano, C. Weiland, Phys. Rev. D **91**, 015001 (2015). https://doi.org/10.1103/PhysRevD.91.015001, arXiv:1405.4300 [hep-ph]
2. V. De Romeri, M.J. Herrero, X. Marcano, F. Scarcella, Phys. Rev. D **95**, 075028 (2017). https://doi.org/10.1103/PhysRevD.95.075028, arXiv:1607.05257 [hep-ph]
3. S. Bravar, O.B.O.T.T.M. Collaboration, *Proceedings of the 38th International Conference on High Energy Physics (ICHEP 2016)*, Chicago, IL, USA, August 3–10, 2016. PoS **ICHEP2016**, 552 (2016)
4. E.P. Hincks, B. Pontecorvo, J. Phys. Rev. **73**, 257 (1948). https://doi.org/10.1103/PhysRev.73.257
5. A.M. Baldini et al. (MEG), Eur. Phys. J. C **76**, 434 (2016). https://doi.org/10.1140/epjc/s10052-016-4271-x, arXiv:1605.05081 [hep-ex]

6. Y. Kuno, Y. Okada, Rev. Mod. Phys. **73**, 151 (2001). https://doi.org/10.1103/RevModPhys.73.151, arXiv:hep-ph/9909265 [hep-ph]
7. R.H. Bernstein, P.S. Cooper, J. Phys. Rept. **532**, 27 (2013). https://doi.org/10.1016/j.physrep.2013.07.002, arXiv:1307.5787 [hep-ex]
8. A.M. Baldini et al. (2013), arXiv:1301.7225 [physics.ins-det]
9. U. Bellgardt et al. (SINDRUM), Nucl. Phys. B **299**, 1 (1988). https://doi.org/10.1016/0550-3213(88)90462-2
10. A. Blondel et al. (2013), arXiv:1301.6113 [physics.ins-det]
11. B. Aubert et al. (BaBar), Phys. Rev. Lett. **104**, 021802 (2010). https://doi.org/10.1103/PhysRevLett.104.021802, arXiv:0908.2381 [hep-ex]
12. T. Aushev et al. (2010), arXiv:1002.5012 [hep-ex]
13. K. Hayasaka et al., Phys. Lett. B **687**, 139 (2010). https://doi.org/10.1016/j.physletb.2010.03.037, arXiv:1001.3221 [hep-ex]
14. K. Hayasaka, *22nd Rencontres de Blois on Particle Physics and Cosmology Blois*, Loire Valley, France, July 15–20, 2010 (2010), http://inspirehep.net/record/873396/files/arXiv:1010.3746.pdf, arXiv:1010.3746 [hep-ex]
15. C. Dohmen et al. (SINDRUM II), Phys. Lett. B **317**, 631 (1993). https://doi.org/10.1016/0370-2693(93)91383-X
16. A. Alekou et al., *Proceedings, 2013 Community Summer Study on the Future of U.S. Particle Physics: Snowmass on the Mississippi (CSS2013)*, Minneapolis, MN, USA, July 29–August 6, 2013 (2013), http://inspirehep.net/record/1256506/files/arXiv:1310.0804.pdf, arXiv:1310.0804 [physics.acc-ph]
17. W.H. Bertl et al. (SINDRUM II), Eur. Phys. J. C **47**, 337 (2006). https://doi.org/10.1140/epjc/s2006-02582-x
18. Y. Kuno (COMET), PTEP **2013**, 022C01 (2013). https://doi.org/10.1093/ptep/pts089
19. R.M. Carey et al. (Mu2e), *Proposal to Search for $\mu^- N \to e^- N$ with a Single Event Sensitivity Below* 10^{-16}. Technical Report (2008)
20. D.F. Measday, J. Phys. Rept. **354**, 243 (2001). https://doi.org/10.1016/S0370-1573(01)00012-6
21. Y. Amhis et al. (2016), arXiv:1612.07233 [hep-ex]
22. R. Aaij et al. (LHCb), JHEP **02**, 121 (2015). https://doi.org/10.1007/JHEP02(2015)121, arXiv:1409.8548 [hep-ex]
23. E. Abouzaid et al. (collaboration KTeV), Phys. Rev. Lett. **100**, 131803 (2008). https://doi.org/10.1103/PhysRevLett.100.131803, arXiv:0711.3472 [hep-ex]
24. D. Ambrose et al. (BNL), Phys. Rev. Lett. **81**, 5734 (1998). https://doi.org/10.1103/PhysRevLett.81.5734, arXiv:hep-ex/9811038 [hep-ex]
25. A. Sher et al., Phys. Rev. D **72**, 012005 (2005). https://doi.org/10.1103/PhysRevD.72.012005, arXiv:hep-ex/0502020 [hep-ex]
26. R. Appel et al., Phys. Rev. Lett. **85**, 2877 (2000). https://doi.org/10.1103/PhysRevLett.85.2877, arXiv:hep-ex/0006003 [hep-ex]
27. J.R. Batley et al. (NA48/2), Phys. Lett. B **697**, 107 (2011). https://doi.org/10.1016/j.physletb.2011.01.042, arXiv:1011.4817 [hep-ex]
28. R. Aaij et al. (LHCb), Phys. Rev. Lett. **108**, 101601 (2012). https://doi.org/10.1103/PhysRevLett.108.101601, arXiv:1110.0730 [hep-ex]
29. R. Akers et al. (OPAL), Z. Phys. C **67**, 555 (1995). https://doi.org/10.1007/BF01553981
30. P. Abreu et al. (collaboration DELPHI), Phys. C **73**, 243 (1997). https://doi.org/10.1007/s002880050313
31. G. Aad et al. (ATLAS), Phys. Rev. D **90**, 072010 (2014). https://doi.org/10.1103/PhysRevD.90.072010, arXiv:1408.5774 [hep-ex]
32. A. Abada, V. De Romeri, S. Monteil, J. Orloff, A.M. Teixeira, JHEP **04**, 051 (2015). https://doi.org/10.1007/JHEP04(2015)051, arXiv:1412.6322 [hep-ph]
33. G. Wilson, Neutrino oscillations: are lepton-flavor violating Z decays observable with the CDR detector? in *DESY-ECFA LC Workshops held at Frascati* (1998)

34. G. Wilson, Update on experimental aspects of lepton-flavour violation, in *DESY-ECFA LC Workshops held at Oxford* (1999)
35. A. Blondel, E. Graverini, N. Serra, M. Shaposhnikov (FCC-ee study Team), *Proceedings of the 37th International Conference on High Energy Physics (ICHEP 2014)*, Valencia, Spain, July 2–9, 2014, vol. 273–275 (2016), pp. 1883–1890, arXiv:1411.5230 [hep-ex]
36. G. Aad et al. (collaboration ATLAS), Eur. Phys. J. C **77**, 70 (2017). https://doi.org/10.1140/epjc/s10052-017-4624-0, arXiv:1604.07730 [hep-ex]
37. V. Khachatryan et al. (CMS), Phys. Lett. B **763**, 472 (2016). https://doi.org/10.1016/j.physletb.2016.09.062, arXiv:1607.03561 [hep-ex]
38. CMS Collaboration, Search for lepton flavour violating decays of the Higgs boson to $\mu\tau$ and eτ in proton-proton collisions at $\sqrt{s} = 13$ TeV (2017), CMS-PAS-HIG-17-001
39. V. Khachatryan et al. (CMS), Phys. Lett. B **749**, 337 (2015). https://doi.org/10.1016/j.physletb.2015.07.053, arXiv:1502.07400 [hep-ex]
40. R. Harnik, J. Kopp, J. Zupan, JHEP **03**, 026 (2013). https://doi.org/10.1007/JHEP03(2013)026, arXiv:1209.1397 [hep-ph]
41. G. Blankenburg, J. Ellis, G. Isidori, Phys. Lett. B **712**, 386 (2012). https://doi.org/10.1016/j.physletb.2012.05.007, arXiv:1202.5704 [hep-ph]
42. S. Davidson, P. Verdier, J. Phys. Rev. D **86**, 111701 (2012). https://doi.org/10.1103/PhysRevD.86.111701, arXiv:1211.1248 [hep-ph]
43. S. Bressler, A. Dery, A. Efrati, Phys. Rev. D **90**, 015025 (2014). https://doi.org/10.1103/PhysRevD.90.015025, arXiv:1405.4545 [hep-ph]
44. The ATLAS collaboration, Projections for measurements of Higgs boson cross sections, branching ratios and coupling parameters with the ATLAS detector at a HL-LHC. Technical Report ATL-PHYS-PUB-2013-014 (institution CERN, 2013)
45. The CMS Collaboration (CMS), J. Proc. Commun. Summer Study 2013: Snowmass on the Mississippi (CSS2013) (2013), http://inspirehep.net/record/1244669/files/arXiv:1307.7135.pdf, arXiv:1307.7135 [hep-ex]
46. A. De Roeck, Higgs Physics at the LHC, experimental review (2014), note talk at Physics Challenges in the face of LHC-14, IFT, Madrid, http://workshops.ift.uam-csic.es/files/157/DeRoeck.pdf
47. H. Baer, T. Barklow, K. Fujii, Y. Gao, A. Hoang, S. Kanemura, J. List, H.E. Logan, A. Nomerotski, M. Perelstein et al. (2013), arXiv:1306.6352 [hep-ph]
48. M. Bicer et al. (TLEP Design Study Working Group), *Proceedings, 2013 Community Summer Study on the Future of U.S. Particle Physics: Snowmass on the Mississippi (CSS2013)*, Minneapolis, MN, USA, July 29–August 6, 2013. JHEP **01**, 164 (2014). https://doi.org/10.1007/JHEP01(2014)164, arXiv:1308.6176 [hep-ex]
49. A. Ilakovac, A. Pilaftsis, J. Nucl. Phys. B **437**, 491 (1995). https://doi.org/10.1016/0550-3213(94)00567-X, arXiv:hep-ph/9403398 [hep-ph]
50. R. Alonso, M. Dhen, M.B. Gavela, T. Hambye, JHEP **01**, 118 (2013). https://doi.org/10.1007/JHEP01(2013)118, arXiv:1209.2679 [hep-ph]
51. T. Appelquist, J. Carazzone, J. Phys. Rev. D **11**, 2856 (1975). https://doi.org/10.1103/PhysRevD.11.2856
52. A. Abada, D. Das, A.M. Teixeira, A. Vicente, C. Weiland, JHEP **02**, 048 (2013). https://doi.org/10.1007/JHEP02(2013)048, arXiv:1211.3052 [hep-ph]
53. A. Abada, A.M. Teixeira, A. Vicente, C. Weiland, JHEP **02**, 091 (2014a). https://doi.org/10.1007/JHEP02(2014)091, arXiv:1311.2830 [hep-ph]
54. V. Cirigliano, I. Rosell, J. Phys. Rev. Lett. **99**, 231801 (2007). https://doi.org/10.1103/PhysRevLett.99.231801, arXiv:0707.3439 [hep-ph]
55. M. Finkemeier, *2nd Workshop on Physics and Detectors for DAPHNE (DAPHNE 95)*, Frascati, Italy, April 4–7 (1995). Phys. Lett. B **387**, 391 (1996). https://doi.org/10.1016/0370-2693(96)01030-1, arXiv:hep-ph/9505434 [hep-ph]
56. E. Goudzovski (NA48/2, NA62), *Proceedings, 21st International Europhysics Conference on High energy physics (EPS-HEP 2011)*, Grenoble, France, July 21–27, 2011. PoS **EPS-HEP2011**, 181 (2011), arXiv:1111.2818 [hep-ex]

57. C. Lazzeroni et al. (NA62), Phys. Lett. B **719**, 326 (2013). https://doi.org/10.1016/j.physletb.2013.01.037, arXiv:1212.4012 [hep-ex]
58. K.A. Olive et al. (collaboration Particle Data Group), Chin. Phys. C **38**, 090001 (2014). https://doi.org/10.1088/1674-1137/38/9/090001
59. E. Fernandez-Martinez, J. Hernandez-Garcia, J. Lopez-Pavon, M. Lucente, JHEP **10**, 130 (2015). https://doi.org/10.1007/JHEP10(2015)130, arXiv:1508.03051 [hep-ph]
60. P. Benes, A. Faessler, F. Simkovic, S. Kovalenko, Phys. Rev. D **71**, 077901 (2005). https://doi.org/10.1103/PhysRevD.71.077901, arXiv:hep-ph/0501295 [hep-ph]
61. A. Abada, V. De Romeri, A.M. Teixeira, JHEP **09**, 074 (2014b). https://doi.org/10.1007/JHEP09(2014)074, arXiv:1406.6978 [hep-ph]
62. M. Blennow, E. Fernandez-Martinez, J. Lopez-Pavon, J. Menendez, JHEP **07**, 096 (2010). https://doi.org/10.1007/JHEP07(2010)096, arXiv:1005.3240 [hep-ph]
63. A. Abada, M. Lucente, J. Nucl. Phys. B **885**, 651 (2014). https://doi.org/10.1016/j.nuclphysb.2014.06.003, arXiv:1401.1507 [hep-ph]
64. M. Agostini et al. (collaboration GERDA), Phys. Rev. Lett. **111**, 122503 (2013). https://doi.org/10.1103/PhysRevLett.111.122503, arXiv:1307.4720 [nucl-ex]
65. M. Auger et al. (collaboration EXO-200), Phys. Rev. Lett. **109**, 032505 (2012). https://doi.org/10.1103/PhysRevLett.109.032505, arXiv:1205.5608 [hep-ex]
66. J.B. Albert et al. (collaboration EXO-200), Nature **510**, 229 (2014). https://doi.org/10.1038/nature13432, arXiv:1402.6956 [nucl-ex]
67. A. Gando et al. (collaboration KamLAND-Zen), Phys. Rev. Lett. **110**, 062502 (2013). https://doi.org/10.1103/PhysRevLett.110.062502, arXiv:1211.3863 [hep-ex]
68. M.E. Peskin, T. Takeuchi, Phys. Rev. D **46**, 381 (1992). https://doi.org/10.1103/PhysRevD.46.381
69. E. Akhmedov, A. Kartavtsev, M. Lindner, L. Michaels, J. Smirnov, JHEP **05**, 081 (2013). https://doi.org/10.1007/JHEP05(2013)081, arXiv:1302.1872 [hep-ph]
70. A. Atre, T. Han, S. Pascoli, B. Zhang, JHEP **05**, 030 (2009). https://doi.org/10.1088/1126-6708/2009/05/030, arXiv:0901.3589 [hep-ph]
71. I. Esteban, M.C. Gonzalez-Garcia, M. Maltoni, I. Martinez-Soler, T. Schwetz, JHEP **01**, 087 (2017). https://doi.org/10.1007/JHEP01(2017)087, arXiv:1611.01514 [hep-ph]
72. D.V. Forero, M. Tortola, J.W.F. Valle, Phys. Rev. D **86**, 073012 (2012). https://doi.org/10.1103/PhysRevD.86.073012, arXiv:1205.4018 [hep-ph]
73. G.L. Fogli, E. Lisi, A. Marrone, D. Montanino, A. Palazzo, A.M. Rotunno, Phys. Rev. D **86**, 013012 (2012). https://doi.org/10.1103/PhysRevD.86.013012, arXiv:1205.5254 [hep-ph]
74. D.V. Forero, M. Tortola, J.W.F. Valle, Phys. Rev. D **90**, 093006 (2014). https://doi.org/10.1103/PhysRevD.90.093006, arXiv:1405.7540 [hep-ph]
75. M. Drewes et al., JCAP **1701**, 025 (2017). https://doi.org/10.1088/1475-7516/2017/01/025, arXiv:1602.04816 [hep-ph]
76. J. Baglio, C. Weiland, JHEP **04**, 038 (2017). https://doi.org/10.1007/JHEP04(2017)038, arXiv:1612.06403 [hep-ph]

Chapter 4
LFV Higgs Decays from Low Scale Seesaw Neutrinos

The recent discovery of the Higgs boson has opened a new experimental area to search for new physics beyond the SM, in particular with new LFV Higgs decay (LFVHD) channels. As we discussed before, LFV transitions are forbidden in the SM, therefore any observation of a LFV Higgs decay would automatically imply the existence of new physics.

The ATLAS and CMS collaborations are actively searching for these LFV Higgs boson decay processes. Interestingly, the CMS collaboration saw an excess on the $H \to \tau\mu$ channel after the run-I, with a significance of 2.4σ and a value of $\mathrm{BR}(H \to \tau\mu) = (0.84^{+0.39}_{-0.37})\%$. Unfortunately, neither this excess, nor other positive LFVHD signal, have been observed at the present run-II, so ATLAS and CMS have set bounds on these processes, as summarized in Table 3.3. At present, ATLAS has released their results after analyzing 20.3 fb^{-1} of data at a center of mass energy of $\sqrt{s} = 8$ TeV, reaching sensitivities of the order of 10^{-2} for the $H \to \tau\mu$ and $H \to \tau e$ channels [1]. On the other hand, CMS has also searched for the $H \to \mu e$ channel after the run-I [2] and has further improved the sensitivities of the $H \to \tau\mu$ and $H \to \tau e$ channels with new run-II data [3] of $\sqrt{s} = 13$ TeV, setting the most stringent upper bounds for the LFV Higgs decays, which at the 95% CL are given by:

$$\mathrm{BR}(H \to \mu e) < 3.5 \times 10^{-4}\,, \tag{4.1}$$

$$\mathrm{BR}(H \to \tau e) < 6.1 \times 10^{-3}\,, \tag{4.2}$$

$$\mathrm{BR}(H \to \tau\mu) < 2.5 \times 10^{-3}\,. \tag{4.3}$$

Additional indirect constraints on LFVHD rates have been also derived using other LFV transitions [4, 5]. For instance, the upper bounds on $\mu \to e\gamma$ can be translated into a very strong upper bound of $\mathrm{BR}(H \to \mu e) < \mathcal{O}(10^{-8})$. On the contrary, much weaker indirect upper bounds, of order $\mathcal{O}(10\%)$, are derived for the other two channels. This fact further motivates the kind of phenomenological scenarios that we introduced in Sect. 3.2.1, where μ-e transitions are *ad-hoc* suppressed.

X. Marcano, *Lepton Flavor Violation from Low Scale Seesaw Neutrinos with Masses Reachable at the LHC*, Springer Theses, https://doi.org/10.1007/978-3-319-94604-7_4

From the theoretical point of view, there are many extensions of the SM that naturally predict large ratios for these LFV Higgs decays. For instance, they have been studied in the context of supersymmetric models [6–23], in composite Higgs models [24], two Higgs doublet models [25–29], the Zee model [30], minimal flavor violation [31–34], Randall-Sundrum models [35, 36], using effective Lagrangians [37–40] and many others [41–51]. Likewise, the addition of new right-handed neutrinos to the SM can induce large LFVHD rates, specially if they are allowed to have large Yukawa interactions, which is in fact the interaction to the Higgs boson. As we saw in Chap. 2, this is precisely the case in the low scale seesaw models, as the ISS or the SUSY-ISS models, where neutrinos can have large Yukawa couplings and moderately heavy neutrino masses. Consequently, we consider extremely timely to study the LFV Higgs boson decays in these low scale seesaw models.

The LFV Higgs decays were analyzed in the context of the SM enlarged with heavy Majorana neutrinos for the first time in Refs. [52, 53]. Later, they were computed in the context of the type-I seesaw model in Ref. [54], and they were found to lead to extremely small rates due to the strong suppression from the very heavy right-handed neutrino masses, at 10^{14-15} GeV, in that case. This motivates our study of the LFV Higgs decays in the case where the right-handeutrino masses lie in contrast at the $\mathcal{O}$(TeV) energy scale and, at the same time, can have large Yukawa couplings. As we saw in Chap. 2, the ISS model contemplates this possibility and, therefore, the rates are expected to be larger than in the type-I seesaw model case.

In this Chapter we perform a detailed study of lepton flavor violating Higgs boson decays $H \to \ell_k \bar{\ell}_m$. We consider the inverse seesaw model as an explicit realization of a low scale seesaw model and analyze, both analytically and numerically, the one-loop induced LFV H decays. Furthermore, we make use of the mass insertion approximation to compute a simple effective LFV $H\ell_k\ell_m$ vertex that allows to rapidly estimate these rates in models with right-handed neutrinos. Additionally, we also explore a supersymmetric realization of the ISS model and study the new one-loop contributions to the LFV H decays coming from sneutrinos with TeV masses. The results presented in this Chapter have been published in Refs. [55–57].

4.1 LFV H Decays in the ISS Model

LFV Higgs decay rates within the SM with new heavy Majorana neutrinos were first studied in Refs. [52–54]. In this Section, we analyze these rates in the context of the ISS model with three pairs of fermionic singlets added to the SM, and fully study their one-loop contributions to the LFVHD rates. As we did for the LFV radiative decays in the previous Chapter, we use the two parametrizations introduced in Sect. 2.3, the Casas-Ibarra and the μ_X parametrization, to explore these LFVHD rates and discuss the main differences of using one parametrization versus the other.

The decay amplitude of the process $H(p_1) \to \ell_k(-p_2)\bar{\ell}_m(p_3)$ can be generically decomposed in terms of two form factors $F_{L,R}$ by:

$$i\mathcal{M} = -ig\bar{u}_{\ell_k}(-p_2)(F_L P_L + F_R P_R)v_{\ell_m}(p_3)\,, \tag{4.4}$$

and the partial decay width is then written as follows:

$$\Gamma(H \to \ell_k \bar{\ell}_m) = \frac{g^2}{16\pi m_H}\sqrt{\left(1-\left(\frac{m_{\ell_k}+m_{\ell_m}}{m_H}\right)^2\right)\left(1-\left(\frac{m_{\ell_k}-m_{\ell_m}}{m_H}\right)^2\right)} \\ \times \left((m_H^2 - m_{\ell_k}^2 - m_{\ell_m}^2)\left(|F_L|^2+|F_R|^2\right) - 4m_{\ell_k}m_{\ell_m}\mathrm{Re}(F_L F_R^*)\right). \tag{4.5}$$

Here, p_1, $-p_2$ and p_3 are the momenta of the ingoing Higgs boson, the outgoing lepton ℓ_k and the outgoing antilepton $\bar{\ell}_m$, respectively, and the conservation of momentum has been implemented as $p_1 = p_3 - p_2$. Moreover, m_H stands for the Higgs mass and $m_\ell = v\,Y_\ell$ for lepton masses (with $v = 174$ GeV). The widths of the CP-conjugate channels $H \to \ell_m \bar{\ell}_k$ are trivially related to the previous ones and

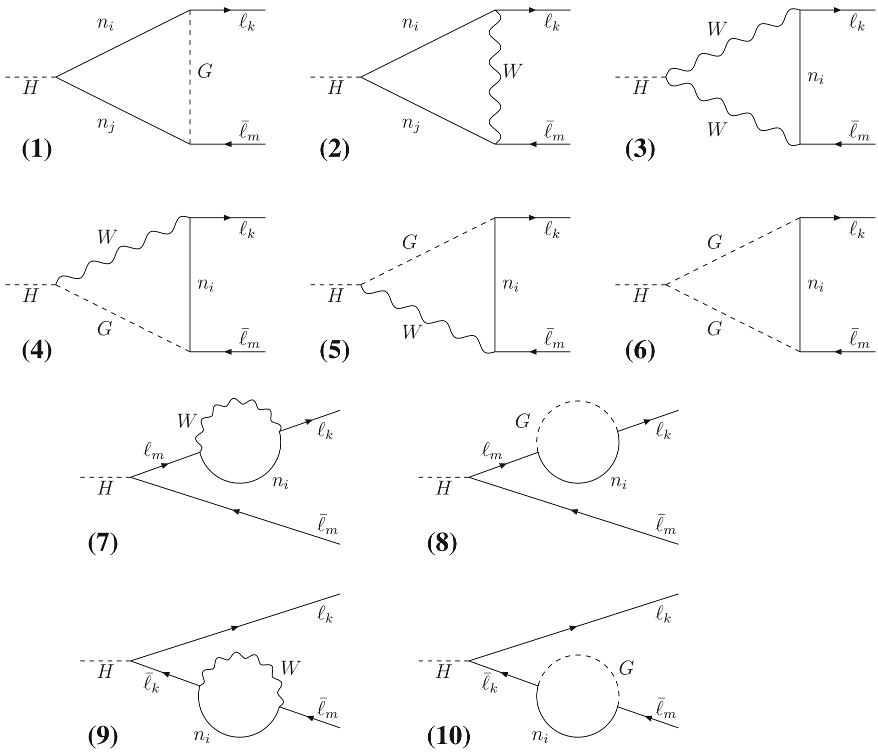

Fig. 4.1 One-loop diagrams contributing to the full computation of $H \to \ell_k \bar{\ell}_m$ decays in the physical neutrino mass eigenstate basis and in the Feynman-'t Hooft gauge

their numerical values will coincide for the case of real mass matrices, as will be the case for most of this Thesis.

In the calculation of the LFV Higgs decay rates, we will first work in the physical basis for the neutrinos and consider the full set of contributing one-loop diagrams in the Feynman-'t Hooft gauge, drawn in Fig. 4.1. The form factors can be written in this case as the sum of the different contributions:

$$F_L = \sum_{i=1}^{10} F_L^{(i)}\,, \qquad F_R = \sum_{i=1}^{10} F_R^{(i)}\,. \tag{4.6}$$

These form factors were computed in the context of the type-I seesaw in Ref. [54] and we have adapted them to our present ISS case. The complete results are given in the Appendix C.

The process $H \to \ell_k \bar{\ell}_m$ with $k \neq m$ does not exist at the tree level, neither in the SM nor in the context of the ISS model we study here, therefore the full one-loop process must be finite. We have explicitly checked that the diagrams (2)-(6) are finite and that the divergent terms from diagrams (7) and (9) are cancelled when adding up to all the neutrinos running in the loop. Hence, the only divergent contributions to the LFV Higgs decays arise from the diagrams (1), (8), and (10), and we have checked that they cancel among each other, giving rise to a total finite result. This cancellation is in agreement with the results for the type-I seesaw [54].

The numerical estimates of these LFV Higgs form factors and the LFV Higgs partial decay widths have been done with our private *Mathematica* code. In order to get numerical predictions for the BR$(H \to \ell_k \bar{\ell}_m)$ rates we use $m_H = 125\,\mathrm{GeV}$ and its corresponding SM total width is computed with *FeynHiggs* [58–60] including two-loop corrections.

In order to be in agreement with present neutrino oscillation data in Eq. (2.6), we will make use of the two parametrizations presented in Chap. 2. We start this study by taking the matrices M_R and μ_X as input parameters and reconstructing the Yukawa coupling by means of the Casas-Ibarra parametrization in Eq. (2.44). Next, we will follow the idea behind the μ_X parametrization of choosing the M_R and Y_ν matrices as input parameters and then building the proper μ_X matrix that leads to the right light neutrino masses and mixing angles.

In order to compare the predictions of the LFVHD rates with other LFV observables, we also present here the predictions for the related radiative decay rates, BR$(\mu \to e\gamma)$, BR$(\tau \to e\gamma)$ and BR$(\tau \to \mu\gamma)$. We will consider a more complete set of constraining observables and the corresponding updated bounds when looking for the maximum allowed LFV H decay rates at the end of this Chapter.

4.1.1 LFVHD with the Casas-Ibarra Parametrization

We present first our numerical results for the LFV Higgs decay rates, BR($H \to \mu\bar{\tau}$), BR($H \to e\bar{\tau}$) and BR($H \to e\bar{\mu}$), when using the Casas-Ibarra parametrization to accommodate light neutrino data. We start by considering the simplest scenario where both M_R and μ_X matrices are diagonal at the same time, $M_R \equiv \text{diag}(M_{R_1}, M_{R_2}, M_{R_3})$ and $\mu_X \equiv \text{diag}(\mu_{X_1}, \mu_{X_2}, \mu_{X_3})$. Although this is not the most general case, it will be very illustrative to learn how these observables depend on the parameters of the model and to find an optimal strategy to study a most general scenario afterwards.

We study the LFV rates as functions of the input ISS parameters in this case, namely, M_{R_i}, μ_{X_i}, the lightest[1] neutrino mass m_{ν_1} and the angles θ_i of the R matrix in Eq. (2.45), trying to localize the areas of the parameter space where the LFV Higgs decays can both be large and respect the constraints on the radiative decays. For a given set of these input parameters, we will build the Yukawa coupling by using Eq. (2.44). Nevertheless, since this procedure can generate arbitrarily large Yukawa couplings, we will enforce their perturbativity in this study by setting an upper limit on the entries of the neutrino Yukawa coupling matrix, given by

$$\frac{|Y_{ij}|^2}{4\pi} < 1.5\,, \quad \text{for } i, j = 1, 2, 3\,. \tag{4.7}$$

The results of this first case will be presented in two generically different scenarios for the heavy neutrinos: the case of (nearly) degenerate heavy neutrinos, and the case of hierarchical heavy neutrinos.

The case of (nearly) degenerate heavy neutrinos is implemented by choosing degenerate entries in M_R and in μ_X, i.e., by setting $M_{R_i} \equiv M_R$ and $\mu_{X_i} \equiv \mu_X$ for $i = 1, 2, 3$, see Fig. 2.4. First we show in Fig. 4.2 the results for all the LFV rates as functions of the common right-handed neutrino mass parameter M_R. The left panel shows the LFV Higgs decay channels, while the right panel displays de LFV radiative decays. Here we have fixed the other input parameters to $\mu_X = 10^{-7}$ GeV, $m_{\nu_1} = 0.05$ eV, and $R = \mathbb{1}$. We find that the largest LFV Higgs decay rates are for BR($H \to \mu\bar{\tau}$) and the largest radiative decay rates are for BR($\tau \to \mu\gamma$). We also see that, for this particular choice of input parameters, all the predictions for the LFV Higgs decays are allowed by the present experimental upper bounds on the three radiative decays (dashed horizontal lines in this and following plots for the radiative decays) for all explored values of M_R in this interval of (200, 10^7) GeV. Nevertheless, it shows clearly that the most constraining radiative decay at present is by far $\mu \to e\gamma$.

Regarding the M_R dependence shown in Fig. 4.2, we manifestly see that the LFVHD rates grow faster with M_R than the radiative decays, which tend, as we already saw in Chap. 3, to a constant value for M_R above $\sim 10^3$ GeV. In fact,

[1] We will show again our results for a Normal Hierarchy, varying the value of the lightest neutrino mass m_{ν_1} and setting the other two masses using the mass differences in Eq. (2.6). Although not shown here, we found similar results for the Inverted Hierarchy.

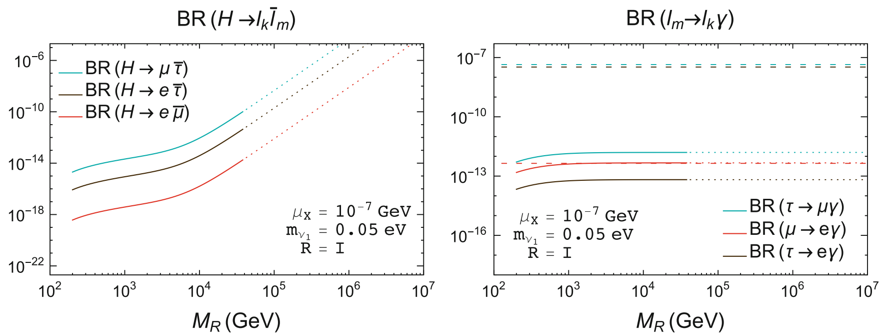

Fig. 4.2 Predictions for the LFV decay rates as functions of M_R in the degenerate heavy neutrinos case with the Casas-Ibarra parametrization in Eq. (2.44). Left panel: BR($H \to \mu\bar{\tau}$) (upper blue line), BR($H \to e\bar{\tau}$) (middle dark brown line), BR($H \to e\bar{\mu}$) (lower red line). Right panel: BR($\tau \to \mu\gamma$) (upper blue line), BR($\mu \to e\gamma$) (middle red line), BR($\tau \to e\gamma$) (lower dark brown line). The other input parameters are set to $\mu_X = 10^{-7}$ GeV, $m_{\nu_1} = 0.05$ eV, $R = \mathbb{1}$. Dotted lines indicate non-perturbative Y_ν, meaning that Eq. (4.7) is not fulfilled. Horizontal dashed lines in the right panel are the (90% C.L.) upper bounds: BR($\tau \to \mu\gamma$) $< 4.4 \times 10^{-8}$ [61] (blue line), BR($\tau \to e\gamma$) $<$ 3.3×10^{-8} [61] (dark brown line), BR($\mu \to e\gamma$) $< 4.2 \times 10^{-13}$ [62] (red line)

the LFVHD rates can reach quite sizable values at the large M_R region of these plots, yet allowed by the constraints on the radiative decays. For example, we obtain BR($H \to \mu\bar{\tau}$) $\sim 10^{-6}$ for $M_R \sim 10^6$ GeV. However, our requirement of perturbativity for the neutrino Yukawa coupling entries in Eq. (4.7) does not allow for such large M_R values as they lead to too large Y_ν values in the framework of the Casas-Ibarra parametrization of Eq. (2.44). This non-perturbative region is illustrated using dotted lines in these plots.

The qualitatively different functional behavior with M_R of the LFVHD and the radiative rates shown in Fig. 4.2 is an interesting feature that we wish to explore further. The results for the radiative decay rates can be understood with the approximated formula in Eq. (3.4), valid for large values of M_R. As already explained in Chap. 3, the $(Y_\nu Y_\nu^\dagger)_{km}$ elements grow with M_R as M_R^2 when using the Casas-Ibarra parametrization in Eq. (2.44), and therefore the radiative decay rates saturate to a constant value at large values of M_R, as can be seen in the plot on the right in Fig. 4.2. This simple behavior with M_R is certainly not the case of the LFVHD rates, and we conclude that these do not follow this same behavior with $|(Y_\nu Y_\nu^\dagger)_{km}|^2$. This different functional behavior of BR($H \to \ell_k\bar{\ell}_m$) with M_R will be further explored and clarified later by our study using the mass insertion approximation. However, we want to emphasize again that the apparent non-decoupling behavior of the LFV rates with the heavy mass scale M_R is an artifact of the Casas-Ibarra parametrization. As we already said in Chap. 3, the expected decoupling behavior with M_R will become manifest when using the μ_X parametrization, as we will see in Sect. 4.1.2.

Next we study the sensitivity of the LFV rates to other choices of μ_X. For this study we focus on the largest LFVHD rates, BR($H \to \mu\bar{\tau}$), and on the most constraining BR($\mu \to e\gamma$) rates, although similar qualitative results are found for the

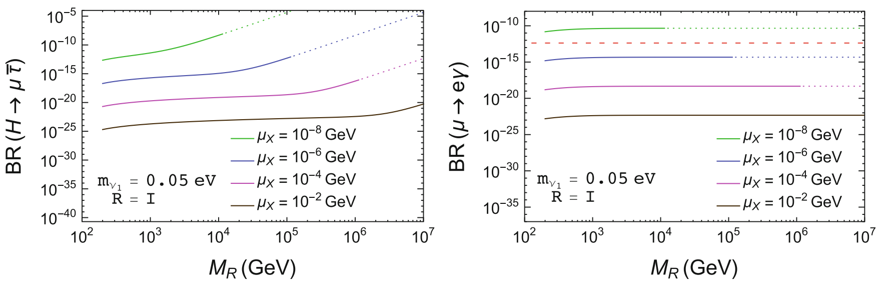

Fig. 4.3 BR($H \to \mu\bar{\tau}$) (left panel) and BR($\mu \to e\gamma$) (right panel) as functions of M_R for different values of $\mu_X = (10^{-8}, 10^{-6}, 10^{-4}, 10^{-2})$ GeV from top to bottom. In both panels, $m_{\nu_1} = 0.05$ eV and $R = \mathbb{1}$. The horizontal red dashed line denotes the current experimental upper bound on $\mu \to e\gamma$ and dotted lines non-perturbative Y_ν as defined in Eq. (4.7)

other channels. In Fig. 4.3 we show the predictions for the LFV rates for different values of $\mu_X = (10^{-8}, 10^{-6}, 10^{-4}, 10^{-2})$ GeV. The other input parameters have been fixed here to $m_{\nu_1} = 0.05$ eV and $R = \mathbb{1}$. On the left panel of Fig. 4.3 we see again the increase of BR($H \to \mu\bar{\tau}$) as M_R grows, which is more pronounced in the region where M_R is large and μ_X is low, i.e., where the Yukawa couplings are large (see Eq. (2.44)). We have checked that, in this region, the dominant diagrams are by far the divergent diagrams (1), (8) and (10), and that the BR($H \to \mu\bar{\tau}$) rates grow as M_R^4. Diagrams (2)-(6) have relevant contributions to BR($H \to \mu\bar{\tau}$) only for low values of the Yukawa couplings, while diagrams (7) and (9) are subleading. Again, this will be further explored using the MIA in Sect. 4.3. We also observe that the LFV Higgs rates grow as μ_X decreases from 10^{-2} GeV to 10^{-8} GeV. However, not all the values of M_R and μ_X are allowed, because they may generate non-perturbative Yukawa entries, as we have already said, expressed again in this figure by dotted lines. Therefore, the largest LFV Higgs rates that are permitted by our perturbativity requirements in Eq. (4.7) are approximately of BR($H \to \mu\bar{\tau}$) $\sim 10^{-9}$, obtained for $\mu_X = 10^{-8}$ GeV and $M_R \simeq 10^4$ GeV. Larger values of M_R, for this choice of μ_X, would produce Yukawa couplings that are not perturbative.

On the other hand, we must also pay attention to the predictions of BR($\mu \to e\gamma$) for this choice of parameters, because the present experimental upper bound on this ratio is quite constraining. We explore this observable in the right panel of Fig. 4.3, where the dependence of BR($\mu \to e\gamma$) on M_R is depicted for the same parameter choice as in the left panel. The horizontal red dashed line denotes again its present bound of BR($\mu \to e\gamma$) $< 4.2 \times 10^{-13}$ [62]. In addition to what we have already learned about the constant behavior of BR($\mu \to e\gamma$) with M_R, we also learn from this figure about the generic behavior with μ_X, which leads to increasing LFV rates for decreasing μ_X values. This latter behavior is actually true for both LFV observables. In particular, we see that too small values of $\mu_X \leq \mathcal{O}(10^{-8}$ GeV) lead to BR($\mu \to e\gamma$) rates that are excluded by the experimental upper bound. Taking this into account, the largest value of BR($H \to \mu\bar{\tau}$), for this choice of parameters that is allowed by the BR($\mu \to e\gamma$)

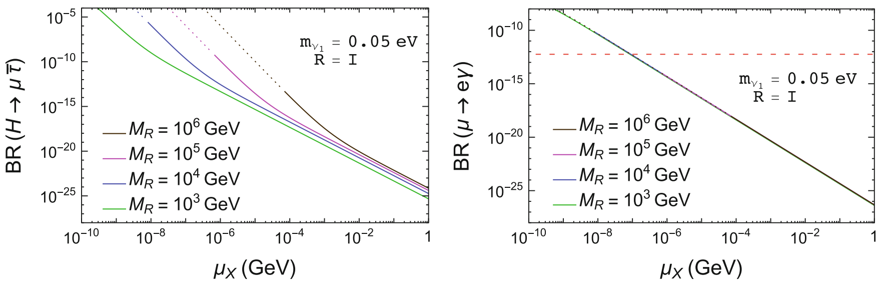

Fig. 4.4 Branching ratios of $H \to \mu\bar{\tau}$ (left) and $\mu \to e\gamma$ (right) as functions of μ_X for different values of $M_R = (10^6, 10^5, 10^4, 10^3)$ GeV from top to bottom. In both panels, $m_{\nu_1} = 0.05$ eV and $R = \mathbb{1}$. The horizontal red dashed line denotes the current experimental upper bound on $\mu \to e\gamma$ and dotted lines non-perturbative Y_ν as defined in Eq. (4.7)

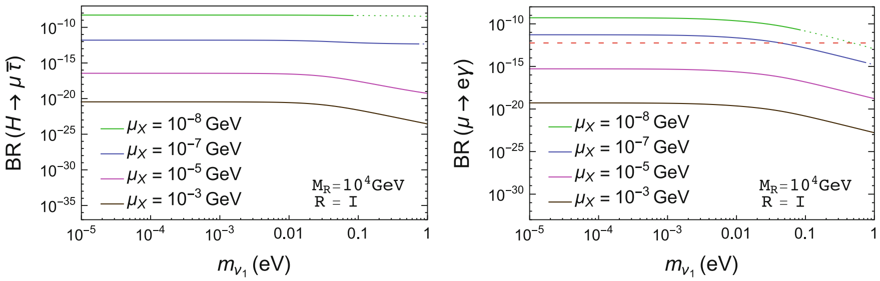

Fig. 4.5 Branching ratios of $H \to \mu\bar{\tau}$ (left panel) and $\mu \to e\gamma$ (right panel) as functions of m_{ν_1} for $M_R = 10^4$ GeV, $R = \mathbb{1}$ and different values of $\mu_X = (10^{-8}, 10^{-7}, 10^{-5}, 10^{-3})$ GeV from top to bottom. The horizontal red dashed line denotes the current experimental upper bound on $\mu \to e\gamma$ and dotted lines non-perturbative Y_ν as defined in Eq. (4.7)

upper bound is around 10^{-12}, which is obtained for $M_R \sim 10^5$ GeV and $\mu_X \sim 10^{-6}$ GeV.

The predictions of BR($H \to \mu\bar{\tau}$) and BR($\mu \to e\gamma$) as functions of μ_X, for several values of M_R, $m_{\nu_1} = 0.05$ eV, and $R = \mathbb{1}$, are displayed in Fig. 4.4. As already seen in Fig. 4.3, both LFV rates decrease as μ_X grows; however, the functional dependence is not the same. The LFV radiative decay rates decrease approximately as μ_X^{-2}, in agreement with the approximate expression in Eq. (3.4), while the LFVHD rates go as μ_X^{-4} in the regime of large Yukawa couplings. For a fixed value of μ_X, the larger M_R is, the larger BR($H \to \mu\bar{\tau}$) can be, while the prediction for BR($\mu \to e\gamma$) is the same for all tested values of M_R. We have already learned this independence of the LFV radiative decays on M_R from the previous figure, which can be easily confirmed on the right panel of Fig. 4.4, where all the lines for different values of M_R are overplaced. We also see in this figure that the smallest value of μ_X that is allowed by the BR($\mu \to e\gamma$) upper bound is $\mu_X \sim 10^{-7}$ GeV, which is directly translated to a maximum allowed value of BR($H \to \mu\bar{\tau}$) $\sim 10^{-9}$, for $M_R \sim 10^4$ GeV.

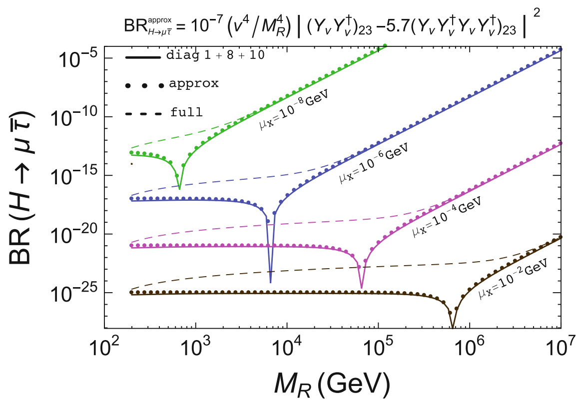

Fig. 4.6 Comparison between the predicted rates for BR($H \to \mu\bar{\tau}$) computed with the full one-loop formulas (dashed lines), just the contributions from diagrams (1), (8), and (10) of Fig. 4.1 (solid lines); and the approximate formula of Eq. (4.10) (dotted lines). Here we set $m_{\nu_1} = 0.05$ eV and $R = \mathbb{1}$

The dependence of BR($H \to \mu\bar{\tau}$) and BR($\mu \to e\gamma$) on the lightest neutrino mass m_{ν_1} is studied in Fig. 4.5, for different values of μ_X with $M_R = 10^4$ GeV and $R = \mathbb{1}$. For the chosen parameters, a similar dependence on m_{ν_1} is observed in both observables, in which there is a nearly flat behavior with m_{ν_1} until $m_{\nu_1} \gtrsim 0.01$ eV, where the LFV rates start to decrease. The behavior of BR($\ell_m \to \ell_k\gamma$) with m_{ν_1} can be understood again from Eq. (3.4). In this simplified case of real R and $U_{\rm PMNS}$ matrices, and degenerate M_R and μ_X, we find the following simple expression for the non-diagonal $\left(Y_\nu Y_\nu^\dagger\right)_{km}$ elements after using Eq. (2.44):

$$\frac{v^2\left(Y_\nu Y_\nu^\dagger\right)_{km}}{M_R^2} \approx \begin{cases} \dfrac{1}{\mu_X}\left(U_{\rm PMNS}\sqrt{\Delta m^2}\,U^T_{\rm PMNS}\right)_{km}, & \text{for } m^2_{\nu_1} \ll |\Delta m^2_{ij}|\,, \\[2ex] \dfrac{1}{\mu_X}\dfrac{\left(U_{\rm PMNS}\,\Delta m^2\,U^T_{\rm PMNS}\right)_{km}}{2m_{\nu_1}}, & \text{for } m^2_{\nu_1} \gg |\Delta m^2_{ij}|\,, \end{cases} \tag{4.8}$$

where we have defined:

$$\Delta m^2 \equiv {\rm diag}(0, \Delta {\rm m}^2_{21}, \Delta {\rm m}^2_{31})\,, \tag{4.9}$$

and we have expanded properly m_{ν_2} and m_{ν_3} in terms of m_{ν_1} and Δm^2_{ij}. Using these equations, we conclude that the BR($\mu \to e\gamma$) rates have a flat behavior with m_{ν_1} for low values of $m_{\nu_1} \lesssim 0.01$ eV, but they decrease with m_{ν_1} for larger values, explaining the observed behavior in Fig. 4.5. Again, the predictions for the BR($H \to \mu\bar{\tau}$) rates do not follow exactly the same pattern as for the BR($\mu \to e\gamma$).

By taking into account all the behaviors learned above, we have tried to find an approximate simple formula that could explain the main features of the BR($H \to \mu\bar{\tau}$) rates. As we have already said, in contrast to what we have seen for the LFV radiative decays in Eq. (3.4), a simple functional dependence being proportional to $|(Y_\nu Y_\nu^\dagger)_{23}|^2$ is not enough to describe our results for the BR($H \to \mu\bar{\tau}$) rates. Considering that, in the interesting region where the Yukawa couplings are large, the LFVHD rates are dominated by diagrams (1), (8) and (10), we have looked for a simple expression that could properly fit the contributions from these dominant diagrams. From this numerical fit we have found the following approximate formula:

$$\mathrm{BR}^{\mathrm{approx}}_{H\to\mu\bar{\tau}} = 10^{-7}\,\frac{v^4}{M_R^4}\left|(Y_\nu Y_\nu^\dagger)_{23} - 5.7(Y_\nu Y_\nu^\dagger Y_\nu Y_\nu^\dagger)_{23}\right|^2, \tag{4.10}$$

which turns out to work reasonably well. This particular analytical form in Eq. (4.10) will be justified later in Sect. 4.3.

In Fig. 4.6 we show the predicted rates of BR($H \to \mu\bar{\tau}$) computed with the full one-loop formulas (dashed lines); taking just the contributions from diagrams (1), (8) and (10) of Fig. 4.1 (solid lines); and using Eq. (4.10) (dotted lines). We see clearly that Eq. (4.10) reproduces extremely well the contributions from diagrams (1), (8), and (10) and approximates reasonably well the full rates, particularly in the fast growing as M_R^4 in the large M_R region.

This approximate expression in Eq. (4.10) contains an extra contribution in the amplitude of $\mathcal{O}(Y_\nu^4)$ with respect to the one for radiative decays in Eq. (3.4). By using again the parametrization in Eq. (2.44), we obtain,

$$\frac{v^2(Y_\nu Y_\nu^\dagger Y_\nu Y_\nu^\dagger)_{km}}{M_R^2} = \frac{M_R^2}{v^2\mu_X^2}\Big(U_{\mathrm{PMNS}}\,\Delta m^2\;U_{\mathrm{PMNS}}^T\Big)_{km}. \tag{4.11}$$

Thus, we can clearly see from the above result that the second contribution in Eq. (4.10) is the one that dominates the LFVHD rates at large M_R and low μ_X, i.e., at large Yukawa couplings, and, indeed, it reproduces properly the behavior of BR($H \to \mu\bar{\tau}$) $\propto M_R^4/\mu_X^4$ in this limit. It is also independent of m_{ν_1}, explaining the flat behavior in Fig. 4.5 for low values of μ_X. Moreover, since the two contributions in Eq. (4.10) have opposite signs, they interfere destructively, leading to dips in the contribution from these diagrams to the full decay rates, as seen in Fig. 4.6. As we said, the particular choice for the fitting functions will become clear from our posterior analysis in Sect. 4.3, where we will study in full analytical detail this observable by applying the MIA.

Next, we study the effects of taking $R \neq \mathbb{1}$. We display in Fig. 4.7 the dependence of the $H \to \mu\bar{\tau}$ and $\mu \to e\gamma$ decay rates on $|\theta_1|$ for different values of $\arg\theta_1 = 0, \pi/8, \pi/4$, with $M_R = 10^4$ GeV, $\mu_X = 10^{-7}$ GeV, and $m_{\nu_1} = 0.1$ eV. First, we wish to highlight the flat behavior of both LFV rates with $|\theta_1|$ for real R matrix ($\arg\theta_1 = 0$). This is a direct consequence of the degeneracy of M_R and μ_X, since the LFV rates for the degenerate heavy neutrinos case are independent of R if it is real. Once we abandon the real case and consider values of $\arg\theta_1$ different from zero, a strong dependence on $|\theta_1|$ appears. The larger $|\theta_1|$ and/or $\arg\theta_1$ are, the larger the LFV rates. However, only values of $|\theta_1|$ lower than $\pi/32$ with $\arg\theta_1 = \pi/8$ in this figure are allowed by the BR($\mu \to e\gamma$) constraint, which allows us to reach values of BR($H \to \mu\bar{\tau}$) $\sim 10^{-12}$ at the most. We have also explored the dependence on

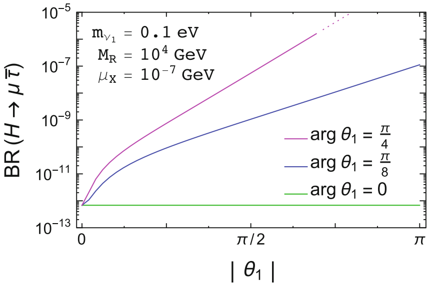

Fig. 4.7 Branching ratios of $H \to \mu\bar{\tau}$ (left panel) and $\mu \to e\gamma$ (right panel) as functions of $|\theta_1|$ for $M_R = 10^4$ GeV, $\mu_X = 10^{-7}$ GeV, $m_{\nu_1} = 0.1$ eV and different values of argθ_1. The horizontal red dashed line denotes the current experimental upper bound on BR($\mu \to e\gamma$) and dotted lines represent non-perturbative Y_ν as defined in Eq. (4.7)

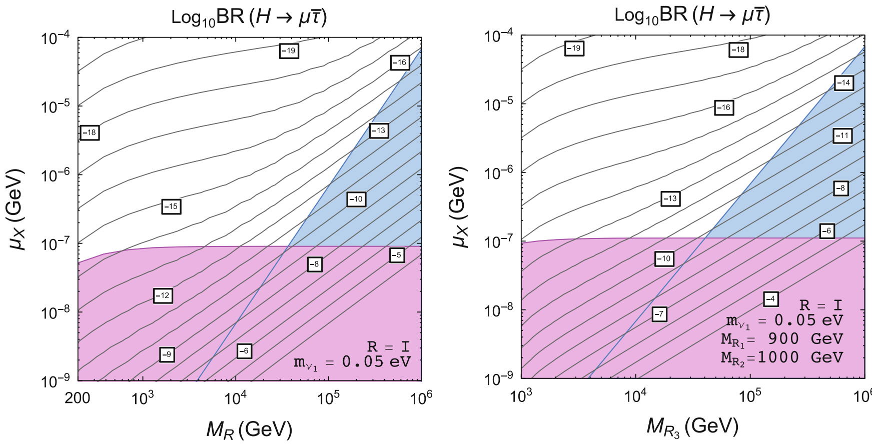

Fig. 4.8 Left panel: Contour lines of BR($H \to \mu\bar{\tau}$) in the (M_R, μ_X) plane in the case of degenerate heavy neutrinos. Right panel: Contour lines of BR($H \to \mu\bar{\tau}$) in the (M_{R_3}, μ_X) plane in the case of hierarchical heavy neutrinos with $M_{R_1} = 900$ GeV and $M_{R_2} = 1000$ GeV. In both panels $R = \mathbb{1}$ and $m_{\nu_1} = 0.05$ eV. Horizontal area in pink is excluded by the upper current bound on $\mu \to e\gamma$ and the oblique area in blue is excluded by the perturbativity requirement for Y_ν in Eq. (4.7)

complex θ_2 and θ_3 and we have reached similar conclusions as for θ_1. Therefore, we conclude that, in the case of degenerate M_R and μ_X matrices, choosing complex $\theta_{1,2,3}$ does not increase the allowed LFVHD rates respect to te previous $R = \mathbb{1}$ case.

Once we have studied the behavior of all the LFV observables considered here with the most relevant parameters, we next present the concluding results for the maximum allowed LFV Higgs decay rates in the case of heavy degenerate neutrinos. The left panel in Fig. 4.8 shows the contour lines of BR($H \to \mu\bar{\tau}$) in the (M_R, μ_X) plane for $R = \mathbb{1}$ and $m_{\nu_1} = 0.05$ eV. The horizontal area in pink is excluded by the upper bound on BR($\mu \to e\gamma$). The oblique area in blue is excluded by not respecting the perturbativity requirement of the neutrino Yukawa couplings, according to

Eq. (4.7). These contour lines summarize the previously learned behavior with M_R and μ_X, which lead to our findings for the largest values for the LFVHD rates that we localized at large M_R and low μ_X, i.e., in the bottom right-hand corner of the plot. As a conclusion from this contour plot in the left panel of Fig. 4.8, we learn that a maximum allowed LFVHD rates of approximately $\mathrm{BR}(H \to \mu\bar{\tau}) \sim 10^{-10}$ are found for degenerate $M_R \sim 2 \times 10^4$ GeV and $\mu_X \sim 10^{-7}$ GeV. We have found similar conclusions for $\mathrm{BR}(H \to e\bar{\tau})$.

We can now move to the case of hierarchical heavy neutrinos. This case refers here to the assumption of hierarchical masses among the heavy neutrino generations and it is implemented, still assuming diagonal M_R and μ_X matrices, but choosing instead hierarchical entries in the $M_R = \mathrm{diag}(M_{R_1}, M_{R_2}, M_{R_3})$ matrix, see Fig. 2.4. As for the $\mu_X = \mathrm{diag}(\mu_{X_1}, \mu_{X_2}, \mu_{X_3})$ matrix that introduces the tiny splitting among the heavy masses in the same generation we choose them still to be degenerate, $\mu_{X_{1,2,3}} = \mu_X$. We focus here on the normal hierarchy case $M_{R_1} < M_{R_2} < M_{R_3}$, since we have found similar conclusions for other hierarchies.

The results of the LFV rates for both Higgs (left panel) and radiative (right panel) decays in this $M_{R_1} < M_{R_2} < M_{R_3}$ hierarchical case are shown in Fig. 4.9. This figure shows that the behavior of these rates in the hierarchical case with respect to the heaviest neutrino mass M_{R_3} is similar to the previously found one for the degenerate case with respect to the common M_R. As before, the $\mathrm{BR}(H \to \ell_k\bar{\ell}_m)$ rates grow fast with M_{R_3} at large $M_{R_3} > 3000$ GeV, whereas the $\mathrm{BR}(\ell_m \to \ell_k\gamma)$ rates stay flat with M_{R_3}. We also see in this plot that, for the chosen parameters, the hierarchical scenario leads to larger $\mathrm{BR}(H \to \ell_k\bar{\ell}_m)$ rates than the previous degenerate case. For instance, $\mathrm{BR}(H \to \mu\bar{\tau})$ reaches 10^{-9} at $M_{R_3} = 3 \times 10^4$ GeV, to be compared with 10^{-11} at $M_R = 3 \times 10^4$ GeV that we got in Fig. 4.2 for the degenerate case. We have found this same behavior of enhanced LFVHD rates by approximately one or two orders of magnitude in the hierarchical case as compared to the degenerate case in most of the explored parameter space regions. This same enhancement can also be seen in the

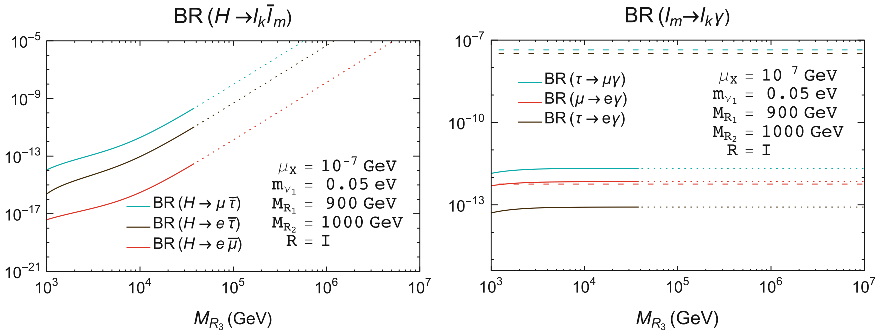

Fig. 4.9 Predictions for the LFV Higgs (left panel) and radiative (right panel) decay rates as functions of M_{R_3} in the hierarchical heavy neutrinos case with $M_{R_1} < M_{R_2} < M_{R_3}$. The other input parameters are set to $M_{R_1} = 900$ GeV, $M_{R_2} = 1000$ GeV, $\mu_X = 10^{-7}$ GeV, $m_{\nu_1} = 0.05$ eV and $R = \mathbb{1}$. The color code is as in Fig. 4.2

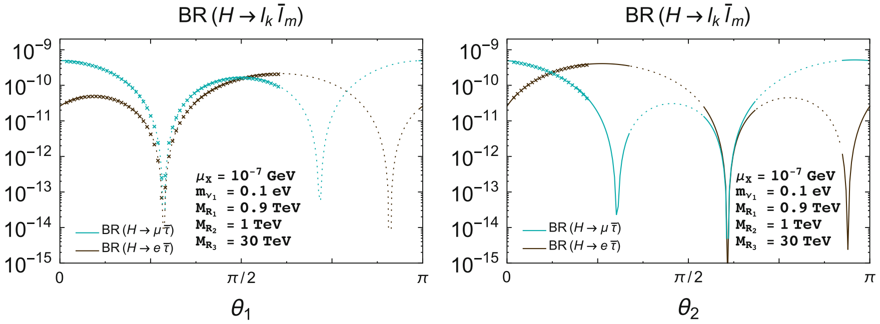

Fig. 4.10 Predictions for BR$(H \to \mu\bar{\tau})$ (blue lines) and BR$(H \to e\bar{\tau})$ (dark brown lines) rates as a function of real θ_1 (left panel) and θ_2 (right panel). The other input parameters are set to $\mu_X = 10^{-7}$ GeV, $m_{\nu_1} = 0.1$ eV, $M_{R_1} = 0.9$ TeV, $M_{R_2} = 1$ TeV, $M_{R_3} = 30$ TeV, $\theta_2 = \theta_3 = 0$ in the left panel and $\theta_1 = \theta_3 = 0$ in the right panel. The dotted lines indicate non-perturbative neutrino Yukawa couplings and the crossed lines are excluded by the present upper bound on BR$(\mu \to e\gamma)$. The solid lines are allowed by all the constraints

contour plot in the right panel of Fig. 4.8, where the maximum allowed BR$(H \to \mu\bar{\tau})$ rates reach larger values up to about 10^{-9} for $M_{R_1} = 900$ GeV, $M_{R_2} = 1000$ GeV, $M_{R_3} = 3 \times 10^4$ GeV, $\mu_X = 10^{-7}$ GeV, $m_{\nu_1} = 0.05$ eV and $R = \mathbb{1}$.

Finally, we study the effects of the R matrix for this case of hierarchical heavy neutrinos. In contrast to the degenerate case, there is a dependence on the R matrix even if it is real. Thus, we explore the behavior with the real $\theta_{1,2}$ angles. We find that for this particular hierarchy of $M_{R_1} < M_{R_2} < M_{R_3}$, there is nearly an independence of θ_3 but there is a clear dependence with θ_1 and θ_2, as it is illustrated in Fig. 4.10. These plots also show that the BR$(H \to \ell_k\bar{\ell}_m)$ rates with $\theta_{1,2} \neq 0$ can indeed increase or decrease with respect to the reference $R = \mathbb{1}$ case. In particular, for $0 < \theta_1 < \pi$ we find that BR$(H \to \mu\bar{\tau})$ is always lower than for $R = \mathbb{1}$, whereas BR$(H \to e\bar{\tau})$ can be one order of magnitude larger if θ_1 is near $\pi/2$. For the case of $0 < \theta_2 < \pi$, we find again that BR$(H \to \mu\bar{\tau})$ is always lower than for $R = \mathbb{1}$, and BR$(H \to e\bar{\tau})$ can be one order of magnitude larger than for $R = \mathbb{1}$ if θ_2 is near $\pi/4$. In this latter case, it is interesting to notice that in the region of θ_2 close to $\pi/4$ BR$(H \to e\bar{\tau})$ reaches the maximum value close to 10^{-9} and it is allowed by the constraints on the radiative decays and by the perturbativity condition. The results for the other decay channel BR$(H \to e\bar{\mu})$ are not shown here because they again give much smaller rates, as in the degenerate case. We have also tried other choices for the hierarchies among the three heavy masses $M_{R_{1,2,3}}$, finding similar conclusions.

4.1.2 LFVHD with the μ_X Parametrization

Next, we explore the implications on LFV Higgs decays of going beyond the simplest previous hypothesis of diagonal μ_X and M_R mass matrices in the ISS model. Here, we will focus on the case of degenerate M_R and will explore only the LFV Higgs decay channels with the largest rates, namely, $H \to \mu\bar{\tau}$ and $H \to e\bar{\tau}$, looking for the maximum rates allowed by the radiative decays.

In order to get an idea of how large the LFVHD rates could be, we first make a rough estimate of the expected maximal rates for the $H \to \mu\bar{\tau}$ channel by using our approximate formula of Eq. (4.10), which is given just in terms of the neutrino Yukawa coupling matrix Y_ν and M_R. On the other hand, in order to keep the predictions for the radiative decays below their corresponding experimental upper bounds, we need to require a maximum value for the non-diagonal $(Y_\nu Y_\nu^\dagger)_{ij}$ entries. By using our approximate formula of Eq. (3.4) and the present bounds in Table 3.1, we obtain:

$$v^2(Y_\nu Y_\nu^\dagger)_{12}^{\max}/M_R^2 \sim 2.5 \times 10^{-5}, \tag{4.12}$$
$$v^2(Y_\nu Y_\nu^\dagger)_{13}^{\max}/M_R^2 \sim 0.015, \tag{4.13}$$
$$v^2(Y_\nu Y_\nu^\dagger)_{23}^{\max}/M_R^2 \sim 0.017. \tag{4.14}$$

Then, in order to simplify our search, and given the above relative strong suppression of the 12 element, it seems reasonable to neglect it against the other off-diagonal elements. In that case, by assuming $(Y_\nu Y_\nu^\dagger)_{12} \simeq 0$ we have

$$(Y_\nu Y_\nu^\dagger Y_\nu Y_\nu^\dagger)_{23} \simeq (Y_\nu Y_\nu^\dagger)_{22}(Y_\nu Y_\nu^\dagger)_{23} + (Y_\nu Y_\nu^\dagger)_{23}(Y_\nu Y_\nu^\dagger)_{33}, \tag{4.15}$$

and the approximate formula of Eq. (4.10) can then be rewritten as follows:

$$\mathrm{BR}^{\mathrm{approx}}_{H\to\mu\bar{\tau}} = 10^{-7} \left|\frac{v^2}{M_R^2}(Y_\nu Y_\nu^\dagger)_{23}\right|^2 \left|1 - 5.7\Big((Y_\nu Y_\nu^\dagger)_{22} + (Y_\nu Y_\nu^\dagger)_{33}\Big)\right|^2. \tag{4.16}$$

This equation clearly shows that the maximal $\mathrm{BR}(H \to \mu\bar{\tau})$ rates are obtained for the maximum allowed values of $(Y_\nu Y_\nu^\dagger)_{23}$, $(Y_\nu Y_\nu^\dagger)_{22}$, and $(Y_\nu Y_\nu^\dagger)_{33}$. Thus, before going to any specific assumption for the Y_ν texture we can already conclude on these maximal rates, by setting the maximum allowed value for $v^2(Y_\nu Y_\nu^\dagger)_{23}^{\max}/M_R^2$ to that given in Eq. (4.14) and fixing the values of $(Y_\nu Y_\nu^\dagger)_{22}$ and $(Y_\nu Y_\nu^\dagger)_{33}$ to their maximum allowed values that are implied by our perturbativity condition in Eq. (4.7). This leads to our approximate prediction for the maximal rates:

$$\mathrm{BR}^{\max}_{H\to\mu\bar{\tau}} \simeq 10^{-5}\,. \tag{4.17}$$

We found similar conclusions for the $H \to e\bar{\tau}$ channel.

For the purpose of reaching these large rates, we find more useful and effective to use the μ_X parametrization instead of the Casas-Ibarra one. As explained in Chap. 3, the main advantage when using this parametrization is that it allows us to consider M_R and Y_ν, the relevant parameters for the LFV processes, as the independent input parameters. Furthermore, it makes very easy to focus our analysis directly on the TM and TE scenarios introduced in Table 3.4, which are designed to explore the parameter space directions where τ-μ or τ-e transitions are maximized, respectively, whereas the μ-e transitions are extremely suppressed.

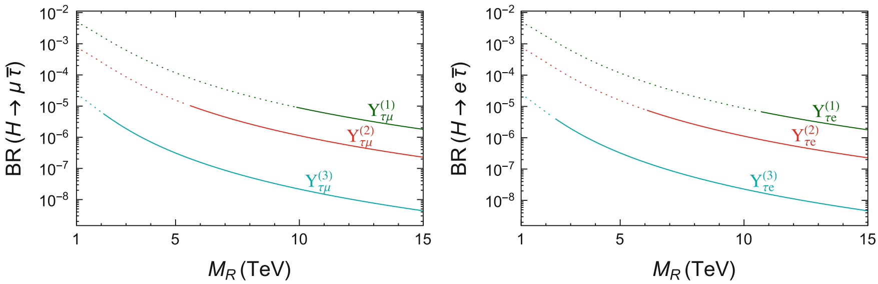

Fig. 4.11 Predictions for the LFVHD rates versus M_R obtained when using the μ_X parametrization. Left panel: BR($H \to \mu\bar{\tau}$) for $Y^{(1)}_{\tau\mu}$ (upper green line), $Y^{(2)}_{\tau\mu}$ (middle red line) and $Y^{(3)}_{\tau\mu}$ (lower blue line) given in Table 3.4 with $f = \sqrt{6\pi}$. Right panel: BR($H \to e\bar{\tau}$) for the equivalent TE scenarios. Solid (dotted) lines indicate input values allowed (disallowed) by upper bounds on radiative decays

We present in Fig. 4.11 our predictions for the LFVHD as a function of the degenerate right-handed neutrino mass M_R when using the μ_X parametrization for accommodating neutrino oscillation data. Here, we show the results in the scenarios TM-5 $\left(Y^{(1)}_{\tau\mu}\right)$, TM-6 $\left(Y^{(2)}_{\tau\mu}\right)$ and TM-7 $\left(Y^{(3)}_{\tau\mu}\right)$ in Table 3.4 for $f = \sqrt{6\pi}$, although similar results are found in other scenarios. As before, we have used the full one-loop formulas, even though we have also checked that the approximate formula in Eq. (4.10), and the equivalent one for $H \to e\bar{\tau}$ obtained by choosing the 13 entries instead of the 23 ones, gives a quite good estimate in the large M_R region. Notice again that the μ_X parametrization makes explicit the expected decoupling behavior with M_R, in contrast with the previous plots done with the Casas-Ibarra parametrization.

The main numerical conclusion from these plots is that in these scenarios one can indeed reach large LFVHD rates of the order of 10^{-5} and still be compatible with all the bounds from radiative decays, mainly $\tau \to \mu\gamma$ ($\tau \to e\gamma$) in the left (right) panel. The scenario with input $Y_{\tau\mu}$ ($Y_{\tau e}$) corresponding to lower $c_{\tau\mu}$ ($c_{\tau e}$) allows for lower M_R values and vice versa. Thus, $Y^{(1)}_{\tau\mu}$ ($Y^{(1)}_{\tau e}$) leads to the maximum allowed BR($H \to \mu\bar{\tau}$) (BR($H \to e\bar{\tau}$)) rates for M_R around 10 TeV, $Y^{(2)}_{\tau\mu}$ ($Y^{(2)}_{\tau e}$) 6 TeV and $Y^{(3)}_{\tau\mu}$ ($Y^{(3)}_{\tau e}$) around 2 TeV.

Summarizing, in this Section we have studied the LFV Higgs and radiative decays, by considering two different parametrizations to accommodate light neutrino data: the Casas-Ibarra and the μ_X parametrization. We have showed the advantages of using the latter for looking for large allowed LFVHD rates. By doing this, we found larger rates for BR($H \to \mu\bar{\tau}$) and BR($H \to e\bar{\tau}$) of about 10^{-5} in the TM and TE scenarios, respectively. Of course, in order to properly conclude on maximum allowed LFVHD rates, one must take into account a more complete set of constraining observables. We will do this at the end of this Chapter, in Sect. 4.4. Furthermore, we have also learnt that LFVHD rates do not behave with the heavy M_R mass as the LFV radiative decays, as can be seen from the plots presented in this Section and by comparing the respective approximated expressions in Eqs. (4.10) and (3.4). We will study this particular behavior un more detail using the MIA in Sect. 4.3.

Nevertheless, before going to the full analysis of the right-handed neutrino contribution to the LFVHD rates, we want to explore these rates also in a different model, where the ISS is embedded in a supersymmetric context. In such a case, new important contributions could arise from diagrams with SUSY particles running in the loops and, as we will present next, they can considerably increase the LFVHD rates.

4.2 LFV H Decays in the SUSY-ISS Model

We have seen in Chap. 2 that the ISS model can be easily embedded into a Supersymmetric context, leading to a new model that we refer to as the SUSY-ISS model. Interestingly, previous studies have demonstrated that supersymmetric contributions usually enhance the LFV rates (see, for instance, Refs. [54, 63–66]). In particular, in the present SUSY-ISS model, we expect that a lower value of the heavy neutrino mass scale M_R in the ISS, compared with the type-I seesaw, will enhance the slepton flavor mixing due to the RGE-induced radiative effects by the large neutrino Yukawa couplings, and this mixing will in turn generate via the slepton loops an enhancement in the LFVHD rates. On the other hand, new relevant couplings appear, like the neutrino trilinear coupling A_ν, which for sneutrinos with $\mathcal{O}(1\,\text{TeV})$ masses may lead to new loop contributions to LFVHD that could even dominate [64]. This calls up for a new evaluation of the LFVHD rates in the SUSY-ISS model.

Additionally, as we said in Sect. 3.1, the CMS experiment saw an interesting excess in the $H \to \mu\tau$ channel after the LHC run-I [67] with a value of $\text{BR}(H \to \mu\tau) = 8.4^{+3.9}_{-3.7} \times 10^{-3}$ and a significance of $2.4\,\sigma$. Motivated by the fact that the ISS model could not explain such a large ratio, we start by exploring the size of the new SUSY particle contribution to these LFVHD rates. Of course, a more detailed analysis considering the full set of contributions in the SUSY-ISS model is needed and will come in a future work. Nonetheless, we expect that the dominant contributions will come from the new SUSY particles and, therefore, we study first their impact on LFVHD rates.

In this Section, then, we consider a full one-loop diagrammatic computation of all the supersymmetric loops within the SUSY-ISS model for $\text{BR}(H_x \to \ell_k \bar{\ell}_m)$, where H_x refers in this Section to the three neutral MSSM Higgs bosons, $H_x = (h, H, A)$. This is in contrast to the previous estimate in Ref. [64], where an effective Lagrangian description of the Higgs mediated contributions to LFV processes was used, which was valid to capture just the relevant contributions at large $\tan\beta$, and where the mass insertion approach was used to incorporate, working in the electroweak basis, the flavor slepton mixing $(\Delta m^2_{\tilde{L}})_{ij}$. However, an expansion up to the first order in the mass insertion approximation may not be enough for the type of scenarios studied here, due to the large value of the flavor-non-diagonal matrix entries. On the other hand, we are interested also in small and moderate $\tan\beta$ values and we also wish to explore more generic soft masses for the SUSY particles and scan over the relevant neutrino/sneutrino parameters, mainly M_R, A_ν and $m_{\tilde{\nu}_R}$, not focusing only on scenarios with universal or partially universal soft parameters nor fixing the relevant parameters to one particular value as in Ref. [64]. Therefore, we perform the calculation instead in the more convenient mass basis for all the SUSY particles involved in the loops, i.e., the charged sleptons, sneutrinos, charginos, and neutralinos.

The decay amplitude for $H_x \to \ell_k \bar{\ell}_m$ can be written, similarly to Eq. (4.4), as

$$iF_x = -ig\bar{u}_{\ell_k}(-p_2)(F_{L,x}P_L + F_{R,x}P_R)v_{\ell_m}(p_3)\,, \tag{4.18}$$

where again $H_x = (h, H, A)$ and $p_1 = p_3 - p_2$ is the ingoing Higgs boson momentum. The full LFVHD widths can be then obtained from Eq. (4.5), with the proper substitution of $m_H \to m_{H_x}$ for the Higgs masses and $F_{L/R} \to F_{L/R,x}$ in the form factors.

Since we work in the mass basis, the set of diagrams contributing to the LFV Higgs decays is the same as in the SUSY type-I seesaw model which was previously considered in Ref. [54]. We display this set of 8 diagrams, four diagrams with charginos and sneutrinos in the loops, and four more with neutralinos and charged sleptons, in Fig. 4.12. The contributions of the SUSY diagrams are summed in $F_{L,x}$ and $F_{R,x}$ according to

$$F_{L,x} = \sum_{i=1}^{8} F_{L,x}^{(i)}, \quad F_{R,x} = \sum_{i=1}^{8} F_{R,x}^{(i)}\,. \tag{4.19}$$

We take the analytical expressions from Ref. [54] and properly adapt them to the SUSY-ISS model. The resulting formulas are collected in Appendix D.

As in the non-SUSY case, this observable does not exist at the tree level and, therefore, the full one loop contributions must give a finite result. In the type-I seesaw SUSY model, we have checked that each diagram in Fig. 4.12 gives a finite contribution to the $H_x \to \ell_k \bar{\ell}_m$ process when summing over all internal indexes, in agreement with Refs. [19, 54]. This is not the case in the SUSY-ISS model, where we have found that the new terms in the coupling factor $A^{(\ell)}_{R\alpha j}$, see Eq. (D.1), give rise

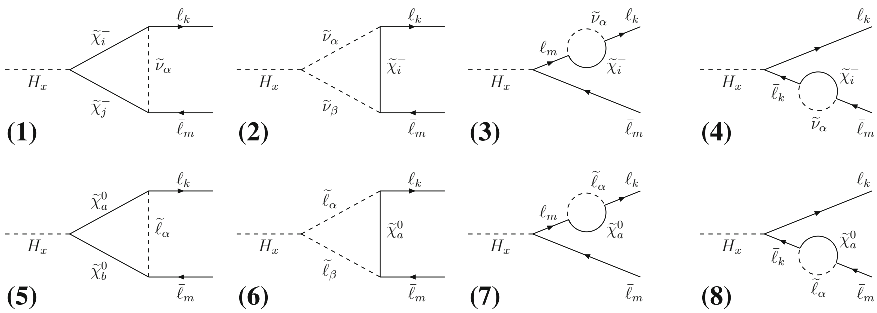

Fig. 4.12 One-loop supersymmetric diagrams contributing to the process $H_x \to \ell_k \bar{\ell}_m$

to divergent terms in diagrams (3) and (4). Nevertheless, these divergences cancel out when adding both diagrams, such that the full result is finite, as expected. Notice that the contributions from the sneutrino-chargino sector, adding diagrams (1)–(4), and the ones from the slepton-neutralino sector, adding diagrams (5)–(8), are finite separately and, therefore, it is legit to study both contributions separately, as we will do below.

Next, we show the numerical results of the LFV decay rates of the lightest neutral Higgs boson, BR($h \to \tau\bar{\mu}$), as a function of the most relevant parameters for the full SUSY contribution to LFVHD, namely, M_R, A_ν and $m_{\tilde{\nu}_R}$. We will assume that the lightest CP-even Higgs boson, h, is the particle found by the LHC with a mass of 125 GeV, and explore, consequently, the process $h \to \tau\bar{\mu}$. In order to ensure a Higgs boson mass in agreement with the experimental value, we will adjust the squark parameters, since they are irrelevant for the LFVHD studied here, and make sure that they lead to a supersymmetric spectrum allowed by ATLAS and CMS searches. As in the non-SUSY case, we restrict ourselves to the case of heavy neutrinos and sneutrinos above the Higgs boson mass, with $M_R > m_h$, avoiding constraints from the invisible Higgs decay widths, and consider only real $U_{\rm PMNS}$ and mass matrices, making constraints from lepton electric dipole moments irrelevant. Furthermore, this absence of CP violation makes BR($h \to \tau\bar{\mu}$) = BR($h \to \mu\bar{\tau}$) and, therefore, a factor of two should be added to our results when comparing with experimental data for BR($h \to \tau\mu$)≡ BR($h \to \tau\bar{\mu}$)+BR($h \to \mu\bar{\tau}$).

As in the previous section, we will also compute here, using the expressions in Ref. [68], the LFV radiative decays as a good reference of the most relevant experimental constraints on LFV, whose current upper limits at the 90% C.L. are

$$\mathrm{BR}(\mu \to e\gamma) \leq 4.2 \times 10^{-13} \text{ [62]}\,, \tag{4.20}$$

$$\mathrm{BR}(\tau \to e\gamma) \leq 3.3 \times 10^{-8} \text{ [61]}\,, \tag{4.21}$$

$$\mathrm{BR}(\tau \to \mu\gamma) \leq 4.4 \times 10^{-8} \text{ [61]}\,. \tag{4.22}$$

In the following plots, the points excluded by LFV radiative decays will be denoted by crosses, while triangles will represent the allowed ones. We present here the predictions of BR($h \to \tau\bar{\mu}$) for three examples of the TM scenarios exposed in the Table 3.4 that maximize τ-μ transitions ensuring, at the same time, practically vanishing LFV in the μ-e sector, in particular, leading to BR($\mu \to e\gamma$) ~ 0 and BR($h \to e\bar{\mu}$) ~ 0. It should be noticed that in these TM scenarios LFV transitions in the τ-e sector are also substantially suppressed and, therefore, the most stringent radiative decay is that of the related LFV radiative decay $\tau \to \mu\gamma$. Although not shown here, we want to emphasize again that equivalent results are obtained for BR($h \to \tau\bar{e}$) in the TE scenarios.

In Fig. 4.13, we show the behavior of BR($h \to \tau\bar{\mu}$) as a function of M_R in the above commented scenarios, $Y_{\tau\mu}^{(1)}$ from TM-5 (upper left panel), $Y_{\tau\mu}^{(2)}$ from TM-6 (upper right panel), and $Y_{\tau\mu}^{(3)}$ from TM-7 (lower left panel), for different values of the scaling factor f. First of all, we clearly see that, as expected, the larger the value of f is, the larger the LFV rates are. We also observe qualitatively different behaviors of

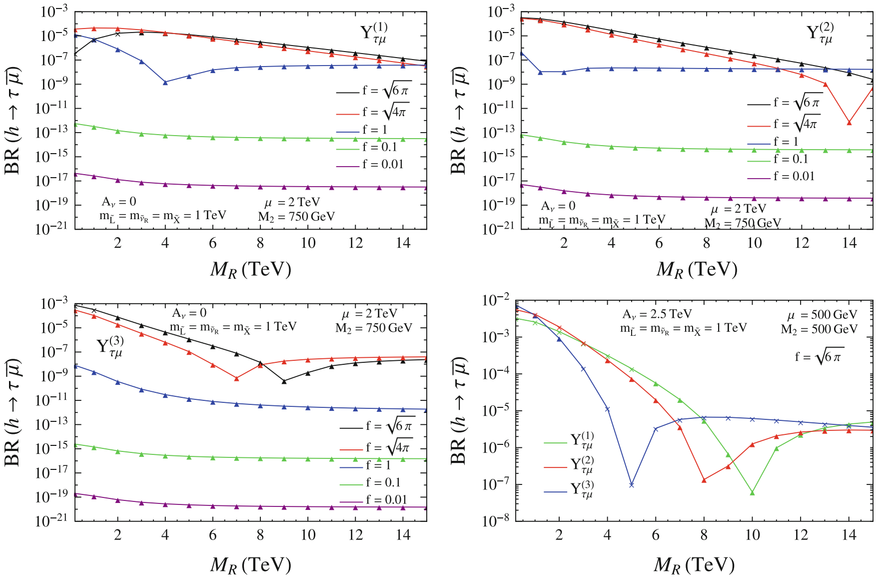

Fig. 4.13 BR($h \to \tau\bar{\mu}$) as a function of M_R for $Y_{\tau\mu}^{(1)}$ (upper left panel), $Y_{\tau\mu}^{(2)}$ (upper right panel), and $Y_{\tau\mu}^{(3)}$ (lower left panel) with $M_2 = 750$ GeV, $\mu = 2$ TeV, $A_\nu = 0$, $\tan\beta = 5$ and different values of the scaling factor $f = 0.01, 0.1, 1, \sqrt{4\pi}, \sqrt{6\pi}$. The lower right panel shows the results in these three scenarios with $M_2 = \mu = 500$ GeV, $A_\nu = 2.5$ TeV, $\tan\beta = 10$ and $f = \sqrt{6\pi}$. In all panels, $m_{\tilde{L}} = m_{\tilde{e}} = m_{\tilde{\nu}_R} = m_{\tilde{X}} = 1$ TeV, $m_A = 800$ GeV and $M_0 = 1$ TeV. We set, in these and all the figures of this Section, $A_0 = A_e = B_X = B_R = 0$, $M = 10^{18}$ GeV and the GUT inspired relation $M_1 = 5/3\ M_2 \tan^2\theta_W$. Crosses (triangles) represent points in the SUSY-ISS parameter space excluded (allowed) by the upper bound BR($\tau \to \mu\gamma$) $< 4.4 \times 10^{-8}$ [61]

the LFV rates between small ($f < 1$) and large ($f > 1$) neutrino Yukawa couplings. This difference comes from the different behavior with the parameters of the two participating types of loops, the ones with charged sleptons, where the LFV is generated exclusively by the mixing $(\Delta m^2_{\tilde{L}})_{ij}$, and the ones with sneutrinos where the LFV is generated by both $(\Delta m^2_{\tilde{L}})_{ij}$ and $(Y_\nu)_{ij}$. For small values of f, the dominant contributions come from the slepton-neutralino loops, which only depend logarithmically on M_R, as can be seen from Eq. (2.63), leading to the apparent flat behavior. Nevertheless, we checked that this flat behavior disappears when both M_R and M_0, and consequently all slepton and sneutrino masses, increase simultaneously. On the other hand, when the scale factor f becomes larger, contributions from sneutrino-chargino loops become sizable and even dominate at low M_R. These contributions decrease with M_R, due to the increase in the singlet sneutrino masses, which explains the decrease in BR($h \to \tau\bar{\mu}$) observed in the plots in Fig. 4.13 for large $f > 1$. In this latter situation, the appearance of dips due to negative interferences between the two types of loops marks the transition between the two regimes, with the main contribution coming from sneutrino-chargino loops at low M_R and from slepton-neutralino loops at large M_R.

Regarding the numerical predictions, we find that, for these parameters, the largest $\mathrm{BR}(h \to \tau\bar{\mu})$ allowed by the $\tau \to \mu\gamma$ upper limit are obtained for $f = \sqrt{4\pi}$ or $\sqrt{6\pi}$ and $M_R < 2$ TeV, with a value of around 10^{-4} for the three shown scenarios, which could be probed in future runs of the LHC. Nonetheless, these predictions can have strong dependencies on the SUSY parameters, as we want to further explore next. In particular, we study the effects on these LFV observables of the trilinear coupling A_ν, which had been set to zero up to now. On the lower right panel of Fig. 4.13 we have chosen $A_\nu = 2.5$ TeV and show the behavior of $\mathrm{BR}(h \to \tau\bar{\mu})$ with M_R for the three textures with a scaling factor $f = \sqrt{6\pi}$. This value of A_ν leads to an enhancement of the $\mathrm{BR}(h \to \tau\bar{\mu})$ while simultaneously suppressing the $\tau \to \mu\gamma$ rates. As a consequence, very large LFVHD branching ratios can be obtained for $Y_{\tau\mu}^{(3)}$ with low M_R close to 1 TeV achieving values up to 7×10^{-3} allowed by $\tau \to \mu\gamma$. These large rates are within the sensitivity of the present experiments.

We next study the behavior of the $h \to \tau\bar{\mu}$ rates as a function of the SUSY mass scales in a simplified scenario where all the SUSY masses are equal to a common parameter m_{SUSY}, namely,

$$m_{\mathrm{SUSY}} = m_{\tilde{L}} = m_{\tilde{e}} = m_{\tilde{\nu}_R} = m_{\tilde{X}} = M_0 = M_1 = M_2\,. \tag{4.23}$$

The left panel of Fig. 4.14 shows the expected decoupling behavior with m_{SUSY}, where $\mathrm{BR}(h \to \tau\bar{\mu})$ decreases when increasing all the heavy sparticle masses. This plot is for the particular case of the TM-5 scenario $\left(Y_{\tau\mu}^{(1)}\right)$, but similar behaviors (not shown) are obtained for the other scenarios. In this figure we have included the full predictions for $\mathrm{BR}(h \to \tau\bar{\mu})$, as well as the separated contributions coming only from sneutrino-chargino loops, diagrams (1)–(4) in Fig. 4.12, and from slepton-neutralino loops, diagrams (5)–(8) in Fig. 4.12. We see that not only the full prediction but also the separated contributions from these two subsets decrease with m_{SUSY}, showing that

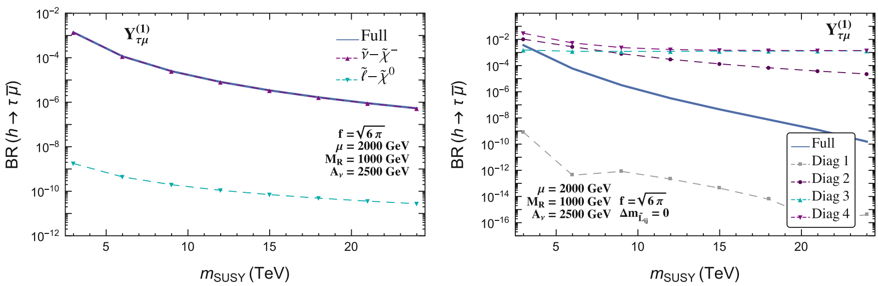

Fig. 4.14 $\mathrm{BR}(h \to \tau\bar{\mu})$ as a function of the common SUSY mass parameter m_{SUSY} in Eq. (4.23) for the TM-5 scenario $\left(Y_{\tau\mu}^{(1)}\right)$ with $M_R = 1$ TeV, $f = \sqrt{6\pi}$, $m_A = 800$ GeV, $\mu = 2$ TeV, $\tan\beta = 10$ and $A_\nu = 2.5$ TeV. Left panel: Contributions from sneutrino-chargino loops, denoted by $\widetilde{\nu}$-$\widetilde{\chi}^-$, slepton-neutralino loops, denoted by $\widetilde{\ell}$-$\widetilde{\chi}^0$, and full results for $\mathrm{BR}(h \to \tau\bar{\mu})$. Right panel: Individual contributions from each $\widetilde{\nu}$-$\widetilde{\chi}^-$, diagrams (1)–(4) in Fig. 4.12, and full result in the case of $\Delta m_{\tilde{L}_{ij}} = 0$, where the $\widetilde{\ell}$-$\widetilde{\chi}^0$ contributions vanish

the decoupling occurs in both, the charginos-sneutrinos and the neutralinos-sleptons sectors, as expected from the decoupling theorem.

In this heavy sparticle scenario, the full predictions are dominated by the contributions from the sneutrino-chargino sector, which is the one containing new sparticles with respect to the MSSM. In order to better understand the contributions from this sector, we study the simple case of $\Delta m_{\tilde{L}_{ij}} = 0$, where the contributions from the slepton-neutralino sector vanish. We show in the right panel of Fig. 4.14 the full result in this situation, as well as the individual contributions from diagrams (1)–(4) in Fig. 4.12. We see that the vertex correction, diagram (2), and the self-energies, diagrams (3) and (4), clearly compete in size and that their interference is destructive, manifesting a strong cancellation among them. The contributions from diagram (1), on the other hand, are subleading by several orders of magnitude. Notice also that the finite contributions from the divergent diagrams (3) and (4) do not decouple individually with $m_{\rm SUSY}$, but their addition does, as expected.

As mentioned before, we have found that the LFVHD rates are indeed very sensitive to the particular value of the trilinear coupling A_ν. Thus, we study in Fig. 4.15 the behavior of BR$(h \to \tau\bar{\mu})$ with A_ν for the two SUSY scenarios considered in Fig. 4.13, with $M_R = 1$ TeV and $f = \sqrt{6\pi}$. The strong dependence on A_ν is manifest in both panels, presenting deep dips in different positions that depend mainly on the values of Y_ν, μ, m_A and $\tan\beta$. These parameters control, in particular, the h-$\tilde{\nu}_L$-$\tilde{\nu}_R$ coupling and the $\tilde{\nu}_L$-$\tilde{\nu}_R$ mixing, which would lead to the appearance of dips in the regime where contributions from sneutrino-chargino loops dominate, as it is the case of Fig. 4.15. It is interesting to note that, for this choice of parameters, practically all the parameter space is excluded by $\tau \to \mu\gamma$ except the points within the dips and surrounding them, where the LFV radiative decay $\tau \to \mu\gamma$ suffers also a strong reduction. We find as a relevant feature that the location of the dips in BR$(h \to \tau\bar{\mu})$ and BR$(\tau \to \mu\gamma)$ usually does not coincide, therefore allowing for large LFV Higgs

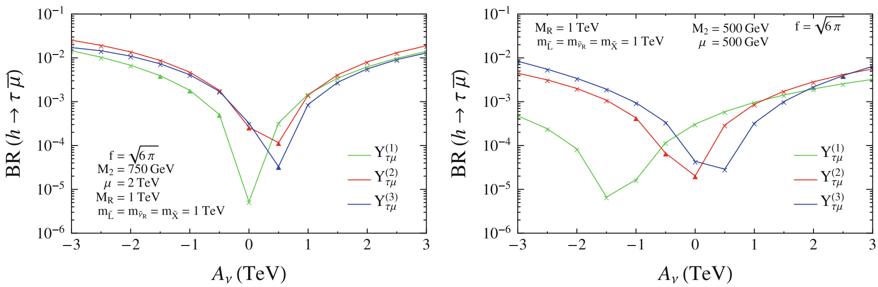

Fig. 4.15 Dependence of BR$(h \to \tau\bar{\mu})$ on A_ν for scenarios TM-5 $\left(Y^{(1)}_{\tau\mu}\right)$, TM-6 $\left(Y^{(2)}_{\tau\mu}\right)$, and TM-7 $\left(Y^{(3)}_{\tau\mu}\right)$, with $M_2 = 750$ GeV, $\tan\beta = 5$ and $\mu = 2$ TeV (left panel) or with $\tan\beta = 10$ and $M_2 = \mu = 500$ GeV (right panel). On both panels, $m_A = 800$ GeV, $M_0 = 1$ TeV, $M_R = m_{\tilde{L}} = m_{\tilde{e}} = m_{\tilde{\nu}_R} = m_{\tilde{X}} = 1$ TeV, and the scaling factor $f = \sqrt{6\pi}$. Crosses (triangles) represent points in the SUSY-ISS parameter space excluded (allowed) by the $\tau \to \mu\gamma$ upper limit, BR$(\tau \to \mu\gamma) < 4.4 \times 10^{-8}$ [61]

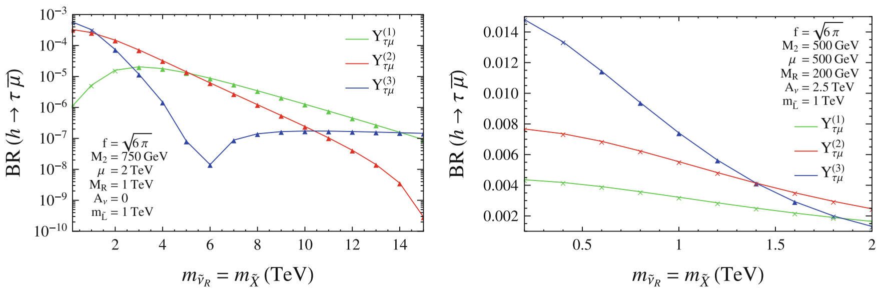

Fig. 4.16 Dependence of BR($h \to \tau\bar{\mu}$) on $m_{\tilde{\nu}_R} = m_{\tilde{X}}$ for scenarios TM-5 $\left(Y^{(1)}_{\tau\mu}\right)$, TM-6 $\left(Y^{(2)}_{\tau\mu}\right)$, and TM-7 $\left(Y^{(3)}_{\tau\mu}\right)$, with $M_R = m_{\tilde{L}} = m_{\tilde{e}} = 1$ TeV, $M_2 = 750$ GeV, $\mu = 2$ TeV, $\tan\beta = 5$ and $A_\nu = 0$ (left panel) or with $M_R = 200$ GeV, $m_{\tilde{L}} = m_{\tilde{e}} = 1$ TeV, $M_2 = \mu = 500$ GeV, $\tan\beta = 10$ and $A_\nu = 2.5$ TeV (right panel). On both panels, $m_A = 800$ GeV, $M_0 = 1$ TeV, and $f = \sqrt{6\pi}$. Crosses (triangles) represent points in the SUSY-ISS parameter space excluded (allowed) by the $\tau \to \mu\gamma$ upper limit, BR($\tau \to \mu\gamma$) $< 4.4 \times 10^{-8}$ [61]

decays rates, above 10^{-3} and within the reach of the LHC experiments, that are not excluded by $\tau \to \mu\gamma$.

Finally, the dependence of the LFVHD rates on the new sneutrino soft SUSY breaking scalar masses, $m_{\tilde{\nu}_R}$ and $m_{\tilde{X}}$, is depicted in Fig. 4.16, where we vary these parameters independently from the SUSY scale. As when modifying M_R, increasing $m_{\tilde{\nu}_R}$ and $m_{\tilde{X}}$ makes the singlet sneutrinos heavier and decreases the size of the chargino contribution. In the case of $Y^{(1)}_{\tau\mu}$ and $Y^{(2)}_{\tau\mu}$ which are dominated by this contribution, the BR($h \to \tau\bar{\mu}$) exhibits a strong decrease in the range explored in Fig. 4.16, by more than five orders of magnitude in the case of $Y^{(2)}_{\tau\mu}$. For $Y^{(3)}_{\tau\mu}$ a dip can be observed, due again to cancellations between the chargino and neutralino contributions, with the latter dominating at large $m_{\tilde{\nu}_R}$. For the benchmark point in the left panel, the largest $h \to \tau\bar{\mu}$ rates allowed by the $\tau \to \mu\gamma$ upper limit are obtained for $Y^{(2)}_{\tau\mu}$ with $m_{\tilde{\nu}_R} = 200$ GeV, with a maximum value of $\sim 3 \times 10^{-4}$, just one order of magnitude below the present LHC sensitivity. In the second benchmark point in the right panel of Fig. 4.16, we found large LFVHD rates with $M_R = 200$ GeV, $A_\nu = 2.5$ TeV and low values of $m_{\tilde{\nu}_R}$. We observe a huge increase in BR($h \to \tau\bar{\mu}$) for the three Yukawa couplings $Y^{(1)}_{\tau\mu}$, $Y^{(2)}_{\tau\mu}$, and $Y^{(3)}_{\tau\mu}$, with maximum values of approximately 4×10^{-3}, 8×10^{-3} and 1.5×10^{-2}, respectively, due mainly to the low values of $m_{\tilde{\nu}_R}$ and M_R. Unfortunately, the $\tau \to \mu\gamma$ upper limit excludes all the parameter space for the $Y^{(1)}_{\tau\mu}$ and $Y^{(2)}_{\tau\mu}$ cases. In contrast, most of the points for the $Y^{(3)}_{\tau\mu}$ texture are in agreement with this upper bound, since they are located in a region where the $\tau \to \mu\gamma$ rates suffer a strong suppression as a consequence of the value set for A_ν, in this case, $A_\nu = 2.5$ TeV. This fact allows us to obtain a maximum value of BR($h \to \tau\bar{\mu}$) $\sim 1.1\%$, completely within the reach of the current LHC experiments and large enough to explain the CMS excess if confirmed by other experiments and/or future data.

Summarizing, in this Section we have studied the LFVHD rates in presence of the SUSY particles in the SUSY-ISS model. We have seen that much larger contributions from the SUSY loops are obtained with respect to the predicted rates in the type-I seesaw due to large $Y_\nu^2/(4\pi) \sim \mathcal{O}(1)$, the presence of right-handed sneutrinos at the TeV scale and an increased RGE-induced slepton mixing from the GUT scale down to the M_R scale. We also demonstrated that in the SUSY-ISS model new contributions coming from the SUSY particle loops can considerably enhance the LFVHD rates with respect to the non-SUSY ISS model. We have found particularly interesting the new contributions from the trilinear coupling A_ν, since, in addition to enhance the LFVHD rates, it can lead to suppressions in the corresponding LFV radiative decay rates. We find these results very promising and therefore this calls up for a more complete analysis. We will therefore present in a future work a complete study including both the SUSY and non-SUSY contributions in the SUSY-ISS model, exploring also the heavy Higgs bosons LFV decays and considering a detailed analysis of experimental constraints beyond radiative LFV decays.

4.3 The Effective LFV $H\ell_k\ell_m$ Vertex from Heavy ν_R Within the Mass Insertion Approximation

As we have seen in Sect. 4.1, LFV H decays in the ISS model do not behave as other LFV processes like the radiative decays. By comparing the approximated expressions for the LFV radiative decays in Eq. (3.4) and for the H decays in Eq. (4.10), it is clear that the latter contains, in addition to the usual $\mathcal{O}(Y_\nu^2)$ contribution, an extra contribution of $\mathcal{O}(Y_\nu^4)$ that is not present in the former.

In order to understand these results, we will perform a completely different and independent analysis of the LFVHD rates within the ISS model. Instead of using the physical neutrino basis, we will perform our computation of the LFVHD widths directly in the chiral electroweak interaction basis with left- and right-handed neutrinos being the fields propagating in the loops. This will allow us to express the results explicitly in terms of the most relevant model parameters, namely, the neutrino Yukawa coupling matrix Y_ν and the right-handed mass matrix M_R.

We will do this new one-loop computation by using the mass insertion approximation (MIA), which turns out to be a very powerful tool in presence of heavy right-handed neutrinos. In this context, the MIA provides the results in terms of a well defined expansion in powers of Y_ν, which is the unique relevant coupling originating lepton flavor violation in this model, and therefore it is a very useful and convenient method for an easier and clearer interpretation of the related phenomenology.

For the present study of the $H \to \ell_k \bar{\ell}_m$ decay amplitude we will calculate this MIA expansion first to the leading order, $\mathcal{O}((Y_\nu Y_\nu^\dagger)_{km})$, and second to the next to leading order $\mathcal{O}((Y_\nu Y_\nu^\dagger Y_\nu Y_\nu^\dagger)_{km})$. In addition, we will also use the MIA to compute the one-loop effective vertex $H\ell_k\ell_m$, that is the relevant one for these decays. For this purpose, we will explore the proper large M_R mass expansion, which in the present case we must apply for the assumed mass hierarchy,

$$m_{\ell_{i,j}} \ll vY_\nu, m_W, m_H \ll M_R\,, \tag{4.24}$$

with $m_{\ell_{i,j}}$ the lepton masses, v the Higgs vacuum expectation value and m_W and m_H, the W boson and Higgs particle masses, respectively. As we will see, the most appealing feature of our computation is that it provides very simple formulas, which turn out to work very well for both the one-loop effective $H\ell_k\ell_m$ LFV vertex and the partial width $\Gamma(H \to \ell_k\bar{\ell}_m)$ in terms of the most relevant parameters Y_ν and M_R. These simple formulas could be easily used by other authors to rapidly estimate, without the need of a heavy numerical computation, the LFVHD rates with their own inputs for Y_ν and M_R. Moreover, since these results are based only in the mass hierarchy in Eq. (4.24) and the fact that Y_ν is the main source of LFV, they could presumably be used in alternative neutrino models that share these properties. In order to make this statement clearer, we explain in more detail the hypothesis behind our calculation in the next Section.

4.3.1 The Proper Basis and Feynman Rules for a MIA Computation

In order to use the MIA for the computation of the one-loop generated effective $H\ell_k\ell_m$ vertex from right-handed neutrinos, it is important first to choose the proper EW interaction basis and to set up the necessary Feynman rules in terms of these fields. The main point of the MIA is precisely based on the use of the EW basis instead of the mass basis, which is the one usually used in the literature for the one-loop generated LFV observables in models with massive Majorana neutrinos. Nevertheless, the MIA computations can be even further simplified by choosing the proper EW basis for each model, as we discuss in the following.

In the case of the ISS model, the 9×9 mass matrix in Eq. (2.35) provides all the relevant masses and mass insertions for the EW eigenstates that are needed for our computation. These mass insertions connect two different neutrino states, they are in general flavor non-diagonal, and can be expressed in terms of the three 3×3 matrices m_D, μ_X and M_R. Specifically, the mass insertion given by m_D connects ν_L and ν_R fields, M_R connects ν_R and X, and μ_X connects two X. To simplify the computation, we will use again the freedom of redefining the new fields (ν_R, X) in such a way that the M_R matrix is flavor diagonal. Thus, all the flavor violation is contained in the matrices μ_X and m_D. Nevertheless, since we are working with μ_X being extremely small as to accommodate the light neutrino masses, this mass matrix will be irrelevant for the LFV physics that we will study in this Thesis. Therefore, the only relevant flavor violating insertion will be provided by the m_D matrix and, in consequence, by the Yukawa coupling matrix Y_ν.

On the other hand, it should be noticed that the flavor preserving mass insertions given by M_R can be very large if M_R is taken to be heavy, as it will be our case with M_R being at the TeV scale. Since we are finally interested in a perturbative MIA computation of the one-loop LFV Higgs form factors and effective vertices that are valid for heavy M_R masses, we find convenient to use a different chiral basis where 'the big insertions' given by M_R are resumed in such a way that the 'large mass' M_R appears effectively in the denominator of the propagators of the new states. The key point in choosing this proper chiral basis is provided by the fact that for the quantities of our interest here, having H, ℓ_k and ℓ_m as the external particles, the only neutrino states that interact with them are ν_L and ν_R. The singlet fields X interact exclusively with the ν_R fields via the M_R mass insertions and, therefore, they will only appear in the computation of the loop diagrams for LFV as internal intermediate states inside internal lines that start and end with ν_R's. This motivates clearly our choice of modified propagators for the ν_R fields which are built on purpose to include inside all the effects of the sequential insertions of the X fields, given each of these insertions by M_R. More concretely, we sum all the M_R insertions and define two types of modified propagators: one with the same initial and final particle, corresponding to an even number of M_R mass insertions which we call *fat propagators*, and one with different initial and final particles, corresponding to an odd number of insertions. The *fat propagator*, which propagates a ν_R into a ν_R and contains the sum of all the infinite series of even number of M_R insertions due to the interactions with X, is the one we need for the present computation. The details of the procedure to reach this proper chiral basis and the derivation of the modified propagators are explained in Appendix E.1. Similar results are obtained within the context of the Flavor Expansion Theorem[2] [69, 70].

In order to complete the set-up for our computations, we summarize the relevant Feynman rules in our previously chosen proper chiral basis in Fig. 4.17. These include the relevant flavor changing mass insertions, given by m_D, the relevant propagators, both the usual SM EW propagators and the new *fat propagators* of the ν_R's, as well as the relevant interaction vertices needed for our computation, both the SM EW vertices and the new ones involving the ν_R's.

Finally, we want to stress that, although we have considered the ISS model to make our computations, our results could be applied in practice to any low scale seesaw model that leads to the same Feynman rules as in Fig. 4.17. These are indeed quite generic Feynman rules in models with right-handed heavy neutrinos. The few specific requirements are that the only relevant LFV source is the Yukawa neutrino coupling matrix and that the heavy right-handed neutrino propagator is like our *fat propagator* introduced above.

---

[2] We warmly thank Michael Paraskevas for his kind comment about the similarities between our *fat propagators* and the results in the Flavor Expansion Theorem.

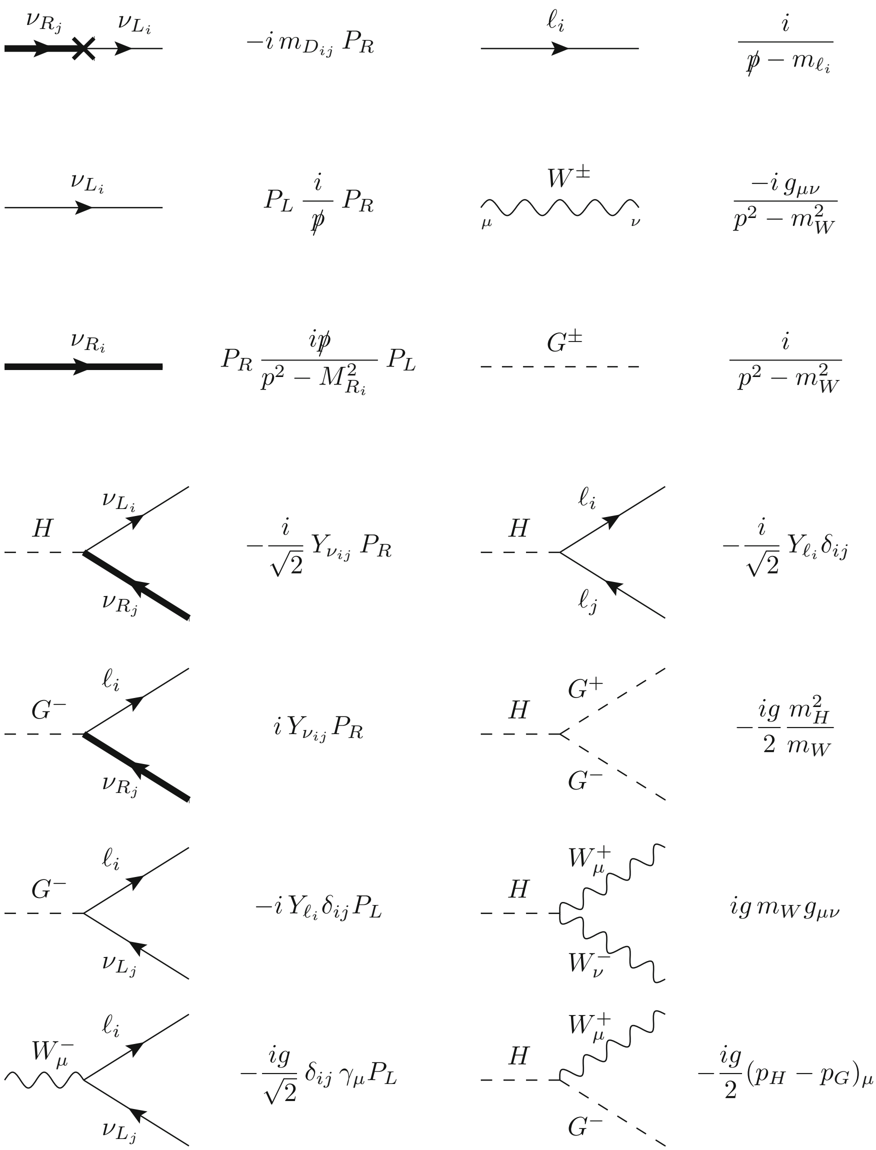

Fig. 4.17 Relevant Feynman rules for the present MIA computation of BR($H \to \ell_k \bar{\ell}_m$) in the Feynman-'t Hooft gauge. The rules involving neutrinos are written in terms of the proper EW chiral basis for ν_R and ν_L, as defined in the text. For completeness, some additional SM Feynman rules that are needed are also included. The momenta p_H and p_G are incoming. The thick solid line represents the *fat propagator* of ν_R introduced in the text

4.3.2 $\Gamma(H \to \ell_k\bar{\ell}_m)$ to One-Loop Within the MIA

Once we have introduced the set-up for our MIA calculation, we are ready to compute the LFVHD rates. We perform a diagrammatic MIA calculation of $\Gamma(H \to \ell_k\bar{\ell}_m)$ considering the following points:

1. We use the EW chiral neutrino basis.
2. We treat the external particles H, ℓ_k and $\bar{\ell}_m$ in their physical mass basis.
3. We use the *fat propagator* for the heavy right-handed neutrinos and the Feynman rules as described in Sect. 4.3.1.
4. The LFVHD amplitude is evaluated at the one-loop order in the Feynman-'t Hooft gauge. In the Appendix E.4 we show that the same result is obtained in the Unitary gauge.
5. All the loops must contain at least one right-handed neutrino, since they are the only particles transmitting LFV through the flavor off-diagonal neutrino Yukawa matrix entries.
6. According to the Feynman rules in Fig. 4.17, these flavor changing Yukawa couplings, appear just in two places, the mass insertions given by m_D and the interactions of H with ν_L and ν_R, being proportional to Y_ν.
7. All the one-loop diagrams will get an even number of powers of Y_ν, since Y_ν appears twice for each ν_R in an internal line, and because of the absence of interactions containing two right-handed neutrinos.
8. We further simplify our computation by considering that the diagonal matrix M_R has degenerate entries, i.e., $M_{R_i} \equiv M_R$. The generalization to the non-degenerate case will be commented in Appendix E.

In summary, taking into account all the points exposed above, the one-loop contributions to the LFV Higgs decay amplitude, as computed with the MIA, will then be given by an expansion in even powers of Y_ν, concretely as $Y_\nu Y_\nu^\dagger$. Therefore, the form factors defined in Eq. (4.4), which we recall here for completeness,

$$i\mathcal{M} = -ig\bar{u}_{\ell_k}(-p_2)(F_L P_L + F_R P_R)v_{\ell_m}(p_3)\,, \qquad (4.25)$$

can be written as follows:

$$F_{L,R}^{\mathrm{MIA}\ (Y^2+Y^4)} = \left(Y_\nu Y_\nu^\dagger\right)^{km} f_{L,R}^{(Y^2)} + \left(Y_\nu Y_\nu^\dagger Y_\nu Y_\nu^\dagger\right)^{km} f_{L,R}^{(Y^4)}\,, \qquad (4.26)$$

where $\mathcal{O}(Y_\nu Y_\nu^\dagger)$ are the Leading Order (LO) terms and $\mathcal{O}(Y_\nu Y_\nu^\dagger Y_\nu Y_\nu^\dagger)$ the Next to Leading Order (NLO) terms in our expansion. We expect that, in the perturbativity regime of the neutrino Yukawa couplings, the next terms in this expansion, i.e., those of $\mathcal{O}(Y_\nu^6)$ and higher, will be very tiny and can be safely neglected. Furthermore, as will be explained in more detail below, considering this expansion in powers of Y_ν and working with the hypothesis of M_R being the heaviest scale, also lead to an implicit ordering of the various contributions in powers of v/M_R. In fact, we will demonstrate, by an explicit analytical expansion of the form factors in the large

$M_R \gg v$ limit, that the dominant terms of the two contributions in Eq. (4.26), the LO $f^{(Y^2)}_{L,R}$ and the NLO $f^{(Y^4)}_{L,R}$, indeed both scale as $(v/M_R)^2$. In contrast, the next order contributions, i.e., those of $\mathcal{O}(Y_\nu^6)$, scale as $(v/M_R)^4$, and therefore they will be negligible for heavy right-handed neutrinos, even when the Yukawa couplings are sizable. Thus, considering just these two first terms of the MIA expansion in Eq. (4.26) will be sufficient to approach quite satisfactorily the full one-loop calculation of the neutrino mass basis in the case of $\mu_X \ll m_D \ll M_R$ that we are interested in.

In order to estimate the validity of the MIA results for the present study of the LFV Higgs decays we include a numerical comparison of these MIA results with those of the full one-loop computation in the physical neutrino basis presented in Sect. 4.1. For an easy comparison, we adopt in the MIA the same notation (i) (i = 1, ..., 10) for the ten types of generic diagrams as in the full computation shown in Fig. 4.1. They can be classified into diagrams with vertex corrections, i = 1, .., 6, and diagrams with external leg corrections, i = 7, .., 10.

For the one-loop computation in the MIA, we also follow a diagrammatic procedure that consists of the systematic insertion of right-handed neutrino *fat-propagators* in all possible places inside the loops, which are built with the interaction vertices and propagators of Fig. 4.17. Generically, diagrams with one right-handed neutrino propagator will contribute to the form factors of $\mathcal{O}(Y_\nu^2)$, whereas diagrams with two right-handed neutrino propagators will contribute to the form factors of $\mathcal{O}(Y_\nu^4)$. We show in Figs. 4.18, 4.19, 4.20 and 4.21 the relevant one-loop diagrams in the MIA corresponding to the dominant contributions of the LO and the NLO in Eq. (4.26), respectively. These are also classified into those of vertex corrections and those of leg corrections type. The MIA form factors are then obtained accordingly as the sum of all these contributions that can be summarized as follows:

$$F^{\rm MIA}_{L,R} = \sum_{\rm i=1}^{10} F^{\rm MIA(i)}_{L,R}\,. \tag{4.27}$$

At LO, i.e., $\mathcal{O}(Y_\nu^2)$, each $F^{\rm MIA(i)}_{L,R}$ receives contributions from all diagrams containing 1 right-handed neutrino propagator and one of these three combinations: (i) 1 vertex with ν_R and 1 m_D insertion, (ii) 0 vertices with ν_R and 2 m_D insertions, (iii) 2 vertices with ν_R and 0 m_D insertions. This leads to the relevant diagrams in Figs. 4.18 and 4.19 whose contributions are given, in an obvious correlated notation, by:

$$\begin{aligned}
F^{\rm MIA(1)\ (Y^2)}_{L,R} &= F^{\rm (1a)}_{L,R} + F^{\rm (1b)}_{L,R} + F^{\rm (1c)}_{L,R} + F^{\rm (1d)}_{L,R}\,,\\
F^{\rm MIA(2)\ (Y^2)}_{L,R} &= F^{\rm (2a)}_{L,R} + F^{\rm (2b)}_{L,R}\,,\\
F^{\rm MIA(3)\ (Y^2)}_{L,R} &= F^{\rm (3a)}_{L,R}\,,\\
F^{\rm MIA(4)\ (Y^2)}_{L,R} &= F^{\rm (4a)}_{L,R} + F^{\rm (4b)}_{L,R}\,,\\
F^{\rm MIA(5)\ (Y^2)}_{L,R} &= F^{\rm (5a)}_{L,R} + F^{\rm (5b)}_{L,R}\,,\\
F^{\rm MIA(6)\ (Y^2)}_{L,R} &= F^{\rm (6a)}_{L,R} + F^{\rm (6b)}_{L,R} + F^{\rm (6c)}_{L,R} + F^{\rm (6d)}_{L,R}\,,
\end{aligned}$$

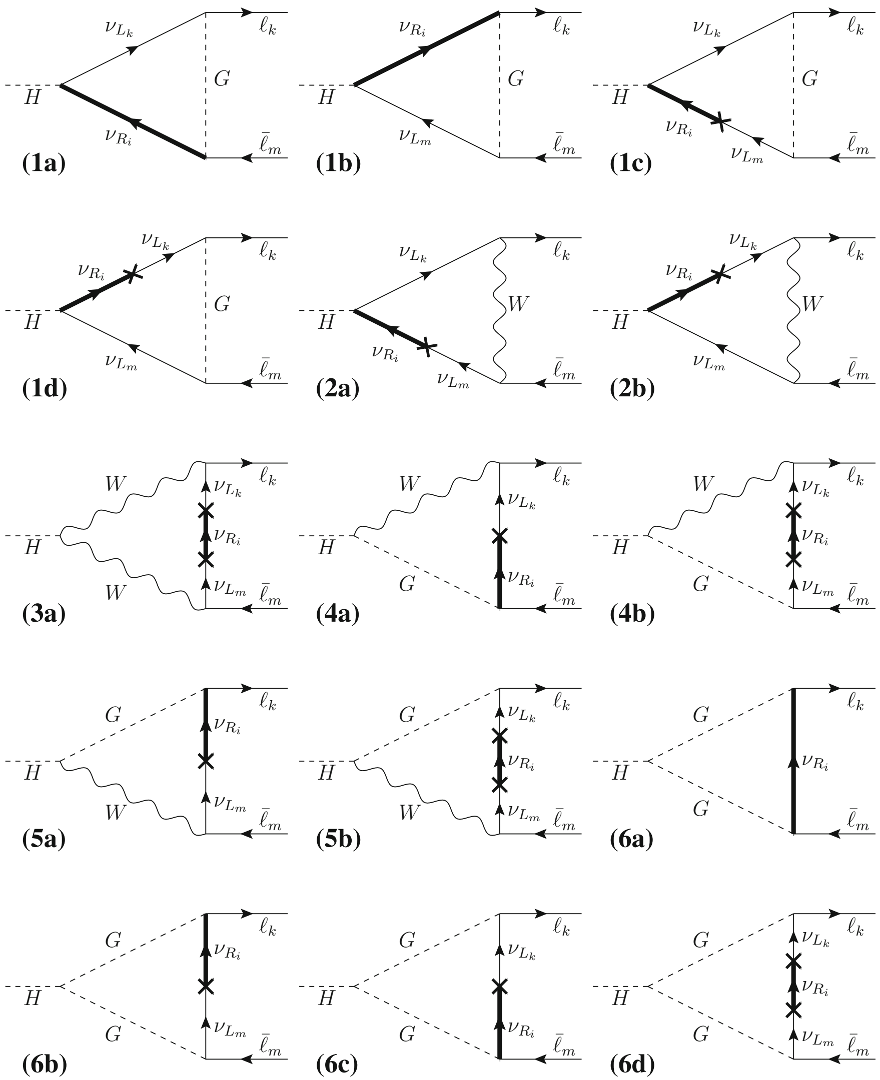

Fig. 4.18 Relevant vertex diagrams for the MIA form factors of LFVHD to $\mathcal{O}(Y_\nu^2)$

$$
\begin{aligned}
F_{L,R}^{\mathrm{MIA(7)\ (Y^2)}} &= F_{L,R}^{(7a)}\,, \\
F_{L,R}^{\mathrm{MIA(8)\ (Y^2)}} &= F_{L,R}^{(8a)} + F_{L,R}^{(8b)} + F_{L,R}^{(8c)} + F_{L,R}^{(8d)}\,, \\
F_{L,R}^{\mathrm{MIA(9)\ (Y^2)}} &= F_{L,R}^{(9a)}\,, \\
F_{L,R}^{\mathrm{MIA(10)\ (Y^2)}} &= F_{L,R}^{(10a)} + F_{L,R}^{(10b)} + F_{L,R}^{(10c)} + F_{L,R}^{(10d)}\,.
\end{aligned}
\tag{4.28}
$$

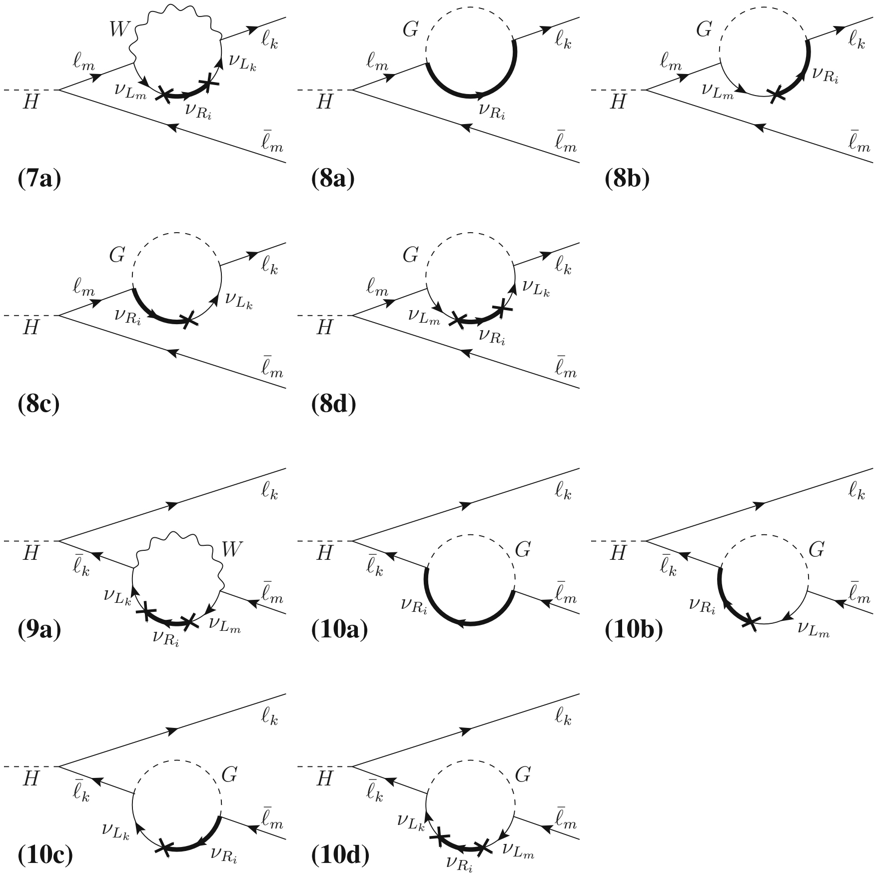

Fig. 4.19 Relevant external leg diagrams for the MIA form factors of LFVHD to $\mathcal{O}(Y_\nu^2)$

The explicit analytical results for all these form factors are given in Eqs. (E.8) and (E.10) of the Appendix E.2. These results are expressed in terms of the usual one-loop Veltman-Passarino functions [71] of two points (B_0 and B_1), three points (C_0, C_{11}, C_{12} and $\tilde{C}_0$) and four points (D_{12}, D_{13} and $\tilde{D}_0$), whose definitions are given in Eqs. (E.5)–(E.7).

At NLO, i.e. $\mathcal{O}(Y_\nu^4)$, each $F_{L,R}^{\mathrm{MIA(i)}}$ receives contributions from all diagrams containing 2 right-handed neutrino propagators and one of these three combinations: (i) 2 vertices with ν_R and 2 m_D insertions, (ii) 3 vertices with ν_R and 1 m_D insertion, (iii) 1 vertex with ν_R and 3 m_D insertions. Other possible combinations will provide subleading corrections in the heavy M_R case of our interest, since they will come with extra powers of M_R in the denominator. Thus, we find that the most relevant diagrams are those of type (1), (8) and (10) summarized in Figs. 4.20 and 4.21, whose respective contributions are given by:

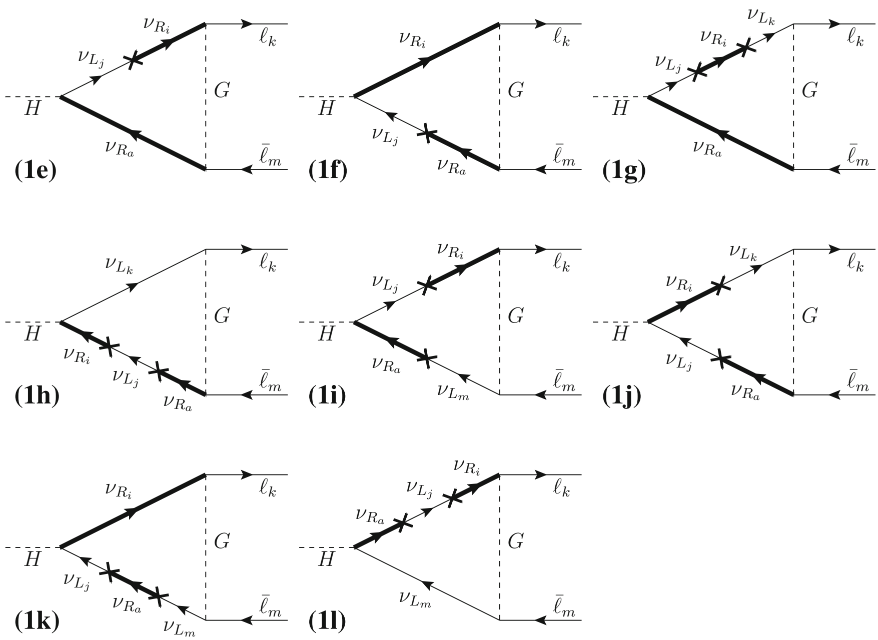

Fig. 4.20 Relevant vertex diagrams for the MIA form factors of LFVHD to $\mathcal{O}(Y_\nu^4)$

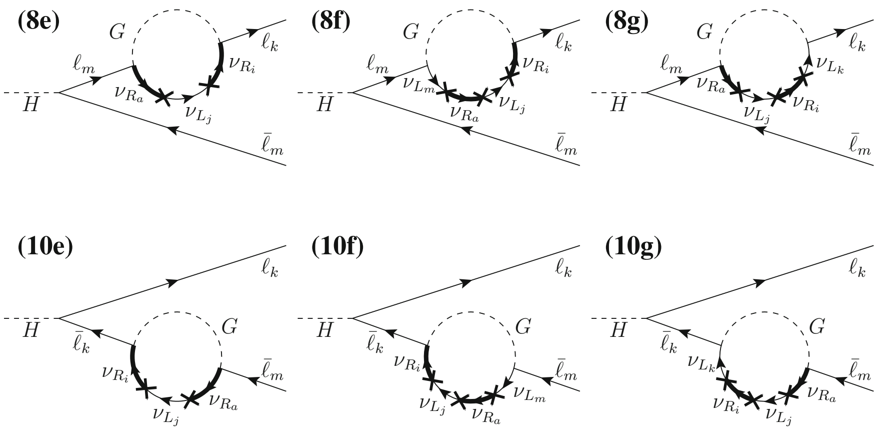

Fig. 4.21 Relevant external leg diagrams for the MIA form factors of LFVHD to $\mathcal{O}(Y_\nu^4)$

$$
\begin{aligned}
F_{L,R}^{\mathrm{MIA}(1)\ (\mathrm{Y}^4)} &= F_{L,R}^{(1e)} + F_{L,R}^{(1f)} + F_{L,R}^{(1g)} + F_{L,R}^{(1h)} + F_{L,R}^{(1i)} + F_{L,R}^{(1j)} + F_{L,R}^{(1k)} + F_{L,R}^{(1\ell)}\,,\\
F_{L,R}^{\mathrm{MIA}(8)\ (\mathrm{Y}^4)} &= F_{L,R}^{(8e)} + F_{L,R}^{(8f)} + F_{L,R}^{(8g)}\,,\\
F_{L,R}^{\mathrm{MIA}(10)\ (\mathrm{Y}^4)} &= F_{L,R}^{(10e)} + F_{L,R}^{(10f)} + F_{L,R}^{(10g)}\,.
\end{aligned}
\tag{4.29}
$$

Their explicit analytical results are collected in Eqs. (E.96) and (E.11) of the Appendix E.2.

Some comments about the analytical properties of the previous MIA results are in order. First, we analyze their ultraviolet behavior. From the results presented in Sect. 4.1, we know that in the full one-loop computation of the mass basis, only the contributions to the amplitude from diagrams (1), (8) and (10) of Fig. 4.1 are ultraviolet divergent separately, and that the total sum from these diagrams (1)+(8)+(10) is finite, therefore providing a total one-loop amplitude that is ultraviolet finite as it must be. We have explored the divergences of the MIA diagrams and found the same results. Our calculation in the MIA also shows that diagrams of type (2), (3), (4), (5), (6), (7) and (9) are convergent separately, while each contribution of $\mathcal{O}(Y_\nu^2)$ from diagrams (1), (8) and (10) is divergent, although their divergences cancel out again in their sum. For this reason, we will show (1)+(8)+(10) whenever we present results for each diagram in the next numerical analysis, which is convergent and therefore meaningful, instead of the contributions from each of these diagrams separately.

Second, it is also worth to comment on the gauge invariance of our previous MIA results for the decay amplitude, computed in the Feynman-'t Hooft gauge. In order to prove the gauge invariance of our results, we have computed the amplitude also in other gauges and checked that we get the same result. Specifically, we have computed the form factors $F_{L,R}$ in the Unitary gauge and in an arbitrary R_ξ gauge. The details of the Unitary gauge computation are collected in Appendix E.4.

Next, we show our numerical results of these LO results in the MIA, together with the outcome from the full computation in the physical basis. We display our results only for scenarios TM-4 and TM-5 in Table 3.4, although we have found similar conclusions for other scenarios and input values of Y_ν.

We first display in Fig. 4.22 the partial decay width of the full calculation together with our predictions from the MIA to $\mathcal{O}(Y_\nu^2)$, separating the contributions from the various diagrams. We observe here that the contribution from each diagram (or group of diagrams in the case of (1)+(8)+(10)) to the form factor, and in consequence to the width, decreases with M_R. This behavior will be very well understood in Sect. 4.3.3 with our simple formulas of the large M_R expansions in Eq. (E.14). In particular, when adding the three contributions (1)+(8)+(10) in the MIA we will see explicitly the cancellation of the divergent contributions from Δ terms and the corresponding cancellation of the regularization μ scale dependent terms. The final behavior of the remaining finite terms in each form factor will go generically as $\sim (v^2/M_R^2)$, and in addition there will also be logarithmic terms going as $\sim (v^2/M_R^2)(\mathrm{Log}(v^2/M_R^2))$.

We see in Fig. 4.22 a consistent agreement between the MIA and full results for diagrams (2), (3), (4), (5), (6), (7) and (9). For the sum (1)+(8)+(10), the MIA reproduces the behavior of the full calculation very well but there is a mismatch in

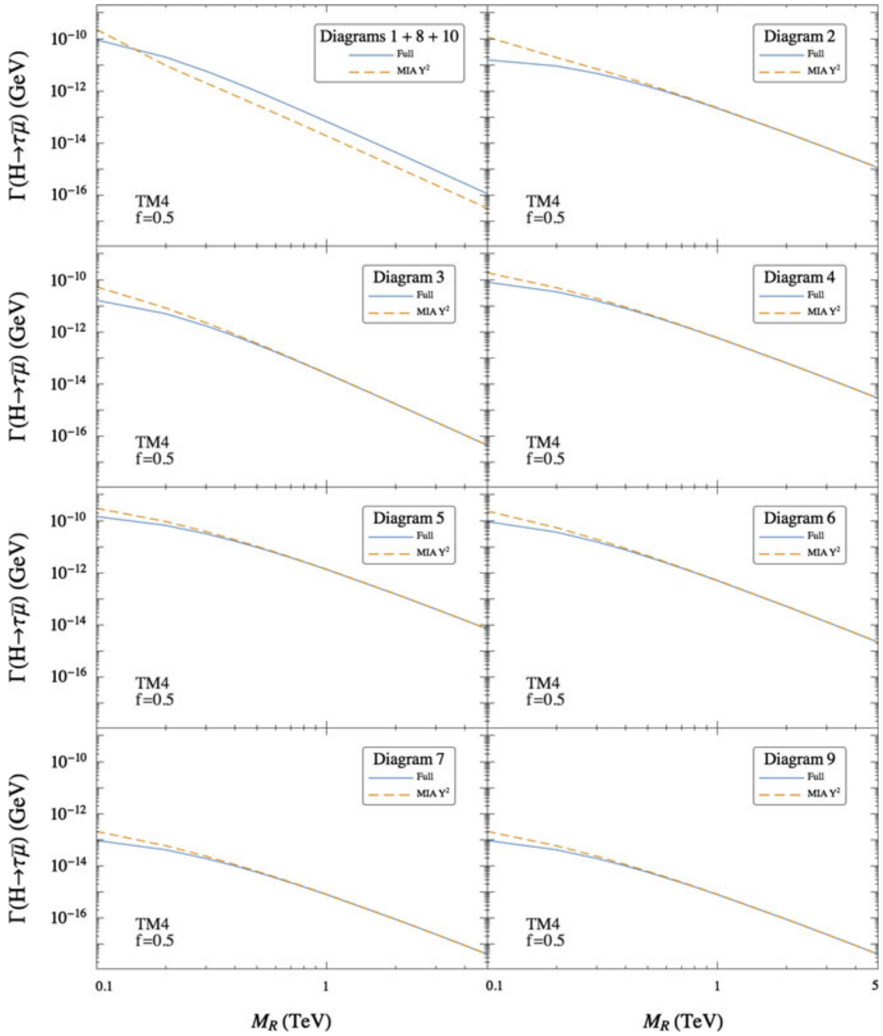

Fig. 4.22 Contributions from the various diagrams to $\Gamma(H \to \tau\bar{\mu})$ as a function of M_R in the TM-4 scenario from Table 3.4 for $f = 0.5$. Dashed lines are the predictions from the MIA to $\mathcal{O}(Y_\nu^2)$, while solid lines are from the full one loop computation in the mass basis

the partial decay width, which depends on the value of f. The larger f, the worse the discrepancy between them. This disagreement is then translated to the total partial width, as can be seen in Fig. 4.23. In order to give a quantitative statement on this observation, we define the ratio $R = \Gamma_{\text{MIA}}/\Gamma_{\text{full}}$. From the bottom of Fig. 4.23, we have R close to 1 for low values of f ($f = 0.1$) and large M_R above 1 TeV. If we increase f up to 1, poor values of R far from 1 are obtained in the whole studied M_R interval, so the MIA results to $\mathcal{O}(Y_\nu^2)$ do not reproduce satisfactorily the results of

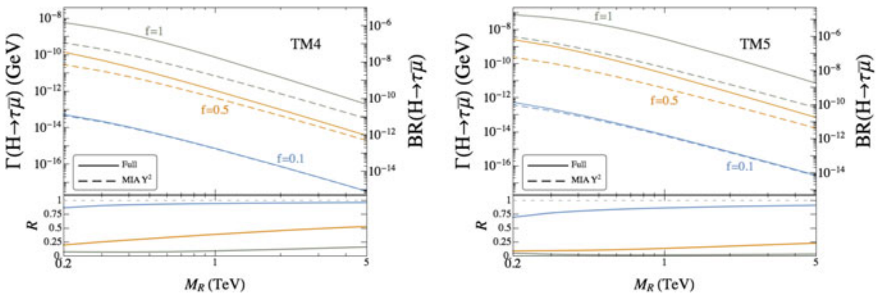

Fig. 4.23 Predictions for the partial width $\Gamma(H \to \tau\bar{\mu})$ and branching ratio $\mathrm{BR}(H \to \tau\bar{\mu})$ as a function of M_R. The dashed lines are the predictions from the MIA to $\mathcal{O}(Y_\nu^2)$. The solid lines are the predictions from the full one-loop computation in the mass basis. Here the scenarios TM4 (left panel) and TM5 (right panel) from Table 3.4 are chosen with f = 0.1, 0.5, 1. In the bottom of these plots the ratio $R = \Gamma_{\mathrm{MIA}}/\Gamma_{\mathrm{full}}$ is also shown

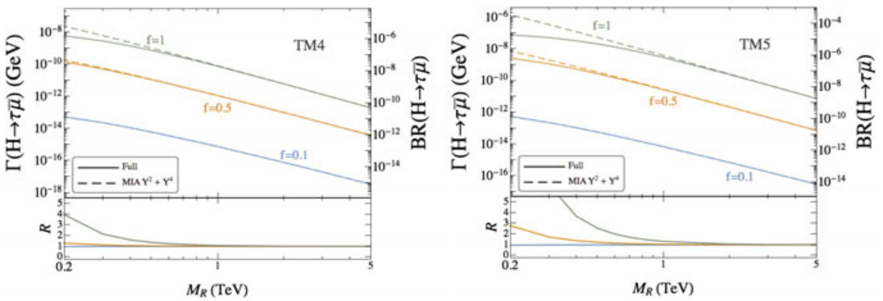

Fig. 4.24 Predictions for the partial width $\Gamma(H \to \tau\bar{\mu})$ and branching ratio $\mathrm{BR}(H \to \tau\bar{\mu})$ as a function of M_R. The dashed lines are the predictions from the MIA to $\mathcal{O}(Y_\nu^2 + Y_\nu^4)$. The solid lines are the predictions from the full one-loop computation in the mass basis. Here the scenarios TM4 (left panel) and TM5 (right panel) from Table 3.4 are chosen with f = 0.1, 0.5, 1. In the bottom of these plots the ratio $R = \Gamma_{\mathrm{MIA}}/\Gamma_{\mathrm{full}}$ is also shown

the full calculation. We conclude that for large values of f, which are the interesting ones from a phenomenological point of view, the MIA only reproduces the functional behavior with M_R but not the numerical values. Thus, it is necessary to include in the MIA computation the next order contributions, i.e., $\mathcal{O}(Y_\nu^4)$.

The results after including all the relevant $\mathcal{O}(Y_\nu^2 + Y_\nu^4)$ contributions are shown in Fig. 4.24. We can clearly see that the sum of the MIA diagrams is in very good agreement with the full results for different values of f. Therefore, we can conclude that our MIA calculation with the inclusion of the most relevant $\mathcal{O}(Y_\nu^4)$ terms, corrects the $\mathcal{O}(Y_\nu^2)$ contributions and achieves a better fit to the full numerical results for this process in the large $M_R \gg vY_\nu$ mass range. In particular, we see this improvement with respect to $\mathcal{O}(Y_\nu^2)$ contributions from the closeness of R to 1 for different values of f. How large M_R should be in order to get a good numerical prediction of the LFVHD rates depends obviously on the size of the Yukawa coupling. For small

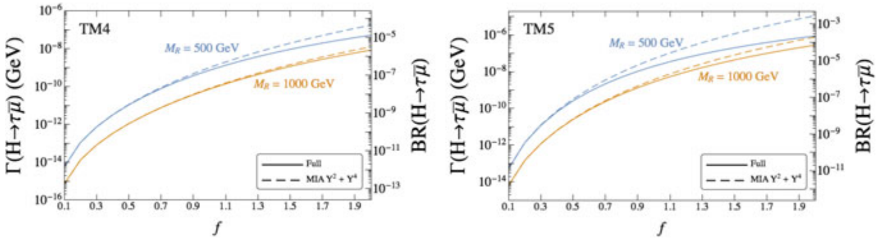

Fig. 4.25 Predictions for the partial width $\Gamma(H \to \tau\bar{\mu})$ and branching ratio $\mathrm{BR}(H \to \tau\bar{\mu})$ as a function of the global Yukawa coupling strength f. The dashed lines are the predictions from the MIA to $\mathcal{O}(Y_\nu^2 + Y_\nu^4)$. The solid lines are the predictions from the full one-loop computation in the mass basis. Here the scenarios TM4 (left panel) and TM5 (right panel) from Table 3.4 are chosen with $M_R = 500, 1000$ GeV

Yukawa coupling, i.e., for small $f \lesssim 0.5$ the MIA works quite well for M_R above 400 GeV, whereas for larger couplings, say f above 0.5, the MIA also provides a good result but requires heavier M_R, above 1000 GeV.

Before going to the derivation of the effective vertex in the large M_R limit, we concentrate on the dependence of the branching ratios with f. In Fig. 4.25, we show the partial width and branching ratio as a function of f for the scenarios TM4 and TM5 with two different values of M_R. In the perturbativity range of Yukawa couplings (implying approximately $f \lesssim 3.5$) we find a significant increase in the branching ratios up to $\mathcal{O}(10^{-4})$ for large $f \sim \mathcal{O}(2)$. However, for such large f values the MIA provides an accurate prediction only for large M_R values, say above 1000 GeV, as can be seen in Fig. 4.25. Overall, we can conclude that the results for the MIA form factors to $\mathcal{O}(Y_\nu^2 + Y_\nu^4)$ work reasonably well for M_R heavy enough, say above 1 TeV, and f values not too large, such that Y_ν is within the perturbativity region, given by $Y_\nu^2/4\pi < 1$.

4.3.3 Computation of the One-Loop Effective Vertex for LFVHD

In this Section we present our results in the large M_R limit of the form factors involved in our computation of the LFVHD rates. In order to reach this simple expression for the effective vertex, valid in the large $M_R \gg v$ regime, we perform a systematic expansion in powers of (v/M_R) of the one-loop MIA amplitude that we have computed in the previous Section. Generically, the first order in this expansion is $\mathcal{O}(v^2/M_R^2)$, the next order is $\mathcal{O}(v^4/M_R^4)$, etc. There is also a logarithmic dependence with M_R, which is not expanded but left explicit in this calculation. In the final result for the effective vertex we will be interested just in the leading terms of $\mathcal{O}(v^2/M_R^2)$, which are by far the dominant ones for sufficiently heavy M_R.

We start with the formulas found in the previous Section and in Appendix E.2 for the one-loop LFVHD form factors in the MIA. Assuming the hierarchy $m_\ell \ll m_W, m_H \ll M_R$, we may first ignore the tiny contributions that come from terms in the sum with factors of the lepton masses in our analytical results of Eqs. (E.8)–(E.11). This leads to the following compact formula for the total one-loop MIA form factors to $\mathcal{O}(Y_\nu^2 + Y_\nu^4)$,

$$
\begin{aligned}
F_L^{\rm MIA} = &\frac{1}{32\pi^2}\frac{m_{\ell_k}}{m_W}\left(Y_\nu Y_\nu^\dagger\right)^{km}\Big(\tilde{C}_0(p_2,p_1,m_W,0,M_R) - B_0(0,M_R,m_W)\\
&- 2m_W^2\big((C_0+C_{11}-C_{12})(p_2,p_1,m_W,0,M_R) + (C_{11}-C_{12})(p_2,p_1,m_W,M_R,0)\big)\\
&+ 4m_W^4(D_{12}-D_{13})(0,p_2,p_1,0,M_R,m_W,m_W)\\
&- 2m_W^2 m_H^2 D_{13}(0,p_2,p_1,0,M_R,m_W,m_W) + 2m_W^2\big(C_0+C_{11}-C_{12}\big)(p_2,p_1,M_R,m_W,m_W)\\
&+ m_H^2\big(C_0+C_{11}-C_{12}\big)(p_2,p_1,M_R,m_W,m_W)\Big)\\
&+ \frac{1}{32\pi^2}\frac{m_{\ell_k}}{m_W}\left(Y_\nu Y_\nu^\dagger Y_\nu Y_\nu^\dagger\right)^{km} v^2\Big(-2(C_{11}-C_{12})(p_2,p_1,m_W,M_R,M_R)\\
&+ \tilde{D}_0(p_2,0,p_1,m_W,0,M_R,M_R) + \tilde{D}_0(p_2,p_1,0,m_W,0,M_R,M_R) - C_0(0,0,M_R,M_R,m_W)\Big).
\end{aligned}
\tag{4.30}
$$

Here, we have ordered the various contributions as follows: the first line is from diagrams (1)+(8)+(10), the second line from (2), the third line from (3), the fourth line from (4)+(5), the fifth line from (6) and the last two lines containing the $\mathcal{O}(Y_\nu^4)$ contribution are from (1)+(8)+(10). Notice that there are not final contributions from (7)+(9), since they cancel each other. Similarly, for the right-handed form factor we get:

$$
\begin{aligned}
F_R^{\rm MIA} = &\frac{1}{32\pi^2}\frac{m_{\ell_m}}{m_W}\left(Y_\nu Y_\nu^\dagger\right)^{km}\Big(\tilde{C}_0(p_2,p_1,m_W,M_R,0) - B_0(0,M_R,m_W)\\
&- 2m_W^2(C_{12}(p_2,p_1,m_W,0,M_R) + (C_0+C_{12})(p_2,p_1,m_W,M_R,0))\\
&+ 4m_W^4 D_{13}(0,p_2,p_1,0,M_R,m_W,m_W)\\
&- 2m_W^2 m_H^2(D_{12}-D_{13})(0,p_2,p_1,0,M_R,m_W,m_W) + 2m_W^2\big(C_0+C_{12}\big)(p_2,p_1,M_R,m_W,m_W)\\
&+ m_H^2\big(C_0+C_{12}\big)(p_2,p_1,M_R,m_W,m_W)\Big)\\
&+ \frac{1}{32\pi^2}\frac{m_{\ell_m}}{m_W}\left(Y_\nu Y_\nu^\dagger Y_\nu Y_\nu^\dagger\right)^{km} v^2\Big(-2C_{12}(p_2,p_1,m_W,M_R,M_R)\\
&+ \tilde{D}_0(p_2,p_1,0,m_W,M_R,M_R,0) + \tilde{D}_0(p_2,0,p_1,m_W,M_R,M_R,0) - C_0(0,0,M_R,M_R,m_W)\Big),
\end{aligned}
\tag{4.31}
$$

where the explanation for the various contributions in each line is as specified for F_L. Note also that the right-handed form factor can be obtained from the left-handed one by exchanging p_2 and m_{ℓ_k} with p_3 and m_{ℓ_m}, respectively. From the previous compact formulas, assuming the hierarchy $m_{\ell_k} \gg m_{\ell_m}$, it is also clear that the left-handed form factor is the dominant one for the decay mode $H \to \ell_k \bar{\ell}_m$. Conversely, the right-handed form factor will be the dominant one in the opposite case $m_{\ell_m} \gg m_{\ell_k}$. For the rest of this Section, we will assume $m_{\ell_k} \gg m_{\ell_m}$ and, therefore, we will focus on the dominant F_L.

The next step is to perform the large M_R expansion of the loop integrals appearing in the MIA form factor. The details of how we perform these expansions are explained in Appendix E.3, where we also collect the results for both the loop integrals and the separate contributions to the form factors from all type of diagrams, i=1…10. Finally, by plugging these large M_R expansions into Eq. (4.30) we get the one-loop effective vertex, $F_L \simeq V^{\rm eff}_{H\ell_k\ell_m}$, which parametrizes the one-loop amplitude of $H \to \ell_k\bar{\ell}_m$ as

$$i\mathcal{M} \simeq -ig\bar{u}_{\ell_k} V^{\rm eff}_{H\ell_k\ell_m} P_L v_{\ell_m}\,, \tag{4.32}$$

with the corresponding partial decay width:

$$\Gamma(H \to \ell_k\bar{\ell}_m) \simeq \frac{g^2}{16\pi} m_H \left|V^{\rm eff}_{H\ell_k\ell_m}\right|^2. \tag{4.33}$$

At the end, we find the following simple result for the on-shell Higgs boson effective LFV vertex:

$$V^{\rm eff}_{H\ell_k\ell_m} = \frac{1}{64\pi^2}\frac{m_{\ell_k}}{m_W}\left[\frac{m_H^2}{M_R^2}\left(r\left(\frac{m_W^2}{m_H^2}\right) + \log\left(\frac{m_W^2}{M_R^2}\right)\right)\left(Y_\nu Y_\nu^\dagger\right)^{km} - \frac{3v^2}{M_R^2}\left(Y_\nu Y_\nu^\dagger Y_\nu Y_\nu^\dagger\right)^{km}\right], \tag{4.34}$$

where,

$$r(\lambda) = -\frac{1}{2} - \lambda - 8\lambda^2 + 2(1-2\lambda+8\lambda^2)\sqrt{4\lambda-1}\arctan\left(\frac{1}{\sqrt{4\lambda-1}}\right) + 16\lambda^2(1-2\lambda)\arctan^2\left(\frac{1}{\sqrt{4\lambda-1}}\right). \tag{4.35}$$

Notice that this solution is valid for $m_H < 2m_W$ and that for the physical values of $m_H = 125$ GeV and $m_W = 80.4$ GeV we obtain numerically $r(m_W^2/m_H^2) \sim 0.31$. The partial width is then simplified correspondingly to:

$$\Gamma(H \to \ell_k\bar{\ell}_m)^{\rm MIA} = \frac{g^2 m_{\ell_k}^2 m_H}{2^{16}\pi^5 m_W^2}\left|\frac{m_H^2}{M_R^2}\left(r\left(\frac{m_W^2}{m_H^2}\right) + \log\left(\frac{m_W^2}{M_R^2}\right)\right)\left(Y_\nu Y_\nu^\dagger\right)^{km} - \frac{3v^2}{M_R^2}\left(Y_\nu Y_\nu^\dagger Y_\nu Y_\nu^\dagger\right)^{km}\right|^2. \tag{4.36}$$

Some comments are in order. First we notice that the dominant behavior with M_R of $V^{\rm eff}_{H\ell_k\ell_m}$ for large M_R goes as $\log(M_R^2)/M_R^2$ and the next dominant one goes as $1/M_R^2$. Second, the terms of $\mathcal{O}(Y_\nu^2)$ depend on m_H, whereas the terms of $\mathcal{O}(Y_\nu^4)$ do not. Notice also that the two contributions of $\mathcal{O}(Y_\nu^2)$ and $\mathcal{O}(Y_\nu^4)$ get M_R^2 in the denominator and not M_R^4 as one could naively expect for the $\mathcal{O}(Y_\nu^4)$ term. Third, we have also checked that we recover the simple phenomenological formula in Eq. (4.10), which we obtained by a naive numerical fit of the dominant contributions at large M_R from diagrams (1)+(8)+(10) in the physical mass basis. Specifically, if we extract the contributions exclusively from diagrams (1), (8) and (10) in our MIA results in Eq. (4.36), we get:

$$\text{BR}(H \to \ell_k \bar{\ell}_m)^{\text{MIA}}_{(1)+(8)+(10)} = \frac{g^2 m_{\ell_k}^2 m_H}{2^{16}\pi^5 m_W^2 \Gamma_H} \left| \frac{m_H^2}{M_R^2} \left(Y_\nu Y_\nu^\dagger\right)^{km} - \frac{3v^2}{M_R^2} \left(Y_\nu Y_\nu^\dagger Y_\nu Y_\nu^\dagger\right)^{km} \right|^2$$
$$\simeq 10^{-7} \frac{v^4}{M_R^4} \left| \left(Y_\nu Y_\nu^\dagger\right)^{km} - 5.7 \left(Y_\nu Y_\nu^\dagger Y_\nu Y_\nu^\dagger\right)^{km} \right|^2, \tag{4.37}$$

where in the last line we have used the numerical values of the physical parameters with $m_H = 125$ GeV and Γ_H given by the predicted value in the SM. As announced, we reach the previous result in Eq. (4.10).

It is also illustrative to compare our previous MIA result in Eq. (4.36) for the partial width in the large M_R regime with the analytical approximate formula in Ref. [52] which was found after expanding the full one-loop computation in the physical neutrino mass basis in inverse powers of the physical heavy neutrino mass m_N. Concretely we compare our result in Eq. (4.36) with those in Eqs. (26), (31)–(34) of Ref. [52], which were obtained assuming $m_H^2/m_W^2 \ll 4$ and $m_H^2/m_N^2 \ll 1$. By doing some algebra to express the physical neutrino couplings $B_{\ell_i n_j}$ and $C_{n_i n_j}$ appearing in those equations in terms of the Yukawa couplings, and by extracting just the m_H independent terms, we obtain complete agreement with our result in Eq. (4.36) in the $m_H \to 0$ limit. Specifically, by using

$$\sum_{i \in \text{Heavy}} B_{\ell_k n_i} B^*_{\ell_m n_i} \simeq \frac{v^2}{m_N^2} \left(Y_\nu Y_\nu^\dagger\right)^{km}, \tag{4.38}$$

$$\sum_{i,j \in \text{Heavy}} B_{\ell_k n_i} C_{n_i n_j} B^*_{\ell_m n_j} \simeq \frac{v^4}{m_N^4} \left(Y_\nu Y_\nu^\dagger Y_\nu Y_\nu^\dagger\right)^{km}, \tag{4.39}$$

and neglecting $\mathcal{O}(1/m_N^4)$ and higher order terms, we get from Ref. [52],

$$\Gamma(H \to \ell_k \bar{\ell}_m)^{\text{full}} = \frac{g^2 m_{\ell_k}^2 m_H}{2^{16}\pi^5 m_W^2} \left| -\frac{3m_W^2}{m_N^2} \left(Y_\nu Y_\nu^\dagger\right)^{km} - \frac{3v^2}{m_N^2} \left(Y_\nu Y_\nu^\dagger Y_\nu Y_\nu^\dagger\right)^{km} \right|^2, \tag{4.40}$$

which matches with our result in Eq. (4.36) after the substitution

$$(m_H^2/m_W^2) r(m_W^2/m_H^2) \to -3, \tag{4.41}$$

corresponding to the limit $m_H \to 0$. In this sense, although a complete comparison is out of the scope of this work, we conclude that our MIA effective vertex and the effective vertex of the mass basis in Ref. [52] agree analytically in the limit $m_H \to 0$. Nevertheless, we have checked by a numerical estimate of the LFVHD widths that the approximation of neglecting the Higgs boson mass in the effective vertex does not provide in general an accurate result and, therefore, in order to obtain a realistic estimate of these branching ratios, our final formula for the effective vertex in Eq. (4.34) should be used, which is specific for on-shell Higgs decays and accounts properly for the Higgs boson mass effects.

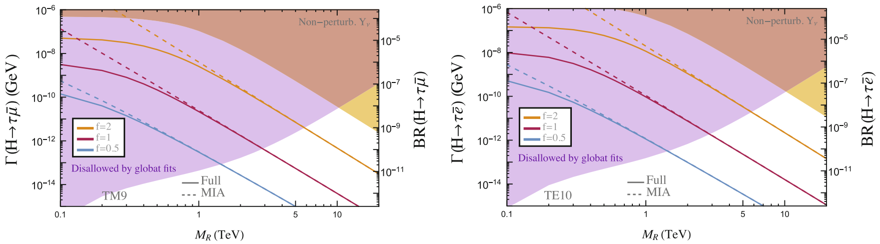

Fig. 4.26 Left panel: Predictions for $H \to \tau\bar{\mu}$ with the effective vertex computed with the MIA (dashed lines) for $Y_\nu^{\rm TM9}$. Right panel: Predictions for $H \to \tau\bar{e}$ with the effective vertex computed with the MIA (dashed lines) for $Y_\nu^{\rm TE10}$. The chosen examples TM9 and TE10 are explained in the text. Solid lines are the corresponding predictions from the full one-loop computation in the mass basis. Shadowed areas to the left part of these plots (in purple) are disallowed by global fits. Shadowed areas to the right part of these plots (in yellow) give a non-perturbative Yukawa coupling

Finally, we wish to illustrate numerically the accuracy of our simple results of the effective vertex and the partial width in Eqs. (4.34) and (4.36), respectively. For that purpose, we compare again our numerical predictions from these simple formulas with the predictions from the full one-loop results of the mass basis in Fig. 4.26. Here, we display the results for the most interesting channels, $H \to \tau\bar{\mu}$ and $H \to \tau\bar{e}$, and for two scenarios, $Y_\nu^{\rm TM9}$ and $Y_\nu^{\rm TE10}$ in Table 3.4. Nonetheless, we have checked that the effective vertex in Eq. (4.34) also works for other choices of scenarios.

The plots in Fig. 4.26 show the predictions of both the LFVHD partial widths and branching ratios, as functions of M_R and three different values of $f = 2, 1, 0.5$, with the colored areas being disallowed by global fit constraints (purple) or by non-perturbative Yukawa couplings (yellow). Concretely, we have imposed the constraints on all the entries of the η matrix (see Eq. 4.42) that we have taken from the global analysis in Ref. [72] at the three sigma level. For the perturbativity bound, we impose the condition $|Y_\nu^{ij}|^2/(4\pi) < 1$ for every entry of the Y_ν coupling matrix. The areas in white are in consequence the regions that are allowed by the global fits and by perturbativity.

From these plots we learn that the agreement between the full prediction and the MIA result obtained from the effective vertices computed in this Section is quite good for values of M_R above 1 TeV and for all the explored Yukawa coupling examples. In fact, the MIA works extremely well for the whole region of interest where both the global fits constraints and the perturbativity of the Yukawa coupling are respected. Consequently, we conclude that the simple expression for the effective vertex in Eq. (4.34) is quite accurate and provides a good approximation for the partial width in Eq. (4.36), in agreement with the full LFVHD rates. Therefore, it is a very useful formula for making fast numerical estimations of these rates in terms of the relevant model parameters Y_ν and M_R.

4.4 Maximum Allowed BR($H \to \ell_k \bar{\ell}_m$)

We conclude this Chapter by combining everything we have learnt about LFV H decays and by trying to conclude on the maximum rates allowed by a more complete set of present constraints, including both LFV and lepton flavor preserving observables. For this purpose, we consider the constraints obtained by the global fit analysis done in Ref. [72], where upper bounds on the η matrix were derived. More concretely, these constraints define a maximum allowed by data η matrix given by:

$$\eta_{3\sigma}^{\max} = \begin{pmatrix} 1.62 \times 10^{-3} & 1.51 \times 10^{-5} & 1.57 \times 10^{-3} \\ 1.51 \times 10^{-5} & 3.92 \times 10^{-4} & 9.24 \times 10^{-4} \\ 1.57 \times 10^{-3} & 9.24 \times 10^{-4} & 3.67 \times 10^{-3} \end{pmatrix}, \tag{4.42}$$

We can easily apply these bounds by means of the μ_X parametrization introduced in Eq. (2.46). As we said, this parametrization allows us to choose the Y_ν and M_R matrices as input parameters of the model. In our situation of degenerate M_R matrix, the η matrix is related to the Yukawa matrix approximately by,

$$\eta = \frac{v^2}{2M_R^2}\, Y_\nu Y_\nu^\dagger\, . \tag{4.43}$$

Therefore, we can combine Eq. (4.42) and (4.43) in order to find a Yukawa matrix that saturates the $\eta_{3\sigma}^{\max}$ bounds. Then, the Eq. (2.46) will ensure the agreement with oscillation data by building the proper μ_X matrix.

A possible solution to this problem is given by our choice:

$$Y_\nu^{\mathrm{GF}} = f \begin{pmatrix} 0.33 & 0.83 & 0.6 \\ -0.5 & 0.13 & 0.1 \\ -0.87 & 1 & 1 \end{pmatrix}, \tag{4.44}$$

which saturates the $\eta_{3\sigma}^{\max}$ bounds in a parameter space line given by the ratio $f/M_R = (3/10)\,\mathrm{TeV}^{-1}$, i.e., for $(f, M_R) = (3, 10\,\mathrm{TeV})$, $(1, 3.3\,\mathrm{TeV})$, $(0.3, 1\,\mathrm{TeV})$, ..., etc. The Yukawa coupling matrix in Eq. (4.44) defines our last scenario, that we refer to as GF.

We show the numerical results in Fig. 4.27 for the most promising channels $H \to \tau\bar{\mu}$ and $H \to \tau\bar{e}$ in the GF scenario. We also computed the $H \to \mu\bar{e}$ channel, but we do not show the results for this case here, since the rates are extremely small due to strong bounds on $\eta_{\mu e}$. As before, the purple area covers the parameter space region where the η matrix is above the 3σ bound in Eq. (4.42), at least in one entry. The yellow area represents violation of the perturbativity bound

$$\frac{|Y_{ij}|^2}{4\pi} < 1\,, \quad \text{for } i, j = 1, 2, 3\,. \tag{4.45}$$

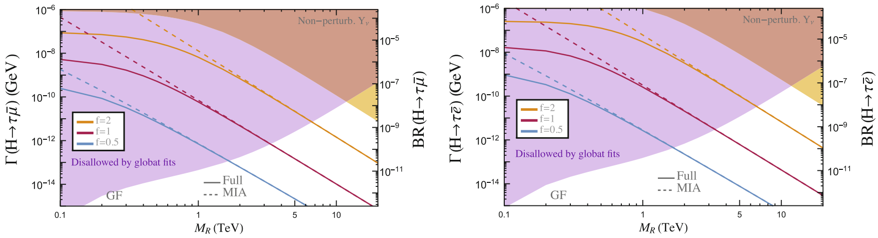

Fig. 4.27 Predictions for $H \to \tau\bar{\mu}$ (left panel) and $H \to \tau\bar{e}$ (right panel) with the effective vertex computed with the MIA (dashed lines) for $Y_\nu^{\rm GF}$. The chosen example GF is explained in the text. Solid lines are the corresponding predictions from the full one-loop computation in the mass basis. Shadowed areas to the left part of these plots (in purple) are disallowed by global fits. Shadowed areas to the right part of these plots (in yellow) give a non-perturbative Yukawa coupling

Our predictions are done with both full expressions in the mass basis, derived in Sect. 4.1, and the effective vertex obtained in Sect. 4.3. We see again that the agreement of the simple formula in Eq. (4.34) is excellent in all the region allowed by both the global fit and the perturbativity constrains. Finally, we can conclude on the maximum LFVHD rates allowed by the complete set of present constraints as extracted from the approach of a global fit analysis. From Fig. 4.27 we learn that the maximum allowed branching ratios values are, respectively:

$$\mathrm{BR}(H \to \tau\bar{\mu})_{\rm max} \sim 10^{-8}\,, \tag{4.46}$$

$$\mathrm{BR}(H \to \tau\bar{e})_{\rm max} \sim 10^{-7}\,. \tag{4.47}$$

Finally, we shortly summarize our findings in this Chapter, where we have explored in full detail the LFV H decays induced from right-handed neutrinos from the ISS model. We found that, having these neutrinos TeV scale masses and large Yukawa couplings at the same time, the LFVHD rates are manifestly enhanced with respect to the standard type-I seesaw, where rates of $\mathcal{O}(10^{-30})$ were obtained [54]. After applying present bounds from a global fit analysis, we found maximum allowed rates of 10^{-7} and 10^{-8} for $H \to \tau\bar{e}$ and $H \to \tau\bar{\mu}$, respectively, which unfortunately are far from present LHC experimental sensitivities. However, in our aim of fully understanding the predictions for this observable, we have derived a one-loop effective vertex for the LFV interaction of our interest here, namely, the interaction of a Higgs boson with two leptons of different flavor $H\ell_k\ell_m$ with $k \neq m$. With such a simple expression for the involved effective vertex, one may perform a fast estimate of the LFV Higgs decay rates for many different input parameter values, mainly for Y_ν and M_R, without the need of a diagonalization process to reach the physical neutrino basis, and thus avoiding the full computation of the one-loop diagrams in this basis, which is by far more computer time consuming. Moreover, the explicit dependence on the relevant parameters Y_ν and M_R facilitates the interpretation of the numerical results. We find this simple formula useful also for other models that share the desired basic properties with the ISS model, since they can be easily used by other authors to obtain a fast estimate of the LFVHD rates, which are ready for an easy test with experimental data.

We have also explored these rates in the SUSY-ISS model, finding that new loops involving SUSY particles, sleptons and sneutrinos, could enhance the predictions for the allowed LFVHD rates close to the present or near future experimental sensitivities.

References

1. G. Aad et al. (ATLAS), Eur. Phys. J. **C77**, 70 (2017). https://doi.org/10.1140/epjc/s10052-017-4624-0, arXiv:1604.07730 [hep-ex]
2. V. Khachatryan et al. (CMS), Phys. Lett. **B763**, 472 (2016). https://doi.org/10.1016/j.physletb.2016.09.062, arXiv:1607.03561 [hep-ex]
3. CMS Collaboration, Search for lepton flavour violating decays of the Higgs boson to $\mu\tau$ and $e\tau$ in proton-proton collisions at $\sqrt{s} = 13$ TeV (2017), CMS-PAS-HIG-17-001
4. R. Harnik, J. Kopp, J. Zupan, JHEP **03**, 026 (2013). https://doi.org/10.1007/JHEP03(2013)026, arXiv:1209.1397 [hep-ph]
5. G. Blankenburg, J. Ellis, G. Isidori, Phys. Lett. **B712**, 386 (2012). https://doi.org/10.1016/j.physletb.2012.05.007, arXiv:1202.5704 [hep-ph]
6. T. Han, D. Marfatia, Phys. Rev. Lett. **86**, 1442 (2001). https://doi.org/10.1103/PhysRevLett.86.1442, arXiv:hep-ph/0008141 [hep-ph]
7. A.M. Curiel, M.J. Herrero, D. Temes, Phys. Rev. **D67**, 075008 (2003). https://doi.org/10.1103/PhysRevD.67.075008, arXiv:hep-ph/0210335 [hep-ph]
8. J.L. Diaz-Cruz, JHEP **05**, 036 (2003). https://doi.org/10.1088/1126-6708/2003/05/036, arXiv:hep-ph/0207030 [hep-ph]
9. A.M. Curiel, M.J. Herrero, W. Hollik, F. Merz, S. Penaranda, Phys. Rev. **D69**, 075009 (2004). https://doi.org/10.1103/PhysRevD.69.075009, arXiv:hep-ph/0312135 [hep-ph]
10. A. Brignole, A. Rossi, Phys. Lett. **B566**, 217 (2003). https://doi.org/10.1016/S0370-2693(03)00837-2, arXiv:hep-ph/0304081 [hep-ph]
11. A. Brignole, A. Rossi, Nucl. Phys. **B701**, 3 (2004). https://doi.org/10.1016/j.nuclphysb.2004.08.037, arXiv:hep-ph/0404211 [hep-ph]
12. J.K. Parry, Nucl. Phys. **B760**, 38 (2007). https://doi.org/10.1016/j.nuclphysb.2006.10.011, arXiv:hep-ph/0510305 [hep-ph]
13. J.L. Diaz-Cruz, D.K. Ghosh, S. Moretti, Phys. Lett. **B679**, 376 (2009). https://doi.org/10.1016/j.physletb.2009.07.065, arXiv:0809.5158 [hep-ph]
14. A. Crivellin, Phys. Rev. **D83**, 056001 (2011). https://doi.org/10.1103/PhysRevD.83.056001, arXiv:1012.4840 [hep-ph]
15. P.T. Giang, L.T. Hue, D.T. Huong, H.N. Long, Nucl. Phys. **B864**, 85 (2012). https://doi.org/10.1016/j.nuclphysb.2012.06.008, arXiv:1204.2902 [hep-ph]
16. A. Arhrib, Y. Cheng, O.C.W. Kong, Europhys. Lett. **101**, 31003 (2013a). https://doi.org/10.1209/0295-5075/101/31003, arXiv:1208.4669 [hep-ph]
17. A. Arhrib, Y. Cheng, O.C.W. Kong, Phys. Rev. **D87**, 015025 (2013b). https://doi.org/10.1103/PhysRevD.87.015025, arXiv:1210.8241 [hep-ph]
18. M. Arana-Catania, E. Arganda, M.J. Herrero, JHEP **09**, 160 (2013), [Erratum: JHEP10,192(2015)]. https://doi.org/10.1007/JHEP10(2015)192, https://doi.org/10.1007/JHEP09(2013)160, arXiv:1304.3371 [hep-ph]
19. E. Arganda, M.J. Herrero, R. Morales, A. Szynkman, JHEP **03**, 055 (2016a). https://doi.org/10.1007/JHEP03(2016)055, arXiv:1510.04685 [hep-ph]
20. D. Aloni, Y. Nir, E. Stamou, JHEP **04**, 162 (2016). https://doi.org/10.1007/JHEP04(2016)162, arXiv:1511.00979 [hep-ph]

21. A. Vicente, Adv. High Energy Phys. **2015**, 686572 (2015). https://doi.org/10.1155/2015/686572, arXiv:1503.08622 [hep-ph]
22. C. Alvarado, R.M. Capdevilla, A. Delgado, A. Martin, Phys. Rev. **D94**, 075010 (2016). https://doi.org/10.1103/PhysRevD.94.075010, arXiv:1602.08506 [hep-ph]
23. A. Hammad, S. Khalil, C.S. Un, Phys. Rev. **D95**, 055028 (2017). https://doi.org/10.1103/PhysRevD.95.055028, arXiv:1605.07567 [hep-ph]
24. K. Agashe, R. Contino, Phys. Rev. **D80**, 075016 (2009). https://doi.org/10.1103/PhysRevD.80.075016, arXiv:0906.1542 [hep-ph]
25. S. Davidson, G.J. Grenier, Phys. Rev. **D81**, 095016 (2010). https://doi.org/10.1103/PhysRevD.81.095016, arXiv:1001.0434 [hep-ph]
26. D. Aristizabal Sierra, A. Vicente, Phys. Rev. **D90**, 115004 (2014). https://doi.org/10.1103/PhysRevD.90.115004, arXiv:1409.7690 [hep-ph]
27. Y. Omura, E. Senaha, K. Tobe, JHEP **05**, 028 (2015). https://doi.org/10.1007/JHEP05(2015)028, arXiv:1502.07824 [hep-ph]
28. N. Bizot, S. Davidson, M. Frigerio, J.L. Kneur, JHEP **03**, 073 (2016). https://doi.org/10.1007/JHEP03(2016)073, arXiv:1512.08508 [hep-ph]
29. F.J. Botella, G.C. Branco, M. Nebot, M.N. Rebelo, Eur. Phys. J. **C76**, 161 (2016). https://doi.org/10.1140/epjc/s10052-016-3993-0, arXiv:1508.05101 [hep-ph]
30. J. Herrero-García, T. Ohlsson, S. Riad, J. Wirén, JHEP **04**, 130 (2017). https://doi.org/10.1007/JHEP04(2017)130, arXiv:1701.05345 [hep-ph]
31. A. Dery, A. Efrati, G. Hiller, Y. Hochberg, Y. Nir, JHEP **08**, 006 (2013a). https://doi.org/10.1007/JHEP08(2013)006, arXiv:1304.6727 [hep-ph]
32. A. Dery, A. Efrati, Y. Nir, Y. Soreq, V. Susič, Phys. Rev. **D90**, 115022 (2014). https://doi.org/10.1103/PhysRevD.90.115022, arXiv:1408.1371 [hep-ph]
33. X.-G. He, J. Tandean, Y.-J. Zheng, JHEP **09**, 093 (2015). https://doi.org/10.1007/JHEP09(2015)093, arXiv:1507.02673 [hep-ph]
34. S. Baek, J. Tandean, Eur. Phys. J. **C76**, 673 (2016). https://doi.org/10.1140/epjc/s10052-016-4486-x, arXiv:1604.08935 [hep-ph]
35. G. Perez, L. Randall, JHEP **01**, 077 (2009). https://doi.org/10.1088/1126-6708/2009/01/077, arXiv:0805.4652 [hep-ph]
36. A. Azatov, M. Toharia, L. Zhu, Phys. Rev. **D80**, 035016 (2009). https://doi.org/10.1103/PhysRevD.80.035016, arXiv:0906.1990 [hep-ph]
37. J.L. Diaz-Cruz, J.J. Toscano, Phys. Rev. **D62**, 116005 (2000). https://doi.org/10.1103/PhysRevD.62.116005, arXiv:hep-ph/9910233 [hep-ph]
38. L. de Lima, C.S. Machado, R.D. Matheus, L.A.F. do Prado, JHEP **11**, 074 (2015). https://doi.org/10.1007/JHEP11(2015)074, arXiv:1501.06923 [hep-ph]
39. M. Buschmann, J. Kopp, J. Liu, X.-P. Wang, JHEP **06**, 149 (2016). https://doi.org/10.1007/JHEP06(2016)149, arXiv:1601.02616 [hep-ph]
40. J. Herrero-Garcia, N. Rius, A. Santamaria, JHEP **11**, 084 (2016). https://doi.org/10.1007/JHEP11(2016)084, arXiv:1605.06091 [hep-ph]
41. A. Falkowski, D.M. Straub, A. Vicente, JHEP **05**, 092 (2014). https://doi.org/10.1007/JHEP05(2014)092, arXiv:1312.5329 [hep-ph]
42. A. Dery, A. Efrati, Y. Hochberg, Y. Nir, JHEP **05**, 039 (2013b). https://doi.org/10.1007/JHEP05(2013)039, arXiv:1302.3229 [hep-ph]
43. J. Heeck, M. Holthausen, W. Rodejohann, Y. Shimizu, Nucl. Phys. **B896**, 281 (2015). https://doi.org/10.1016/j.nuclphysb.2015.04.025, arXiv:1412.3671 [hep-ph]
44. M.D. Campos, A.E. Cárcamo Hernández, H. Päs, E. Schumacher, Phys. Rev. **D91**, 116011 (2015). https://doi.org/10.1103/PhysRevD.91.116011, arXiv:1408.1652 [hep-ph]
45. I. Doršner, S. Fajfer, A. Greljo, J.F. Kamenik, N. Košnik, I. Nišandžic, JHEP **06**, 108 (2015). https://doi.org/10.1007/JHEP06(2015)108, arXiv:1502.07784 [hep-ph]
46. A. Crivellin, G. D'Ambrosio, J. Heeck, Phys. Rev. Lett. **114**, 151801 (2015). https://doi.org/10.1103/PhysRevLett.114.151801, arXiv:1501.00993 [hep-ph]
47. A.E. Cárcamo Hernández, I. de Medeiros Varzielas, E. Schumacher, Phys. Rev. **D93**, 016003 (2016). https://doi.org/10.1103/PhysRevD.93.016003, arXiv:1509.02083 [hep-ph]

48. W. Altmannshofer, M. Carena, A. Crivellin, Phys. Rev. **D94**, 095026 (2016). https://doi.org/10.1103/PhysRevD.94.095026, arXiv:1604.08221 [hep-ph]
49. K. Huitu, V. Keus, N. Koivunen, O. Lebedev, JHEP **05**, 026 (2016). https://doi.org/10.1007/JHEP05(2016)026, arXiv:1603.06614 [hep-ph]
50. S. Baek, T. Nomura, H. Okada, Phys. Lett. **B759**, 91 (2016). https://doi.org/10.1016/j.physletb.2016.05.055, arXiv:1604.03738 [hep-ph]
51. A. Di Iura, J. Herrero-Garcia, D. Meloni, Nucl. Phys. **B911**, 388 (2016). https://doi.org/10.1016/j.nuclphysb.2016.08.005, arXiv:1606.08785 [hep-ph]
52. A. Pilaftsis, Phys. Lett. **B285**, 68 (1992). https://doi.org/10.1016/0370-2693(92)91301-O
53. J.G. Korner, A. Pilaftsis, K. Schilcher, Phys. Rev. **D47**, 1080 (1993). https://doi.org/10.1103/PhysRevD.47.1080, arXiv:hep-ph/9301289 [hep-ph]
54. E. Arganda, A.M. Curiel, M.J. Herrero, D. Temes, Phys. Rev. **D71**, 035011 (2005). https://doi.org/10.1103/PhysRevD.71.035011, arXiv:hep-ph/0407302 [hep-ph]
55. E. Arganda, M.J. Herrero, X. Marcano, C. Weiland, Phys. Rev. **D91**, 015001 (2015). https://doi.org/10.1103/PhysRevD.91.015001, arXiv:1405.4300 [hep-ph]
56. E. Arganda, M.J. Herrero, X. Marcano, C. Weiland, Phys. Rev. **D93**, 055010 (2016b). https://doi.org/10.1103/PhysRevD.93.055010, arXiv:1508.04623 [hep-ph]
57. E. Arganda, M. Herrero, X. Marcano, R. Morales, A. Szynkman, Phys. Rev. **D95**, 095029 (2017). https://doi.org/10.1103/PhysRevD.95.095029, arXiv:1612.09290 [hep-ph]
58. S. Heinemeyer, W. Hollik, G. Weiglein, Comput. Phys. Commun. **124**, 76 (2000). https://doi.org/10.1016/S0010-4655(99)00364-1, arXiv:hep-ph/9812320 [hep-ph]
59. S. Heinemeyer, W. Hollik, G. Weiglein, Eur. Phys. J. **C9**, 343 (1999). https://doi.org/10.1007/s100529900006, https://doi.org/10.1007/s100520050537, arXiv:hep-ph/9812472 [hep-ph]
60. G. Degrassi, S. Heinemeyer, W. Hollik, P. Slavich, G. Weiglein, Eur. Phys. J. **C28**, 133 (2003). https://doi.org/10.1140/epjc/s2003-01152-2, arXiv:hep-ph/0212020 [hep-ph]
61. B. Aubert et al. (BaBar), Phys. Rev. Lett. **104**, 021802 (2010). https://doi.org/10.1103/PhysRevLett.104.021802, arXiv:0908.2381 [hep-ex]
62. A.M. Baldini et al. (MEG), Eur. Phys. J. **C76**, 434 (2016). https://doi.org/10.1140/epjc/s10052-016-4271-x, arXiv:1605.05081 [hep-ex]
63. F. Deppisch, J.W.F. Valle, Phys. Rev. **D72**, 036001 (2005). https://doi.org/10.1103/PhysRevD.72.036001, arXiv:hep-ph/0406040 [hep-ph]
64. A. Abada, D. Das, C. Weiland, JHEP **03**, 100 (2012a). https://doi.org/10.1007/JHEP03(2012)100, arXiv:1111.5836 [hep-ph]
65. A. Abada, D. Das, A. Vicente, C. Weiland, JHEP **09**, 015 (2012b). https://doi.org/10.1007/JHEP09(2012)015, arXiv:1206.6497 [hep-ph]
66. A. Abada, M.E. Krauss, W. Porod, F. Staub, A. Vicente, C. Weiland, JHEP **11**, 048 (2014). https://doi.org/10.1007/JHEP11(2014)048, arXiv:1408.0138 [hep-ph]
67. V. Khachatryan et al. (CMS), Phys. Lett. **B749**, 337 (2015). https://doi.org/10.1016/j.physletb.2015.07.053, arXiv:1502.07400 [hep-ex]
68. J. Hisano, T. Moroi, K. Tobe, M. Yamaguchi, Phys. Rev. **D53**, 2442 (1996). https://doi.org/10.1103/PhysRevD.53.2442, arXiv:hep-ph/9510309 [hep-ph]
69. A. Dedes, M. Paraskevas, J. Rosiek, K. Suxho, K. Tamvakis, JHEP **06**, 151 (2015). https://doi.org/10.1007/JHEP06(2015)151, arXiv:1504.00960 [hep-ph]
70. J. Rosiek, Comput. Phys. Commun. **201**, 144 (2016). https://doi.org/10.1016/j.cpc.2015.12.011, arXiv:1509.05030 [hep-ph]
71. G. Passarino, M.J.G. Veltman, Nucl. Phys. **B160**, 151 (1979). https://doi.org/10.1016/0550-3213(79)90234-7
72. E. Fernandez-Martinez, J. Hernandez-Garcia, J. Lopez-Pavon, JHEP **08**, 033 (2016). https://doi.org/10.1007/JHEP08(2016)033, arXiv:1605.08774 [hep-ph]

Chapter 5
LFV Z Decays from Low Scale Seesaw Neutrinos

As we previously discussed, the LHC is providing new data on lepton flavor violating Z boson decays, $Z \to \ell_k \bar{\ell}_m$. After LHC run-I, the ATLAS experiment has improved previous bounds for $Z \to \mu e$ [1] and it is already at the level of the LEP results for the $Z \to \tau\mu$ channel. These searches will continue in the next LHC runs with more luminosity and higher energies and, thus, the LHC will provide new data on these LFV observables. Furthermore, the sensitivity to LFVZD rates is expected to highly improve at future linear colliders, with an expected sensitivity of 10^{-9} [2, 3], or at a Future Circular e^+e^- Collider (such as FCC-ee (TLEP)[4]), where it is estimated that up to 10^{13} Z bosons would be produced and the sensitivities to LFVZD rates could be improved up to 10^{-13}. Therefore, we consider extremely timely to explore the predictions for these LFVZD rates in any new physics scenario that could be related to neutrino physics, as it has been previously done in beyond the Standard Model frameworks like those with massive (Majorana and/or Dirac) neutrinos [5–14], or those using an effective field theory approach [15–18].

In this Chapter, we consider again the inverse seesaw model with three pairs of right-handed neutrinos as a specific realization of the low scale seesaw models, which, as we saw in previous chapters, it is an appealing model with a very rich phenomenology, in particular for the charged LFV processes. Nevertheless, as we discussed before, the present experimental upper bounds in Table 3.1 for cLFV processes involving μ-e transitions, here called LFV$_{\mu e}$ in short, are much stronger that the ones in the other sectors, i.e., cLFV processes involving τ-μ and τ-e transitions, named here in short LFV$_{\tau\mu}$ and LFV$_{\tau e}$, respectively. These very stringent constraints in the μ-e sector motivate the directions in the parameter space considered here, which incorporate automatically this suppression in their input. Specifically, we will implement this μ-e suppression requirement within the context of the ISS, by working with the TM and TE scenarios we introduced in Table 3.4. These particular ISS settings with suppressed LFV$_{\mu e}$ rates provide very interesting scenarios for exploring the relevant ISS parameter space directions that may lead to large cLFV rates in the other sectors, τ-μ and/or τ-e.

X. Marcano, *Lepton Flavor Violation from Low Scale Seesaw Neutrinos with Masses Reachable at the LHC*, Springer Theses, https://doi.org/10.1007/978-3-319-94604-7_5

Motivated by all the peculiarities exposed above, in this chapter we perform a dedicated study of the LFVZD rates, in particular BR($Z \to \tau\mu$) and BR($Z \to \tau e$), in the context of these ISS scenarios with an ad-hoc suppression of LFV$_{\mu e}$ rates, which will be called from now on ISS-$\cancel{\text{LFV}}_{\mu e}$ in short. LFVZD processes in the presence of low scale heavy neutrinos have recently been studied considering the full one-loop contributions [13] or computing the relevant Wilson coefficients [14]. In these works, maximum allowed LFVZD rates in the reach of future linear colliders were found when considering a minimal "3+1" toy model, with BR($Z \to \tau\mu$) up to $\mathcal{O}(10^{-8})$ for a neutrino mass in the few TeV range. For more realistic models, like the (2, 3) or (3, 3) realizations of the ISS model, and after imposing all the relevant theoretical and experimental bounds, smaller LFVZD rates were achieved, BR($Z \to \tau\mu$) $\lesssim \mathcal{O}(10^{-9})$, which would be below the reach of future linear colliders sensitivities and might be accessible only at future circular e^+e^- colliders. The main difference of our study with the ones previously done relies on the different settings of the ISS parameters, as we will focus on some specific directions that are more difficult to access with a random scan of the ISS parameter space. We have learnt about this issue when studying the LFV Higgs boson decays in Chap. 4. In the following, we will perform a complementary analysis to the one in Ref. [13] and we will show that larger maximum allowed rates for BR($Z \to \tau\mu$) and BR($Z \to \tau e$) can be obtained by considering the particular TM and TE scenarios in Table 3.4, such that for some specific directions of the parameter space they could be reached at future linear colliders. The results presented in this chapter have been published in Ref. [19].

5.1 LFV Z Decays in the ISS Model

LFV Z decays (LFVZD) in the context of right-handed neutrinos were first studied in Refs. [5, 11, 12]. More recently, LFVZD processes in the presence of low-scale heavy neutrinos have been studied [13, 14], considering a simplified "3+1" model as well as different realizations of the ISS model. In this Section, we revisit these decay rates in the ISS model with three pairs of fermionic singlets, focusing on the μ_X parametrization and the scenarios in Table 3.4, which have been proven to be useful for finding large rates in the case of LFV Higgs decays, as discussed in Chap. 4.

Following Refs. [11–13], we can write the partial decay width for the LFV process $Z \to \ell_k \ell_m$ process as,

$$\Gamma(Z \to \ell_k \ell_m) = \frac{\alpha_W^3}{192\pi^2 c_W^2}\, m_Z \left|\mathcal{F}_Z\right|^2, \tag{5.1}$$

after neglecting final state lepton masses. In the Feynman-'t Hooft gauge, the one-loop form factor $\mathcal{F}_Z$ receives contributions from the ten diagrams shown in Fig. 5.1. Then, we can write it as,

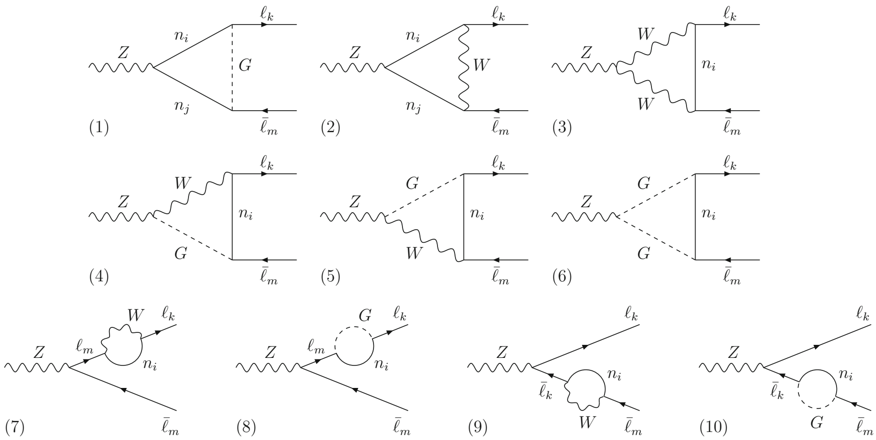

Fig. 5.1 One-loop diagrams in the Feynman-'t Hooft gauge for LFV Z decays with massive neutrinos

$$\mathcal{F}_Z = \sum_{a=1}^{10} \mathcal{F}_Z^{(a)} \,. \tag{5.2}$$

We have taken the full one-loop formulas from Ref. [11] and we have adapted them to the ISS model we consider, rewriting them in terms of the proper physical neutrino masses and couplings introduced in Sect. 2.3. We include these formulas, for completeness, in Appendix F where we have also adapted the loop functions to the usual notation in the literature.

For the numerical analysis of the BR($Z \to \ell_k \ell_m$) = BR($Z \to \ell_k \bar{\ell}_m$) + BR($Z \to \ell_m \bar{\ell}_k$) rates, we will evaluate these expressions with our code and with the help of the *LoopTools* [20] package for *Mathematica*. As for the LFV H decays analysis, we will always demand a good agreement with experimental data coming from neutrino oscillations. This can be easily done by using any of the two parametrizations explained in Chap. 2, i.e., the Casas-Ibarra parametrization in Eq. (2.44) or the μ_X-parametrization in Eq. (2.46). As explained before, the choice of parametrization cannot change physics, however it can help to study the parameter space more efficiently or to design scenarios with phenomenologically appealing features.

As we said, the LFVZD in the context of the ISS model with three pairs of fermionic singlets were first studied in Ref. [13]. In this work, the Authors used the Casas-Ibarra parametrization to accommodate the neutrino oscillation data and they scanned over a large range of the parameter space. Concretely, the modulus of the entries of the input M_R and μ_X matrices were randomly taken between (0.1 MeV, 10^6 GeV) and (0.01 eV, 1 MeV), respectively, with complex entries for μ_X and varying also the complex angles of the R matrix in Eq. (2.45) between 0 and 2π. After applying all the constraints, the Authors concluded from the scatter

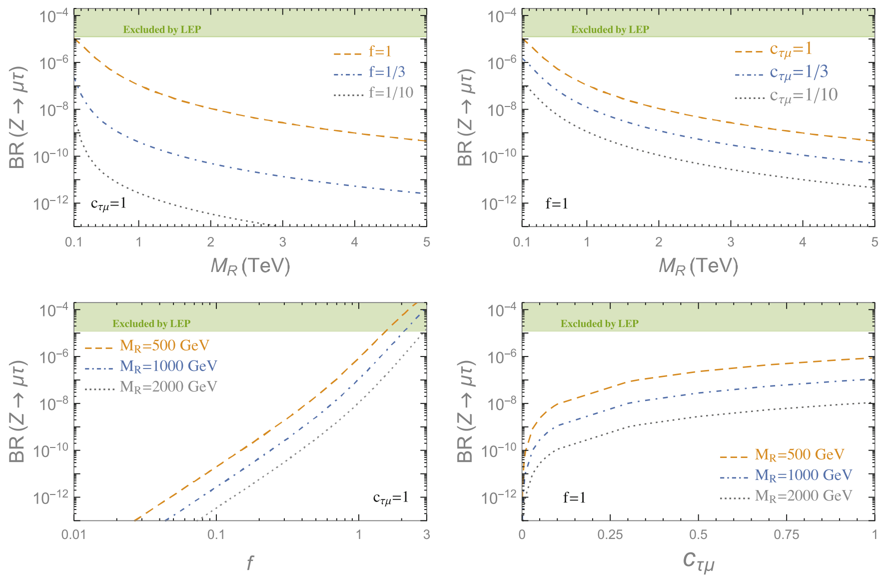

Fig. 5.2 Predictions for BR($Z \to \tau\mu$) within the ISS model as a function of the heavy neutrino mass parameter M_R (two upper panels), the neutrino Yukawa coupling strength f (lower left panel) and $c_{\tau\mu}$ (lower right panel) for various choices of the relevant parameters. In all plots we have fixed, $c_{\tau e} = 0$ and $|\boldsymbol{n}_{e,\mu,\tau}| = 1$. The upper shadowed areas (in green) are excluded by LEP [21]. We found similar results for BR($Z \to \tau e$) by exchanging $c_{\tau e}$ and $c_{\tau\mu}$

plots in their Figs. 8–10 that maximum allowed rates of BR($Z \to \tau\mu$) $\sim 10^{-9}$ can be obtained in our same realization of the ISS model.

As we saw in the context of LFV Higgs decays in Chap. 4, random scans with the Casas-Ibarra parametrization allow one to explore a large region of the parameter space and to study the general features of the model, however, they are not always optimal to reach specific directions along the parameter space that are still allowed by experimental constraints and that can give indeed large predictions for some LFV observables. In the case of LFVHD, for instance, we found maximum allowed rates for $H \to \tau\mu$ and $H \to \tau e$ when using the μ_X parametrization and the scenarios in Table 3.4 that were two orders of magnitude larger than those found when using the Casas-Ibarra parametrization. In this sense, the study of this ad-hoc scenarios looking for maximum allowed rates is complementary to the general scan over the full parameter space. Therefore, in the following we focus on the LFV Z decays along these particular directions in the parameters space, with the aim of complementing the study in Ref. [13] covering points that a generic random scan could have missed.

Looking again at the present experimental upper bounds, summarized in Sect. 3.1, we see that the constraints on cLFV processes involving μ-e transitions are much stronger that the ones in the other sectors, i.e., cLFV processes involving τ-μ and τ-e transitions. These very stringent constraints in the μ-e sector motivated the class of scenarios introduced in Table 3.4, which incorporate automatically this suppression in their input. We showed that these directions were not usually reached by the scans using the Casas-Ibarra parametrization, however they were easily implemented by using our μ_X parametrization and the geometrical interpretation of the Yukawa matrix introduced in Eq. (3.5). On the other hand, these particular ISS settings with suppressed LFV$_{\mu e}$ rates provide very interesting scenarios for exploring the relevant ISS parameter space directions that may lead to large cLFV rates in the other sectors, τ-μ and/or τ-e, as we saw in the context of LFV Higgs decays in Chap. 4. Thus, we will analyze the LFV Z decay rates $Z \to \tau\mu$ and $Z \to \tau e$ within these directions.

Before going to the analysis of maximum allowed LFV Z decay rates in these directions, we study how this observable depends on the most relevant parameters. We show here our results for the particular case of BR($Z \to \tau\mu$) within the TM scenarios, which are defined by taking $c_{\tau e} = 0$ in Eq. (3.7), although similar results are found for BR($Z \to \tau e$) within the TE scenarios. Along these directions, only the $Z \to \tau\mu$ channel gives relevant ratios and their predictions depend mainly on M_R, f, $|\boldsymbol{n}_\tau|$, $|\boldsymbol{n}_\mu|$ and $c_{\tau\mu}$.

We display in Fig. 5.2 the behavior of the BR($Z \to \tau\mu$) rates with the M_R, f and $c_{\tau\mu}$ parameters for fixed values of $|\boldsymbol{n}_e| = |\boldsymbol{n}_\mu| = |\boldsymbol{n}_\tau| = 1$, $c_{\tau e} = 0$ and $\mathcal{O} = \mathbb{1}$. As can be seen in this figure, these ISS directions give in general large rates for the LFV $Z \to \tau\mu$ decay, close, indeed, to the upper bound from LEP (and also close to the present LHC sensitivity) in the upper left corner of the two upper plots and in the upper right corner of the two lower plots. We also see that the rates decrease with the heavy scale M_R and grow with the Yukawa coupling strength f, as expected. We found this growth to be approximately as f^4 in the low f region and as f^8 in the high f region of the studied interval of this parameter. This suggests that, in contrast to the radiative decays, two kinds of contributions $Y_\nu Y_\nu^\dagger$ and $Y_\nu Y_\nu^\dagger Y_\nu Y_\nu^\dagger$ participate in this observable, similar to what we obtained for the LFV H decays (see Eq. 4.34). These dependencies will be further studied by means of the mass insertion approximation in a forthcoming work.

In the lower right panel, we observe that the rates also grow with $c_{\tau\mu}$, albeit the dependence is milder, approximately as $c_{\tau\mu}^2$. Although not shown here, we have also studied the dependence of the decay rates with the modulus of the vectors, $|\mathbf{n}_i|$, finding that the predictions for BR($Z \to \tau\mu$) grow with both $|\boldsymbol{n}_\mu|$ and $|\boldsymbol{n}_\tau|$, while they are constant with $|\boldsymbol{n}_e|$, as expected. Finally, we checked that the results do not depend on the global rotation $\mathcal{O}$, as argued when the parametrization for the Y_ν coupling matrix was motivated.

In order to conclude on the maximum allowed LFV Z decay rates, we need to consider all the relevant constraints. Nevertheless, prior to the full study, we find interesting first to compare the predictions of these LFV Z decays with the predictions of the three body LFV lepton decays in our particular ISS scenarios with suppressed μ-e transitions. Looking back to the right panel of Fig. 3.6, we notice again that in these ISS directions, the $\tau \to \mu\mu\mu$ decay is mostly dominated by the Z penguin. This fact implies a strong correlation between $\tau \to \mu\mu\mu$ and $Z \to \tau\mu$, as it was already found in Ref. [13]. We have also checked in some examples of the ISS parameter space that our numerical predictions of these two observables are in agreement with that reference.

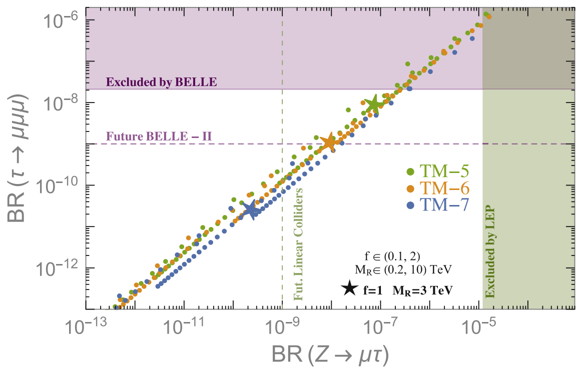

Fig. 5.3 Correlation plot for BR($Z \to \mu\tau$) and BR($\tau \to \mu\mu\mu$) for scenarios TM-5 (green), TM-6 (yellow) and TM-7 (blue) defined in Table 3.4. The dots are obtained by varying $f \in (0.1, 2)$ and $M_R \in (0.2, 10)$ TeV, while the stars are for the reference point $f = 1$ and $M_R = 3$ TeV. Purple (green) shadowed area is excluded by BELLE [22] (LEP [21]), while the dashed line denotes expected future sensitivity from BELLE-II (future linear colliders)

We study this correlation in more detail in Fig. 5.3, where we consider three of the scenarios given in Table 3.4, concretely TM-5, TM-6 and TM-7, and vary the values of the parameters within the ranges of $f \in (0.1, 2)$ and $M_R \in (0.2, 10)$ TeV. We see that both observables grow with f and decrease with M_R in approximately the same way, due to the already mentioned Z penguin dominance in the three body decays. Although the predicted rates in each scenario are obviously different, see for instance the position of the reference points with $f = 1$ and $M_R = 3$ TeV, we clearly see that there is a strong correlation between the two observables in these ISS directions. We can also conclude from this plot that by considering just the constraints from the three body decays, i.e., the present upper bound on $\tau \to \mu\mu\mu$ from BELLE, it already suggests a maximum allowed rate of BR($Z \to \tau\mu$) $\sim 2 \times 10^{-7}$, which is clearly within the reach of future linear colliders (10^{-9} in the most conservative option). Interestingly, comparing the future expected sensitivities for both observables, we find some parameter space points where the LFVZD rates are in the reach of future linear colliders while the cLFV three body decay rates would not be accessible in other facilities, as BELLE-II. This fact suggests that experiments looking for LFVZD would be able to provide additional information about the model that complements the results of other searches, like the ones in Table 3.1. We found a similar correlation between BR($\tau \to eee$) and BR($Z \to \tau e$) in the TE scenarios.

5.2 Maximum Allowed BR($Z \to \ell_k \ell_m$)

In the following we present our full analysis of the LFVZD rates in the ISS scenarios with suppressed μ-e transitions introduced in Sect. 3.2.1, including all the most relevant constraints. For this analysis we have explored the (M_R, f) plane for the eight TM scenarios given in Table 3.4 and provide numerical predictions for the BR($Z \to \ell_k \ell_m$) rates together with the predictions of the most constraining observables and their present bounds, which we reviewed in Chap. 3. Alternative checks of the allowed ISS parameter space can be made by using global fits results [23–29], but we prefer to make the explicit computations of the selected observables here and to compare them directly to their experimental bounds.

We show in Fig. 5.4 the results for BR($Z \to \tau\mu$) together with the constraints from: $\tau \to \mu\mu\mu$, $\tau \to \mu\gamma$, $Z \to$ inv., Δr_K and the EWPO (S, T and U). As in the previous Section, we show our results only for the LFV$_{\tau\mu}$ sector in the TM scenarios, although the conclusions are very similar for LFV$_{\tau e}$ in the TE scenarios. We use different colors in the shadowed areas to represent the exclusion regions from each of the constraints listed above. Specifically, the purple area is excluded by the upper bound on BR($\tau \to \mu\mu\mu$), the green area by BR($\tau \to \mu\gamma$), the yellow area by the Z invisible width, the cyan area by Δr_k and the area above the pink solid line is excluded by the S, T, U parameters. Although we are not explicitly showing them here, we have also checked that the total parameter space allowed by all these constraints is also permitted by our requirements on perturbativity and on the validity of the μ_X parametrization explored in Sect. 3.3.6. Notice that some of the colored areas are hidden below the excluded regions corresponding to the more constraining observables.

On top of all the bounds, we display in Fig. 5.4 the predicted contour lines for BR($Z \to \tau\mu$) as dashed lines. As expected from the correlation studied in Fig. 5.3, we see that these contour lines have approximately the same slope as the border of the exclusion region from BR($\tau \to \mu\mu\mu$), and in particular, the line corresponding to BR($Z \to \tau\mu$) $= 2 \times 10^{-7}$ is very close to the upper bound line of the three body decay in all the TM scenarios (i.e., the border of the purple line). Furthermore, in the large M_R and large f region of these plots we see that for several TM scenarios, concretely TM-2, TM-3, TM-4 and TM-5, the BR($\tau \to \mu\mu\mu$) is indeed the most constraining observable.

In contrast, in the low M_R and low f region, the most constraining cLFV observable is the radiative decay $\tau \to \mu\gamma$. On the other hand, regarding the flavor preserving observables, it is clear that the EWPO do not play a relevant role here, but both Δr_K and the invisible Z width put relevant constraints in some scenarios. In particular, Δr_K is the most constraining observable in the case of TM-8, and the Z invisible width is so in the scenarios TM-1, TM-6 and TM-7. We also learn that, typically, the Z invisible width is the most constraining observable in the region of low M_R values, whereas BR($\tau \to \mu\mu\mu$) is the most constraining observable in the region of high M_R values. Thus, generically, it is the crossing of these two excluded areas in the (M_R, f) plane what gives the focus area of the maximum allowed LFV Z decay rates with a value of BR($Z \to \tau\mu$) $\sim 2 \times 10^{-7}$, as we already inferred from Fig. 5.3. This crossing occurs at different values of M_R and f in each scenario. For example, in the TM-4 and TM-5 scenarios it happens at $M_R \sim 2 - 4$ TeV and for $f \sim \mathcal{O}(1)$, while in the TM-6 M_R is around 10 TeV and $f \sim \mathcal{O}(2)$. On the other hand, if we focus our attention on the mass range of interest for present direct neutrino production searches at LHC, say masses around 1 TeV and below, we observe that the allowed

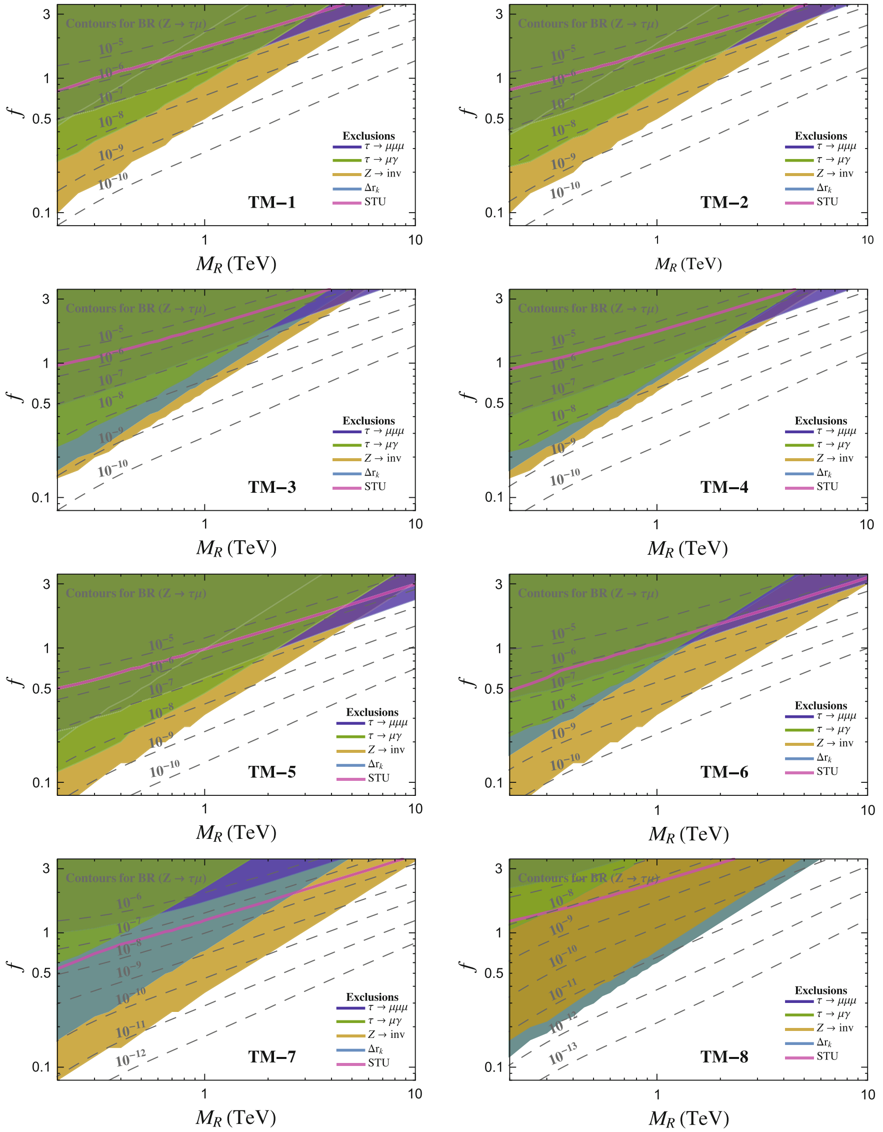

Fig. 5.4 Contour lines for BR($Z \to \tau\mu$) (dashed lines) in the (M_R, f) plane of the ISS model for the eight TM scenarios in Table 3.4. Shadowed areas are the excluded regions by $\tau \to \mu\mu\mu$ (purple), $\tau \to \mu\gamma$ (green), Z invisible width (yellow) and Δr_k (cyan). The region above the pink solid line is excluded by the S, T, U parameters. We obtain similar results for BR($Z \to \tau e$) in the TE scenarios by exchanging μ and e in these plots of the TM scenarios

BR($Z \to \tau\mu$) rates are smaller than this maximum value 2×10^{-7}; nevertheless they are still in the reach of future linear colliders (10^{-9}) for some scenarios, like TM-4 or TM-5.

Summarizing, in this chapter we have studied in full detail the LFV Z decays in scenarios with suppressed μ-e transitions that are designed to find large rates for processes including a τ lepton, and we have investigated those that are allowed by all the present constraints. We have therefore fully explored in parallel also the most relevant constraints within these scenarios of the ISS model. Important constraints come from experimental upper bounds on the LFV three body lepton decays, since they are strongly correlated to the LFVZD in these scenarios. Taking into account all the relevant bounds, we found that heavy ISS neutrinos with masses in the few TeV range can induce maximal rates of BR($Z \to \tau\mu$) $\sim 2 \times 10^{-7}$ and BR($Z \to \tau e$) $\sim 2 \times 10^{-7}$ in the TM and TE scenarios, respectively, larger than what was found in previous studies. These rates are potentially measurable at future linear colliders and FCC-ee. Therefore, we have shown that searches for LFVZD at future colliders may be a powerful tool to probe cLFV in low scale seesaw models, in complementarity with low-energy (high-intensity) facilities searching for cLFV processes. Another appealing feature of our results is that the here presented improved sensitivity to LFVZD rates could come together with the possibility that the heavy neutrinos could be directly produced at LHC, as we will explore in the next chapter.

References

1. G. Aad et al. (ATLAS), Phys. Rev. D **90**, 072010 (2014). https://doi.org/10.1103/PhysRevD.90.072010, arXiv:1408.5774 [hep-ex]
2. G. Wilson, Neutrino oscillations: are lepton-flavor violating Z decays observable with the CDR detector?, in *dESY-ECFA LC Workshops held at Frascati* (Nov 1998)
3. G. Wilson, Update on experimental aspects of lepton-flavour violation, in *dESY-ECFA LC Workshops held at Oxford* (March 1999)
4. A. Blondel, E. Graverini, N. Serra, M. Shaposhnikov (FCC-ee study Team), in *Proceedings of the 37th International Conference on High Energy Physics* (ICHEP 2014), Valencia, Spain, July 2–9, 2014, vol. 273–275 (2016), pp. 1883–1890. https://doi.org/10.1016/j.nuclphysbps.2015.09.304, arXiv:1411.5230 [hep-ex]
5. A. Ilakovac, A. Pilaftsis, Nucl. Phys. B **437**, 491 (1995). https://doi.org/10.1016/0550-3213(94)00567-X, arXiv:hep-ph/9403398 [hep-ph]
6. G. Mann, T. Riemann, Ann. Phys. **40**, 334 (1984)
7. J. Bernabeu, A. Santamaria, J. Vidal, A. Mendez, J.W.F. Valle, Phys. Lett. B **187**, 303 (1987). https://doi.org/10.1016/0370-2693(87)91100-2
8. M. Dittmar, A. Santamaria, M.C. Gonzalez-Garcia, J.W.F. Valle, Nucl. Phys. B **332**, 1 (1990). https://doi.org/10.1016/0550-3213(90)90028-C
9. J.G. Korner, A. Pilaftsis, K. Schilcher, Phys. Lett. B **300**, 381 (1993). https://doi.org/10.1016/0370-2693(93)91350-V, arXiv:hep-ph/9301290 [hep-ph]
10. A. Ilakovac, Phys. Rev. D **62**, 036010 (2000). https://doi.org/10.1103/PhysRevD.62.036010, arXiv:hep-ph/9910213 [hep-ph]
11. J.I. Illana, M. Jack, T. Riemann, (1999), http://www-library.desy.de/cgi-bin/showprep.pl?LC-TH-2000-007, arXiv:hep-ph/0001273 [hep-ph]

12. J.I. Illana, T. Riemann, Phys. Rev. D **63**, 053004 (2001). https://doi.org/10.1103/PhysRevD.63.053004, arXiv:hep-ph/0010193 [hep-ph]
13. A. Abada, V. De Romeri, S. Monteil, J. Orloff, A.M. Teixeira, JHEP **04**, 051 (2015). https://doi.org/10.1007/JHEP04(2015)051, arXiv:1412.6322 [hep-ph]
14. A. Abada, D. Bečirević, M. Lucente, O. Sumensari, Phys. Rev. D **91**, 113013 (2015). https://doi.org/10.1103/PhysRevD.91.113013, arXiv:1503.04159 [hep-ph]
15. M.A. Perez, G. Tavares-Velasco, J.J. Toscano, Int. J. Mod. Phys. A **19**, 159 (2004). https://doi.org/10.1142/S0217751X04017100, arXiv:hep-ph/0305227 [hep-ph]
16. A. Flores-Tlalpa, J.M. Hernandez, G. Tavares-Velasco, J.J. Toscano, Phys. Rev. D **65**, 073010 (2002). https://doi.org/10.1103/PhysRevD.65.073010, arXiv:hep-ph/0112065 [hep-ph]
17. D. Delepine, F. Vissani, Phys. Lett. B **522**, 95 (2001). https://doi.org/10.1016/S0370-2693(01)01254-0, arXiv:hep-ph/0106287 [hep-ph]
18. S. Davidson, S. Lacroix, P. Verdier, JHEP **09**, 092 (2012). https://doi.org/10.1007/JHEP09(2012)092, arXiv:1207.4894 [hep-ph]
19. V. De Romeri, M.J. Herrero, X. Marcano, F. Scarcella, Phys. Rev. D **95**, 075028 (2017). https://doi.org/10.1103/PhysRevD.95.075028, arXiv:1607.05257 [hep-ph]
20. T. Hahn, M. Perez-Victoria, Comput. Phys. Commun. **118**, 153 (1999). https://doi.org/10.1016/S0010-4655(98)00173-8, arXiv:hep-ph/9807565 [hep-ph]
21. P. Abreu et al. (DELPHI), Z. Phys. C **73**, 243 (1997). https://doi.org/10.1007/s002880050313
22. K. Hayasaka et al., Phys. Lett. B **687**, 139 (2010). https://doi.org/10.1016/j.physletb.2010.03.037, arXiv:1001.3221 [hep-ex]
23. E. Fernandez-Martinez, J. Hernandez-Garcia, J. Lopez-Pavon, M. Lucente, JHEP **10**, 130 (2015). https://doi.org/10.1007/JHEP10(2015)130, arXiv:1508.03051 [hep-ph]
24. S. Antusch, C. Biggio, E. Fernandez-Martinez, M.B. Gavela, J. Lopez-Pavon, JHEP **10**, 084 (2006). https://doi.org/10.1088/1126-6708/2006/10/084, arXiv:hep-ph/0607020 [hep-ph]
25. E. Fernandez-Martinez, M.B. Gavela, J. Lopez-Pavon, O. Yasuda, Phys. Lett. B **649**, 427 (2007). https://doi.org/10.1016/j.physletb.2007.03.069, arXiv:hep-ph/0703098 [hep-ph]
26. F. del Aguila, J. de Blas, M. Perez-Victoria, Phys. Rev. D **78**, 013010 (2008). https://doi.org/10.1103/PhysRevD.78.013010, arXiv:0803.4008 [hep-ph]
27. S. Antusch, J.P. Baumann, E. Fernandez-Martinez, Nucl. Phys. B **810**, 369 (2009). https://doi.org/10.1016/j.nuclphysb.2008.11.018, arXiv:0807.1003 [hep-ph]
28. S. Antusch, O. Fischer, JHEP **10**, 094 (2014). https://doi.org/10.1007/JHEP10(2014)094, arXiv:1407.6607 [hep-ph]
29. E. Fernandez-Martinez, J. Hernandez-Garcia, J. Lopez-Pavon, JHEP **08**, 033 (2016). https://doi.org/10.1007/JHEP08(2016)033, arXiv:1605.08774 [hep-ph]

Chapter 6
Exotic LFV Signals from Low Scale Seesaw Neutrinos at the LHC

One of the most interesting phenomenological implications of the existence of low scale seesaw neutrinos with masses in the energy range from the hundreds of GeV up to few TeV, is that they can be directly searched for at the CERN LHC and that, if their couplings to the SM particle are large, the probability of producing them can be sizable. The most frequently studied signatures of heavy neutrinos are those related to their Majorana nature [1–4] and, in particular, the most characteristic signal is the same-sign dilepton plus two jets events which is being searched for at the LHC.

In the low scale seesaw models we are interested in, as long as they assume an approximated lepton number conservation to fit the observed light neutrino masses, the heavy neutrinos form pseudo-Dirac pairs, with a small Majorana character proportional precisely to the small LN breaking scale. Therefore, the rates of the smoking-gun signal of Majorana neutrinos are suppressed in these models. Alternative searches for this pseudo-Dirac character of the heavy neutrinos have also been explored in the literature in connection with the appearance of other interesting multilepton signals [5] at the LHC, like the trilepton final state [6–13].

In this Chapter, we propose a new exotic signal of the right-handed neutrinos at the LHC that is based on another interesting feature of the low scale seesaw models, the fact that they incorporate large lepton flavor violation for specific choices of the model parameters, as we have extensively studied in the previous Chapters of this Thesis. We focus again on the inverse seesaw model as a specific realization of these low scale seesaw models and study the LFV effects coming from the neutrino Yukawa couplings Y_ν. Our specific proposal here is to look at rare LHC events of the type of $\ell_k^\pm \ell_m^\mp jj$, and more specifically with one muon, one tau lepton and two jets in the final state that are produced in these ISS scenarios with large LFV, and that presumably will have a very small SM background. This Chapter then summarizes our computation of the rates for these exotic $\mu\tau jj$ events due to the production and decays of the heavy quasi-Dirac neutrinos at the LHC within the ISS. The results presented in this Chapter have been published in Ref. [14].

X. Marcano, *Lepton Flavor Violation from Low Scale Seesaw Neutrinos with Masses Reachable at the LHC*, Springer Theses, https://doi.org/10.1007/978-3-319-94604-7_6

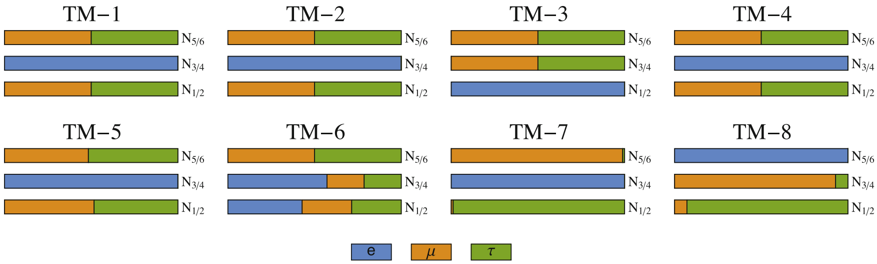

Fig. 6.1 Heavy neutrino flavor mixings, as defined in Eq. (6.1), within some of the ISS scenarios of Table 3.4. Blue, orange and green colors represent the relative mixing with the electron, muon and tau flavor, respectively

6.1 The Flavor of the Heavy Neutrinos

As we have seen in previous Chapters, radiatively induced LFV processes are sensitive to a particular combination of the Yukawa coupling matrix, i.e., to $|Y_\nu Y_\nu^\dagger|$. Therefore, in terms of the heavy neutrino flavor mixing, $B_{\ell N}$ as introduced in Eq. (2.52), they constrain the combination $|B_{\ell N_i} B^*_{\ell' N_i}|$, but not the $B_{\ell N}$ itself, which is the relevant element that controls the flavor pattern of each of the heavy neutrinos.

In Fig. 6.1 we show the flavor content of each heavy neutrino for some of the TM scenarios in Table 3.4 in the same language of the flavor structure in Fig. 2.1 for the light neutrinos. Concretely we chose as examples the scenarios from TM-1 to TM-8, and define the length of the colored bars as

$$S_{\ell N_i} = \frac{|B_{\ell N_i}|^2}{\sum\limits_{\ell=e,\mu,\tau} |B_{\ell N_i}|^2}\,, \tag{6.1}$$

and, therefore, it represents the relative mixing of the heavy neutrino N_i with a given flavor ℓ. It should be further noticed, that the values of these $B_{\ell N}$ mixing parameters are determined within the ISS model in terms of the input m_D and M_R mass matrices and, therefore, in the range where $m_D \ll M_R$ they are suppressed as $B_{\ell N} \sim \mathcal{O}(m_D M_R^{-1})$. This fact implies that, for our assumptions of degenerate entries of the diagonal M_R matrix, the relative mixings defined as in Eq. (6.1) are independent of M_R in this situation.

We learn from Fig. 6.1 that, although these TM scenarios share the property of suppressing the LFV μ-e and τ-e rates while maximizing the τ-μ ones, the heavy neutrino flavor mixing pattern is not always the same in each scenario. We also see that some heavy neutrinos carry an interesting amount of both μ and τ flavors, specially in the first six scenarios, pointing towards signals with both μ and τ leptons simultaneously. Therefore, in the following we will explore the possibility of producing this kind of events at the LHC, concretelly $\tau^\pm \mu^\mp jj$ events, which can be considered as naively background free in the SM, and are therefore interesting

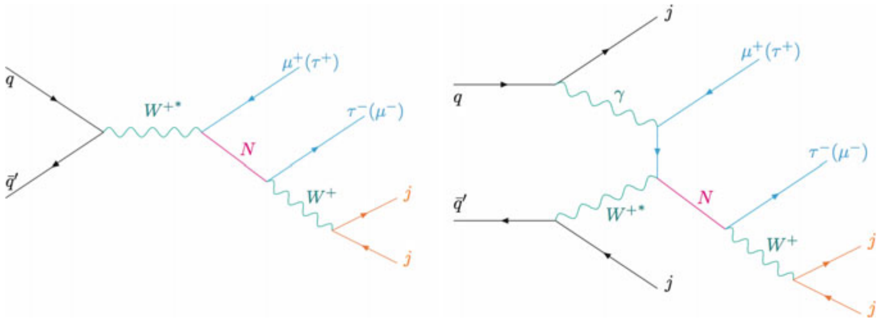

Fig. 6.2 The two main processes, Drell-Yan and γW fusion, producing exotic $\tau^{\pm}\mu^{\mp}jj$ events via heavy neutrino production and decay at the LHC

exotic events to search for. Moreover, we notice that similar results can be obtained for $\tau e j j$ events if the TE scenarios are considered.

6.2 Predictions of Exotic $\tau\mu jj$ Event Rates from Heavy Neutrinos

Heavy neutrinos with masses of the TeV order and below can be produced at present and future colliders, in particular in the new runs of the LHC. The dominant production mechanism in this case is the Drell-Yan (DY) process, Fig. 6.2 left, where the heavy neutrino is produced in association with a charged lepton. The γW fusion, Fig. 6.2 right, also produces the same signal with two extra jets and, in fact, can be also relevant especially for large neutrino masses in the $\mathcal{O}(1\text{ TeV})$ energy range [15, 16].

In order to estimate the heavy neutrino production at the LHC, we have used *Feynrules* [17] to implemente the model in *MadGraph5* [18]. Following Ref. [16], we have used a K-factor of 1.2 for the DY-process and split the γW process in three regimes characterized by the virtuality of the photon[1]: elastic, inelastic and deep inelastic scattering (DIS) regimes. In particular, we have set the boundaries between these three regimes to $\Lambda_\gamma^{\text{Elas}} = 1.22$ GeV and $\Lambda_\gamma^{\text{DIS}} = 15$ GeV. In order to detect them and to regularize possible collinear singularities, we have also imposed the following cuts to the transverse momentum and pseudorapidity of the outgoing leptons:

$$p_T^\ell > 10\text{ GeV}, \quad |\eta^\ell| < 2.4\,. \tag{6.2}$$

The results for the scenarios TM-5, TM-6 and TM-7 from Table 3.4 are shown in Fig. 6.3, where the dominant DY production cross sections normalized by f^2 are

[1] We warmly thank Richard Ruiz, Tao Han and Daniel Alva for their generous help and clarifications in the implementation of the γW process.

plotted as a function of the heavy mass parameter M_R. We see that the production cross sections can be of the fb order, reachable then at the LHC, for masses $M_R \lesssim 600\,\text{GeV}$. Notice that the results are always equal for the pseudo-Dirac pairs, since their Majorana character plays a subleading role in their production.

We can also learn that the flavor of the associated charged lepton is different depending on the heavy neutrino produced and the scenario considered, and that this pattern can be understood looking at the mixing in Fig. 6.1. For example, $N_{3/4}$ are mainly electronic neutrinos in the TM-1,2,4,5,7 scenarios and, therefore, they are basically produced exclusively with electrons. $N_{1/2}$ are equally produced with muons and taus in the TM-1,2,4,5 scenarios, dominantly produced with electrons in the TM-3 scenario, and mainly produced with taus in the TM-7 and 8 scenarios. On the other hand, $N_{5/6}$ are equally produced with muons and taus in TM-1,2,3,4,5,6 scenarios, mainly produced with muons in the TM-7 scenario and mostly produced with electrons in the TM-8 scenario.

Once the heavy neutrinos are produced, they will decay inside the detector. As mentioned in Sect. 3.3.5, in the limit $M_R \gg m_D$ the heavy neutrino masses are close to M_R, with small differences of $\mathcal{O}(m_D^2 M_R^{-1})$ between the different pseudo-Dirac pairs and, therefore, assuming that they are practically degenerate, their decay into each other should be suppressed, with the dominant channels, then, being $N_j \to Z\nu_i$, $H\nu_i$, $W^\pm \ell_i^\mp$. The expressions for these relevant decay channels are given in Eqs. (3.20) and (3.21).

It is interesting to study the rich flavor structure of the decay products, which depends on the decaying heavy neutrino and the scenario we are considering. Like in the production, the flavor preference of the decays to $W^\pm \ell^\mp$, which are the ones relevant to this study (see Fig. 6.2), also follows the same pattern as in Fig. 6.1. Therefore, we can expect the production and decay of the heavy neutrinos to lead to exotic $\mu\tau jj$ events with no missing energy and $M_{jj} \sim M_W$, with M_{jj} the invariant mass of the two jets.

Using the narrow width approximation, the total cross section of the exotic events we are interested in is given by:

$$\sigma(pp \to \mu\tau jj) = \sum_{i=1}^{6} \left\{ \sigma(pp \to N_i \mu^\pm) \text{BR}(N_i \to W^\pm \tau^\mp) + \sigma(pp \to N_i \tau^\pm) \text{BR}(N_i \to W^\pm \mu^\mp) \right\} \\ \times \text{BR}(W^\pm \to jj)\,, \tag{6.3}$$

with $\mu\tau jj = \mu^+\tau^- jj + \mu^-\tau^+ jj$.

Figure 6.3 shows the expected number of exotic events $\mu\tau jj$ at the LHC for an integrated luminosity of $\mathcal{L} = 300\ \text{fb}^{-1}$ at $\sqrt{s} = 14$ TeV. The lower solid lines for each choice of f are the number of events considering only the DY-production.

Moreover, γW fusion processes can also contribute to this kind of exotic events if the p_T of the extra jets are below a maximum value p_T^{max} and, therefore, they can be considered as soft or collinear jets which can escape detection. In this case the predicted total number of exotic events is the sum of the events produced by DY and γW channels. These total contributions for different values of $p_T^{\text{max}} = 10, 20$ and

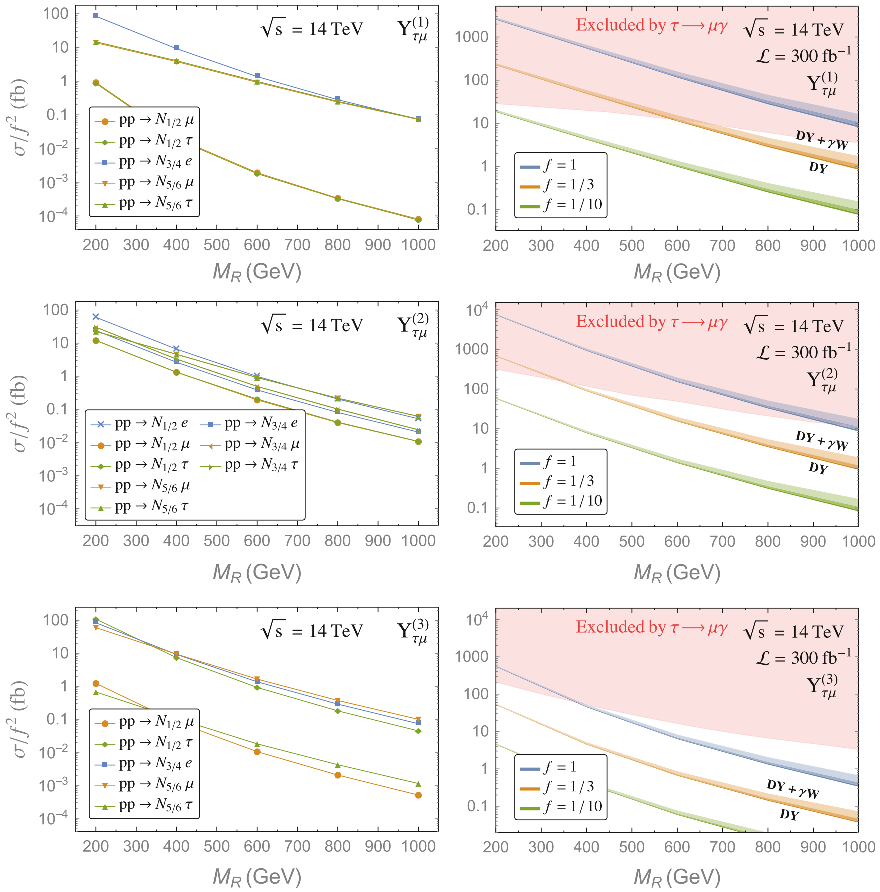

Fig. 6.3 Left panels: Heavy neutrino DY-production, normalized by f^2, at the LHC for scenarios TM-5 ($Y_{\tau\mu}^{(1)}$), TM-6 ($Y_{\tau\mu}^{(2)}$), TM-7 ($Y_{\tau\mu}^{(3)}$) from Table 3.4. Processes not shown are negligible. Right panels: Number of exotic $\mu\tau jj$ events at the LHC for the same scenarios and for three values of f. For each f, the bottom solid line is the prediction of $\mu\tau jj$ events from DY and the upper lines on top of each of the three shadowed regions are the predictions after adding the $\mu\tau jj$ events from γW, and imposing $p_T^{\max} = 10, 20, 40$ GeV, from bottom to top, to the two extra jets. The upper red shadowed areas are excluded by $\tau \to \mu\gamma$

40 GeV are shown as the border lines on top of the shadowed areas with gradual decreasing intensity above each solid line. In addition we have included in the plots red shadowed areas that represent the regions excluded by the experimental upper bound on BR($\tau \to \mu\gamma$), which, as we saw in the previous Chapters, is the most constraining LFV observable at this range of masses. We can see that, after considering all the LFV constraints, the three scenarios lead to an interesting number of $\mathcal{O}(10-100)$ total $\mu\tau jj$ exotic events for the range of M_R studied here of [200 GeV, 1 TeV]. Applying constraints from other observables beyond the LFV ones,

like the ones studied in Sect. 3.3, could change this final conclusion. For example, looking at Fig. 5.4, we see that in the TM-5 scenario for M_R values in the (200, 1000) GeV interval, the Z invisible width sets a maximum value for f of about 1.5 times stronger, meaning that the maximum allowed number of events would be about 2–3 times smaller. Similarly, considering the global fit constraints as in Sect. 4.4 would increase the excluded red area, reducing the maximum number of events predicted in the allowed parameter space. A more complete analysis deserves further study and will be done in a forthcoming work, where we will also explore the larger luminosity options for future LHC phases.

The SM backgrounds for events with two leptons of different flavor have been studied in Ref. [19]. However, a high efficiency in the τ-tagging and a good reconstruction of the W boson invariant mass from the two leading jets would help in reducing the background. In that case, the main background would come from processes with photons or jets misidentified as leptons, mainly from $W/Z + \gamma^*$, $W/Z+$ jets and multijet events with at least four jets with one of them misidentified as a muon and another as a tau; and from $Z/\gamma^* + \text{jets} \to \mu^+\mu^- + \text{jets}$ if one of the muons is misidentified as a τ candidate. Nevertheless, a dedicated background study for these particular $\mu\tau jj$ exotic events is needed and will be done in a future work.

Summarizing, in this Chapter we have proposed a new interesting way to study the production and decay of the heavy neutrinos of the ISS in connection with LFV. We have presented the computation of the predicted number of exotic $\mu\tau jj$ events which can be produced in these ISS scenarios with large LFV by the production of heavy pseudo-Dirac neutrinos together with a lepton of flavor ℓ, both via DY and γW fusion processes, and their subsequent decay into W plus a lepton of different flavor. We have concluded that, for the three TM-like scenarios studied here, a number of $\mathcal{O}(10-100)$ total $\mu\tau jj$ exotic events without missing energy can be produced at the next run of the LHC when $300\,\text{fb}^{-1}$ are collected, for values of M_R from 200 GeV to 1 TeV. Similarly, rare $\tau e jj$ processes could be produced within the equivalent TE ISS scenarios. Although in other scenarios with large LFV $\mu e jj$ events could also be produced, which would be interesting since they could provide in addition observable CP asymmetries [20], the number of events would be strongly limited by the $\mu \to e\gamma$ upper bound. This idea of looking for $\tau\mu jj$ exotic events has been recently explored in the context of a 100 TeV pp collider in Ref. [21], finding promising results for a luminosity of $L = 10\,\text{ab}^{-1}$. Of course, a more realistic study of these exotic events, including detector simulation, together with a full background study should be done in order to reach a definitive conclusion, but this will be addressed in a future work.

References

1. A. Pilaftsis, Z. Phys. **C55**, 275 (1992). https://doi.org/10.1007/BF01482590, arXiv:9901206 [hep-ph]
2. A. Datta, M. Guchait, A. Pilaftsis, Phys. Rev. **D50**, 3195 (1994). https://doi.org/10.1103/PhysRevD.50.3195, arXiv:9311257 [hep-ph]

3. F. del Aguila, J.A. Aguilar-Saavedra, R. Pittau, JHEP **10**, 047 (2007). https://doi.org/10.1088/1126-6708/2007/10/047, arXiv:0703261 [hep-ph]
4. A. Atre, T. Han, S. Pascoli, B. Zhang, JHEP **05**, 030 (2009). https://doi.org/10.1088/1126-6708/2009/05/030, arXiv:0901.3589 [hep-ph]
5. F. del Aguila, J.A. Aguilar-Saavedra, Nucl. Phys. **B813**, 22 (2009). https://doi.org/10.1016/j.nuclphysb.2008.12.029, arXiv:0808.2468 [hep-ph]
6. C.-Y. Chen, P.S.B. Dev, Phys. Rev. **D85**, 093018 (2012). https://doi.org/10.1103/PhysRevD.85.093018, arXiv:1112.6419 [hep-ph]
7. P.S. Bhupal Dev, R. Franceschini, R.N. Mohapatra, Phys. Rev. **D86**, 093010 (2012). https://doi.org/10.1103/PhysRevD.86.093010, arXiv:1207.2756 [hep-ph]
8. A. Das, N. Okada, Phys. Rev. **D88**, 113001 (2013). https://doi.org/10.1103/PhysRevD.88.113001, arXiv:1207.3734 [hep-ph]
9. A. Das, P.S. Bhupal Dev, N. Okada, Phys. Lett. **B735**, 364 (2014). https://doi.org/10.1016/j.physletb.2014.06.058, arXiv:1405.0177 [hep-ph]
10. G. Bambhaniya, S. Goswami, S. Khan, P. Konar, T. Mondal, Phys. Rev. **D91**, 075007 (2015). https://doi.org/10.1103/PhysRevD.91.075007, arXiv:1410.5687 [hep-ph]
11. G. Bambhaniya, S. Khan, P. Konar, T. Mondal, Phys. Rev. **D91**, 095007 (2015). https://doi.org/10.1103/PhysRevD.91.095007, arXiv:1411.6866 [hep-ph]
12. A. Das, N. Okada, Phys. Rev. **D93**, 033003 (2016). https://doi.org/10.1103/PhysRevD.93.033003, arXiv:1510.04790 [hep-ph]
13. A. Das, P. Konar, S. Majhi, JHEP **06**, 019 (2016). https://doi.org/10.1007/JHEP06(2016)019, arXiv:1604.00608 [hep-ph]
14. E. Arganda, M.J. Herrero, X. Marcano, C. Weiland, Phys. Lett. **B752**, 46 (2016). https://doi.org/10.1016/j.physletb.2015.11.013, arXiv:1508.05074 [hep-ph]
15. P.S.B. Dev, A. Pilaftsis, U.-K. Yang, Phys. Rev. Lett. **112**, 081801 (2014). https://doi.org/10.1103/PhysRevLett.112.081801, arXiv:1308.2209 [hep-ph]
16. D. Alva, T. Han, R. Ruiz, JHEP **02**, 072 (2015). https://doi.org/10.1007/JHEP02(2015)072, arXiv:1411.7305 [hep-ph]
17. A. Alloul, N.D. Christensen, C. Degrande, C. Duhr, B. Fuks, Comput. Phys. Commun. **185**, 2250 (2014). https://doi.org/10.1016/j.cpc.2014.04.012, arXiv:1310.1921 [hep-ph]
18. J. Alwall, R. Frederix, S. Frixione, V. Hirschi, F. Maltoni, O. Mattelaer, H.S. Shao, T. Stelzer, P. Torrielli, M. Zaro, JHEP **07**, 079 (2014). https://doi.org/10.1007/JHEP07(2014)079, arXiv:1405.0301 [hep-ph]
19. G. Aad et al. (ATLAS), Phys. Rev. Lett. **115**, 031801 (2015). https://doi.org/10.1103/PhysRevLett.115.031801, arXiv:1503.04430 [hep-ex]
20. S. Bray, J.S. Lee, A. Pilaftsis, Nucl. Phys. **B786**, 95 (2007). https://doi.org/10.1016/j.nuclphysb.2007.07.002, arXiv:hep-ph/0702294 [HEP-PH]
21. T. Golling et al., CERN Yellow Report, 441 (2017). https://doi.org/10.23731/CYRM-2017-003.441, arXiv:1606.00947 [hep-ph]

Chapter 7
Conclusions

Flavor violating processes have been, are and will be crucial for the construction and development of Particle Physics theory. In the last years, the observation of lepton flavor violation in the neutral sector via neutrino oscillations has established that neutrinos do have masses, which is at present the most clear experimental evidence telling us that the SM must be extended. In the same manner, any evidence of LFV transitions in the charged sector would automatically imply the presence of new physics, even beyond the SM with neutrino masses minimally added. This fact makes charged LFV processes an optimal place to look for new physics. Unfortunately, no such cLFV processes have been observed yet, although a strong experimental effort is being made in this direction, and future experiments are planning to improve the sensitivities up to really impressive levels.

In general, any modification of the neutral lepton sector in order to account for neutrino masses will affect directly or indirectly, mainly via quantum corrections, to the charged lepton sector, leaving a trail of phenomenological implications that experiments could potentially observe. Among the many different extensions for addressing neutrino mass generation, we have focused on low scale seesaw models, in particular in the ISS and SUSY-ISS models, which share the appealing feature of adding new right-handed neutrinos with masses at the TeV range, i.e., at the energy scale that present colliders as the LHC are exploring. Therefore, in this Thesis we have explored the connection between the presence of right-handed neutrinos at the TeV mass scale and the potential existence of processes with charged LFV.

As we discussed when introducing the inverse seesaw model in Chap. 2, one of its most important features is that it introduces three different mass scales with three different purposes: a small lepton number violating scale, μ_X, responsible of explaining the smallness of the light neutrino masses; a large M_R scale that governs the masses of the heavy pseudo-Dirac neutrino pairs; and a Dirac mass at the electroweak scale, $m_D = vY_\nu$, which controls the interaction between the (mainly left-handed) light and (mainly right-handed) heavy neutrinos with the Higgs boson. Along this Thesis, we have clearly seen that the most relevant parameters for the cLFV processes

X. Marcano, *Lepton Flavor Violation from Low Scale Seesaw Neutrinos with Masses Reachable at the LHC*, Springer Theses, https://doi.org/10.1007/978-3-319-94604-7_7

that we are interested in are M_R and Y_ν. Consequently, we have introduced a new parametrization for accommodating neutrino oscillation data, the μ_X parametrization, alternative to the often used Casas-Ibarra parametrization, that allows to choose precisely M_R and Y_ν as independent input parameters of the model.

In order to gain intuition on the general properties of cLFV processes in the ISS model, we have first revisited in Chap. 3 the LFV lepton decays, meaning the radiative decays $\ell_m \to \ell_k\gamma$ and the three body decays $\ell_m \to \ell_k\ell_k\ell_k$ with $k \neq m$. This study has allowed us to establish the basic ideas of our analysis, as well as to understand the main differences of using the Casas-Ibarra parametrization or the μ_X parametrization. We have seen that, although physics must not depend on the parametrization one chooses, the efficiency of an analysis in reaching some particular but interesting directions in the parameter space may radically change. As a particular example of this idea, we have studied the LFV radiative decays when using the μ_X parametrization, where the Yukawa coupling matrix is one of the independent input parameters. Using this freedom, and the geometrical interpretation of the Yukawa matrix discussed in Sect. 3.21, we were able to define directions in the parameter space where the cLFV transitions are favored between two particular flavors, while keeping μ-e transitions always highly suppressed. This is particularly interesting in the light of present experimental constraints on cLFV processes, since there are very strong bounds in the μ-e sector, while they are weaker in the τ-e and τ-μ sectors and, therefore, there is more room for larger allowed LFV predictions in these two latter sectors.

In Chap. 4 we have studied in full detail the LFV Higgs decays $H \to \ell_k\bar{\ell}_m$ induced at the one-loop level from the ISS right-handed neutrinos. We have presented a full one-loop computation of the BR($H \to \ell_k\bar{\ell}_m$) rates for the three possible channels, $\ell_k\bar{\ell}_m = \mu\bar{\tau}, e\bar{\tau}, e\bar{\mu}$, and have also analyzed in full detail the predictions as functions of the various relevant ISS parameters. We found, as in the LFV lepton decays, that the most relevant parameters are M_R and Y_ν. Nevertheless, we have seen that, interestingly, the dependence of the LFVHD rates on these parameters is not the same as that of the LFV radiative decays.

In order to better understand these differences, we have performed a new and independent computation using a very different approach which turns out to provide simpler and more useful analytical results. Instead of applying the usual diagrammatic method of the full one-loop computation, we have used the mass insertion approximation, which works with the chiral EW neutrino basis, including the left- and right-handed states ν_L and ν_R and the extra singlets X of the ISS, instead of dealing with the nine physical neutrino states, $n_{1\ldots9}$, of the mass basis.

To further simplify this MIA computation, we have first prepared the chiral basis in a convenient way, such that all the effects of the singlet X states are collected into a redefinition of the ν_R propagator, which we have called here *fat propagator*, and then we have derived the set of Feynman rules for these proper chiral states that summarizes the relevant interactions involved in the one-loop computation of the LFVHD rates. The peculiarity of using this particular chiral basis is that it leads to a quite generic set of Feynman rules for the subset of interactions involving the neutrino sector, mainly ν_L and ν_R, which are the relevant ones for the LFV observables of our interest here, and therefore our results could be valid for other low scale seesaw models sharing these same Feynman rules. With the MIA we have then organized the one-loop computation of the LFVHD rates in terms of a perturbative expansion in powers of the neutrino Yukawa coupling matrix Y_ν. It is worth recalling that in the ISS model, the Y_ν matrix is the unique relevant origin of LFV and, thus, it is the proper expansion parameter in the MIA computation.

We have presented the analytical results using the MIA for the form factors that define the one-loop LFVHD amplitude, and we have done this computation first to leading order, $\mathcal{O}((Y_\nu Y_\nu^\dagger)_{km})$, and later to the next to leading order, i.e., including terms up to $\mathcal{O}((Y_\nu Y_\nu^\dagger Y_\nu Y_\nu^\dagger)_{km})$. Moreover, we have demonstrated that our analytical results are gauge invariant, obtaining the same result in the Feynman-'t Hooft gauge and in the unitary gauge. This is certainly a good check of our analytical results. Numerically, we have found that in order to get a good numerical convergence of the MIA with the full results, it is absolutely necessary to include both $\mathcal{O}(Y_\nu^2)$ and $\mathcal{O}(Y_\nu^4)$ terms. Indeed, the presence of the $\mathcal{O}(Y_\nu^4)$ terms is what explains the different functional behavior with the parameters that we observed for the LFVHD rates with respect to the radiative decays, which are well described with only the $\mathcal{O}(Y_\nu^2)$ terms. We have then checked numerically that the MIA works pretty well in a big range of the relevant model parameters Y_ν and M_R. For a small Yukawa coupling, given in our notation by a small global factor, say $f < 0.5$, we have obtained an extremely good convergence of the MIA and the full results even for moderate M_R of a few hundred GeV and above. For larger Yukawa couplings, say with $0.5 < f < 2$ we have also found a good convergence, but for heavier M_R of above $\mathcal{O}(1\text{TeV})$.

In addition to the form factors, we have also derived in Sect. 4.3.3 an analytical expression of the LFV effective vertex describing the $H\ell_k\ell_m$ coupling that is radiatively generated to one-loop from the heavy right-handed neutrinos. For that computation we have presented our systematic expansion of the form factors in inverse powers of M_R, which is valid in the mass range of our interest, $m_\ell \ll m_D, m_W, m_H \ll M_R$, and we have found the most relevant terms of $\mathcal{O}(v^2/M_R^2)$ in this series. In doing this expansion, we have taken care of the contributions from the external Higgs boson momentum which are relevant since in this observable the Higgs particle is on-shell, and we have also followed the track of all the EW masses involved, like m_W and m_H, which are both of order v and therefore contribute to the wanted $\mathcal{O}(v^2/M_R^2)$ terms. The lepton masses (except for the global factor from the heaviest lepton $m_{\ell_k} \gg m_{\ell_m}$) do not provide relevant corrections and have been neglected in this computation of the effective vertex. We have shown with several examples that this simple MIA formula works extremely well for the interesting window in the (Y_ν, M_R) parameter space which is allowed by the present experimental constraints. Therefore, we believe that our final analytical formula for the LFV effective $H\ell_k\ell_m$ vertex given in Eq. 4.34 is very simple and can be useful for other authors who wish to perform a fast estimate of the LFVHD rates in terms of their own preferred input parameter values for Y_ν and M_R.

For the numerical estimates of the full one-loop results of the LFVHD rates, we have explored the ISS parameter space considering again the two discussed parametrizations for accommodating light neutrino masses and mixings. First, we have considered the Casas-Ibarra parametrization and explored the LFVHD rates from the simplest case of diagonal μ_X and M_R matrices with degenerate entries for M_{R_i}, to a more general case with hierarchical heavy neutrinos. In these cases, we concluded that the largest maximum LFV Higgs decay rates within the ISS that are allowed by the constraints on the LFV radiative decays are for BR($H \to e\bar{\tau}$) and BR($H \to \mu\bar{\tau}$) and reach at most 10^{-10} for the degenerate heavy neutrino case and 10^{-9} for the hierarchical case. Second, we have considered the μ_X parametrization and explored the phenomenologically well motivated scenarios that are more promising for LFVHD searches in the τ-e and τ-μ sectors. We have demonstrated that in this kind of ISS scenarios there are solutions with much larger allowed LFVHD rates than in the previous cases, leading to maximal rates allowed by the bounds on the radiative decays of around 10^{-5} for either BR($H \to \mu\bar{\tau}$) or BR($H \to e\bar{\tau}$).

Finally, we have considered the effects of other kind of constraints to the ISS parameter space by making use of the global fit analysis to present data and the perturbativity requirements on the Yukawa couplings. These constraints result in allowed BR($H \to e\bar{\tau}$) and BR($H \to \mu\bar{\tau}$) ratios being at most of about 10^{-7}, which are unfortunately far below the present experimental sensitivities and, therefore, future experiments would be needed for testing these predictions.

In Sect. 4.2, we have also addressed the question of whether the SUSY realization of the ISS model can lead to enhanced predictions for the LFV Higgs decay rates. We have considered the MSSM model with the lightest CP-even Higgs boson h identified as the SM-like Higgs boson, and extended with three pairs of ISS neutrinos and their corresponding SUSY partners, the sneutrinos. We have then presented the results of an updated and full one-loop calculation of the SUSY contributions to lepton flavor violating Higgs decays in the SUSY-ISS model. These contributions come from chargino-sneutrino loops with sneutrino couplings off-diagonal in flavor, and from neutralino-slepton loops, due to the misalignment in flavor between the slepton and lepton sectors caused by running effects. We found much larger contributions than in the type-I seesaw model coming from the lower values of $M_R \sim \mathcal{O}(1\text{ TeV})$, an increased RGE-induced slepton mixing, and the presence of new right-handed sneutrinos at the TeV scale. Then, the couplings of both sleptons and sneutrinos can transmit sizable LFV due to the large $Y_\nu^2/(4\pi) \sim \mathcal{O}(1)$ we considered. We showed that the branching ratio of $h \to \tau\bar{\mu}$ exhibits different behaviors as a function of the seesaw and SUSY scale if it is dominated by chargino or neutralino loops. Moreover, a non-zero trilinear coupling A_ν leads to increased LFVHD rates. Choosing different benchmark points, we found that BR($h \to \tau\bar{\mu}$) of the order of 10^{-2} can be reached while agreeing with the experimental limits on radiative decays, which can be tested at the present runs of the LHC. This calls up for a complete study including non-supersymmetric contributions in the SUSY-ISS model, like those from the extended Higgs sector, and a detailed analysis of experimental constraints beyond radiative LFV decays, which will be addressed in a future work.

In Chap. 5 we have revisited the LFV Z decays in presence of right-handed neutrinos with TeV range masses, which are very interesting observables that are currently being searched for at the LHC and will be further explored by the next generation of experiments. A first study of these observables within the ISS context with three pairs of fermionic singlets was done in Ref. [1], finding maximum allowed ratios of about 10^{-9}. Here, we have alternatively studied in full detail the LFVZD rates in our selected TM and TE scenarios, which as we said are designed to find large rates for processes including a τ lepton, and we have investigated those that are allowed by all the present constraints. In addition to the radiative decays, important constraints come from experimental upper bounds on the LFV three body lepton decays, since they are strongly correlated to the LFVZD in these scenarios. Taking into account all the relevant bounds, we found that heavy ISS neutrinos with masses in the few TeV range can induce maximal rates of $\mathrm{BR}(Z \to \tau\mu) \sim 2 \times 10^{-7}$ and $\mathrm{BR}(Z \to \tau e) \sim 2 \times 10^{-7}$ in the TM and TE scenarios, respectively. These rates are considerably larger than what was found in previous studies and potentially measurable at future linear colliders and FCC-ee. Therefore, we have seen that searches for LFVZD at future colliders may be a powerful tool to probe cLFV in low scale seesaw models, in complementarity with low-energy (high-intensity) facilities searching for cLFV processes.

Another appealing feature of our results is that the predictions for the cLFV processes come together with the possibility that the heavy neutrinos could be directly produced at the LHC. Being the ISS neutrinos pseudo-Dirac fermions, the standard same-sign dilepton searches for heavy Majorana neutrinos are not effective, implying that new search strategies need to be explored. In Chap. 6 we have proposed a new interesting way of studying the production and decay of the heavy neutrinos of the ISS in connection with LFV. We have presented the computation of the predicted number of exotic $\mu\tau jj$ events, which can be produced in the TM scenarios with large LFV, where the heavy pseudo-Dirac neutrinos are produced together with a lepton of a given flavor, both via Drell-Yan and γW fusion processes, and then decay into a W and a lepton of different flavor. We have concluded that, for the studied benchmark scenarios, a number of $\mathcal{O}(10-100)$ total $\mu\tau jj$ exotic events without missing energy can be produced at the next run of the LHC when 300 fb^{-1} of integrated luminosity are reached, and for values of M_R from 200 GeV to 1 TeV respecting the constraints from LFV violating observables. Similarly, other rare processes like $\tau e jj$ or $\mu e jj$ could be produced within other ISS scenarios with large LFV, although for the latter ones the number of events would be strongly limited by the $\mu \to e\gamma$ upper bound. These promising results deserve a more realistic study of these exotic events, including detector simulation, together with a full background study, which should be done in order to reach a definitive conclusion and it will be addressed in a future work.

As an overall conclusion of this Thesis, we can state that searching for charged lepton flavor violating processes is a very powerful strategy for testing the presence of low scale seesaw neutrinos with masses of a few TeV or below, which on the other hand are common in many models for explaining the observed neutrino masses. As we have seen along this Thesis, the addition to the SM of these new states, not much heavier that the EW scale and with a potentially complex flavor structure, has an important impact in the phenomenology of the charged leptons, which could be seen at lepton flavor violating processes. Flavor physics has been crucial in the history of the SM and it will play a major role in the discovery of new physics.

Reference

1. A. Abada, V. De Romeri, S. Monteil, J. Orloff, A.M. Teixeira, JHEP **04**, 051 (2015). https://doi.org/10.1007/JHEP04(2015)051, arXiv:1412.6322 [hep-ph]

Appendix A
Formulas for LFV Lepton Decays

In this Appendix we collect, for completeness, the needed formulas for the full one-loop computation of the LFV lepton decays in the particle mass basis, both the three body $\ell_m \to \ell_k \ell_k \ell_k$ and the radiative $\ell_m \to \ell_k \gamma$ decays, with $k \neq m$. We have taken these expressions from Refs. [1, 2] and implemented them in our code.

In the case of the three body decays, the branching ratio $\mathrm{BR}(\ell_m \to \ell_k \ell_k \ell_k)$ can be expressed as [1, 2]:

$$\begin{aligned}
\mathrm{BR}(\ell_m \to \ell_k \ell_k \ell_k) = \frac{\alpha_W^4}{24576\pi^3} \frac{m_{\ell_m}^4}{m_W^4} \frac{m_{\ell_m}}{\Gamma_{\ell_m}} \times \Bigg\{ 2 \left| \frac{1}{2} F_{\mathrm{Box}}^{\ell_m \ell_k \ell_k \ell_k} + F_Z^{\ell_m \ell_k} - 2 s_W^2 \left(F_Z^{\ell_m \ell_k} - F_\gamma^{\ell_m \ell_k} \right) \right|^2 \\
+ 16 s_W^2 \,\mathrm{Re} \left[\left(F_Z^{\ell_m \ell_k} + \frac{1}{2} F_{\mathrm{Box}}^{\ell_m \ell_k \ell_k \ell_k} \right) G_\gamma^{\ell_m \ell_k^*} \right] - 48 s_W^4 \,\mathrm{Re} \left[\left(F_Z^{\ell_m \ell_k} - F_\gamma^{\ell_m \ell_k} \right) G_\gamma^{\ell_m \ell_k^*} \right] \\
+ 4 s_W^4 \left| F_Z^{\ell_m \ell_k} - F_\gamma^{\ell_m \ell_k} \right|^2 + 32 s_W^4 \left| G_\gamma^{\ell_m \ell_k} \right|^2 \left[\ln \frac{m_{\ell_m}^2}{m_{\ell_k}^2} - \frac{11}{4} \right] \Bigg\} .
\end{aligned} \tag{A.1}$$

The $\mathrm{BR}(\ell_m \to \ell_k \ell_k \ell_k)$ contains several form factors, corresponding to the dipole, penguin (photon and Z) and box diagrams. The expressions for these form factors are given by:

$$\begin{aligned}
G_\gamma^{\ell_m \ell_k} &= \sum_{i=1}^{9} B_{\ell_k n_i} B_{\ell_m n_i}^* G_\gamma(x_i) , \\
F_\gamma^{\ell_m \ell_k} &= \sum_{i=1}^{9} B_{\ell_k n_i} B_{\ell_m n_i}^* F_\gamma(x_i) , \\
F_Z^{\ell_m \ell_k} &= \sum_{i,j=1}^{9} B_{\ell_k n_i} B_{\ell_m n_j}^* \left(\delta_{ij} F_Z(x_i) + C_{n_i n_j} G_Z(x_i, x_j) + C_{n_i n_j}^* H_Z(x_i, x_j) \right) , \\
F_{\mathrm{Box}}^{\ell_m \ell_k \ell_k \ell_k} &= \sum_{i,j=1}^{9} B_{\ell_k n_i} B_{\ell_m n_j}^* \left(B_{\ell_k n_i} B_{\ell_k n_j}^* G_{\mathrm{Box}}(x_i, x_j) + 2\, B_{\ell_k n_i}^* B_{\ell_k n_j} F_{\mathrm{Box}}(x_i, x_j) \right) ,
\end{aligned} \tag{A.2}$$

X. Marcano, *Lepton Flavor Violation from Low Scale Seesaw Neutrinos with Masses Reachable at the LHC*, Springer Theses, https://doi.org/10.1007/978-3-319-94604-7

where x_i stands for the dimensionless ratio of masses ($x_i = m_{n_i}^2/m_W^2$). Moreover, the following loop functions enter in the previous form factors [1, 2]:

$$
\begin{aligned}
F_Z(x) &= -\frac{5x}{2(1-x)} - \frac{5x^2}{2(1-x)^2}\ln x\,,\\
G_Z(x,y) &= -\frac{1}{2(x-y)}\left[\frac{x^2(1-y)}{1-x}\ln x - \frac{y^2(1-x)}{1-y}\ln y\right],\\
H_Z(x,y) &= \frac{\sqrt{xy}}{4(x-y)}\left[\frac{x^2-4x}{1-x}\ln x - \frac{y^2-4y}{1-y}\ln y\right],\\
F_\gamma(x) &= \frac{x(7x^2-x-12)}{12(1-x)^3} - \frac{x^2(x^2-10x+12)}{6(1-x)^4}\ln x\,,\\
G_\gamma(x) &= -\frac{x(2x^2+5x-1)}{4(1-x)^3} - \frac{3x^3}{2(1-x)^4}\ln x\,,\\
F_{\text{Box}}(x,y) &= \frac{1}{x-y}\left\{\left(1+\frac{xy}{4}\right)\left[\frac{1}{1-x}+\frac{x^2}{(1-x)^2}\ln x\right] - 2xy\left[\frac{1}{1-x}+\frac{x}{(1-x)^2}\ln x\right] - (x\to y)\right\},\\
G_{\text{Box}}(x,y) &= -\frac{\sqrt{xy}}{x-y}\left\{(4+xy)\left(\frac{1}{1-x}+x\frac{\ln x}{(1-x)^2}\right) - 2\left(\frac{1}{1-x}+x^2\frac{\ln x}{(1-x)^2}\right) - (x\to y)\right\}.
\end{aligned}
\tag{A.3}
$$

In the limit of degenerate neutrino masses ($x = y$), we get the following expressions:

$$
\begin{aligned}
G_Z(x,x) &= x(-1+x-2\ln x)/(2(1-x))\,,\\
H_Z(x,x) &= -x(4-5x+x^2+(4-2x+x^2)\ln x)/(4(1-x)^2)\,,\\
F_{\text{Box}}(x,x) &= (4-19x^2+16x^3-x^4-2x(-4+4x+3x^2)\ln x)/(4(1-x)^3)\,,\\
G_{\text{Box}}(x,x) &= x\left(6-8x+4x^2-2x^3+(4+x^2+x^3)\ln x\right)/(-1+x)^3\,.
\end{aligned}
\tag{A.4}
$$

For the LFV radiative decay rates, we use the analytical formulas appearing in [1–3] that have also been implemented in our code:

$$
\text{BR}(\ell_m \to \ell_k\gamma) = \frac{\alpha_W^3 s_W^2}{256\pi^2}\left(\frac{m_{\ell_m}}{m_W}\right)^4 \frac{m_{\ell_m}}{\Gamma_{\ell_m}}\left|G_{mk}\right|^2, \tag{A.5}
$$

where Γ_{ℓ_m} is the total decay width of the lepton ℓ_m, and

$$
G_{mk} = \sum_{i=1}^{9} B_{\ell_k n_i} B^*_{\ell_m n_i}\, G_\gamma(x_i)\ , \tag{A.6}
$$

with $G_\gamma(x)$ defined in Eq. (A.3) and, again, $x_i \equiv m_{n_i}^2/m_W^2$.

Appendix B
Formulas for Low Energy Flavor Conserving Observables

In this Appendix we collect the expressions needed for computing the low energy observables described in Sect. 3.3. These formulas are taken from the literature and summarized here for completeness.

Lepton Universality: $\boldsymbol{\Delta r_k}$

We collect here the formulas to calculate the quantity Δr_K (see Eq. 3.10), which parametrizes the deviation with respect to the SM prediction arising from the sterile neutrinos contribution, as a test of lepton flavor universality. The expression for Δr_K in a generic SM extension with sterile neutrinos has been given in [4]:

$$\Delta r_K \;=\; \frac{m_\mu^2(m_K^2-m_\mu^2)^2}{m_e^2(m_K^2-m_e^2)^2}\,\frac{\sum_{i=1}^{N_{\max}^{(e)}}|B_{en_i}|^2\left[m_K^2(m_{n_i}^2+m_e^2)-(m_{n_i}^2-m_e^2)^2\right]\lambda^{1/2}(m_K,m_{n_i},m_e)}{\sum_{j=1}^{N_{\max}^{(\mu)}}|B_{\mu n_j}|^2\left[m_K^2(m_{n_j}^2+m_\mu^2)-(m_{n_j}^2-m_\mu^2)^2\right]\lambda^{1/2}(m_K,m_{n_j},m_\mu)}-1\,, \tag{B.1}$$

where $N_{\max}^{e,\mu}$ is the heaviest neutrino mass eigenstate kinematically allowed in association with e or μ respectively, and the kinematical function $\lambda(m_K, m_{n_i}, m_\ell)$ reads [4]:

$$\lambda(a,b,c) \;=\; (a^2-b^2-c^2)^2-4\,b^2\,c^2\,. \tag{B.2}$$

The $\boldsymbol{Z}$ invisible decay width

The Z invisible decay width in presence of massive Majorana neutrinos, like it is the case of the present ISS model, reads [5]:

$$\Gamma(Z\to \text{inv.})_{\text{ISS}}=\sum_n \Gamma(Z\to nn)_{\text{ISS}}=\sum\nolimits_{i\le j=1}^{N_{\max}}(1-\frac{1}{2}\delta_{ij})\frac{\sqrt{2}G_F}{48\,\pi\,m_Z}\times\lambda^{1/2}(m_Z,m_{n_i},m_{n_j})$$
$$\times\left[2|C_{n_in_j}|^2\left(2m_Z^2-m_{n_i}^2-m_{n_j}^2-\frac{(m_{n_i}^2-m_{n_j}^2)^2}{m_Z^2}\right)-12m_{n_i}m_{n_j}\text{Re}\Big[\big(C_{n_in_j}\big)^2\Big]\right]. \tag{B.3}$$

X. Marcano, *Lepton Flavor Violation from Low Scale Seesaw Neutrinos with Masses Reachable at the LHC*, Springer Theses, https://doi.org/10.1007/978-3-319-94604-7

where $N_{\max}$ is the heaviest neutrino mass which is kinematically allowed and λ is given in Eq. (B.2).

Oblique parameters: ***S*, *T*, *U***

The Majorana neutrino contributions to the S, T, U parameters have been computed in Ref. [6]. We apply those formulas to compute the sterile neutrinos contributions to the oblique parameters in the ISS model.

The equation for the T parameter reads:

$$T_{\text{tot}} = T_{\text{ISS}} + T_{\text{SM}} = \frac{-1}{8\pi s_W^2 m_W^2}\left\{\sum_{\alpha=1}^{3} m_{\ell_\alpha}^2 B_0(0, m_{\ell_\alpha}^2, m_{\ell_\alpha}^2) - 2\sum_{i=1}^{9}\sum_{\alpha=1}^{3}\left|B_{\ell_\alpha n_i}\right|^2 Q(0, m_{n_i}^2, m_{\ell_\alpha}^2)\right.$$
$$\left. + \sum_{i,j=1}^{9}\left(C_{n_i n_j} C_{n_j n_i} Q(0, m_{n_i}^2, m_{n_j}^2) + (C_{n_i n_j})^2 m_{n_i} m_{n_j} B_0(0, m_{n_i}^2, m_{n_j}^2)\right)\right\}, \tag{B.4}$$

with the index α refering to the charged leptons and

$$Q(q^2, m_1^2, m_2^2) \equiv (D-2)B_{00}(q^2, m_1^2, m_2^2) + q^2\left[B_1(q^2, m_1^2, m_2^2) + B_{11}(q^2, m_1^2, m_2^2)\right], \tag{B.5}$$

where $D \equiv 4 - 2\epsilon$ ($\epsilon \to 0$) and B_0, B_1, B_{11} and B_{00} are the Passarino-Veltman functions [7] in the *LoopTools* [8] notation.

The SM contribution can be cast as:

$$T_{\text{SM}} = -\frac{1}{8\pi s_W^2 m_W^2}\left\{3Q(0,0,0) - 2\sum_{\alpha=1}^{3} Q(0, 0, m_{\ell_\alpha}^2) + \sum_{\alpha=1}^{3} m_{\ell_\alpha}^2 B_0(0, m_{\ell_\alpha}^2, m_{\ell_\alpha}^2)\right\}, \tag{B.6}$$

where it has been used that the active neutrino masses are zero and the leptonic mixing matrix U is unitary in the SM.

The equation for the S parameter is:

$$S_{\text{tot}} = S_{\text{ISS}} + S_{\text{SM}} = -\frac{1}{2\pi m_Z^2}\left\{\sum_{i,j=1}^{9} C_{n_i n_j} C_{n_j n_i} \Delta Q(m_Z^2, m_{n_i}^2, m_{n_j}^2)\right.$$
$$+ \sum_{i,j=1}^{9} (C_{n_i n_j})^2 m_{n_i} m_{n_j}\left(B_0(0, m_{n_i}^2, m_{n_j}^2) - B_0(m_Z^2, m_{n_i}^2, m_{n_j}^2)\right)$$
$$\left. + \sum_{\alpha=1}^{3} m_{\ell_\alpha}^2\left(B_0(0, m_{\ell_\alpha}^2, m_{\ell_\alpha}^2) - 2B_0(m_Z^2, m_{\ell_\alpha}^2, m_{\ell_\alpha}^2)\right) + Q(m_Z^2, m_{\ell_\alpha}^2, m_{\ell_\alpha}^2)\right\}, \tag{B.7}$$

where $\Delta Q(q^2, m_1^2, m_2^2) \equiv Q(0, m_1^2, m_2^2) - Q(q^2, m_1^2, m_2^2)$ and

$$S_{\rm SM} = -\frac{1}{2\pi m_Z^2}\left\{3\Delta Q(m_Z^2, 0, 0) + \sum_{\alpha=1}^{3} m_{\ell_\alpha}^2 \big(B_0(0, m_{\ell_\alpha}^2, m_{\ell_\alpha}^2) - 2B_0(m_Z^2, m_{\ell_\alpha}^2, m_{\ell_\alpha}^2)\big) + Q(m_Z^2, m_{\ell_\alpha}^2, m_{\ell_\alpha}^2)\right\}. \tag{B.8}$$

Finally, the U parameter is given by:

$$\begin{aligned} U_{\rm tot} = U_{\rm ISS} + U_{\rm SM} = \frac{1}{2\pi m_Z^2}\Bigg\{ &\sum_{i,j=1}^{9} C_{n_i n_j} C_{n_j n_i} \Delta Q(m_Z^2, m_{n_i}^2, m_{n_j}^2) \\ &+ \sum_{i,j=1}^{9} (C_{n_i n_j})^2 m_{n_i} m_{n_j} \Big(B_0(0, m_{n_i}^2, m_{n_j}^2) - B_0(m_Z^2, m_{n_i}^2, m_{n_j}^2)\Big) \\ &- \sum_{i=1}^{9}\sum_{\alpha=1}^{3} 2\,\frac{m_Z^2}{m_W^2} \big|B_{\ell_\alpha n_i}\big|^2 \Delta Q(m_W^2, m_{n_i}^2, m_{\ell_\alpha}^2) \\ &+ \sum_{\alpha=1}^{3} m_{\ell_\alpha}^2 \big(B_0(0, m_{\ell_\alpha}^2, m_{\ell_\alpha}^2) - 2B_0(m_Z^2, m_{\ell_\alpha}^2, m_{\ell_\alpha}^2)\big) - Q(m_Z^2, m_{\ell_\alpha}^2, m_{\ell_\alpha}^2)\Bigg\}, \end{aligned} \tag{B.9}$$

and its SM contribution reads:

$$\begin{aligned} U_{\rm SM} = \frac{1}{2\pi m_Z^2}\Bigg\{3\Delta Q(m_Z^2, 0, 0) + \sum_{\alpha=1}^{3} \Big(& m_{\ell_\alpha}^2 \big(B_0(0, m_{\ell_\alpha}^2, m_{\ell_\alpha}^2) - 2B_0(m_Z^2, m_{\ell_\alpha}^2, m_{\ell_\alpha}^2)\big) \\ &- Q(m_Z^2, m_{\ell_\alpha}^2, m_{\ell_\alpha}^2) - 2\,\frac{m_Z^2}{m_W^2} \Delta Q(m_W^2, 0, m_{\ell_\alpha}^2)\Big)\Bigg\}. \end{aligned} \tag{B.10}$$

Appendix C
Form Factors for LFVHD in the ISS Model

In this Appendix we collect the analytical results for the form factors contributing to the LFV Higgs decay $H \to \ell_k \bar{\ell}_m$, as defined in Eq. (4.4). They are computed in the Feynman-'t Hooft gauge and expressed in the physical basis. The numbers (1)–(10) correspond to the diagrams in Fig. 4.1. These formulas are taken from Ref. [9] and adapted for the case of the ISS model with three pairs of fermionic singlets. Notice that we have corrected the global signs of $F_L^{(1)}$, $F_{L,R}^{(4)}$ and $F_{L,R}^{(5)}$, which were typos in the original expressions given in [9].

In all these formulas, summation over neutrino indices is understood, which run as $i, j = 1, \ldots, 9$. The loop functions are the Passarino-Veltman functions [7] and they are defined in Eqs. (E.5) and (E.6).

$$
\begin{aligned}
F_L^{(1)} = {} & \frac{g^2}{4m_W^3}\frac{1}{16\pi^2} B_{\ell_k n_i} B^*_{\ell_m n_j} \Big\{ m_{\ell_k} m_{n_j} \Big[(m_{n_i} + m_{n_j}) \mathrm{Re}\left(C_{n_i n_j}\right) + i (m_{n_j} - m_{n_i}) \mathrm{Im}\left(C_{n_i n_j}\right) \Big] \tilde{C}_0 \\
& + (C_{12} - C_{11}) \Big[(m_{n_i} + m_{n_j}) \mathrm{Re}\left(C_{n_i n_j}\right) \left(-m_{\ell_k}^3 m_{n_j} - m_{n_i} m_{\ell_k} m_{\ell_m}^2 + m_{n_i} m_{n_j}^2 m_{\ell_k} + m_{n_i}^2 m_{n_j} m_{\ell_k} \right) \\
& + i (m_{n_j} - m_{n_i}) \mathrm{Im}\left(C_{n_i n_j}\right) \left(-m_{\ell_k}^3 m_{n_j} + m_{n_i} m_{\ell_k} m_{\ell_m}^2 - m_{n_i} m_{n_j}^2 m_{\ell_k} + m_{n_i}^2 m_{n_j} m_{\ell_k} \right) \Big] \Big\}, \\
F_R^{(1)} = {} & \frac{g^2}{4m_W^3}\frac{1}{16\pi^2} B_{\ell_k n_i} B^*_{\ell_m n_j} \Big\{ m_{n_i} m_{\ell_m} \Big[(m_{n_i} + m_{n_j}) \mathrm{Re}\left(C_{n_i n_j}\right) - i (m_{n_j} - m_{n_i}) \mathrm{Im}\left(C_{n_i n_j}\right) \Big] \tilde{C}_0 \\
& + C_{12} \Big[(m_{n_i} + m_{n_j}) \mathrm{Re}\left(C_{n_i n_j}\right) \left(m_{\ell_m}^3 m_{n_i} - m_{n_i} m_{n_j}^2 m_{\ell_m} - m_{n_i}^2 m_{n_j} m_{\ell_m} + m_{n_j} m_{\ell_k}^2 m_{\ell_m} \right) \\
& + i (m_{n_j} - m_{n_i}) \mathrm{Im}\left(C_{n_i n_j}\right) \left(-m_{\ell_m}^3 m_{n_i} + m_{n_i} m_{n_j}^2 m_{\ell_m} - m_{n_i}^2 m_{n_j} m_{\ell_m} + m_{n_j} m_{\ell_k}^2 m_{\ell_m} \right) \Big] \Big\},
\end{aligned}
$$

where $C_{11,12} = C_{11,12}(m_{\ell_k}^2, m_H^2, m_W^2, m_{n_i}^2, m_{n_j}^2)$ and $\tilde{C}_0 = \tilde{C}_0(m_{\ell_k}^2, m_H^2, m_W^2, m_{n_i}^2, m_{n_j}^2)$.

X. Marcano, *Lepton Flavor Violation from Low Scale Seesaw Neutrinos with Masses Reachable at the LHC*, Springer Theses, https://doi.org/10.1007/978-3-319-94604-7

$$F_L^{(2)} = \frac{g^2}{2m_W}\frac{1}{16\pi^2}B_{\ell_k n_i}B^*_{\ell_m n_j}m_{\ell_k}\Big\{-m_{n_j}\Big[(m_{n_i}+m_{n_j})\mathrm{Re}\left(C_{n_i n_j}\right)+i(m_{n_j}-m_{n_i})\mathrm{Im}\left(C_{n_i n_j}\right)\Big]C_0$$
$$+(C_{12}-C_{11})\Big[(m_{n_i}+m_{n_j})^2\,\mathrm{Re}\left(C_{n_i n_j}\right)+i(m_{n_j}-m_{n_i})^2\,\mathrm{Im}\left(C_{n_i n_j}\right)\Big]\Big\},$$
$$F_R^{(2)} = -\frac{g^2}{2m_W}\frac{1}{16\pi^2}B_{\ell_k n_i}B^*_{\ell_m n_j}m_{\ell_m}\Big\{m_{n_i}\Big[(m_{n_i}+m_{n_j})\mathrm{Re}\left(C_{n_i n_j}\right)-i(m_{n_j}-m_{n_i})\mathrm{Im}\left(C_{n_i n_j}\right)\Big]C_0$$
$$+C_{12}\Big[(m_{n_i}+m_{n_j})^2\,\mathrm{Re}\left(C_{n_i n_j}\right)+i(m_{n_j}-m_{n_i})^2\,\mathrm{Im}\left(C_{n_i n_j}\right)\Big]\Big\},$$

where $C_{0,11,12} = C_{0,11,12}(m^2_{\ell_k}, m^2_H, m^2_W, m^2_{n_i}, m^2_{n_j})$.

$$F_L^{(3)} = \frac{g^2}{16\pi^2}B_{\ell_k n_i}B^*_{\ell_m n_i}m_{\ell_k}m_W\,(C_{11}-C_{12})\ ,$$
$$F_R^{(3)} = \frac{g^2}{16\pi^2}B_{\ell_k n_i}B^*_{\ell_m n_i}m_{\ell_m}m_W C_{12}\ ,$$

where $C_{11,12} = C_{11,12}(m^2_{\ell_k}, m^2_H, m^2_{n_i}, m^2_W, m^2_W)$.

$$F_L^{(4)} = \frac{g^2}{4m_W}\frac{1}{16\pi^2}B_{\ell_k n_i}B^*_{\ell_m n_i}m_{\ell_k}\Big\{m^2_{\ell_m}(C_{12}-2C_{11})+m^2_{n_i}(C_{11}-C_{12})-m^2_{n_i}C_0\Big\},$$
$$F_R^{(4)} = \frac{g^2}{4m_W}\frac{1}{16\pi^2}B_{\ell_k n_i}B^*_{\ell_m n_i}m_{\ell_m}\Big\{\tilde{C}_0+2m^2_{\ell_m}C_{11}+m^2_{n_i}C_{12}+(m^2_{\ell_k}-2m^2_H)(C_{11}-C_{12})+2m^2_{n_i}C_0\Big\},$$

where $C_{0,11,12} = C_{0,11,12}(m^2_{\ell_k}, m^2_H, m^2_{n_i}, m^2_W, m^2_W)$ and $\tilde{C}_0 = \tilde{C}_0(m^2_{\ell_k}, m^2_H, m^2_{n_i}, m^2_W, m^2_W)$.

$$F_L^{(5)} = \frac{g^2}{4m_W}\frac{1}{16\pi^2}B_{\ell_k n_i}B^*_{\ell_m n_i}m_{\ell_k}\Big\{\tilde{C}_0+2m^2_{n_i}C_0+(m^2_{n_i}+2m^2_{\ell_k})C_{11}+(m^2_{\ell_m}-m^2_{n_i}-2m^2_H)C_{12}\Big\},$$
$$F_R^{(5)} = -\frac{g^2}{4m_W}\frac{1}{16\pi^2}B_{\ell_k n_i}B^*_{\ell_m n_i}m_{\ell_m}\Big\{m^2_{n_i}C_0+m^2_{\ell_k}C_{11}+(m^2_{\ell_k}-m^2_{n_i})C_{12}\Big\},$$

where $C_{0,11,12} = C_{0,11,12}(m^2_{\ell_k}, m^2_H, m^2_{n_i}, m^2_W, m^2_W)$ and $\tilde{C}_0 = \tilde{C}_0(m^2_{\ell_k}, m^2_H, m^2_{n_i}, m^2_W, m^2_W)$.

$$F_L^{(6)} = \frac{g^2}{4m_W^3}\frac{1}{16\pi^2}B_{\ell_k n_i}B^*_{\ell_m n_i}m_{\ell_k}m^2_H\Big\{m^2_{n_i}(C_0+C_{11})+(m^2_{\ell_m}-m^2_{n_i})C_{12}\Big\},$$
$$F_R^{(6)} = \frac{g^2}{4m_W^3}\frac{1}{16\pi^2}B_{\ell_k n_i}B^*_{\ell_m n_i}m_{\ell_m}m^2_H\Big\{m^2_{n_i}(C_0+C_{12})+m^2_{\ell_k}(C_{11}-C_{12})\Big\},$$

where $C_{0,11,12} = C_{0,11,12}(m^2_{\ell_k}, m^2_H, m^2_{n_i}, m^2_W, m^2_W)$.

$$F_L^{(7)} = \frac{g^2}{2m_W}\frac{1}{16\pi^2}B_{\ell_k n_i}B^*_{\ell_m n_i}\frac{m^2_{\ell_m}m_{\ell_k}}{m^2_{\ell_k}-m^2_{\ell_m}}B_1\ ,$$
$$F_R^{(7)} = \frac{g^2}{2m_W}\frac{1}{16\pi^2}B_{\ell_k n_i}B^*_{\ell_m n_i}\frac{m^2_{\ell_k}m_{\ell_m}}{m^2_{\ell_k}-m^2_{\ell_m}}B_1\ ,$$

$$F_L^{(8)} = \frac{g^2}{4m_W^3}\frac{1}{16\pi^2} B_{\ell_k n_i} B^*_{\ell_m n_i} \frac{m_{\ell_k}}{m_{\ell_k}^2 - m_{\ell_m}^2}\left\{ m_{\ell_m}^2 (m_{\ell_k}^2 + m_{n_i}^2) B_1 + 2m_{n_i}^2 m_{\ell_m}^2 B_0 \right\},$$

$$F_R^{(8)} = \frac{g^2}{4m_W^3}\frac{1}{16\pi^2} B_{\ell_k n_i} B^*_{\ell_m n_i} \frac{m_{\ell_m}}{m_{\ell_k}^2 - m_{\ell_m}^2}\left\{ m_{\ell_k}^2 (m_{\ell_m}^2 + m_{n_i}^2) B_1 + m_{n_i}^2 (m_{\ell_k}^2 + m_{\ell_m}^2) B_0 \right\},$$

where $B_{0,1} = B_{0,1}(m_{\ell_k}^2, m_{n_i}^2, m_W^2)$.

$$F_L^{(9)} = \frac{g^2}{2m_W}\frac{1}{16\pi^2} B_{\ell_k n_i} B^*_{\ell_m n_i} \frac{m_{\ell_m}^2 m_{\ell_k}}{m_{\ell_m}^2 - m_{\ell_k}^2} B_1 ,$$

$$F_R^{(9)} = \frac{g^2}{2m_W}\frac{1}{16\pi^2} B_{\ell_k n_i} B^*_{\ell_m n_i} \frac{m_{\ell_k}^2 m_{\ell_m}}{m_{\ell_m}^2 - m_{\ell_k}^2} B_1 ,$$

$$F_L^{(10)} = \frac{g^2}{4m_W^3}\frac{1}{16\pi^2} B_{\ell_k n_i} B^*_{\ell_m n_i} \frac{m_{\ell_k}}{m_{\ell_m}^2 - m_{\ell_k}^2}\left\{ m_{\ell_m}^2 (m_{\ell_k}^2 + m_{n_i}^2) B_1 + m_{n_i}^2 (m_{\ell_k}^2 + m_{\ell_m}^2) B_0 \right\},$$

$$F_R^{(10)} = \frac{g^2}{4m_W^3}\frac{1}{16\pi^2} B_{\ell_k n_i} B^*_{\ell_m n_i} \frac{m_{\ell_m}}{m_{\ell_m}^2 - m_{\ell_k}^2}\left\{ m_{\ell_k}^2 (m_{\ell_m}^2 + m_{n_i}^2) B_1 + 2m_{n_i}^2 m_{\ell_k}^2 B_0 \right\},$$

where $B_{0,1} = B_{0,1}(m_{\ell_m}^2, m_{n_i}^2, m_W^2)$.

Appendix D
Form Factors for LFVHD in the SUSY-ISS Model

In this Appendix we present the form factors that correspond to the diagrams of Fig. 4.12, together with the relevant couplings needed for performing the computation. The original calculation in the SUSY type-I seesaw was done in Ref. [9] in the mass basis and in the Feynman-'t Hooft gauge, which we have adapted to the SUSY-ISS model. In order to do that, we have derived the new relevant couplings with respect to the SUSY type-I seesaw model, which we give in the following.

When compared with the SUSY type-I seesaw, only the coupling factors $A^{(\ell)}_{R\alpha j}$ and $g_{H_x\tilde{\nu}_\alpha\tilde{\nu}_\beta}$ are modified. In the SUSY inverse seesaw, they are defined in the mass basis with diagonal charged leptons by

$$
\begin{aligned}
A^{(e,\mu,\tau)}_{R\alpha j} &= \tilde{U}_{(1,2,3)\alpha} V_{j1} - \frac{m_{D(1,2,3)k}}{\sqrt{2} m_W \sin\beta} \tilde{U}_{k+9,\alpha} V_{j2}\,,\\
g_{H_x\tilde{\nu}_\alpha\tilde{\nu}_\beta} &= -ig\Big[(g^{(x)}_{LL,\nu})_{ik}\tilde{U}^*_{i\alpha}\tilde{U}_{k\beta} + (g^{(x)}_{RR,\nu})_{ik}\tilde{U}^*_{i+9,\alpha}\tilde{U}_{k+9,\beta} + (g^{(x)}_{LR,\nu})_{ik}\tilde{U}^*_{i,\alpha}\tilde{U}_{k+9,\beta}\\
&\qquad + (g^{(x)}_{LR,\nu})^*_{ik}\tilde{U}^*_{k+9,\alpha}\tilde{U}_{i,\beta} + (g^{(x)}_{LX,\nu})_{ik}\tilde{U}^*_{i,\alpha}\tilde{U}_{k+12,\beta} + (g^{(x)}_{LX,\nu})^*_{ik}\tilde{U}^*_{k+12,\alpha}\tilde{U}_{i,\beta}\Big]\,,\\
(g^{(x)}_{LL,\nu})_{ik} &= -\frac{m_Z}{2\cos\theta_W}\sigma^{(x)}_3\delta_{ik} + \frac{(m_D m_D^\dagger)_{ik}}{m_W \sin\beta}\sigma^{(x)}_6\,,\\
(g^{(x)}_{RR,\nu})_{ik} &= \frac{(m_D^\dagger m_D)_{ik}}{m_W \sin\beta}\sigma^{(x)}_6\,,\\
(g^{(x)}_{LR,\nu})_{ik} &= \frac{(m_D A_\nu^\dagger)_{ik}}{2m_W \sin\beta}\sigma^{(x)}_2 + \frac{\mu}{2m_W\sin\beta}(m_D)_{ik}\sigma^{(x)}_7\,,\\
(g^{(x)}_{LX,\nu})_{ik} &= \frac{(m_D M_R^*)_{ik}}{2m_W \sin\beta}\sigma^{(x)}_2\,,
\end{aligned}
\tag{D.1}
$$

which are summed over the internal indices, with $i, k = 1, \ldots, 3$ and x referring to $H_x = (h, H, A)$. We reproduce below, for completeness, the unmodified coupling factors from Ref. [9] (correcting a typo in $W^{(x)}_{Rij}$) in the mass basis with diagonal charged leptons

X. Marcano, *Lepton Flavor Violation from Low Scale Seesaw Neutrinos with Masses Reachable at the LHC*, Springer Theses, https://doi.org/10.1007/978-3-319-94604-7

$$
\begin{aligned}
A^{(e,\mu,\tau)}_{L\alpha j} &= -\frac{m_{e,\mu,\tau}}{\sqrt{2}m_W cos\beta} U^*_{j2}\tilde{U}_{(1,2,3)\alpha}\,,\\
B^{(e,\mu,\tau)}_{L\alpha a} &= \sqrt{2}\left[\frac{m_{e,\mu,\tau}}{2m_W cos\beta} N^*_{a3} R^{(\ell)}_{(1,3,5)\alpha} + \left[\sin\theta_W N'^*_{a1} - \frac{\sin^2\theta_W}{cos\theta_W} N'^*_{a2}\right] R^{(\ell)}_{(2,4,6)\alpha}\right],\\
B^{(e,\mu,\tau)}_{R\alpha a} &= \sqrt{2}\left[\left(-\sin\theta_W N'_{a1} - \frac{1}{\cos\theta_W}(\frac{1}{2} - \sin^2\theta_W) N'_{a2}\right) R^{(\ell)}_{(1,3,5)\alpha} + \frac{m_{e,\mu,\tau}}{2m_W\cos\beta} N_{a3} R^{(\ell)}_{(2,4,6)\alpha}\right],\\
W^{(x)}_{Lij} &= \frac{1}{\sqrt{2}}\left(-\sigma^{(x)}_1 U^*_{j2}V^*_{i1} + \sigma^{(x)}_2 U^*_{j1}V^*_{i2}\right)\,,\\
W^{(x)}_{Rij} &= \frac{1}{\sqrt{2}}\left(-\sigma^{(x)*}_1 U_{i2}V_{j1} + \sigma^{(x)*}_2 U_{i1}V_{j2}\right)\,,\\
D^{(x)}_{Lab} &= \frac{1}{2\cos\theta_W}\Big[(\sin\theta_W N^*_{b1} - \cos\theta_W N^*_{b2})(\sigma^{(x)}_1 N^*_{a3} + \sigma^{(x)}_2 N^*_{a4})\\
&\quad + (\sin\theta_W N^*_{a1} - \cos\theta_W N^*_{a2})(\sigma^{(x)}_1 N^*_{b3} + \sigma^{(x)}_2 N^*_{b4})\;\Big]\,,\\
D^{(x)}_{Rab} &= D^{(x)*}_{Lab}\,,\\
S^{(x)}_{L,\ell} &= -\frac{m_\ell}{2m_W\cos\beta}\sigma^{(x)*}_1\,,\\
S^{(x)}_{R,\ell} &= S^{(x)*}_{L,\ell}\,,\\
g_{H_x\tilde{\ell}_\alpha\tilde{\ell}_\beta} &= -ig\Big[g^{(x)}_{LL,e}R^{*(\ell)}_{1\alpha}R^{(\ell)}_{1\beta} + g^{(x)}_{RR,e}R^{*(\ell)}_{2\alpha}R^{(\ell)}_{2\beta} + g^{(x)}_{LR,e}R^{*(\ell)}_{1\alpha}R^{(\ell)}_{2\beta} + g^{(x)}_{RL,e}R^{*(\ell)}_{2\alpha}R^{(\ell)}_{1\beta}\\
&\quad + g^{(x)}_{LL,\mu}R^{*(\ell)}_{3\alpha}R^{(\ell)}_{3\beta} + g^{(x)}_{RR,\mu}R^{*(\ell)}_{4\alpha}R^{(\ell)}_{4\beta} + g^{(x)}_{LR,\mu}R^{*(\ell)}_{3\alpha}R^{(\ell)}_{4\beta} + g^{(x)}_{RL,\mu}R^{*(\ell)}_{4\alpha}R^{(\ell)}_{3\beta}\\
&\quad + g^{(x)}_{LL,\tau}R^{*(\ell)}_{5\alpha}R^{(\ell)}_{5\beta} + g^{(x)}_{RR,\tau}R^{*(\ell)}_{6\alpha}R^{(\ell)}_{6\beta} + g^{(x)}_{LR,\tau}R^{*(\ell)}_{5\alpha}R^{(\ell)}_{6\beta} + g^{(x)}_{RL,\tau}R^{*(\ell)}_{6\alpha}R^{(\ell)}_{5\beta}\Big]\,,\\
g^{(x)}_{LL,\ell} &= \frac{m_Z}{\cos\theta_W}\sigma^{(x)}_3\left(\frac{1}{2} - \sin^2\theta_W\right) + \frac{m^2_\ell}{m_W\cos\beta}\sigma^{(x)}_4\,,\\
g^{(x)}_{RR,\ell} &= \frac{m_Z}{\cos\theta_W}\sigma^{(x)}_3\left(\sin^2\theta_W\right) + \frac{m^2_\ell}{m_W\cos\beta}\sigma^{(x)}_4\,,\\
g^{(x)}_{LR,\ell} &= \left(-\sigma^{(x)}_1 A_\ell - \sigma^{(x)}_5\mu\right)\frac{m_\ell}{2m_W\cos\beta}\,,\\
g^{(x)}_{RL,\ell} &= g^{(x)*}_{LR,\ell}\,.
\end{aligned}
\tag{D.2}
$$

Here, $\tilde{U}$ is the sneutrino rotation matrix defined in Eq. (2.71), $R^{(\ell)}$ the rotation of charged sleptons according to Eq. (2.76), U and V are the rotation matrices for the charginos, N the ones that rotates the neutralinos, with $N^{(')}_{a1,a2}$ defined in Eq. (2.75), and,

$$
\begin{aligned}
&\sigma^{(x)}_1 = \begin{pmatrix}\sin\alpha\\ -\cos\alpha\\ i\sin\beta\end{pmatrix},\quad \sigma^{(x)}_2 = \begin{pmatrix}\cos\alpha\\ \sin\alpha\\ -i\cos\beta\end{pmatrix},\quad \sigma^{(x)}_3 = \begin{pmatrix}\sin(\alpha+\beta)\\ -\cos(\alpha+\beta)\\ 0\end{pmatrix},\quad \sigma^{(x)}_4 = \begin{pmatrix}-\sin\alpha\\ \cos\alpha\\ 0\end{pmatrix},\\
&\sigma^{(x)}_5 = \begin{pmatrix}\cos\alpha\\ \sin\alpha\\ i\cos\beta\end{pmatrix},\quad \sigma^{(x)}_6 = \begin{pmatrix}\cos\alpha\\ \sin\alpha\\ 0\end{pmatrix},\quad \sigma^{(x)}_7 = \begin{pmatrix}\sin\alpha\\ -\cos\alpha\\ -i\sin\beta\end{pmatrix},\quad \text{for } H_x = \begin{pmatrix}h^0\\ H^0\\ A^0\end{pmatrix}.
\end{aligned}
\tag{D.3}
$$

Besides using these new couplings, the only changes required to adapt the original form factors to the SUSY-ISS model are the sum over sneutrinos that has to be extended to the 18 mass eigenstates. In the following formulas, summation over all indices corresponding to internal propagators is understood, meaning $\alpha, \beta = 1, \ldots, 18$ for the sneutrinos, $i, j = 1, 2$ for the charginos, $\alpha, \beta = 1, \ldots, 6$ for the charged sleptons and $a, b = 1, \ldots, 4$ for the neutralinos. The contributions from the sneutrino-chargino loops are given by,

$$
\begin{aligned}
F_{L,x}^{(1)} &= -\frac{g^2}{16\pi^2}\Big[\Big(B_0 + m_{\tilde{\nu}_\alpha}^2 C_0 + m_{\ell_m}^2 C_{12} + m_{\ell_k}^2 (C_{11} - C_{12})\Big)\,\kappa_{L1}^{x,\tilde{\chi}^-} \\
&\quad + m_{\ell_k} m_{\ell_m} (C_{11} + C_0)\,\kappa_{L2}^{x,\tilde{\chi}^-} + m_{\ell_k} m_{\tilde{\chi}_j^-} (C_{11} - C_{12} + C_0)\,\kappa_{L3}^{x,\tilde{\chi}^-} + m_{\ell_m} m_{\tilde{\chi}_j^-} C_{12}\,\kappa_{L4}^{x,\tilde{\chi}^-} \\
&\quad + m_{\ell_k} m_{\tilde{\chi}_i^-} (C_{11} - C_{12})\,\kappa_{L5}^{x,\tilde{\chi}^-} + m_{\ell_m} m_{\tilde{\chi}_i^-} (C_{12} + C_0)\,\kappa_{L6}^{x,\tilde{\chi}^-} + m_{\tilde{\chi}_i^-} m_{\tilde{\chi}_j^-} C_0\,\kappa_{L7}^{x,\tilde{\chi}^-}\Big], \\
F_{L,x}^{(2)} &= -\frac{i g g_{H_x \tilde{\nu}_\alpha \tilde{\nu}_\beta}}{16\pi^2}\Big[-m_{\ell_k}(C_{11} - C_{12})\,\iota_{L1}^{x,\tilde{\chi}^-} - m_{\ell_m} C_{12}\,\iota_{L2}^{x,\tilde{\chi}^-} + m_{\tilde{\chi}_i^-} C_0\,\iota_{L3}^{x,\tilde{\chi}^-}\Big], \\
F_{L,x}^{(3)} &= \frac{-S_{L,\ell_m}^{(x)}}{m_{\ell_k}^2 - m_{\ell_m}^2}\Big[m_{\ell_k}^2 \Sigma_R^{\tilde{\chi}^-}(m_{\ell_k}^2) + m_{\ell_k}^2 \Sigma_{Rs}^{\tilde{\chi}^-}(m_{\ell_k}^2) + m_{\ell_m}\Big(m_{\ell_k} \Sigma_L^{\tilde{\chi}^-}(m_{\ell_k}^2) + m_{\ell_k} \Sigma_{Ls}^{\tilde{\chi}^-}(m_{\ell_k}^2)\Big)\Big], \\
F_{L,x}^{(4)} &= \frac{-S_{L,\ell_k}^{(x)}}{m_{\ell_m}^2 - m_{\ell_k}^2}\Big[m_{\ell_m}^2 \Sigma_L^{\tilde{\chi}^-}(m_{\ell_m}^2) + m_{\ell_m} m_{\ell_k} \Sigma_{Rs}^{\tilde{\chi}^-}(m_{\ell_m}^2) + m_{\ell_k}\Big(m_{\ell_m} \Sigma_R^{\tilde{\chi}^-}(m_{\ell_m}^2) + m_{\ell_k} \Sigma_{Ls}^{\tilde{\chi}^-}(m_{\ell_m}^2)\Big)\Big],
\end{aligned}
\tag{D.4}
$$

where the contributions from slepton-neutralino loops read as,

$$
\begin{aligned}
F_{L,x}^{(5)} &= -\frac{g^2}{16\pi^2}\Big[\Big(B_0 + m_{\tilde{\ell}_\alpha}^2 C_0 + m_{\ell_m}^2 C_{12} + m_{\ell_k}^2 (C_{11} - C_{12})\Big)\,\kappa_{L1}^{x,\tilde{\chi}^0} \\
&\quad + m_{\ell_k} m_{\ell_m} (C_{11} + C_0)\,\kappa_{L2}^{x,\tilde{\chi}^0} + m_{\ell_k} m_{\tilde{\chi}_b^0} (C_{11} - C_{12} + C_0)\,\kappa_{L3}^{x,\tilde{\chi}^0} + m_{\ell_m} m_{\tilde{\chi}_b^0} C_{12}\,\kappa_{L4}^{x,\tilde{\chi}^0} \\
&\quad + m_{\ell_k} m_{\tilde{\chi}_a^0} (C_{11} - C_{12})\,\kappa_{L5}^{x,\tilde{\chi}^0} + m_{\ell_m} m_{\tilde{\chi}_a^0} (C_{12} + C_0)\,\kappa_{L6}^{x,\tilde{\chi}^0} + m_{\tilde{\chi}_a^0} m_{\tilde{\chi}_b^0} C_0\,\kappa_{L7}^{x,\tilde{\chi}^0}\Big], \\
F_{L,x}^{(6)} &= -\frac{i g g_{H_x \tilde{\ell}_\alpha \tilde{\ell}_\beta}}{16\pi^2}\Big[-m_{\ell_k}(C_{11} - C_{12})\,\iota_{L1}^{x,\tilde{\chi}^0} - m_{\ell_m} C_{12}\,\iota_{L2}^{x,\tilde{\chi}^0} + m_{\tilde{\chi}_a^0} C_0\,\iota_{L3}^{x,\tilde{\chi}^0}\Big], \\
F_{L,x}^{(7)} &= \frac{-S_{L,\ell_m}^{(x)}}{m_{\ell_k}^2 - m_{\ell_m}^2}\Big[m_{\ell_k}^2 \Sigma_R^{\tilde{\chi}^0}(m_{\ell_k}^2) + m_{\ell_k}^2 \Sigma_{Rs}^{\tilde{\chi}^0}(m_{\ell_k}^2) + m_{\ell_m}\Big(m_{\ell_k} \Sigma_L^{\tilde{\chi}^0}(m_{\ell_k}^2) + m_{\ell_k} \Sigma_{Ls}^{\tilde{\chi}^0}(m_{\ell_k}^2)\Big)\Big], \\
F_{L,x}^{(8)} &= \frac{-S_{L,\ell_k}^{(x)}}{m_{\ell_m}^2 - m_{\ell_k}^2}\Big[m_{\ell_m}^2 \Sigma_L^{\tilde{\chi}^0}(m_{\ell_m}^2) + m_{\ell_m} m_{\ell_k} \Sigma_{Rs}^{\tilde{\chi}^0}(m_{\ell_m}^2) + m_{\ell_k}\Big(m_{\ell_m} \Sigma_R^{\tilde{\chi}^0}(m_{\ell_m}^2) + m_{\ell_k} \Sigma_{Ls}^{\tilde{\chi}^0}(m_{\ell_m}^2)\Big)\Big],
\end{aligned}
\tag{D.5}
$$

where,

$$
B_0 = \begin{cases} B_0(m_{H_x}^2, m_{\tilde{\chi}_i^-}^2, m_{\tilde{\chi}_j^-}^2) \text{ in } F_{L,x}^{(1)}, \\ B_0(m_{H_x}^2, m_{\tilde{\chi}_a^0}^2, m_{\tilde{\chi}_b^0}^2) \text{ in } F_{L,x}^{(5)}, \end{cases}
$$

and

$$
C_{0,11,12} = \begin{cases} C_{0,11,12}(m_{\ell_k}^2, m_{H_x}^2, m_{\tilde{\nu}_\alpha}^2, m_{\tilde{\chi}_i^-}^2, m_{\tilde{\chi}_j^-}^2) \text{ in } F_{L,x}^{(1)}, \\ C_{0,11,12}(m_{\ell_k}^2, m_{H_x}^2, m_{\tilde{\chi}_i^-}^2, m_{\tilde{\nu}_\alpha}^2, m_{\tilde{\nu}_\beta}^2) \text{ in } F_{L,x}^{(2)}, \\ C_{0,11,12}(m_{\ell_k}^2, m_{H_x}^2, m_{\tilde{l}_\alpha}^2, m_{\tilde{\chi}_a^0}^2, m_{\tilde{\chi}_b^0}^2) \text{ in } F_{L,x}^{(5)}, \\ C_{0,11,12}(m_{\ell_k}^2, m_{H_x}^2, m_{\tilde{\chi}_a^0}^2, m_{\tilde{l}_\alpha}^2, m_{\tilde{l}_\beta}^2) \text{ in } F_{L,x}^{(6)}. \end{cases}
$$

The couplings and self-energies from the neutralino contributions to the form factors were defined as

$$
\begin{aligned}
\kappa_{L1}^{x,\tilde{\chi}^0} &= B^{(\ell_k)}_{L\alpha a} D^{(x)}_{Rab} B^{(\ell_m)*}_{R\alpha b}\,, \quad \iota_{L1}^{x,\tilde{\chi}^0} = B^{(\ell_k)}_{R\alpha a} B^{(\ell_m)*}_{R\beta a}\,,\\
\kappa_{L2}^{x,\tilde{\chi}^0} &= B^{(\ell_k)}_{R\alpha a} D^{(x)}_{Lab} B^{(\ell_m)*}_{L\alpha b}\,, \quad \iota_{L2}^{x,\tilde{\chi}^0} = B^{(\ell_k)}_{L\alpha a} B^{(\ell_m)*}_{L\beta a}\,,\\
\kappa_{L3}^{x,\tilde{\chi}^0} &= B^{(\ell_k)}_{R\alpha a} D^{(x)}_{Lab} B^{(\ell_m)*}_{R\alpha b}\,, \quad \iota_{L3}^{x,\tilde{\chi}^0} = B^{(\ell_k)}_{L\alpha a} B^{(\ell_m)*}_{R\beta a}\,,\\
\kappa_{L4}^{x,\tilde{\chi}^0} &= B^{(\ell_k)}_{L\alpha a} D^{(x)}_{Rab} B^{(\ell_m)*}_{L\alpha b}\,,\\
\kappa_{L5}^{x,\tilde{\chi}^0} &= B^{(\ell_k)}_{R\alpha a} D^{(x)}_{Rab} B^{(\ell_m)*}_{R\alpha b}\,,\\
\kappa_{L6}^{x,\tilde{\chi}^0} &= B^{(\ell_k)}_{L\alpha a} D^{(x)}_{Lab} B^{(\ell_m)*}_{L\alpha b}\,,\\
\kappa_{L7}^{x,\tilde{\chi}^0} &= B^{(\ell_k)}_{L\alpha a} D^{(x)}_{Lab} B^{(\ell_m)*}_{R\alpha b}\,,
\end{aligned}
$$

$$
\begin{aligned}
\Sigma_L^{\tilde{\chi}^0}(k^2) &= -\frac{g^2}{16\pi^2} B_1(k^2, m^2_{\tilde{\chi}^0_a}, m^2_{\tilde{\ell}_\alpha}) B^{(\ell_k)}_{R\,\alpha a} B^{(\ell_m)*}_{R\,\alpha a}\,,\\
m_{\ell_k}\Sigma_{Ls}^{\tilde{\chi}^0}(k^2) &= \frac{g^2 m_{\tilde{\chi}^0_a}}{16\pi^2} B_0(k^2, m^2_{\tilde{\chi}^0_a}, m^2_{\tilde{\ell}_\alpha}) B^{(\ell_k)}_{L\,\alpha a} B^{(\ell_m)*}_{R\,\alpha a}\,. \qquad \text{(D.6)}
\end{aligned}
$$

The couplings and self energies from the chargino contributions to the form factors, $\kappa^{x,\tilde{\chi}^-}$, $\iota^{x,\tilde{\chi}^-}$, and $\Sigma^{\tilde{\chi}^-}$ can be obtained from the previous expressions $\kappa^{x,\tilde{\chi}^0}$, $\iota^{x,\tilde{\chi}^0}$ and $\Sigma^{\tilde{\chi}^0}$ by using the following replacement rules $m_{\tilde{\chi}^0_a} \to m_{\tilde{\chi}^-_i}$, $m_{\tilde{\ell}_\alpha} \to m_{\tilde{\nu}_\alpha}$, $B^{(\ell)} \to A^{(\ell)}$, $D^{(x)} \to W^{(x)}$, $a \to i$, and $b \to j$.

The form factors $F^{(i)}_{R,x}, i = 1, \ldots, 8$ can be obtained from $F^{(i)}_{L,x}, i = 1, \ldots, 8$ through the exchange $L \leftrightarrow R$ in all places.

Appendix E
Formulas for the MIA Computation

In this Appendix we give the technical details of our MIA computation of the LFV Higgs decay rates in Sect. 4.3. More concretely, we explain the derivation of the *fat propagators*, used in our MIA computation in the Feynman-'t Hooft and unitary gauges. We give our results for the form factors, up to $\mathcal{O}(Y_\nu^4)$ order in the MIA expansion, showing explicitly that we obtain the same in both gauges. Furthermore, we explore the large M_R limit and derive useful approximate expressions for the loop integrals needed for computing the $H\ell_k\ell_m$ effective vertex of Eq. (4.34).

E.1 Modified Neutrino Propagators

Here we derive the right-handed neutrino *fat propagators* used for the computations in Sect. 4.3. The idea is to resum all possible large flavor diagonal M_R mass insertions, which we denote with a dot in order to distinguish them from the flavor off-diagonal ones, in a way such that the large mass appears effectively in the denominator of the propagators of the new states.

In order to make a MIA computation in the electroweak basis (ν_L , ν_R^c , X^c), we need to take into account all the propagators and mass insertions given by the neutrino mass matrix. In the ISS model we are considering, this mass matrix is given by Eq. (2.35), which we repeat here for completeness:

$$M_{\rm ISS} = \begin{pmatrix} 0 & m_D & 0 \\ m_D^T & 0 & M_R \\ 0 & M_R^T & \mu_X \end{pmatrix} . \tag{E.1}$$

From this mass matrix, we obtain the propagators and mass insertions summarized in Fig. E.1. It is important to notice the presence of the P_L and P_R projectors for the chiral fields, which have been properly added according to:

X. Marcano, *Lepton Flavor Violation from Low Scale Seesaw Neutrinos with Masses Reachable at the LHC*, Springer Theses, https://doi.org/10.1007/978-3-319-94604-7

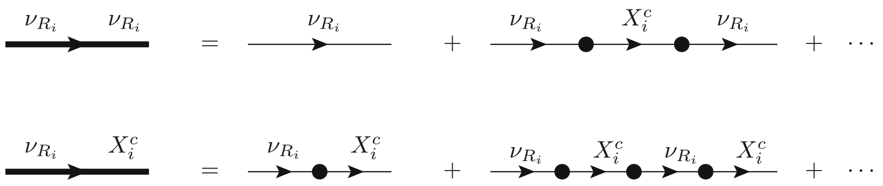

Fig. E.1 Propagators and mass insertions in the electroweak basis. Big black dots denote flavor diagonal mass insertions

$$\begin{aligned} \nu_L^c, \nu_R, X &\longrightarrow \textbf{RH fields}, \\ \nu_L, \nu_R^c, X^c &\longrightarrow \textbf{LH fields}. \end{aligned} \tag{E.2}$$

As previously mentioned, there are three types of mass insertions and they are controlled by the matrices m_D, M_R and μ_X. The mass insertions M_R that relate ν_R and X fields are taken to be flavor diagonal and are denoted by a big dot in Fig. E.1. On the other hand, crosses indicate flavor non-diagonal insertions coming from m_D (big cross) and μ_X (small cross), which connect the fields ν_L-ν_R and two X's respectively. Nevertheless, given that we work under the assumption that μ_X is a tiny scale, we neglect μ_X mass insertions for our LFVHD computations and, therefore, we consider m_D as the only relevant LFV insertion.

Since our motivation in this work is to make a MIA computation for LFV H decays by perturbatively inserting LFV mass insertions, we find convenient to take into account first the effects of all possible flavor diagonal M_R insertions. Moreover, this procedure allows us to consider M_R also as a heavy scale so we can define an effective vertex for the H-ℓ_i-ℓ_j interaction. This can be done by defining two types of modified propagators, one for same initial and final state consisting of all possible even number of M_R insertions (which we call *fat propagator*), and one for different initial and final states with an odd number of M_R insertions, as it is schematically shown in Fig. E.2. We can then define two modified propagators starting with ν_R by adding the corresponding series:

$$\begin{aligned} \mathrm{Prop}_{\nu_{R_i}\to\nu_{R_i}} &= P_R \frac{i}{\not p} P_L + P_R \frac{i}{\not p} P_L \left(-iM_{R_i}^* P_L\right) P_L \frac{i}{\not p} P_R \left(-iM_{R_i} P_R\right) P_R \frac{i}{\not p} P_L + \cdots \\ &= P_R \frac{i}{\not p} \sum_{n\geq 0} \left(\frac{|M_{R_i}|^2}{p^2}\right)^n P_L = P_R \frac{i\not p}{p^2 - |M_{R_i}|^2} P_L \,, \end{aligned} \tag{E.3}$$

$$\begin{aligned} \mathrm{Prop}_{\nu_{R_i}\to X_i^c} &= P_L \frac{i}{\not p} P_R \left(-iM_{R_i} P_R\right) P_R \frac{i}{\not p} P_L \\ &+ P_L \frac{i}{\not p} P_R \left(-iM_{R_i} P_R\right) P_R \frac{i}{\not p} P_L \left(-iM_{R_i}^* P_L\right) P_L \frac{i}{\not p} P_R \left(-iM_{R_i} P_R\right) P_R \frac{i}{\not p} P_L + \cdots \\ &= P_L \frac{iM_{R_i}}{p^2} \sum_{n\geq 0} \left(\frac{|M_{R_i}|^2}{p^2}\right)^n P_L = P_L \frac{iM_{R_i}}{p^2 - |M_{R_i}|^2} P_L \,. \end{aligned} \tag{E.4}$$

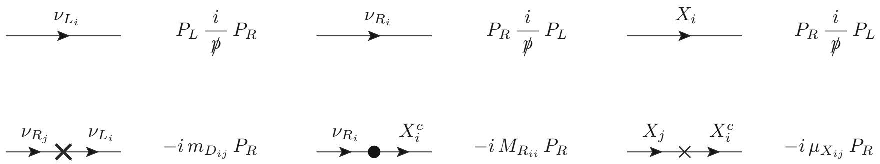

Fig. E.2 Modified neutrino propagators after resuming an infinite number of M_R mass insertions, denoted here by big black dots. We use fat arrow lines with same (different) initial and final states to denote that all possible even (odd) number of M_R insertions have been considered. The fat lines with same initial and final ν_R states are referred to in this work as *fat propagators*

And we can similarly define other modified propagators considering also the ν_R^c and X states. In the present study of LFVHD, it happens that the X fields do not interact with any of the external legs involved in the LFV process we want to compute. Consequently, to take into account the effects from X in the LFVHD, it is enough to consider the *fat propagator* in Eq. (E.3) when computing the one-loop contributions to $H \to \ell_k \bar{\ell}_m$.

E.2 MIA Form Factors in the Feynman-'t Hooft Gauge

Here we present the analytical results for the form factors $F_{L,R}$ involved in the computation of the LFVHD decay rates when computed with the MIA to one-loop order. We consider the leading order corrections, $\mathcal{O}(Y_\nu^2)$, and the next to leading corrections, $\mathcal{O}(Y_\nu^4)$, as explained in the text. This means the computation of all the one-loop diagrams in Figs. 4.18, 4.19, 4.20 and 4.21. They are written in terms of the usual one-loop functions for the two-point $B's$, three-point $C's$, and four-point $D's$ functions. We follow these definitions and conventions:

$$\mu^{4-D} \int \frac{d^D k}{(2\pi)^D} \frac{\{1; k^\mu\}}{[k^2 - m_1^2][(k+p_1)^2 - m_2^2]} = \frac{i}{16\pi^2} \left\{B_0;\, p_1^\mu B_1\right\}(p_1, m_1, m_2)\,, \tag{E.5}$$

$$\begin{aligned}&\mu^{4-D} \int \frac{d^D k}{(2\pi)^D} \frac{\{1; k^2; k^\mu\}}{[k^2 - m_1^2][(k+p_1)^2 - m_2^2][(k+p_1+p_2)^2 - m_3^2]} \\ &\quad = \frac{i}{16\pi^2} \left\{C_0;\, \tilde{C}_0;\, p_1^\mu C_{11} + p_2^\mu C_{12}\right\}(p_1, p_2, m_1, m_2, m_3)\,,\end{aligned} \tag{E.6}$$

$$\begin{aligned}&\mu^{4-D} \int \frac{d^D k}{(2\pi)^D} \frac{\{1; k^2; k^\mu\}}{[k^2 - m_1^2][(k+p_1)^2 - m_2^2][(k+p_1+p_2)^2 - m_3^2][(k+p_1+p_2+p_3)^2 - m_4^2]} \\ &\quad = \frac{i}{16\pi^2} \left\{D_0;\, \tilde{D}_0;\, p_1^\mu D_{11} + p_2^\mu D_{12} + p_3^\mu D_{13}\right\}(p_1, p_2, p_3, m_1, m_2, m_3, m_4)\,.\end{aligned} \tag{E.7}$$

We start with the left-handed form factors and present the contributions diagram by diagram, following the notation explained in the text and shortening $m_{k,m} \equiv m_{\ell_{k,m}}$. We will restrict ourselves to the dominant contributions, meaning those that will provide $\mathcal{O}(v^2/M_R^2)$ terms when doing the large M_R expansion, as explained in the next Appendix. For instance, contributions from loop functions of type D_i where M_R appears in two of the mass arguments go as $1/M_R^4$ and provide subdominant corrections that are not considered here.

The results of the $\mathcal{O}(Y_\nu^2)$ contributions are:

$$
\begin{aligned}
F_L^{\mathrm{MIA(1)\ (Y^2)}} &= \frac{1}{32\pi^2}\frac{m_k}{m_W}\left(Y_\nu Y_\nu^\dagger\right)^{km}\Big((\tilde{C}_0 + m_k^2(C_{11}-C_{12}) + m_m^2 C_{12})_{(1a)} \\
&\quad + m_m^2(C_0 + C_{11})_{(1b)} - m_m^2(C_{12})_{(1c)} - m_m^2(C_0 + C_{12})_{(1d)}\Big)\,, \\
F_L^{\mathrm{MIA(2)\ (Y^2)}} &= \frac{-1}{16\pi^2} m_k m_W \left(Y_\nu Y_\nu^\dagger\right)^{km}\Big((C_0 + C_{11} - C_{12})_{(2a)} + (C_{11} - C_{12})_{(2b)}\Big)\,, \\
F_L^{\mathrm{MIA(3)\ (Y^2)}} &= \frac{1}{8\pi^2} m_k m_W^3 \left(Y_\nu Y_\nu^\dagger\right)^{km}(D_{12} - D_{13})_{(3a)}\,, \\
F_L^{\mathrm{MIA(4)\ (Y^2)}} &= \frac{-1}{32\pi^2} m_k m_W \left(Y_\nu Y_\nu^\dagger\right)^{km}\Big((C_0 - C_{11} + C_{12})_{(4a)} + m_m^2(2D_{12} - D_{13})_{(4b)}\Big)\,, \\
F_L^{\mathrm{MIA(5)\ (Y^2)}} &= \frac{1}{32\pi^2} m_k m_W \left(Y_\nu Y_\nu^\dagger\right)^{km}\Big((2C_0 + C_{11} - C_{12})_{(5a)} \\
&\quad + (C_0 + 2m_k^2 D_{12} - (2m_H^2 - m_m^2)D_{13})_{(5b)}\Big)\,, \\
F_L^{\mathrm{MIA(6)\ (Y^2)}} &= \frac{1}{32\pi^2}\frac{m_k}{m_W} m_H^2 \left(Y_\nu Y_\nu^\dagger\right)^{km}\Big((C_{11} - C_{12})_{(6a)} + (C_0)_{(6c)} + m_m^2(D_{13})_{(6d)}\Big)\,, \\
F_L^{\mathrm{MIA(7)\ (Y^2)}} &= \frac{1}{16\pi^2} m_k m_W \frac{m_m^2}{m_k^2 - m_m^2}\left(Y_\nu Y_\nu^\dagger\right)^{km}(C_{12})_{(7a)}\,, \\
F_L^{\mathrm{MIA(8)\ (Y^2)}} &= \frac{1}{32\pi^2}\frac{m_k}{m_W}\frac{m_m^2}{m_k^2 - m_m^2}\left(Y_\nu Y_\nu^\dagger\right)^{km}\Big((B_1)_{(8a)} + (B_0)_{(8b)} + (B_0)_{(8c)} + m_k^2(C_{12})_{(8d)}\Big)\,, \\
F_L^{\mathrm{MIA(9)\ (Y^2)}} &= \frac{-1}{16\pi^2} m_k m_W \frac{m_m^2}{m_k^2 - m_m^2}\left(Y_\nu Y_\nu^\dagger\right)^{km}(C_{12})_{(9a)}\,, \\
F_L^{\mathrm{MIA(10)\ (Y^2)}} &= \frac{-1}{32\pi^2}\frac{m_k}{m_W}\frac{m_m^2}{m_k^2 - m_m^2}\left(Y_\nu Y_\nu^\dagger\right)^{km}\Big((B_1)_{(10a)} + (B_0)_{(10b)} + \frac{m_k^2}{m_m^2}(B_0)_{(10c)} \\
&\quad + m_k^2(C_{12})_{(10d)}\Big)\,.
\end{aligned}
\tag{E.8}
$$

The results of the dominant $\mathcal{O}(Y_\nu^4)$ contributions are:

$$
\begin{aligned}
F_L^{\mathrm{MIA(1)\ (Y^4)}} &= \frac{1}{32\pi^2}\frac{m_k}{m_W}\left(Y_\nu Y_\nu^\dagger Y_\nu Y_\nu^\dagger\right)^{km} v^2\Big(-(C_{11} - C_{12})_{(1e)} - (C_{11} - C_{12} + C_0)_{(1f)} \\
&\quad + (\tilde{D}_0)_{(1g)} + (\tilde{D}_0)_{(1h)} + (C_0)_{(1j)}\Big)\,, \\
F_L^{\mathrm{MIA(8)\ (Y^4)}} &= \frac{1}{32\pi^2}\frac{m_k}{m_W}\frac{m_m^2}{m_k^2 - m_m^2}\left(Y_\nu Y_\nu^\dagger Y_\nu Y_\nu^\dagger\right)^{km} v^2\Big((C_{12})_{(8e)} + (C_0)_{(8f)} + (C_0)_{(8g)}\Big)\,, \\
F_L^{\mathrm{MIA(10)\ (Y^4)}} &= \frac{-1}{32\pi^2}\frac{m_k}{m_W}\frac{m_m^2}{m_k^2 - m_m^2}\left(Y_\nu Y_\nu^\dagger Y_\nu Y_\nu^\dagger\right)^{km} v^2\Big((C_{12})_{(10e)} + (C_0)_{(10f)} + \frac{m_k^2}{m_m^2}(C_0)_{(10g)}\Big)\,.
\end{aligned}
\tag{E.9}
$$

Next, we present the right-handed form factors. The results of the $\mathcal{O}(Y_\nu^2)$ contributions are:

$$
\begin{aligned}
F_R^{\text{MIA(1) (Y}^2)} &= \frac{1}{32\pi^2}\frac{m_m}{m_W}\left(Y_\nu Y_\nu^\dagger\right)^{km}\Big(m_k^2(C_0+C_{11})_{(1a)} + (\tilde{C}_0 + m_k^2(C_{11}-C_{12}) + m_m^2 C_{12})_{(1b)} \\
&\quad - m_k^2(C_0+C_{11}-C_{12})_{(1c)} - m_k^2(C_{11}-C_{12})_{(1d)}\Big)\,, \\
F_R^{\text{MIA(2) (Y}^2)} &= \frac{-1}{16\pi^2} m_m m_W \left(Y_\nu Y_\nu^\dagger\right)^{km}\Big((C_{12})_{(2a)} + (C_0+C_{12})_{(2b)}\Big)\,, \\
F_R^{\text{MIA(3) (Y}^2)} &= \frac{1}{8\pi^2} m_m m_W^3 \left(Y_\nu Y_\nu^\dagger\right)^{km}(D_{13})_{(3a)}\,, \\
F_R^{\text{MIA(4) (Y}^2)} &= \frac{1}{32\pi^2} m_m m_W \left(Y_\nu Y_\nu^\dagger\right)^{km}\Big((2C_0+C_{12})_{(4a)} \\
&\quad + \big(C_0 + 2m_m^2 D_{12} - (2m_H^2 - m_k^2)(D_{12}-D_{13})\big)_{(4b)}\Big)\,, \\
F_R^{\text{MIA(5) (Y}^2)} &= \frac{-1}{32\pi^2} m_m m_W \left(Y_\nu Y_\nu^\dagger\right)^{km}\Big((C_0-C_{12})_{(5a)} + m_k^2(D_{12}+D_{13})_{(5b)}\Big)\,, \\
F_R^{\text{MIA(6) (Y}^2)} &= \frac{1}{32\pi^2}\frac{m_m}{m_W} m_H^2 \left(Y_\nu Y_\nu^\dagger\right)^{km}\Big((C_{12})_{(6a)} + (C_0)_{(6b)} + m_k^2(D_{12}-D_{13})_{(6d)}\Big)\,, \\
F_R^{\text{MIA(7) (Y}^2)} &= \frac{1}{16\pi^2} m_m m_W \frac{m_k^2}{m_k^2 - m_m^2}\left(Y_\nu Y_\nu^\dagger\right)^{km}(C_{12})_{(7a)}\,, \\
F_R^{\text{MIA(8) (Y}^2)} &= \frac{1}{32\pi^2}\frac{m_m}{m_W}\frac{m_k^2}{m_k^2 - m_m^2}\left(Y_\nu Y_\nu^\dagger\right)^{km}\Big((B_1)_{(8a)} + \frac{m_m^2}{m_k^2}(B_0)_{(8b)} + (B_0)_{(8c)} + m_m^2(C_{12})_{(8d)}\Big)\,, \\
F_R^{\text{MIA(9) (Y}^2)} &= \frac{-1}{16\pi^2} m_m m_W \frac{m_k^2}{m_k^2 - m_m^2}\left(Y_\nu Y_\nu^\dagger\right)^{km}(C_{12})_{(9a)}\,, \\
F_R^{\text{MIA(10) (Y}^2)} &= \frac{-1}{32\pi^2}\frac{m_m}{m_W}\frac{m_k^2}{m_k^2 - m_m^2}\left(Y_\nu Y_\nu^\dagger\right)^{km}\Big((B_1)_{(10a)} + (B_0)_{(10b)} + (B_0)_{(10c)} \\
&\quad + m_m^2(C_{12})_{(10d)}\Big)\,.
\end{aligned}
\tag{E.10}
$$

The results of the dominant $\mathcal{O}(Y_\nu^4)$ contributions are:

$$
\begin{aligned}
F_R^{\text{MIA(1) (Y}^4)} &= \frac{1}{32\pi^2}\frac{m_m}{m_W}\left(Y_\nu Y_\nu^\dagger Y_\nu Y_\nu^\dagger\right)^{km} v^2\Big(-(C_0+C_{12})_{(1e)} - (C_{12})_{(1f)} \\
&\quad + (C_0)_{(1i)} + (\tilde{D}_0)_{(1k)} + (\tilde{D}_0)_{(1l)}\Big)\,, \\
F_R^{\text{MIA(8) (Y}^4)} &= \frac{1}{32\pi^2}\frac{m_m}{m_W}\frac{m_k^2}{m_k^2 - m_m^2}\left(Y_\nu Y_\nu^\dagger Y_\nu Y_\nu^\dagger\right)^{km} v^2\Big((C_{12})_{(8e)} + \frac{m_m^2}{m_k^2}(C_0)_{(8f)} + (C_0)_{(8g)}\Big)\,, \\
F_R^{\text{MIA(10) (Y}^4)} &= \frac{-1}{32\pi^2}\frac{m_m}{m_W}\frac{m_k^2}{m_k^2 - m_m^2}\left(Y_\nu Y_\nu^\dagger Y_\nu Y_\nu^\dagger\right)^{km} v^2\Big((C_{12})_{(10e)} + (C_0)_{(10f)} + (C_0)_{(10g)}\Big)\,.
\end{aligned}
\tag{E.11}
$$

The arguments of the above one-loop integrals are the following:

$$
\begin{aligned}
\tilde{C}_0, C_i &= \tilde{C}_0, C_i(p_2, p_1, m_W, 0, M_R) && \text{in } (1a), (1c), (2a) \\
\tilde{C}_0, C_i &= \tilde{C}_0, C_i(p_2, p_1, m_W, M_R, 0) && \text{in } (1b), (1d), (2b) \\
C_i &= C_i(p_2, p_1, m_W, M_R, M_R) && \text{in } (1e), (1f), (1i), (1j) \\
\tilde{D}_0 &= \tilde{D}_0(p_2, 0, p_1, m_W, 0, M_R, M_R) && \text{in } (1g) \\
\tilde{D}_0 &= \tilde{D}_0(p_2, p_1, 0, m_W, 0, M_R, M_R) && \text{in } (1h) \\
\tilde{D}_0 &= \tilde{D}_0(p_2, p_1, 0, m_W, M_R, M_R, 0) && \text{in } (1k) \\
\tilde{D}_0 &= \tilde{D}_0(p_2, 0, p_1, m_W, M_R, M_R, 0) && \text{in } (1l) \\
D_i &= D_i(0, p_2, p_1, 0, M_R, m_W, m_W) && \text{in } (3a), (4b), (5b), (6d) \\
C_i &= C_i(p_2, p_1, M_R, m_W, m_W) && \text{in } (4a), (4b), (5a), (5b), (6a), (6b), (6c) \\
C_{12} &= C_{12}(0, p_2, 0, M_R, m_W) && \text{in } (7a), (8d) \\
B_i &= B_i(p_2, M_R, m_W) && \text{in } (8a), (8b), (8c) \\
C_i &= C_i(0, p_2, M_R, M_R, m_W) && \text{in } (8e), (8f), (8g) \\
C_{12} &= C_{12}(0, p_3, 0, M_R, m_W) && \text{in } (9a), (10d) \\
B_i &= B_i(p_3, M_R, m_W) && \text{in } (10a), (10b), (10c) \\
C_i &= C_i(0, p_3, M_R, M_R, m_W) && \text{in } (10e), (10f), (10g)\,.
\end{aligned}
$$

We want to remark that the above formulas are valid for the degenerate $M_{R_i} = M_R$ case. Nevertheless, they can be easily generalized to the non-degenerate case by properly including the summation indices. For example, it would be enough to change

$$
\begin{aligned}
(Y_\nu Y_\nu^\dagger)^{km} C_\alpha(p_2, p_1, m_W, 0, M_R) &\to (Y_\nu^{ka} Y_\nu^{\dagger am}) C_\alpha(p_2, p_1, m_W, 0, M_{R_a})\,, \\
(Y_\nu Y_\nu^\dagger Y_\nu Y_\nu^\dagger)^{km} C_\alpha(p_2, p_1, m_W, M_R, M_R) &\to (Y_\nu^{ka} Y_\nu^{\dagger ai} Y_\nu^{ib} Y_\nu^{\dagger bm}) C_\alpha(p_2, p_1, m_W, M_{R_a}, M_{R_b})\,,
\end{aligned}
\tag{E.12}
$$

and similarly for all the terms.

E.3 The Large M_R Expansion

Here we present our analytical results for the loop-functions and form factors involved in our computation of LFVHD rates in the large M_R limit. To reach this limit we perform a systematic expansion of the amplitude in powers of (v^2/M_R^2). Generically, the first order in this expansion is $\mathcal{O}(v^2/M_R^2)$ the next order is $\mathcal{O}(v^4/M_R^4)$, etc. The logarithmic dependence with M_R is left unexpanded. In the final expansion we will keep just the dominant terms in the form factors of $\mathcal{O}(v^2/M_R^2)$ which have been shown to be sufficient to describe successfully the final amplitude for LFVHD in the heavy right-handed neutrino mass region of our interest, i.e., $M_R \gg v$.

We first calculate the large M_R expansions of all the one-loop functions and second we plug these expansions in the form factors formulas. To do this, we perform first the integration of the Feynman's parameters and next expand them for large $M_R \gg v$. Since the mass of the Higgs boson enters here, we cannot take the most used approximation of neglecting external momentum particles. In fact our expansions presented in this Appendix will apply to the present case of on-shell Higgs boson, i.e., with $p_1^2 = m_H^2$ and m_H being the realistic Higgs boson mass. Furthermore, it should be noticed that in principle there are three very different scales of masses involved in the computation: the lepton sector masses (m_{ℓ_m} and m_{ℓ_k}), the electroweak sector masses (m_W and m_H) and the new physics scale M_R. As we said, in a good approximation we can neglect the lepton masses in the one-loop functions at the beginning. However, both electroweak masses m_W and m_H must be retained in order to calculate the $\mathcal{O}(M_R^{-2})$ terms of the one-loop functions. Actually, in practice we consider the vacuum expectation value v, which is the common scale entering in both electroweak masses within the SM, and as we said above, we perform a well defined expansion in powers of an unique dimensionless parameter that is given by the ratio v^2/M_R^2.

At the numerical level, we have checked that all the expansions presented in the following are in very good accordance with the numerical results from *LoopTools*. The analytical expansions that we get for the dominant terms of the loop functions, i.e., up to $\mathcal{O}(M_R^{-2})$, are summarized as,

$$
\begin{aligned}
&B_0\left(p, M_R, m_W\right) = \Delta + 1 - \log\left(\frac{M_R^2}{\mu^2}\right) + \frac{m_W^2 \log\left(\frac{m_W^2}{M_R^2}\right)}{M_R^2} + \frac{p^2}{2M_R^2}\,,\\
&C_0\left(p_2, p_1, m_W, 0, M_R\right) = C_0\left(p_2, p_1, m_W, M_R, 0\right) = \frac{\log\left(\frac{m_W^2}{M_R^2}\right)}{M_R^2}\,,\\
&C_0\left(p_2, p_1, M_{R,} m_W, m_W\right) = \frac{2\sqrt{4\lambda - 1}\arctan\left(\sqrt{\frac{1}{4\lambda-1}}\right) - 1 + \log\left(\frac{m_W^2}{M_R^2}\right)}{M_R^2}\,,\\
&C_0\left(p_2, p_1, m_W, M_R, M_R\right) = -\frac{1}{M_R^2}\,,\\
&C_0\left(0, p_{lep}, M_R, M_R, m_W\right) = -\frac{1}{M_R^2}\,,\\
&\tilde{C}_0\left(p_2, p_1, m_W, M_R, 0\right) = \tilde{C}_0\left(p_2, p_1, m_W, 0, M_R\right)\\
&= \Delta + 1 - \log\left(\frac{M_R^2}{\mu^2}\right) + \frac{m_W^2 \log\left(\frac{m_W^2}{M_R^2}\right)}{M_R^2} + \frac{m_H^2}{2M_R^2}\,,\\
&\tilde{D}_0\left(p_2, 0, p_1, m_W, 0, M_R, M_R\right) = \tilde{D}_0\left(p_2, p_1, 0, m_W, 0, M_R, M_R\right) = -\frac{1}{M_R^2}\,,\\
&\tilde{D}_0\left(p_2, 0, p_1, m_W, M_R, M_R, 0\right) = \tilde{D}_0\left(p_2, p_1, 0, m_W, M_R, M_R, 0\right) = -\frac{1}{M_R^2}\,,\\
&B_1\left(p, M_R, m_W\right) = -\frac{\Delta}{2} - \frac{3}{4} + \frac{1}{2}\log\left(\frac{M_R^2}{\mu^2}\right) - \frac{m_W^2\left(2\log\left(\frac{m_W^2}{M_R^2}\right) + 1\right)}{2M_R^2} - \frac{p^2}{3M_R^2}\,,\\
&C_{11}\left(p_2, p_1, m_W, 0, M_R\right) = \frac{1 - \log\left(\frac{m_W^2}{M_R^2}\right)}{2M_R^2}\,,
\end{aligned}
$$

$$
\begin{aligned}
&C_{12}\left(p_2, p_1, m_W, 0, M_R\right) = \frac{1}{2M_R^2}\,,\\
&C_{11}\left(p_2, p_1, m_W, M_R, 0\right) = \frac{1-\log\left(\frac{m_W^2}{M_R^2}\right)}{2M_R^2}\,,\\
&C_{12}\left(p_2, p_1, m_W, M_R, 0\right) = -\frac{\log\left(\frac{m_W^2}{M_R^2}\right)}{2M_R^2}\,,\\
&C_{11}\left(p_2, p_1, M_R, m_W, m_W\right) = 2C_{12}\left(p_2, p_1, M_R, m_W, m_W\right)\\
&\qquad = -\frac{4\sqrt{4\lambda-1}\arctan\left(\sqrt{\frac{1}{4\lambda-1}}\right)+2\log\left(\frac{m_W^2}{M_R^2}\right)-1}{2M_R^2}\,,\\
&C_{11}\left(p_2, p_1, m_W, M_R, M_R\right) = 2C_{12}\left(p_2, p_1, m_W, M_R, M_R\right) = \frac{1}{2M_R^2}\,,\\
&C_{12}\left(0, p_{lep}, 0, M_R, m_W\right) = \frac{-\log\left(\frac{m_W^2}{M_R^2}\right)-1}{2M_R^2}\,,\\
&C_{12}\left(0, p_{lep}, M_R, M_R, m_W\right) = \frac{1}{2M_R^2}\,,\\
&D_{12}\left(0, p_2, p_1, 0, M_R, m_W, m_W\right) = 2D_{13}\left(0, p_2, p_1, 0, M_R, m_W, m_W\right)\\
&\qquad = \frac{2\left(-4\lambda\arctan^2\left(\sqrt{\frac{1}{4\lambda-1}}\right)+2\sqrt{4\lambda-1}\arctan\left(\sqrt{\frac{1}{4\lambda-1}}\right)-1\right)}{M_R^2 m_H^2}\,,
\end{aligned}
\tag{E.13}
$$

where we have used the usual definitions in dimensional regularization, $\Delta = 2/\epsilon - \gamma_E + \mathrm{Log}(4\pi)$ with $D = 4-\epsilon$ and μ the usual scale, and we have denoted the mass ratio $\lambda = m_W^2/m_H^2$ to shorten the result.

Taking into account the formulas in Eq. (E.13), plugging them into the results of the form factors in the Appendix E.2, neglecting the tiny terms with lepton masses, and pairing diagrams conveniently, we finally get the results for the dominant terms of the various type diagrams (i), see Fig. 4.1, of the MIA form factors valid in the large $M_R \gg v$ regime:

$$
\begin{aligned}
F_L^{(1)} &= \frac{1}{32\pi^2}\frac{m_k}{m_W}\Bigg[\left(Y_\nu Y_\nu^\dagger\right)^{km}\left(\Delta+1-\log(\frac{M_R^2}{\mu^2})+\frac{m_W^2\log\left(\frac{m_W^2}{M_R^2}\right)}{M_R^2}+\frac{m_H^2}{2M_R^2}\right)\\
&\quad -\frac{5}{2}\frac{v^2}{M_R^2}\left(Y_\nu Y_\nu^\dagger Y_\nu Y_\nu^\dagger\right)^{km}\Bigg],\\
F_L^{(2)} &= -\frac{1}{32\pi^2}\frac{m_k}{m_W}\left(Y_\nu Y_\nu^\dagger\right)^{km}\frac{m_W^2}{M_R^2}\left(1+\log\left(\frac{m_W^2}{M_R^2}\right)\right),
\end{aligned}
$$

$$
\begin{aligned}
F_L^{(3)} &= \frac{1}{8\pi^2}\frac{m_k}{m_W}\left(Y_\nu Y_\nu^\dagger\right)^{km}\frac{\lambda m_W^2}{M_R^2}\left(-4\lambda\arctan^2\left(\frac{1}{\sqrt{4\lambda-1}}\right)\right. \\
&\quad \left. +2\sqrt{4\lambda-1}\arctan\left(\frac{1}{\sqrt{4\lambda-1}}\right)-1\right), \\
F_L^{(4+5)} &= \frac{1}{32\pi^2}\frac{m_k}{m_W}\left(Y_\nu Y_\nu^\dagger\right)^{km}\frac{m_W^2}{M_R^2}\left(8\lambda\arctan^2\left(\frac{1}{\sqrt{4\lambda-1}}\right)\right. \\
&\quad \left. -2\sqrt{4\lambda-1}\arctan\left(\frac{1}{\sqrt{4\lambda-1}}\right)+\frac{1}{2}+\log\left(\frac{m_W^2}{M_R^2}\right)\right), \\
F_L^{(6)} &= \frac{1}{32\pi^2}\frac{m_k}{m_W}\left(Y_\nu Y_\nu^\dagger\right)^{km}\frac{m_H^2}{M_R^2}\left(\sqrt{4\lambda-1}\arctan\left(\frac{1}{\sqrt{4\lambda-1}}\right)-\frac{3}{4}+\frac{\log\left(\frac{m_W^2}{M_R^2}\right)}{2}\right), \\
F_L^{(7+9)} &= 0\,, \\
F_L^{(8+10)} &= -\frac{1}{32\pi^2}\frac{m_k}{m_W}\left[\left(Y_\nu Y_\nu^\dagger\right)^{km}\left(\Delta+1-\log(\frac{M_R^2}{\mu^2})+\frac{m_W^2\log\left(\frac{m_W^2}{M_R^2}\right)}{M_R^2}\right)\right. \\
&\quad \left. -\frac{v^2}{M_R^2}\left(Y_\nu Y_\nu^\dagger Y_\nu Y_\nu^\dagger\right)^{km}\right].
\end{aligned}
\tag{E.14}
$$

And similar formulas can be obtained for the F_R form factors. Notice that in the results above we have included all the relevant contributions, i.e., up to $\mathcal{O}(Y_\nu^2+Y_\nu^4)$ and it turns out, as announced in Sect. 4.3, that they are just the diagrams (1)+(8)+(10) that provide contributions of $\mathcal{O}(Y_\nu^4)$ with a v^2/M_R^2 dependence. The other diagrams will also give $\mathcal{O}(Y_\nu^4)$ contributions but they will be suppressed since they go with a v^4/M_R^4 dependence, and we do not keep these small contributions in our expansions.

E.4 MIA Form Factors in the Unitary Gauge

In order to check the gauge invariance of our results for the LFVHD form factors (and therefore the partial width) that we have computed in the MIA by using the Feynman-'t Hooft gauge, we present here the computation of these same form factors but using a different gauge choice, in particular the unitary gauge (UG). We will demonstrate that when computing the MIA form factor F_L to $\mathcal{O}(Y_\nu^2+Y_\nu^4)$ we get the same result as in Eq. (4.30). A similar demonstration can be done for F_R but we do not include it here for shortness. For this exercise, we ignore the tiny terms suppressed by factors of the lepton masses as we did in Eq. (4.30).

First, we list the relevant one-loop diagrams contributing to the form factor F_L in the UG. Since, in this gauge there are not Goldstone bosons, there will be just diagrams of type: (2), (3), (7) and (9). Generically, each of these diagrams will get contributions of $\mathcal{O}(Y_\nu^2)$ and $\mathcal{O}(Y_\nu^4)$. Second, we write the propagator of the W gauge boson in the UG, P_W^{UG}, by splitting it into two parts, P_W^a and P_W^b:

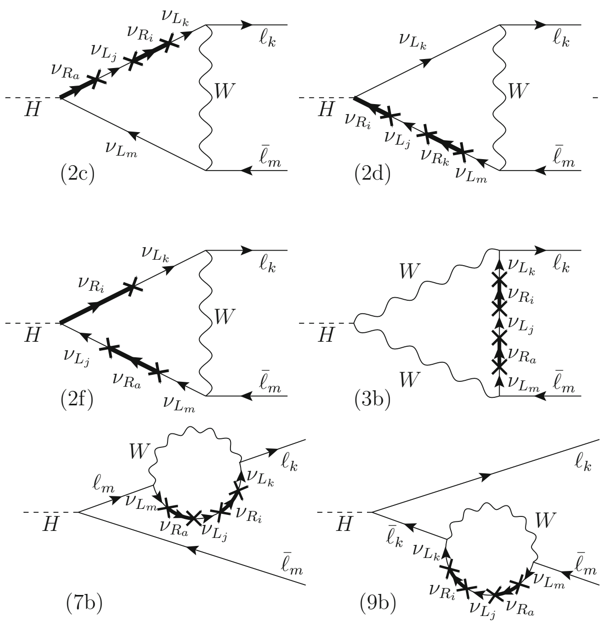

Fig. E.3 Relevant diagrams for the form factors to $\mathcal{O}(Y_\nu^4)$ in the unitary gauge

$$P_W^{\text{UG}} = P_W^a + P_W^b = -\frac{i g_{\mu\nu}}{p^2 - m_W^2} + \frac{i p_\mu p_\nu}{m_W^2 (p^2 - m_W^2)}\,, \tag{E.15}$$

such that, P_W^a coincides with the W propagator in the Feynman-'t Hooft gauge. Then, each diagram of type (i), i = 2, 3, 7, 9, will receive three kind of contributions: (1) from the part P_W^a one gets the same contributions to $\mathcal{O}(Y_\nu^2)$ as those we got in the Feynman-'t Hooft gauge from the five diagrams (2a), (2b), (3a), (7a) and (9a) in Figs. 4.18 and 4.19; (2) new contributions to $\mathcal{O}(Y_\nu^2)$ that come from considering the new propagator term P_W^b in these same diagrams (2a), (2b), (3a), (7a) and (9a); (3) contributions to $\mathcal{O}(Y_\nu^4)$ that come from new diagrams which were not relevant in the Feynman-'t Hooft gauge, but they are relevant in the UG. By relevant we mean leading to dominant $\mathcal{O}(M_R^{-2})$ contributions in the large M_R expansion. These new diagrams contributing to order $\mathcal{O}(Y_\nu^4)$ in the UG are the seven diagrams shown in Fig. E.3. Thus, we get in total twelve one-loop diagrams contributing in the UG: (2a), (2b), (2c), (2d), (2e), (2f), (3a), (3b), (7a), (7b), (9a) and (9b).

Next we present the results in the UG for each type of diagram (i), specifying the various contributions explained above, which for clarity we present correspondingly ordered in three lines, the first line is for kind (1), the second line is for kind (2) and the third line is for kind (3). The UG F_L form factors to $\mathcal{O}(Y_\nu^2 + Y_\nu^4)$ that we get are, as follows:

$$
\begin{aligned}
F_L^{\mathrm{UG}(2)} &= -\frac{1}{16\pi^2} m_k m_W \left(Y_\nu Y_\nu^\dagger\right)^{km} \left((C_0 + C_{11} - C_{12})_{(2a)} + (C_{11} - C_{12})_{(2b)}\right) \\
&+ \frac{1}{32\pi^2} \frac{m_k}{m_W} \Big[\left(Y_\nu Y_\nu^\dagger\right)^{km} \left((\tilde{C}_0)_{(2a)} - (B_1)_{(2b)}\right) \\
&+ \left(Y_\nu Y_\nu^\dagger Y_\nu Y_\nu^\dagger\right)^{km} v^2 \left(-(C_{11})_{(2c)} + (\tilde{D}_0)_{(2d)} + (\tilde{D}_0 - (C_{11} - C_{12}))_{(2e)} - (C_{11} - C_{12})_{(2f)}\right)\Big], \\
F_L^{\mathrm{UG}(3)} &= \frac{1}{8\pi^2} m_k m_W^3 \left(Y_\nu Y_\nu^\dagger\right)^{km} (D_{12} - D_{13})_{(3a)} \\
&- \frac{1}{32\pi^2} \left(Y_\nu Y_\nu^\dagger\right)^{km} \frac{m_k}{m_W} \left[2B_0 + B_1 - (2m_W^2 + m_H^2)(C_0 + C_{11} - C_{12}) + 2m_W^2 m_H^2 D_{13}\right]_{(3a)} \\
&- \frac{1}{32\pi^2} \left(Y_\nu Y_\nu^\dagger Y_\nu Y_\nu^\dagger\right)^{km} \frac{m_k}{m_W} v^2 \left[2C_0 + C_{12}\right]_{(3b)}, \\
F_L^{\mathrm{UG}(7)} &= \frac{1}{16\pi^2} m_k m_W \frac{m_m^2}{m_k^2 - m_m^2} \left(Y_\nu Y_\nu^\dagger\right)^{km} (C_{12})_{(7a)} \\
&\frac{1}{32\pi^2} \frac{m_k m_m^2}{m_W (m_k^2 - m_m^2)} \Big[\left(Y_\nu Y_\nu^\dagger\right)^{km} (2B_0 + B_1)_{(7a)} \\
&+ \left(Y_\nu Y_\nu^\dagger Y_\nu Y_\nu^\dagger\right)^{km} v^2 (2C_0 + C_{12})_{(7b)}\Big], \\
F_L^{\mathrm{UG}(9)} &= -\frac{1}{16\pi^2} m_k m_W \frac{m_m^2}{m_k^2 - m_m^2} \left(Y_\nu Y_\nu^\dagger\right)^{km} (C_{12})_{(9a)}, \\
&- \frac{1}{32\pi^2} \frac{m_k m_m^2}{m_W (m_k^2 - m_m^2)} \Big[\left(Y_\nu Y_\nu^\dagger\right)^{km} (2B_0 + B_1)_{(9a)} \\
&+ \left(Y_\nu Y_\nu^\dagger Y_\nu Y_\nu^\dagger\right)^{km} v^2 (2C_0 + C_{12})_{(9b)}\Big],
\end{aligned} \tag{E.16}
$$

where the arguments of the one-loop functions are:

$$
\begin{aligned}
\tilde{C}_0, C_i &= \tilde{C}_0, C_i(p_2, p_1, m_W, 0, M_R) && \text{in } (2a) \\
B_i &= B_i(p_{lep}, m_W, M_R) && \text{in } (2b) \\
C_i &= C_i(p_2, p_1, m_W, M_R, 0) && \text{in } (2b) \\
C_i &= C_i(p_{lep}, 0, m_W, M_R, M_R) && \text{in } (2c) \\
\tilde{D}_0 &= \tilde{D}_0(p_2, p_1, 0, m_W, 0, M_R, M_R) && \text{in } (2d) \\
C_i &= C_i(p_2, p_1, m_W, M_R, M_R) && \text{in } (2e), (2f) \\
\tilde{D}_0 &= \tilde{D}_0(p_2, 0, p_1, m_W, 0, M_R, M_R) && \text{in } (2e) \\
B_i &= B_i(p_{lep}, M_R, m_W) && \text{in } (3a), (7a), (9a) \\
C_i &= C_i(p_2, p_1, M_R, m_W, m_W) && \text{in } (3a) \\
D_i &= D_i(0, p_2, p_1, 0, M_R, m_W, m_W) && \text{in } (3a) \\
C_i &= C_i(0, p_{lep}, M_R, M_R, m_W) && \text{in } (3b), (7b), (9b) \\
C_i &= C_i(0, p_{lep}, 0, M_R, m_W) && \text{in } (7a), (9a).
\end{aligned}
$$

The comparison of the previous results with that in Eq. (4.30) then goes as follows. First, it is clear from the above results, that once again the contributions from diagrams (7) and (9) cancel out fully, as it happened in the Feynman-'t Hooft gauge. Therefore, $F_L^{\mathrm{UG}} = F_L^{\mathrm{UG}(2)} + F_L^{\mathrm{UG}(3)}$. Then, the first line in $F_L^{\mathrm{UG}(2)}$ and the first line in $F_L^{\mathrm{UG}(3)}$ match correspondingly with the contributions from (2) and (3) in the Feynman-'t Hooft gauge. Next, by using the relation,

$$
B_0(p_{lep}, M_R, m_W) + B_1(p_{lep}, M_R, m_W) + B_1(p_{lep}, m_W, M_R) = 0, \tag{E.17}
$$

we get that the sum of the second line in $F_L^{\mathrm{UG}(2)}$ and the second line in $F_L^{\mathrm{UG}(3)}$ gives exactly the contributions to $\mathcal{O}(Y_\nu^2)$ from (1)+(8)+(10)+(4)+(5)+(6) in the Feynman-'t Hooft gauge. Finally, by using the relation

$$C_{11}(p_{lep}, 0, m_W, M_R, M_R) + (C_0 + C_{12})(0, p_{lep}, M_R, M_R, m_W) = 0\,, \quad \text{(E.18)}$$

we get that the sum of the third line in $F_L^{\mathrm{UG}(2)}$ and the third line in $F_L^{\mathrm{UG}(3)}$ gives exactly the contributions to $\mathcal{O}(Y_\nu^4)$ from (1)+(8)+(10). Therefore, in summary, we get the identity of the total result for F_L computed in both gauges, leading to the gauge invariant result of Eq. (4.30).

Appendix F
Form Factors for LFVZD in the ISS Model

In this Appendix we give the analytical expressions for the form factors contributing to $Z \to \ell_k \ell_m$, as they are defined in Eqs. (5.1) and (5.2). In the Feynman-t'Hooft gauge, they are obtained by computing the ten diagrams shown in Fig. 5.1. We take the results from [10–12] and adapt them to our notation and to the convection of *LoopTools* [8] for the loop functions.

The form factors of the different diagrams are

$$\mathcal{F}_Z^{(1)} = \frac{1}{2} B_{\ell_k n_i} B^*_{\ell_m n_j} \left\{ -C_{n_i n_j} x_i x_j m_W^2 C_0 + C^*_{n_i n_j} \sqrt{x_i x_j} \left[m_Z^2 C_{12} - 2C_{00} + \frac{1}{2} \right] \right\}, \tag{F.1}$$

where $C_{0,12,00} \equiv C_{0,12,00}(0, m_Z^2, 0, m_W^2, m_{n_i}^2, m_{n_j}^2)$;

$$\mathcal{F}_Z^{(2)} = B_{\ell_k n_i} B^*_{\ell_m n_j} \left\{ -C_{n_i n_j} \left[m_Z^2 \Big(C_0 + C_1 + C_2 + C_{12} \Big) - 2C_{00} + 1 \right] + C^*_{n_i n_j} \sqrt{x_i x_j} \, m_W^2 C_0 \right\}, \tag{F.2}$$

where $C_{0,1,2,12,00} \equiv C_{0,1,2,12,00}(0, m_Z^2, 0, m_W^2, m_{n_i}^2, m_{n_j}^2)$;

$$\mathcal{F}_Z^{(3)} = 2c_W^2 B_{\ell_k n_i} B^*_{\ell_m n_i} \left\{ m_Z^2 \Big(C_1 + C_2 + C_{12} \Big) - 6C_{00} + 1 \right\}, \tag{F.3}$$

where $C_{1,2,12,00} \equiv C_{1,2,12,00}(0, m_Z^2, 0, m_{n_i}^2, m_W^2, m_W^2)$;

$$\mathcal{F}_Z^{(4)} + \mathcal{F}_Z^{(5)} = -2s_W^2 \, B_{\ell_k n_i} B^*_{\ell_m n_i} \, x_i \, m_W^2 C_0, \tag{F.4}$$

where $C_0 \equiv C_0(0, m_Z^2, 0, m_{n_i}^2, m_W^2, m_W^2)$;

$$\mathcal{F}_Z^{(6)} = -(1 - 2s_W^2) \, B_{\ell_k n_i} B^*_{\ell_m n_i} \, x_i \, C_{00}, \tag{F.5}$$

where $C_{00} \equiv C_{00}(0, m_Z^2, 0, m_{n_i}^2, m_W^2, m_W^2)$;

X. Marcano, *Lepton Flavor Violation from Low Scale Seesaw Neutrinos with Masses Reachable at the LHC*, Springer Theses, https://doi.org/10.1007/978-3-319-94604-7

$$\mathcal{F}_Z^{(7)} + \mathcal{F}_Z^{(8)} + \mathcal{F}_Z^{(9)} + \mathcal{F}_Z^{(10)} = \frac{1}{2}(1 - 2c_W^2)\, B_{\ell_k n_i} B^*_{\ell_m n_i}\, \{(2 + x_i)B_1 + 1\}\,, \qquad \text{(F.6)}$$

where $B_1 \equiv B_1(0, m_{n_i}^2, m_W^2)$.

In all these formulas, sum over neutrino indices, $i,\ j = 1, \ldots, 9$ has to be understood, $x_i \equiv m_{n_i}^2/m_W^2$ and the charged lepton masses have been neglected.

References

1. A. Ilakovac, A. Pilaftsis, Nucl. Phys. B **437**, 491 (1995). https://doi.org/10.1016/0550-3213(94)00567-X. arXiv:hep-ph/9403398 [hep-ph]
2. R. Alonso, M. Dhen, M.B. Gavela, T. Hambye, JHEP **01**, 118 (2013). https://doi.org/10.1007/JHEP01(2013)118. arXiv:1209.2679 [hep-ph]
3. F. Deppisch, J.W.F. Valle, Phys. Rev. D **72**, 036001 (2005). https://doi.org/10.1103/PhysRevD.72.036001. arXiv:hep-ph/0406040 [hep-ph]
4. A. Abada, D. Das, A.M. Teixeira, A. Vicente, C. Weiland, JHEP **02**, 048 (2013). https://doi.org/10.1007/JHEP02(2013)048. arXiv:1211.3052 [hep-ph]
5. A. Abada, A.M. Teixeira, A. Vicente, C. Weiland, JHEP **02**, 091 (2014). https://doi.org/10.1007/JHEP02(2014)091. arXiv:1311.2830 [hep-ph]
6. E. Akhmedov, A. Kartavtsev, M. Lindner, L. Michaels, J. Smirnov, JHEP **05**, 081 (2013). https://doi.org/10.1007/JHEP05(2013)081. arXiv:1302.1872 [hep-ph]
7. G. Passarino, M.J.G. Veltman, Nucl. Phys. B **160**, 151 (1979). https://doi.org/10.1016/0550-3213(79)90234-7
8. T. Hahn, M. Perez-Victoria, Comput. Phys. Commun. **118**, 153 (1999). https://doi.org/10.1016/S0010-4655(98)00173-8. arXiv:hep-ph/9807565 [hep-ph]
9. E. Arganda, A.M. Curiel, M.J. Herrero, D. Temes, Phys. Rev. D **71**, 035011 (2005). https://doi.org/10.1103/PhysRevD.71.035011. arXiv:hep-ph/0407302 [hep-ph]
10. J.I. Illana, M. Jack, T. Riemann (1999), arXiv:hep-ph/0001273 [hep-ph]
11. J.I. Illana, T. Riemann, Phys. Rev. D **63**, 053004 (2001). https://doi.org/10.1103/PhysRevD.63.053004. arXiv:hep-ph/0010193 [hep-ph]
12. A. Abada, V. De Romeri, S. Monteil, J. Orloff, A.M. Teixeira, JHEP **04**, 051 (2015). https://doi.org/10.1007/JHEP04(2015)051. arXiv:1412.6322 [hep-ph]

Curriculum Vitae

Xabier Marcano
Posdoctoral Researcher
Laboratoire de Physique Théorique d'Orsay
Bat. 210, Office 123
Univ. Paris-Sud 11
91405 Orsay, France
xabier.marcano@th.u-psud.fr

Education

2013–2017	**Ph.D In Theoretical Physics** Instituto de Física Teórica and Universidad Autónoma de Madrid, Spain Supervisor: Prof. María José Herrero
2011–2013	**Master in Theoretical Physics** Universidad Autónoma de Madrid, Spain
2006–2011	**Bachelor Degree in Physics** Universidad del País Vasco/Euskal Herriko Unibertsitatea, Basque Country, Spain

Publications

1. **Production of vector resonances at the LHC via WZ-scattering: a unitarized EChL analysis**
JHEP 11 (2017) 098 [arXiv:1707.04580]
R.L. Delgado, A. Dobado, D. Espriu, C. Garcia-Garcia, M.J. Herrero, X. Marcano, J.J. Sanz-Cillero
2. **Effective LFV $H\ell_i\ell_j$ vertex from right-handed neutrinos within the Mass Insertion Approximation**
Phys.Rev. D95 (2017) no.9, 095029 [arXiv:1612.09290]
E. Arganda, M.J. Herrero, X. Marcano, R. Morales, A. Szynkman

X. Marcano, *Lepton Flavor Violation from Low Scale Seesaw Neutrinos with Masses Reachable at the LHC*, Springer Theses, https://doi.org/10.1007/978-3-319-94604-7

3. **Lepton flavor violating Z decays: A promising window to low scale seesaw neutrinos**
   Phys.Rev. D95 (2017) no.7, 075028 [arXiv:1607.05257]
   V. De Romeri, M.J. Herrero, X. Marcano, F. Scarcella
4. **Exotic $\mu\tau jj$ events from heavy ISS neutrinos at the LHC**
   Phys.Lett. B752 (2016) 46-50 [arXiv:1508.05074]
   E. Arganda, M.J. Herrero, X. Marcano, C. Weiland
5. **Enhancement of the lepton flavor violating Higgs boson decay rates from SUSY loops in the inverse seesaw model**
   Phys.Rev. D93 (2016) no.5, 055010 [arXiv:1508.04623]
   E. Arganda, M.J. Herrero, X. Marcano, C. Weiland
6. **Radiative corrections to M_h from three generations of Majorana neutrinos and sneutrinos**
   Adv.High Energy Phys. 2015 (2015) 152394 [arXiv:1407.1083]
   S. Heinemeyer, J. Hernández-García, M.J. Herrero, X. Marcano, A.M. Rodríguez-Sánchez
7. **Imprints of massive inverse seesaw model neutrinos in lepton flavor violating Higgs decays**
   Phys.Rev. D91 (2015) no.1, 015001 [arXiv:1405.4300]
   E. Arganda, M.J. Herrero, X. Marcano, C. Weiland